Low-Grade Heat Conversion into Electricity by Thermoelectric and Electrochemical Systems

by

Dongwook Lee

B.S. Materials Science and Engineering
Korea Advanced Institute of Science and Technology, 2012

Submitted to the Department of Materials Science and Engineering
in Partial Fulfillment of the Requirements for the Degree of

Doctor of Philosophy

at the

MASSACHUSETTS INSTITUTE OF TECHNOLOGY

August 2018

Author ……
Dongwook Lee
Department of Materials Science and Engineering
August 17, 2018

Certified by ……
Yang Shao-Horn
W.M. Keck Professor of Energy
Thesis Supervisor

Accepted by …..…….....
Donald R. Sadoway
John F. Elliot Professor of Materials Chemistry
Chair, Department Committee on Graduate Students

Low-Grade Heat Conversion into Electricity by Thermoelectric and Electrochemical Systems

by

Dongwook Lee

Submitted to the Department of Materials Science and Engineering on
August 17, 2018, in partial fulfillment of the requirements for the degree of
Doctor of Philosophy

ABSTRACT

Developing cost effective technologies that convert low-grade heat into electricity is essential to meet the increasing demand for renewable energy systems. Thermoelectric and recently emergent electrochemical heat conversion devices are promising candidates for this purpose. However, current performance and cost of these devices limit their widespread application. In this thesis, we investigate design guidelines for heterostructured thermoelectric systems and electrochemical heat energy harvesters to address these challenges.

Material cost and scarcity of elements in state-of-the-art thermoelectric materials are current limitations. Conductive polymers has become an attractive alternative to those materials, however they suffer from low Seebeck coefficient. Nanoscale composites of inorganic semiconductors with conductive polymers could improve low Seebeck coefficients and power factors of conductive polymers, however quantitative understandings on the mechanisms lying behind the enhancements were often missing. In our research, thin film heterostructures of a conductive polymer, PEDOT:PSS / undoped Si or undoped Ge were selected as templates for mechanistic investigations on thermoelectric performance enhancements. With the combination of experiments and simulation, it was determined that p-type PEDOT:PSS transferred holes to the interfaces of adjacent Si and Ge, and these holes could take advantage of higher hole mobility of Si and Ge. This phenomenon called modulation doping, was responsible for thermoelectric power factor enhancements in Si / PEDOT:PSS and Ge / PEDOT:PSS heterostructures.

Another technology to transform low-grade heat into electricity is electrochemical heat conversion. Traditionally, the electrochemical heat conversion into electricity suffered from low conversion efficiency originating from low ionic conductivity of electrolytes, even though high thermopowers often reaching several mV/K has been an alluring advantage. Recently developed breakthrough on operating such devices under thermodynamic cycles bypassed low ionic conductivity issue, thereby improving the conversion efficiency by multiple orders of magnitude. In this study, we focused on improving efficiency by increasing thermopowers and suppressing heat capacity of the system, while maintaining the autonomy of thermodynamic cycles without need for recharging by external sources of electricity. These detailed interpretations on nanoscale composite thermoelectric systems and electrochemical heat harvester provide insights for the design of next-generation thermoelectric and electrochemical heat energy harnessing solutions.

Thesis Supervisor: Professor Yang Shao-Horn
Title: W.M. Keck Professor of Energy

Thesis Committee

Prof. Yang Shao-Horn
W.M. Keck Professor of Energy
Mechanical Engineering, Materials Science and Engineering, MIT, Chair/Advisor

Prof. Jeffrey Grossman
Morton and Claire Goulder and Family Professor in Environmental Systems, MacVicar Fellow
Materials Science and Engineering, MIT

Prof. Karen Gleason
Alexander and I. Michael Kasser (1960) Professor, Associate Provost
Chemical Engineering, MIT

Prof. Silvija Gradečak
Professor in Materials Science and Engineering
Materials Science and Engineering, MIT

Acknowledgements

None of the work presented in this thesis would have been possible without the help and guidance of many individuals.

My advisor Prof. Yang Shao-Horn has been a great mentor during course of my Ph.D., and has always encouraged to think systematically and to keep curiosity. I am truly grateful for her guidance during my pursuit of a doctoral degree.

I also want to thank my committee members, Prof. Jeffrey Grossman, Prof. Silvija Gradečak, and Prof. Karen Gleason, who always provided great insight that will last during rest of my academic life.

I truly appreciate Prof. Gang Chen on providing critical insights to elevate my thermoelectric works to certain level.

The work in this thesis, I have to say, is not only my work but the work of many individuals in my lab. Not one of the projects was solely conceptualized or carried out by myself, but was done through idea gathering, countless long discussions and collaborative experiments. A few people I would like to acknowledge personally include:

Prof. Dongkyu Lee as a full-blown individual taught me everything about how to live in the laboratory, in MIT, and rest of my life.

My first mentors at MIT, Dr. Christopher Carlton and Mr. Chris Kuryak taught me how to perform research and work in the Electrochemical Energy Lab. Their long hours of instruction and advice were instrumental in my initial developments.

Prof. Sayed Youssef Sayed and Prof. Sangyeop Lee helped me greatly on rational and systematic design of experiments. They also cared me a lot so that our collaboration does not go in the wrong directions.

Mr. Jiawei Zhou played the most critical role in the development of simulation tool for thermoelectric research. I truly enjoyed active discussion with him.

When transitioning to projects on electrochemical heat conversion, I was very fortunate to have Dr. Botao Huang and Mr. Patrick Linford. They taught me all the details I need to consider for designing electrochemical heat harvesters.

Mr. Jame Sun was very helpful on every aspect in transforming ideas into real experimental installations. He machined a lot of electrochemical cells and revived an electrochemical thermopower measurement setup. His talents on architecting devices and practical machining were invaluable.

I have learnt so much about rechargeable batteries for the last part of my thesis from Dr. Ryoichi Tatara, Ms. Pinar Karayaylali and Mr. Yang Yu, and Dr. Soo Kim.

I also received incredible guidance and support from our collaborators including: Dr. Kurt Broderick (MIT MTL), Dr. Dimitre Karpuzov (University of Alberta), Dr. Shihong Xu (University of Alberta), Dr. Charlie Settens (MIT CMSE), and Dr. Hao-Yu Lin (Harvard CNS).

Finally, I must thank my beautiful and amazing wife and daughter, Sophie and Elena. They have supported me every day physically and emotionally. I cannot possibly thank them enough.

Table of Contents

1. Introduction

1.1. Motivation for Thermoelectrics and Electrochemical Heat Harvesting

As energy demand around the world increases and the amount of non-renewable fossil fuels decreases, the need for sustainable renewable energy sources is evident. In addition to the growing demand for energy, there is also a push for reducing the amount of emitted pollution, in the form of greenhouse gasses, by using clean energy sources. A solution to both of these energy problems can be realized by reducing the amount of wasted energy. The United States wastes about 57.5 % of the energy it produces, the majority of which takes the form of waste heat (**Figure 1.1**). Thermoelectric materials and electrochemical heat conversion devices which directly convert heat to electricity have the ability to recycle the wasted heat into a useful energy, electricity. Therefore, both technologies have the potential to increase the efficiency of energy production and reduce the amount of emitted pollution.

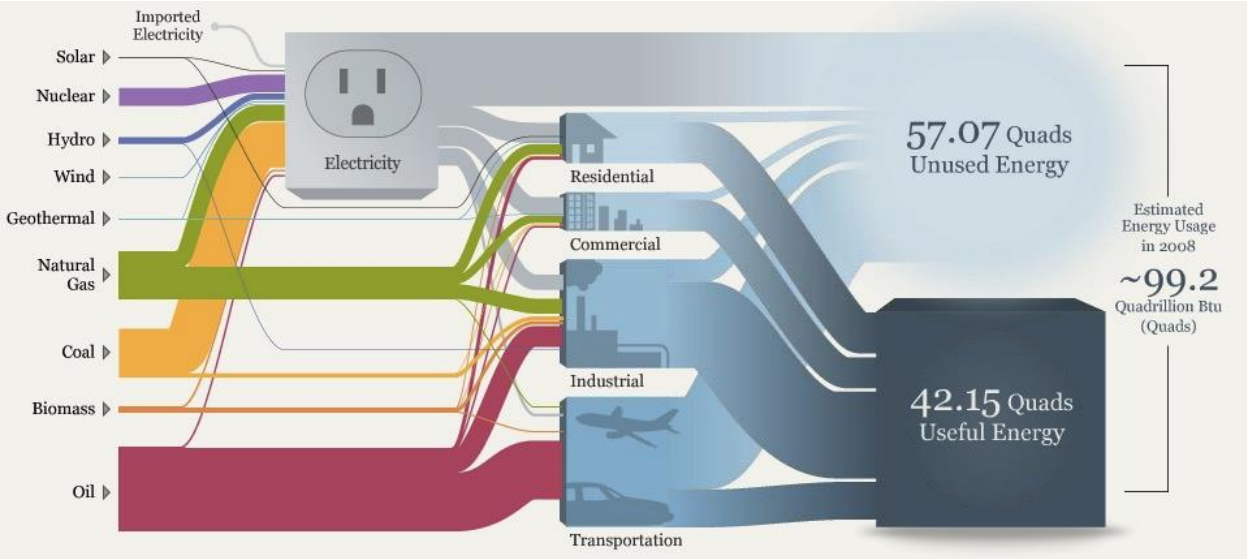

Figure 1.1. The energy flow of the United States in 2014, based on the energy flow diagram produced by Lawrence Livermore National Laboratory for 2014. Sources of energy are on the left and uses of the energy on the right. About 58% of the energy goes unused. The majority of this unused energy is in the form of waste heat[1]. The data are from the Energy Information Administration of the U.S. Department of Energy (DOE/EIA-0035(2015–03)).

However, high material cost prohibits thermoelectric technology to be adopted broadly. The state-of-the-art thermoelectric materials are typically compounds of Bismuth or Antimony chalcogenides (Bi_2Te_3, Bi_2Se_3, Sb_2Te_3, Sb_2Se_3), or their alloys. Thus, the technology becomes expensive due to the limited supply of the those constituent elements[2]. For this reason, research about conductive polymers of which constituent elements are earth-abundant carbon, hydrogen, oxygen and sulfur has been spurred. Other advantages of conductive polymers as thermoelectric materials include their lower prices[3], flexibility[4,5], and easiness to process using techniques such as inkjet printing[6,7], spin-coating[8], and drop casting[9]. However, conductive polymers in general could not match the thermoelectric performance of the state-of-the-art thermoelectric materials so far. For instance, even the best conductive polymer for thermoelectric application, PEDOT:PSS has a much lower thermoelectric performance[10] that should be improved in order to become competitive. Thus, an alternative approach of forming nanoscale composites with conductive polymers was explored to enhance thermoelectric performance of the conductive polymers in this research.

Another most serious challenge for thermoelectric technology is low heat to electricity conversion efficiency[11]. Even though recent progress during the last decade achieved significant increase in conversion efficiency[12-19], the conversion efficiency still could not reach that of the traditional heat engines (**Figure 1.2**). For certain circumstances where large volume and heavy weight of traditional heat engine are not favorable, thermoelectrics can be preferably applied. Otherwise, it is projected that current thermoelectric technology cannot deliver sufficient efficiency to be competitive in the market[11], combined with cost issues[2].

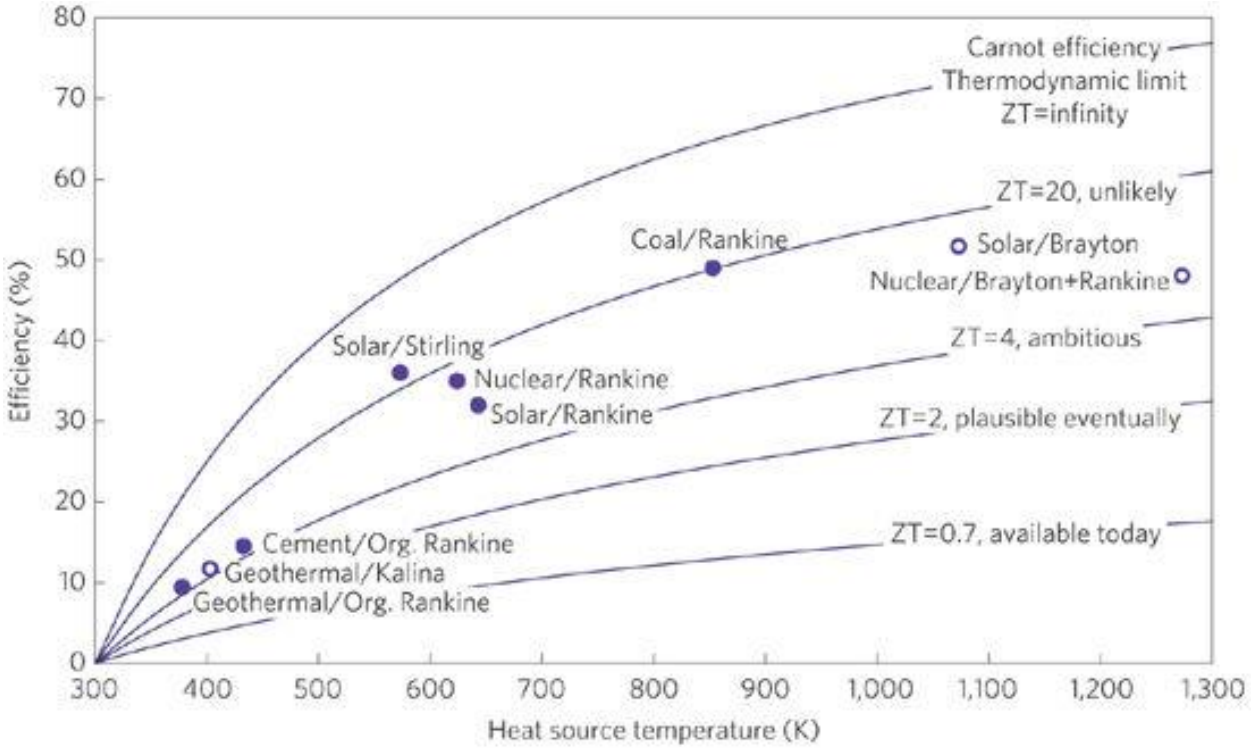

Figure 1.2. The conversion efficiency via thermoelectric technology still remains limited, compared to those of other forms of heat conversion technologies. Plot from *An inconvenient truth about thermoelectrics* and used with permission from the Nature Publishing Group[11].

This projection stimulated research for alternative heat to electricity conversion technologies. One of the most prominent alternative technologies is electrochemical heat harvesting, because it can usually produce much higher thermopower (often above 1 mV/K) than those of conventional thermoelectric materials (**Figure 1.4**). Electrochemical heat harvesting itself is not a new concept, and has been actively investigated since a few decades ago[20-28]. However, the electrochemical heat harvesting technology had always suffered a lot from the bottleneck limitation in low ionic conductivity, which is usually 4 to 6 orders of magnitude smaller than electronic conductivity of state-of-the-art thermoelectric materials[29]. Novel thermodynamic cycles[30-40] for electrochemical heat harvesting were developed recently to dodge the critical low ionic conductivity issue. This innovation is proven to enable much higher conversion efficiency than that of conventional thermoelectrics (**Figure 1.4**). This new technology can possibly lead to

more widespread application of waste heat recovery devices, eventually contributing to reduce the greenhouse gas emission.

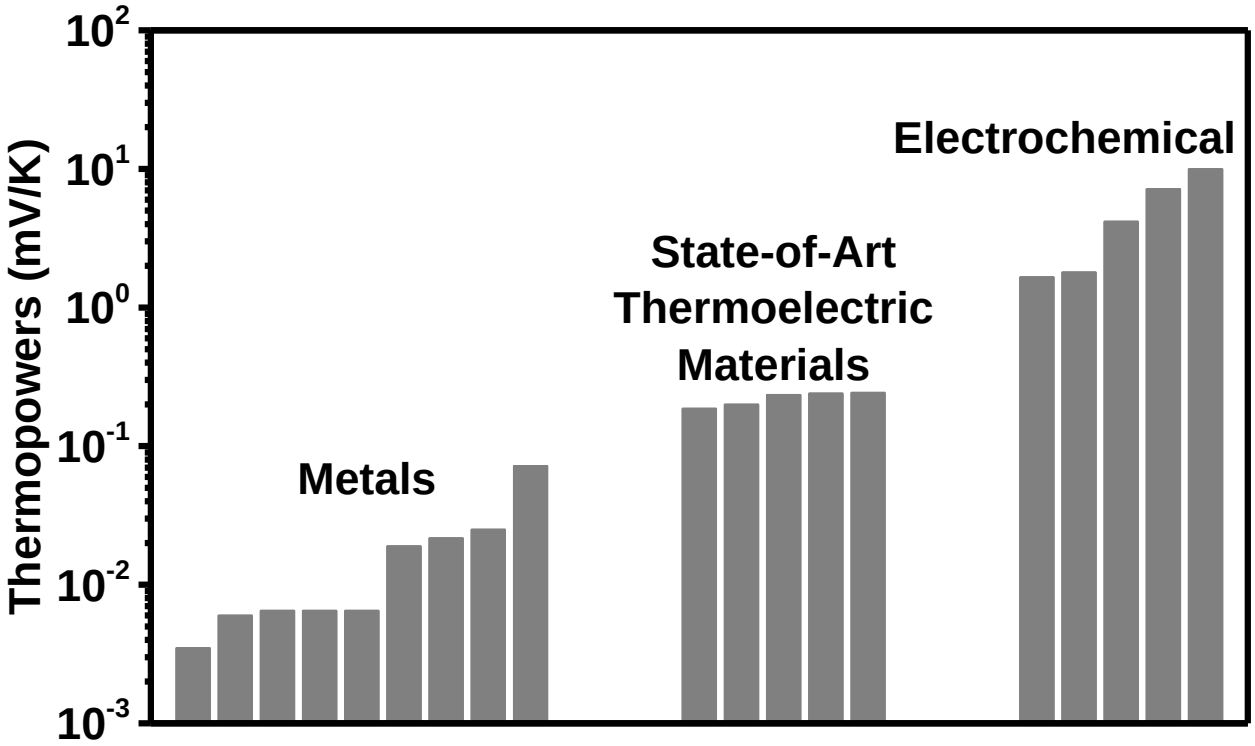

Figure 1.3. Thermopowers of redox active species are generally 10 – 100 fold larger than Seebeck coefficients of conventional semiconductors and metals. From the left, the listed materials correspond to Al[41], Rh[42], Cu[43], Ag[43], Au[43], Fe[43], Chromel[43], Nichrome[42], Bi[44] in 'Metals' category, and $Bi_2Sb_xTe_{3-x}$[45], Bi_2Te_3[46], Si nanowires[47,48], $PbSe_{1-x}Te_x/PbTe$[49], Bi_2Te_3/Sb_2Te_3[50] in 'State-of-the-art Thermoelectric Materials' category, and $Co(bpy)_3^{2+/3+}$ in [EMIM][NTf2][51], $Fe(CN)_6^{3-/4-}{}_{(aq)}$[32], $Cu(bpy)_2^{1+/2+}$ in gamma-butyrolactone (GBL)[28], $TBAN^+$ in dodecanol[52], NaOH in PEO[37] in 'Electrochemical' category, respectively.

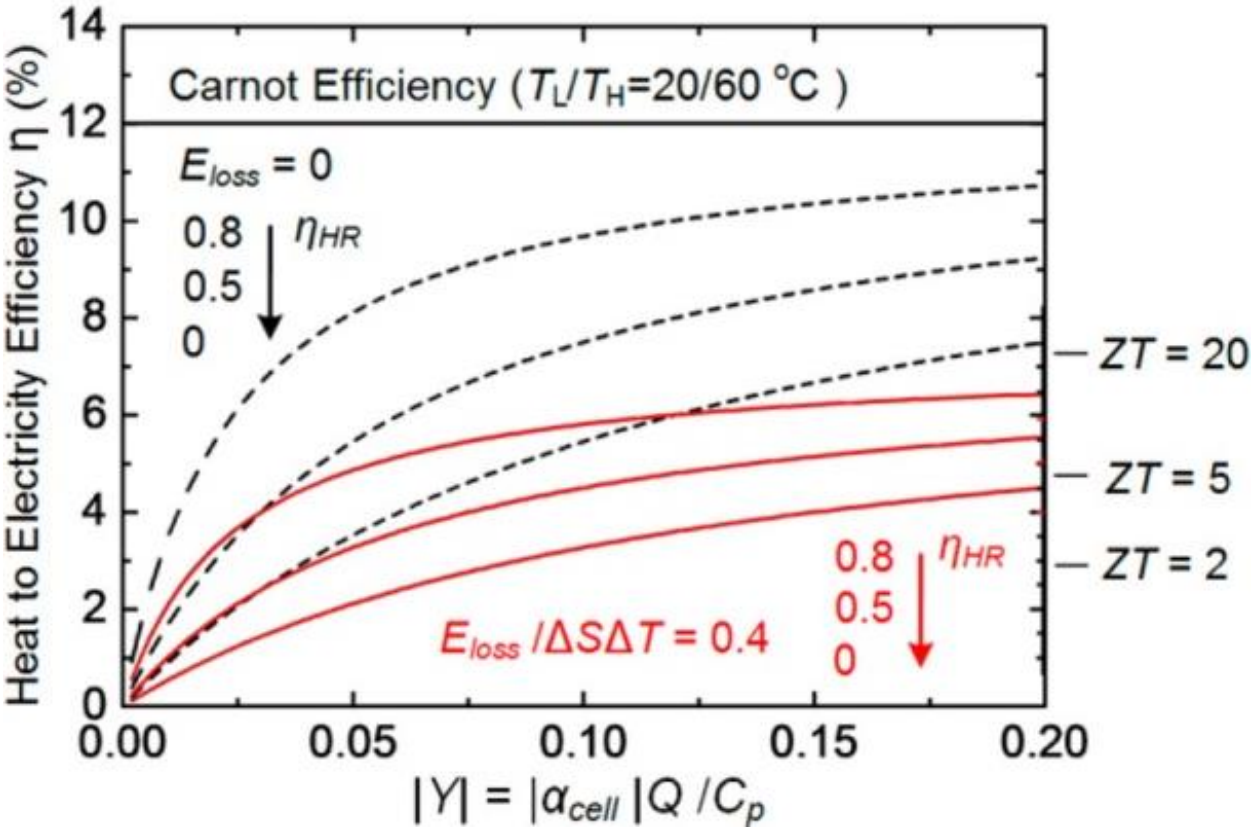

Figure 1.4. Recently reemerging electrochemical heat conversion can be an attractive alternative or a supplemental technology to the conventional thermoelectric technology, because of potentially much improved heat conversion efficiency. Figure from *Thermally Regenerative Electrochemical Cycle for Low-Grade Heat Harvesting* and used with permission from the American Chemical Society[53].

1.2. Fundamentals of Thermoelectrics

1.2.1. Seebeck Coefficient (S)

The thermoelectric materials are usually narrow band gap semiconductors with a certain concentration of charge carriers (holes or electrons, h^+ or e^-) in it. When thermoelectric materials are subject to thermal gradient, the carriers tend to migrate to the cold side of the materials (**Figure 1.5**). This disparity in carrier concentration under the thermal gradient stems from the larger diffusivity of hot carriers than that of cold carriers (**Figure 1.6**). The "build-up" of carriers on the cold side creates a voltage difference across the material. Seebeck coefficient of a material (S) quantifies the amount of voltage generated (ΔV) by a given temperature gradient (ΔT), as can be seen in Equation 1.1. Then the material is connected across an external load, and a current will flow creating electrical power output. The harvested voltage should be consumed simultaneously with presence of thermal gradient, due to lack of electrical energy storage ability in thermoelectric materials. It is also worth noting that the Seebeck coefficient has negative correlation with the carrier concentration (n) for materials with parabolic bands, as shown in Equation 1.1[54].

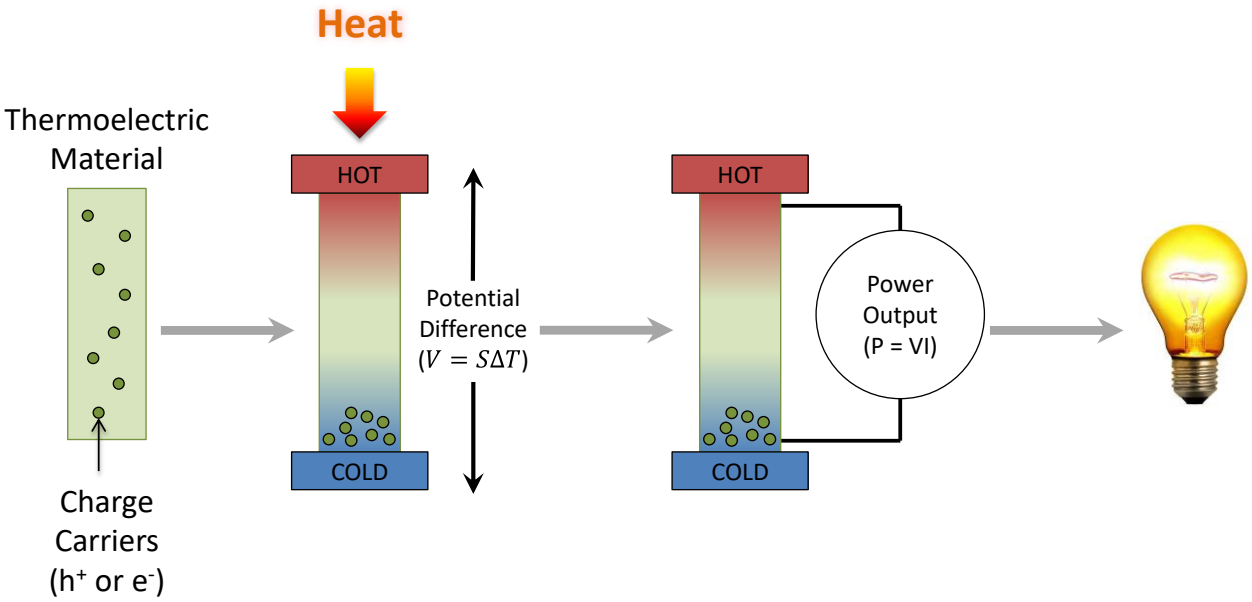

Figure 1.5. Description of Seebeck coefficient in a conductive material (semiconductors or metals). In the presence of a temperature gradient, these carriers will be polarized on the cold side of the material creating a voltage potential across the material. Completing the circuit across an external load will induce a current and create power.

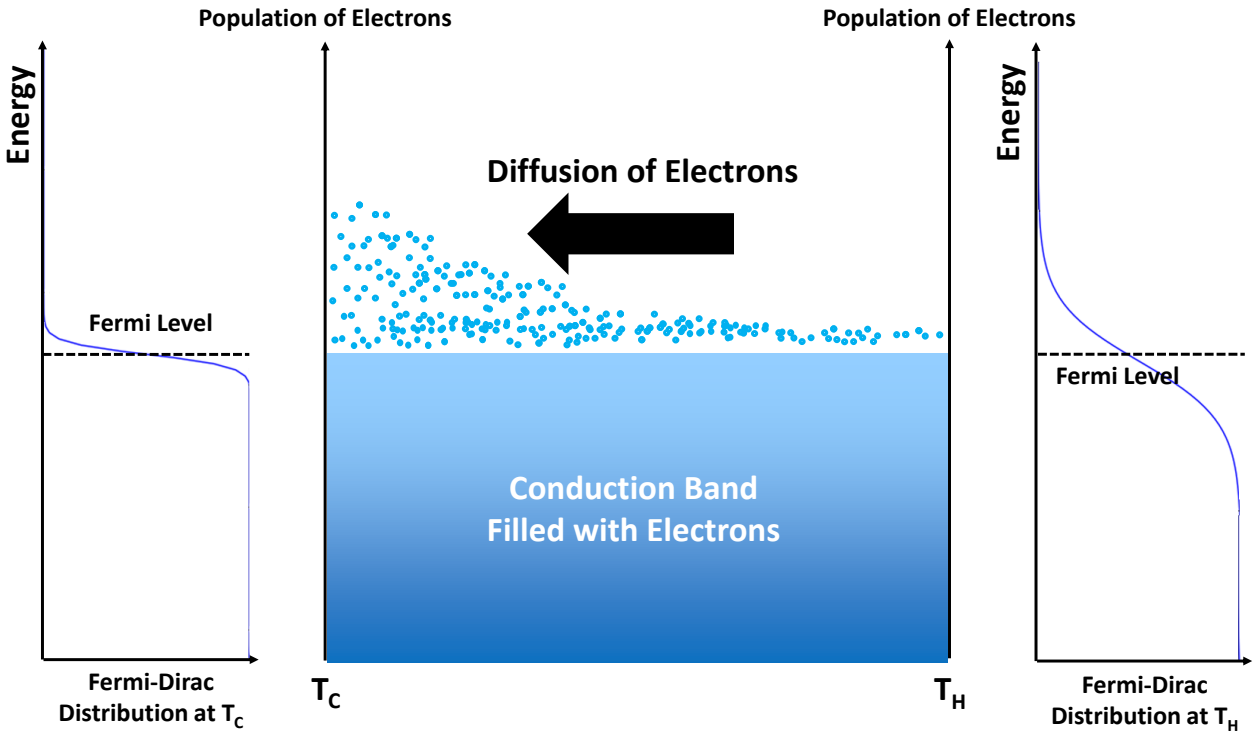

Figure 1.6. Origin of Seebeck effect in a metal. The electrons at the hot side (T_H) have a larger thermal velocity than those on the cold end (T_C). Therefore, the distribution of electrons at the steady-state will be polarized at colder side, due to the changed diffusivities at different temperatures.

$$S = \frac{\Delta V}{\Delta T} \propto n^{-\frac{2}{3}} \qquad (1.1)$$

1.2.2. Electrical Conductivity (σ)

The electrical conductivity (σ) of a material quantifies how well it conducts electrons. Materials that conduct electrons well, such as copper, have a high electrical conductivity; whereas materials that conduct electrons poorly, such as SiO_2 quartz, have a low electrical conductivity. The electrical conductivity (σ) of a material is a product of its carrier concentration (n), mobility (μ), and the elementary charge constant (e). The carrier concentration (n) is the concentration of electrons in the conduction band or holes in the valence band of a material. The mobility (μ)

describes how easily the carriers can move through the material. The elementary charge constant (e) is defined as the electric charge carried by a single electron (1.6×10^{-19} C).

$$\sigma = ne\mu \tag{1.2}$$

1.2.3. Thermal Conductivity (κ)

The total thermal conductivity (κ) of a material quantifies how well it conducts heat. Materials that conduct heat well, such as copper, have a high thermal conductivity. Materials that conduct heat poorly, such as polymers, have a low thermal conductivity. The total thermal conductivity is composed of two parts: the lattice thermal conductivity (κ_L) and the electronic thermal conductivity (κ_e). The lattice component (κ_L) comes from lattice vibrations that are transmitted through the material. These lattice vibrations are also known as phonons. The electronic component of thermal conductivity comes from collision between the transported charge carriers and the atoms in the materrials, as they move through the material. The electronic thermal conductivity is proportional to multiplication of Lorentz number (L) and electrical conductivity (σ).

$$\kappa = \kappa_e + \kappa_L \tag{1.3}$$

$$\kappa_e = \sigma LT \tag{1.4}$$

1.2.4. Thermoelectric Figure of Merit and Conversion Efficiency

The thermoelectric device efficiency (η) is a product of two different constituents: Carnot efficiency and material efficiency (Equation 1.5). The Carnot efficiency is a thermal efficiency that is limited by the second law of thermodynamics using the hot side (T_H) and the cold side (T_C) temperatures. The material efficiency is governed by the properties of the thermoelectric material used in the device.

$$\eta = \frac{T_H - T_C}{T_H} \frac{\sqrt{ZT+1}-1}{\sqrt{ZT+1}+\frac{T_C}{T_H}} \tag{1.5}$$

The material efficiency contains a metric of performance known as the dimensionless figure of merit (ZT). This variable is derived from maximizing the Peltier refrigeration efficiency for a given thermoelectric material. One can determine the dimensionless figure of merit using the

electrical conductivity (σ), Seebeck coefficient (S), thermal conductivity (κ), and mean temperature (T) of the material (Equation. 1.6).

$$ZT = \frac{\sigma S^2}{\kappa} T \quad (1.6)$$

To maximize the efficiency of a thermoelectric device, one needs to maximize the dimensionless figure of merit (ZT). Therefore, when investigating thermoelectric materials, the primary goal, and indeed the focus of this thesis, is to increase the thermoelectric figure of merit (ZT) of the material.

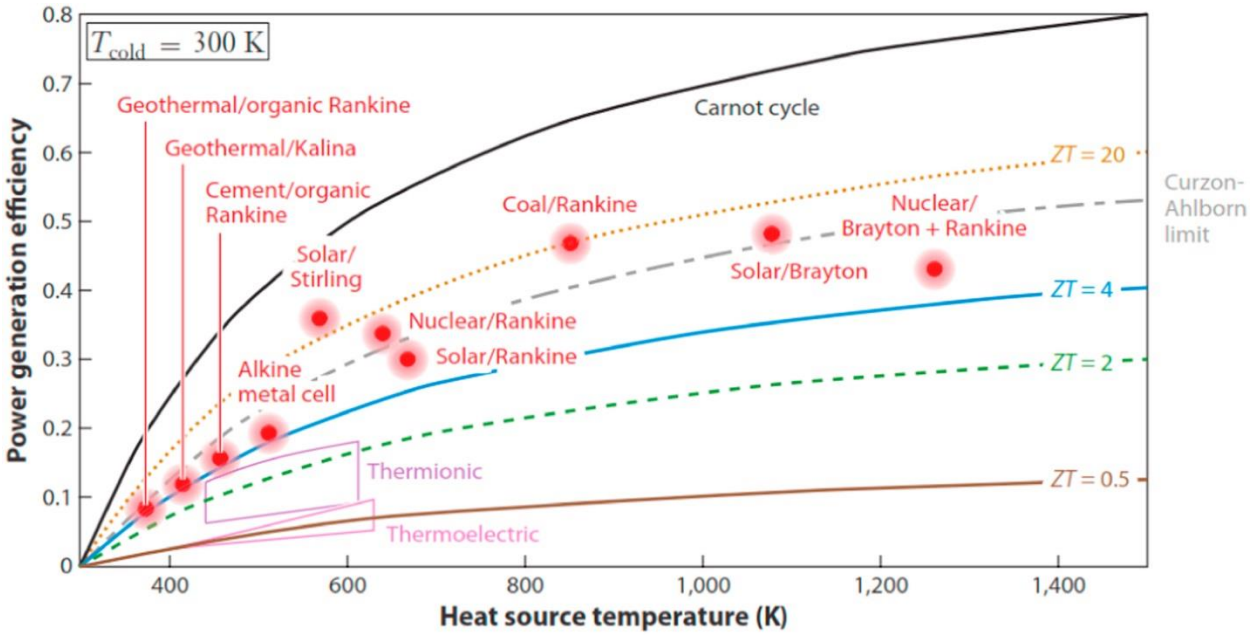

Figure 1.7. The conversion efficiency of thermoelectrics has monotonically positive correlation with thermoelectric figure of merit, ZT. For the estimation of the efficiency, the temperature at cold side is held constant at 300 K, while the hot side temperature is set as a control variable to create thermal gradient. Figure from *An overview of cooling of thermoelectric devices* and used with permission from Elsevier[55].

1.2.5. Interdependency of the Thermoelectric Parameters in Single-material Thermoelectric Systems

As indicated at Equation 1.6, increase in electrical conductivity (σ), and Seebeck coefficient (S) and decrease in thermal conductivity is desirable to achieve high ZT. However, accomplishing high ZT is not straightforward, as all these thermoelectric parameters are correlated to each other.

Figure 1.8 (a) shows that Seebeck coefficient, electrical and thermal conductivities as functions of charge carrier concentration inside a thermoelectric material. The electrical conductivity increases with increasing carrier density, whereas Seebeck coefficient decreases with increasing carrier concentration. It is noteworthy that the relationship between the Seebeck coefficient and major carrier density in a material system is called Pisarenko relation. These two contrary trends of Seebeck coefficient and electrical conductivity result in the existence of peak of the power factor ($S^2\sigma$) at a particular carrier density. The thermal conductivity stays almost constant in the low carrier concentration region as lattice thermal conductivity is the major contributor to the overall thermal conductivity. However, with increasing carrier density, the thermal conductivity increases as well. The electronic contribution to the thermal conductivity becomes larger, which is proportional to electrical conductivity. From this, ZT is also expected to have a global maximum at a specific location.

In order to maximize ZT, researchers investigated different thermoelectric materials. **Figure 1.8** (b) shows various thermoelectric materials at optimized dopant concentration. Regardless of doping condition and operational temperature, the maximum ZT almost always is ceiled around 1. For further amelioration of ZT, alternative classes of materials have been intensively sought for the thermoelectric application.

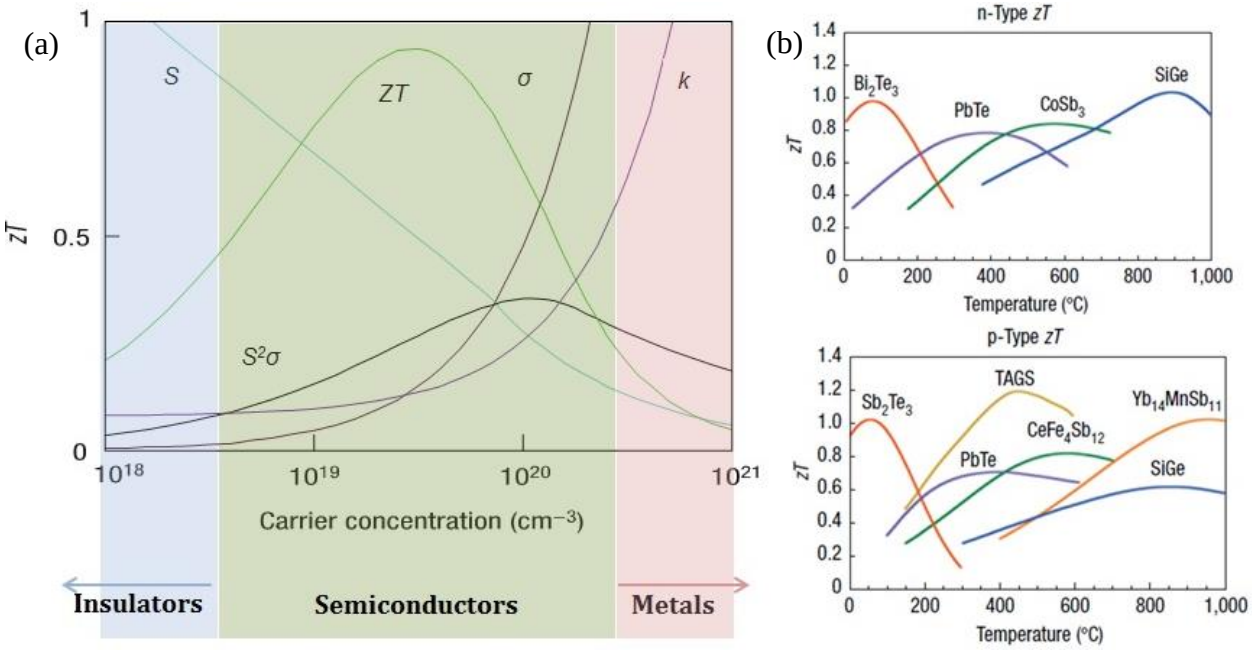

Figure 1.8. (a) Optimizing ZT through carrier concentration tuning. Maximizing the efficiency (ZT) of a thermoelectric involves a compromise of thermal conductivity (κ) and Seebeck coefficient (S) with electrical conductivity (σ). All thermoelectric parameters are based on Bi_2Te_3 properties[56]. (b) p-type and n-type ZT of state-of-the-art commercial materials and those used or being developed by NASA for thermoelectric power generation[56]. Figure from *Complex thermoelectric materials* and used with permission from the Nature Publishing Group[57].

1.2.6. Thermoelectric Performance Enhancing Mechanisms in Nanoscale Composite Systems

Modulation Doping

Modulation doping enables increased population of charge carriers in a semiconductor not by incorporation of foreign species, but by relying on diffusion of charge carriers (hole or electrons, h^+ or e^-) from a chemically doped semiconductor to the adjacent undoped semiconductor (**Figure 1.9** (a)). Modulation doping is composed of two processes: (i) generation of charge carriers at the doped semiconductor layer and (ii) migration of part of the charge carriers to the contacting undoped layer with higher mobility. Therefore, in some sense, it can be alternatively referred to 'spillover' of charge carriers. The reason for the higher charge carrier mobility in the undoped layer is less scattering by dopant atoms, which function as ionized impurity scattering centers.

Under this mechanism, the overall population of charge carriers remains the same, because this mechanism does not additionally create the charge carriers. However, electrical conductivity increases, because some of charge carriers in the undoped layer now have higher mobility. This principle was firstly demonstrated in GaAs–$Al_xGa_{1-x}As$ superlattice, where many alternate thin layers of n-type $Al_xGa_{1-x}As$ and undoped GaAs were deposited[58]. The first application of this concept was high electron mobility transistor (HEMT), where high mobility of charge carriers is directly linked to the performance[59].

In order for the modulation doping phenomenon to be realized, suitable band offset is the primary requisite, as it determines whether the migration of the charge carriers is thermodynamically uphill or downhill. Band offset is the amount of discontinuity in conduction or valence band edges at the interfaces of two dissimilar materials. If the band offset is thermodynamically uphill, diffusion from the originating material to the adjacent undoped semiconductor will be inhibited significantly. In the contrast, when the redistribution of the charge carriers is thermodynamically favorable (downhill), the majority of charge carriers would prefer to migrate. **Figure 1.9** (b) exemplifies when the modulation doping is a thermodynamic downhill reaction. In this occasion, conduction band edge of the modulation dopant material (highly doped n-type Si_xGe_{1-x}) locates higher than that of the undoped counterpart Si, so that modulation doping can occur. In other words, the redistribution of electrons is promoted due to the thermodynamically favorable energy band alignment.

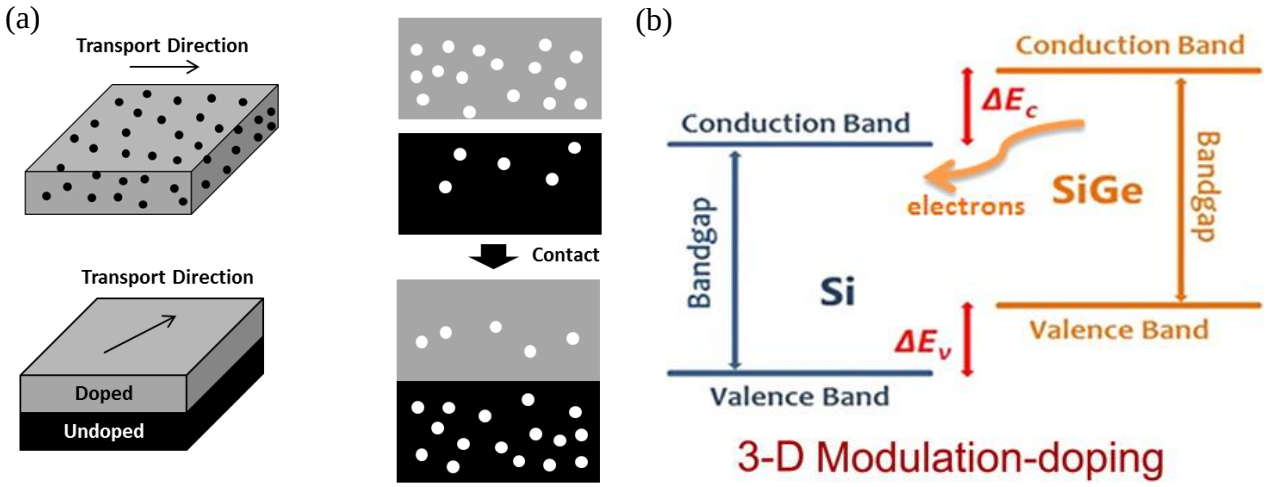

Figure 1.9. Schematic illustration of modulation doping mechanism in nanoscale thermoelectric composite systems. (a) Modulation doping can be an operating principle for composites and heterostructures, of which transport direction is in-plane. Heterostructure is a heterojunction between two co-planar layers or regions of dissimilar semiconductors. Grey slabs, black slabs, black dots, and white dots represent planar doped semiconductor, planar undoped semiconductor, nanostructures of undoped semiconductor, and charge carriers, respectively. The interface is magnified at the right hand side. (b) Modulation doping is a deluge of charge carriers from a chemically doped material to another adjacent material with a higher mobility. Band offset is the key requirement to promote modulation doping, as it determines how large portion of the carriers can migrate. For this case, electrons generated in heavily doped Si_xGe_{1-x} nanoparticles diffuse into the neighboring undoped Si matrix, driven by both concentration and energy gradient. Figure (a) from *Quantitative analyses of enhanced thermoelectric properties of modulation-doped PEDOT:PSS/undoped Si (001) nanoscale heterostructures*[60]. Reproduced by permission of the Royal Society of Chemistry. Figure (b) from *Enhancement of thermoelectric properties by modulation-doping in silicon germanium alloy nanocomposites* and used with permission from the American Chemical Society[61].

Figure 1.10 (a) illustrates the modulation doping process with graphically represented mobilities in the undoped Si matrix embedding highly n-type Si_xGe_{1-x} nanoparticles. The modulation dopant in this particular occasion, nanoparticles are usually considered as scattering centers for electrons[62,63]. If this is true, then the modulation doping principle may not lead to enhancement in electrical conductivity. Fortunately for this case, the mobility of the undoped Si matrix is largely preserved because the nanoparticles have a large volumetric fraction, and the diameters of the Si_xGe_{1-x} nanoparticles (~20 nm) are much larger than the electron mean free paths (1 – 2 nm)[64,65]. In other words, electrons are scattered anyway in the undoped Si matrix, before nanoparticles scatter them. This lesson should be carefully followed when sizes of the nano-inclusions (modulation dopant) are comparable to the mean free path of charge carriers. As a result of the modulation doping, electrical conductivity is improved without sacrificing Seebeck coefficient. Therefore, compared to uniformly doped system where scattering of electrons by

ionized impurity are present, power factor is boosted due to this enhanced electrical conductivity (**Figure 1.10** (b)). An additional advantage in this system is the suppression of thermal conductivity[61], because of active scattering of phonons by the Si_xGe_{1-x} nanoparticles. As wavelengths and mean free path of phonons are much longer than those of electrons, they are more readily scattered by interfaces with nanoparticles[15,66,67].

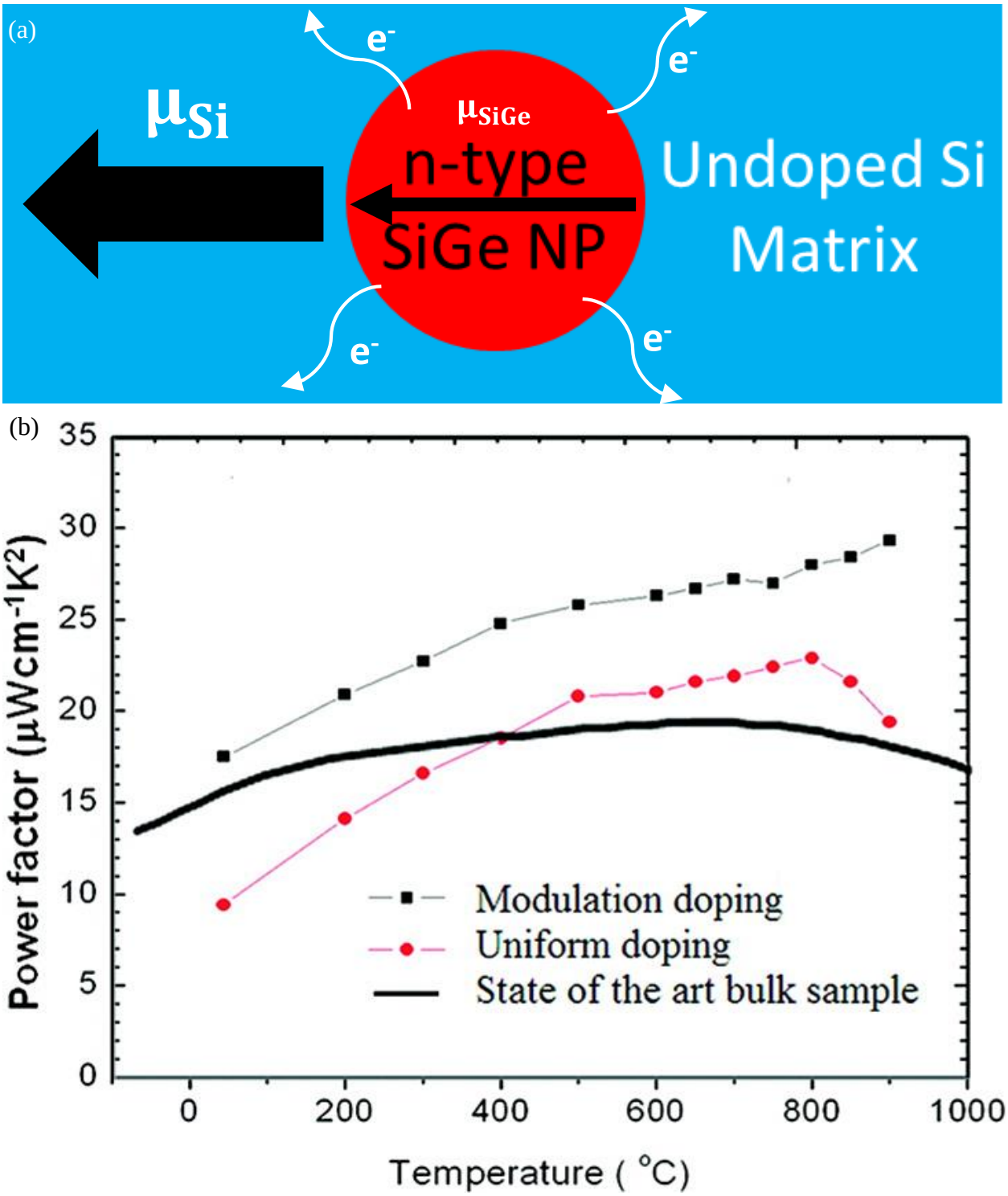

Figure 1.10. (a) A schematic depiction of modulation doping at the undoped Si matrix / highly n-type Si_xGe_{1-x} nanocrystals composite system. Electrons originating from the highly n-type Si_xGe_{1-x} nanostructures take a highway for conduction, thereby improving electrical conductivity. (b)

Improvement on the thermoelectric power factor in the undoped Si matrix embedding highly n-type Si_xGe_{1-x} nanocrystals, compared to that of uniformly doped Si material. This enhancement is largely attributed to the increased electrical conductivity without tradeoff in Seebeck coefficient. Figure (b) from *Power factor enhancement by modulation doping in bulk nanocomposites* and used with permission from the American Chemical Society[68].

Energy-dependent Charge Carrier Scattering

This mechanism relies on the energy-selective scattering of charge carrier transport via energy barrier at the abrupt interfaces between two dissimilar materials. Band offset is also important for this mechanism as well, because it determines the barrier height. Superlattice[69] or matrix embedding nanoparticles[70,71] are preferred sample configurations, so that transport across the interfaces where the charge carrier scattering mechanism happens can become more pronounced (**Figure 1.11** (a)).

Figure 1.11 (b) shows that the imposed thermal gradient across these nanoscale composite systems causes shift in kinetic energies of all respective electrons at each position. Because the thermal gradient is applied perpendicular to the interfaces (marked as z-direction here), the energy profile along the z-direction shows a linear slope. Quantum wells are assumed in this theoretical explanation because the assumed thin dimension of each layer of the superlattice often induces the quantum well effect[72-75]. Periodic arrangement of quantum wells is presumed (superlattice), as shown in top side of **Figure 1.11** (a). If electrons are transported along the z-direction, the majority of electrons confined below the Fermi level (i.e. the energy which has a 50 % probability of being occupied by an electron at a temperature) cannot further proceed along z-direction due to the energy hurdle (E_b); only the small portion of electrons with higher kinetic energy than barrier height ($E > E_b$) can move to the neighboring quantum well. Sufficiently thick periodic barriers are assumed in this case, in order to disregard transport of the electrons by tunneling effect[76].

Portion of electrons capable of transmission across the interfaces out of the total electron population is expressed as V_1 and V_2 at **Figure 1.11** (c), depending on the conservation of the momenta. The energy of entire population of electrons is displayed in a momenta space (k-space). The spherical distribution of kinetic energies of electrons in the momenta space appear, because

isotropic free electron is assumed, reflecting typical characteristic of metal (Fermi gas). The kinetic energy, the criterion for filtration of the electrons, is related to the momenta by this formula:

$$E = \frac{\hbar^2 k^2}{2m_e^*} \quad (1.7)$$

where E, $\hbar$, k, m_e^* represent kinetic energy of an electron, reduced Planck constant, momentum of the electron, and effective mass of the electron respectively. Hence, according to Equation 1.7, the barrier height (E_b), can be alternatively expressed as k_b in this momenta space, such that $E_b = \frac{\hbar^2 k_b^2}{2m_e^*}$. Then momenta of electrons eligible for the transport across the barriers are $k_z > k_b$ if momenta is not conserved, and $k > k_b$ if momenta is conserved, where k_z corresponds to the momenta of electrons along z-direction. Population of electrons meet these two different criteria is expressed as V_1 and V_2, respectively.

As a result of the selective propagation of electrons, the overall electrical conductivity decreases, as the number of electrons capable of conduction has reduced. The contribution from electrons to the electrical conductivity over the kinetic energy is shown in **Figure 1.11** (d). This electrical conductivity at the particular kinetic energy is called differential electrical conductivity ($\sigma(E)$). The differential electrical conductivity at that specific energy can be defined as multiplication of electron population at that kinetic energy and mobility. The integration of the differential conductivity over the entire energy range is the experimentally observed electrical conductivity of a material. When the charge carrier scattering mechanism is in effect, the electrons with low kinetic energy are localized. Thus, their contribution to the total electrical conductivity becomes zero, meaning that the differential conductivity below E_b becomes zero. It in turn creates an asymmetric profile, as shown in the right hand side of **Figure 1.11** (d). It is noteworthy that the zero differential conductivity below E_b originates from the zero mobility, not the disappearance of electron population lower than E_b. Therefore, Fermi level stands invariant in both cases of **Figure 1.11** (d). The unchanged Fermi level and transformed differential conductivity influence Seebeck coefficient of the system, by following a formula (Mott formula) below:

$$S = \frac{\pi^2 k_B^2 T}{3e} \frac{\partial \ln \sigma(E)}{\partial E}\Big|_{E=E_F} \quad (1.8)$$

The Seebeck coefficient of a thermoelectric system is proportional to derivative of the differential conductivity with respect to the energy at Fermi level, where k_B, T, and e represent

Boltzmann constant, temperature, and elementary charge. The slope of the differential electrical conductivity against the energy becomes much sharper at 'metal-based superlattice' case. This indicates that the Seebeck coefficient is enhanced due to the energy-dependent charge carrier scattering mechanism, at the expense of electrical conductivity. Also, another lesson can be obtained that the barrier height determines the differential conductivity profile. Hence, selection of materials to adjust the barrier height would be decisive to govern ZT.

Figure 1.11 (e) demonstrates that the increased Seebeck coefficient can eventually lead to the enhancement in ZT, despite the decreased electrical conductivity. This tradeoff is only possible toward higher Seebeck coefficient with less electrical conductivity, not the opposite way; therefore this mechanism is only suitable for materials innate in high electrical conductivity and low Seebeck coefficient. This specification matches well with properties of metal, and this explains why metal-based superlattice in particular was discussed here. In comparison, modulation doping mechanism augments the electrical conductivity without discounting Seebeck coefficient.

In the projection of ZT, additional assumptions on phonon transport across the interfaces are set. The mean free paths of phonons are typically larger than those of charge carriers by several orders of magnitude. In this study, superlattice with 5 nm – 20 nm periods was assumed, which in turn would lead to hugely suppressed thermal conductivity. The introduced work here estimated the thermal conductivity around 1 W/m·K, as a result of repressed phonon propagation by more frequent scatterings at more frequently encountered interfaces. In comparison, thermal conductivity of common metals and several semiconductors in the bulk form are typically 1 – 2 orders of magnitude higher.

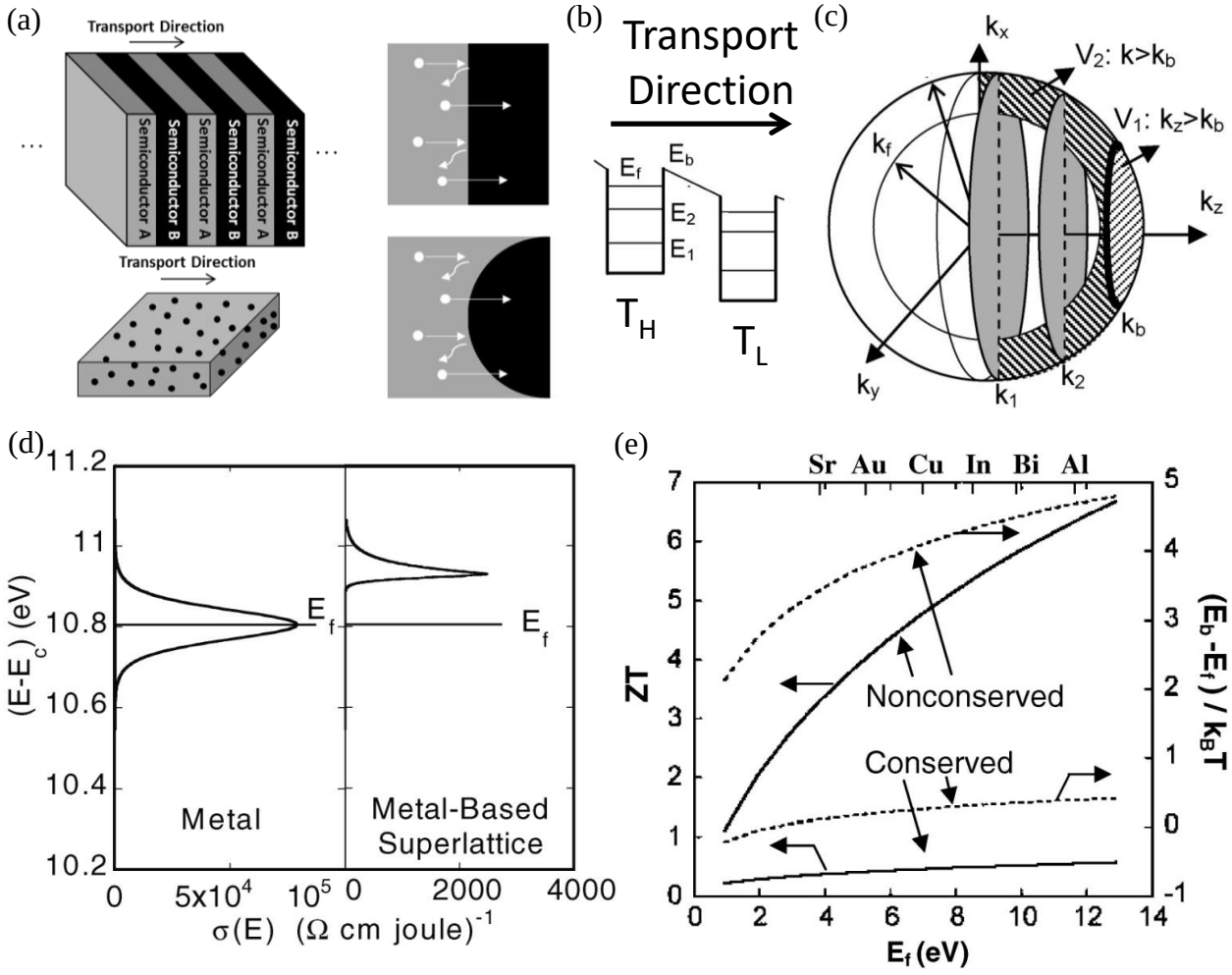

Figure 1.11. (a) A schematic diagram of energy-dependent charge carrier scattering mechanism in nanoscale thermoelectric composite systems and superlattices. The energy-dependent charge carrier scattering mechanism can be a Seebeck coefficient enhancing principle for nanoscale composites of nanoparticles / enveloping matrix, and heterostructures. For the charge carrier scattering mechanism, electronic and thermal transports should mainly occur across interfaces between the dissimilar materials. The interfaces function as an effective tool to facilitate the charge carrier scattering mechanism. Grey slabs, black slab, black dots, and white dots represent a conductive material A, another conductive material B, the nanostructured material A, and, charge carriers, respectively. The interface is magnified at the right hand side. (b) Conduction band and energy levels within two neighboring quantum wells generated by the quantum confinement effect, separated by another material. The barrier height of each well and Fermi level are represented as E_b and E_f respectively. The shift in temperatures (T_H and T_L) also moved all energy levels of

electrons in the quantum well by the same magnitude. (c) Distribution of kinetic energy of all electrons in the material is represented in a momenta-space (k-space). Only electrons with kinetic energies larger than the barrier height E_b can be propagated (corresponding to V_1); otherwise, they are scattered. (d) Modified differential electrical conductivity as a consequence of introduction of the energy barrier. (e) Projected improvement in ZT by the energy-dependent charge scattering mechanism. Figure (a) from *Quantitative analyses of enhanced thermoelectric properties of modulation-doped PEDOT:PSS/undoped Si (001) nanoscale heterostructures*[60]. Reproduced by permission of the Royal Society of Chemistry. Figure (b) – (e) from *Improved thermoelectric power factor in metal-based superlattices* and used with permission from the American Physical Society[69].

Even though experimental investigation on energy-dependent charge carrier scattering had been hampered by technical difficulties[69], it could be realized experimentally at Sb_2Te_3 thermoelectric matrix embedding Ag nanoparticles (**Figure 1.12**). It is noteworthy that p-type Sb_2Te_3 matrix is already a state-of-the-art thermoelectric material, which readily conducts holes. The key idea for this study lies on the materials choice, so that appropriate band offset is actualized and it in turn permits the energy-dependent charge carrier scattering mechanism.

With this design consideration, Te and Ag nanoparticles were incorporated in this thermoelectric system. When the samples were fabricated, excessive Te elemental crystal was put in addition to the stoichiometric Sb_2Te_3 compound. As a result, there were remnant Te inclusions in the matrix, and they are free from the chemical bonding with Sb. Heat treatment on the samples allowed the excessive Te to diffuse and eventually surround Ag nanoparticles, because Te has particularly high chemical affinity to Ag. The choice of Ag was also very intentional, in order to prepare the suitable band offset (or barrier height) for the pronounced charge carrier scattering mechanism at the interfaces between Te and Ag. Because they have similar ionization potentials (i.e. distance between the vacuum level and the valence band edges), the valence band offset (barrier height) was expected to be adequate, so that only minority portion of the hole transport can be selectively filtered. At a glance, it may be strange that the barrier layer is surprisingly metallic Ag nanoparticles, because Ag is a well-known electronic conductor. However, these metallic nanoparticles create Schottky barrier, functioning as a suitable energy filter for the charge

carrier scattering mechanism. Moreover, Ag nanoparticles are largely segregated from each other and exhibit as Schottky contact; meaning that charge carrier conduction solely thought them is not possible due to both thermodynamic and geometric reasons.

As a consequence of the energy barrier placed by the Ag nanoparticles, the differential conductivity profile becomes asymmetric, with differential conductivity at the low kinetic energy region disappearing (**Figure 1.11** (c)). Then the Seebeck coefficient obtained from the Mott formula (Equation 1.8) becomes enlarged, improving the power factor as well (the right hand side graph in **Figure 1.12**).

Despite not represented in **Figure 1.12**, another bonus enhancement in ZT is achieved by suppression of the thermal conductivity. As explained earlier in this section, scattering centers for hole transport (Ag nanoparticles) definitely can act as phonon scattering center, because of their orders of magnitude different mean free paths[31,32].

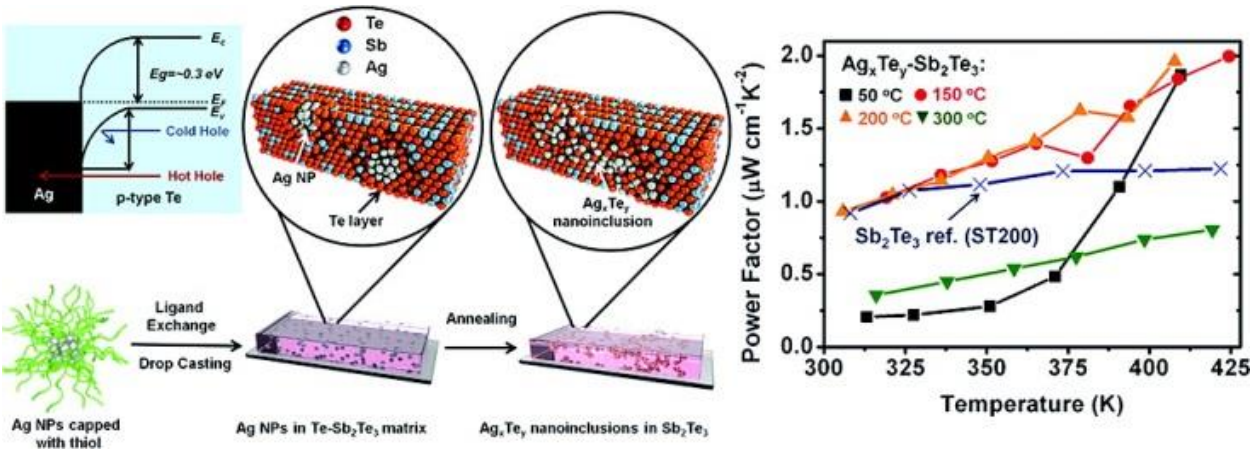

Figure 1.12. The band alignment at the interfaces of p-type Sb_2Te_3 matrix embedding the Ag nanoparticles show the energy-dependent charge carrier filtering effect. Excessive Te atoms encapsulate Ag nanoparticles spontaneously, and these neighboring materials form a suitable band offset to induce the charge carrier scattering mechanism. This in turn increases thermoelectric power factor. Figure from *Silver-based intermetallic heterostructures in Sb_2Te_3 thick films with enhanced thermoelectric power factors* and used with permission from the American Chemical Society[71].

1.3. Fundamentals of Thermogalvanics

1.3.1. Origins of Electrochemical Thermopowers and Their Trends

There are 3 different physical origins of electrochemical thermopowers: thermogalvanic effect by redox-active species, thermal-electrical double layer (EDL) effect by the adsorbed ions on the electrode surfaces, and thermodiffusion effect by the ions in the electrolyte (**Figure 1.13** (a) – (c)). All these 3 mechanisms can be exploited to harness heat into electricity. It is remarkable that voltage change per unit temperature difference is no longer called Seebeck coefficient, because the thermally generated voltage does not stem from the Seebeck effect. Instead, this metric is indicated as thermopower, because it implies no information about the physical origin.

Thermogalvanic Effect

Thermogalvanic effect represents shift of electrochemical equilibrium of redox reactions by temperature change. As a consequence, the electrochemical potential is also altered (**Figure 1.13** (a)). As each redox reaction has corresponding Gibbs free energy, following formulae hold:

$$\Delta G(T) = \Delta H - T\Delta S = -zFE(T) \tag{1.9}$$

$$\frac{\partial \Delta G(T)}{\partial T} = -\Delta S = -zF\frac{\partial E(T)}{\partial T} \tag{1.10}$$

$$\alpha = \frac{\partial E(T)}{\partial T} = \frac{\Delta S}{zF} \tag{1.11}$$

where $\Delta G(T)$ is Gibbs free energy change accompanied by the redox reaction as a function of temperature, ΔH is enthalpy change accompanied by the redox reaction, ΔS is entropy change accompanied by the redox reaction, $E(T)$ is electrochemical potential of the redox species as a function of temperature, z is the exchanged moles of electrons during the one mole of redox reaction, and F is Faraday constant. As can be noticed, the redox entropy is directly proportional to the thermopower by thermogalvanic effect (Equation 1.10 and Equation 1.11). Also, the Gibbs free energy is proportional to the electrochemical potential (Equation 1.9). As redox reactions for each redox couple involve different Gibbs free energy change and entropy change, the electrochemical potentials and thermopowers of individual redox couples can be regarded unique as will be explained later. For instance, Cu metal and copper hexacyanoferrate, Prussian blue

($KFe_2(CN)_{6(s)}$), and $Fe(CN)_6^{3-/4-}{}_{(aq)}$ all have distinct electrochemical thermopowers and potentials[30,32].

It is also experimentally demonstrated that more entropy exchange can be incorporated in addition to the redox entropy (ΔS_{redox}), in order to further raise the thermopower[77]. Then the thermopower is modified to reflect the additional contribution (Equation 1.12). In this occasion, the entropy exchanged via evaporation (ΔS_{evap}) was added to the total contribution, reaching up to -9.9 mV/K[77]. It is interesting because non-electrochemical phenomenon of evaporation can contribute to the overall thermally harnessed voltage. When multiple physical phenomena with high entropy exchange are coupled with electrochemical redox reactions, the total thermopower can be further improved.

$$\alpha = \frac{\partial E(T)}{\partial T} = \frac{\Delta S_{redox} + \Delta S_{evap}}{zF} \quad (1.12)$$

Thermal Voltage Induction at Electrical Double Layer Capacitor (EDLC)

The electrochemical potentials of EDLC electrodes can be also altered in a response to the varied temperatures. Basically the voltage at EDLC electrode is a function of surface charge density, and this weakly bound surface charge density is prone to be affected by temperature[38] (**Figure 1.13** (b)). Depending on the electrolyte composition and electrode materials, the electrochemical thermopower can range from 0.6 mV/K to 6.5 mV/K[78,79]. However, further detailed studies are required to fully reveal the nature behind this high electrochemical thermopowers.

Thermodiffusion (Soret effect)

This effect utilizes the diffusivity difference of ions in electrolytes, as a result of different temperatures (**Figure 1.13** (c)). The thermal velocity of the ions in the electrolyte is increased when the temperature becomes higher, resulting in larger diffusivity. As a consequence, polarization of the concentrations of ions is induced in the electrolyte. It produces the potential difference across the electrolyte under thermal gradient. This can be regarded as an electrochemical analogy to the Seebeck effect. The concepts are identical, except ions replace the charge carriers (holes or electrons), and the system is substituted from a solid-state electronic conductors to an ionic conductor. Whereas single type of charge carriers can only be present in

thermoelectric systems, electrolytes typically include both cations and anions. As both oppositely charged species are transported toward the same cold side of the electrolytes, the thermopower contributions from the cations and the anions subtract each other, often resulting in low thermopower. In order to resolve this issue, high molecular mass of either cation or anion is deliberately selected, so that transport of the high mass ions can be significantly minimal. As a result of this approach, entropy transport from the lighter ionic species is solely reflected to the thermopower, thereby increasing the thermopower. Such idea was successfully demonstrated in Na^+ – polystyrene sulfonate$^-$ (PSS^-) electrolyte[39,40], and Na^+ – poly(ethylene oxide) (PEO^-) electrolyte[37]. The thermally-induced unequal distributions of ions in those electrolytes were converted to electrochemical energy at redox-inert electrodes (EDLC electrodes). Further expansion of this concept into charged colloids was also carried out. The key idea was that the enlargement in the mass can enhance the transported entropy as well, resulting in very high theoretical thermopower around 85 mV/K[80].

In this thesis, 2 principles out of 3 phenomena will be applied for electrochemical heat harvesting; thermogalvanic effect in Chapter 3; both thermogalvanic effect and thermal-EDL effect in Chapter 4.

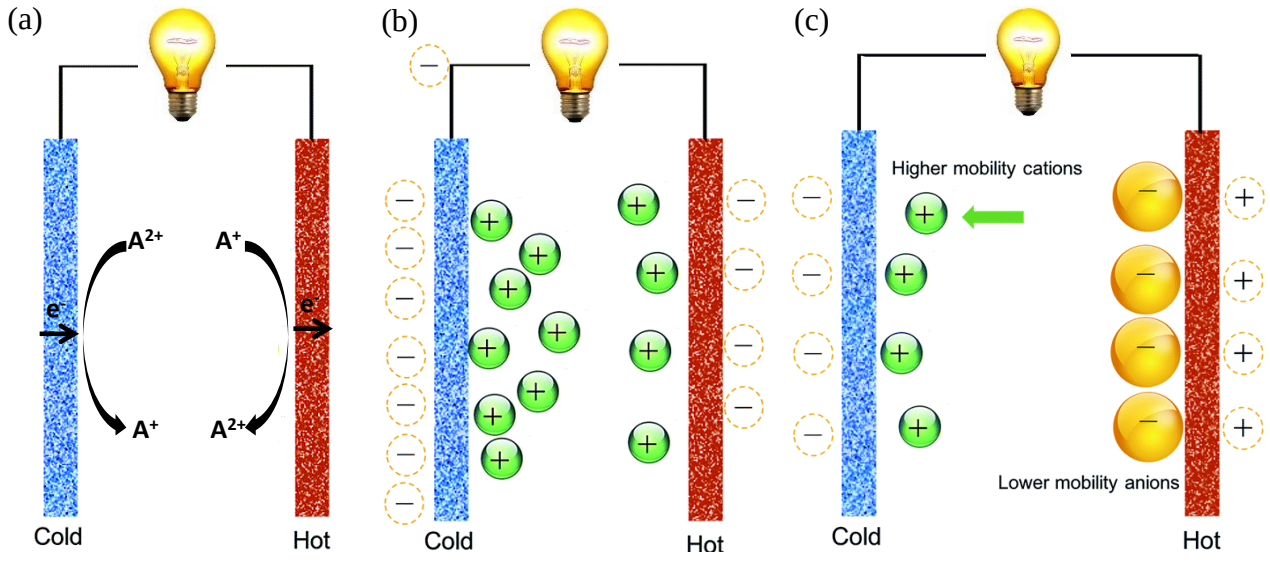

Figure 1.13. The 3 major physical origins of electrochemical thermopowers. (a) Thermogalvanic effect based on redox phenomenon. (b) Thermal-EDL effect based on change in surface charge densities on EDL under different temperatures. (c) Thermodiffusion effect (Soret effect) driven by

diffusivity difference at unequal temperatures. The thermodiffusion effect is an electrochemical analogy to Seebeck effect in solid-state electronic conductors. Reproduced from *Thermal charging of supercapacitors: a perspective*[81] with permission from the Royal Society of Chemistry.

Electrochemical thermopowers more than 1 mV/K are easily achieved from all 3 mechanisms. Even among these mechanisms, difference in magnitudes of thermopowers exists. **Figure 1.14** compares thermopowers from the two different driving forces: thermogalvanic effect and EDLC. The left side of the graph depicts thermopowers of several Li-ion battery electrode materials, which clearly show that thermopowers of the Li-intercalation materials do not exceed 2.1 mV/K[82]. On the contrary the thermopowers based on EDLC range between 3 mV/K and 8 mV/K. This difference will be utilized in the Chapter 4, where a combination of EDLC and a rechargeable battery works as a single electrochemical heat harvester. Besides the utility of this difference, it can further raise fundamental questions about physical origins. The trend may be understood from a viewpoint that the orders of magnitude of entropy exchanged may be completely different for Li-ion battery electrodes and EDL electrodes, because EDL typically store charge as ions in the electrolyte on the electrode surface, where the stored charges are likely to be disordered. In comparison, as the battery materials form much stronger chemical bonding with the stored ionic charges. Allowed modes of movement (or degree of freedom) for the stored ions in the crystal is limited, hardly permitting disorder.

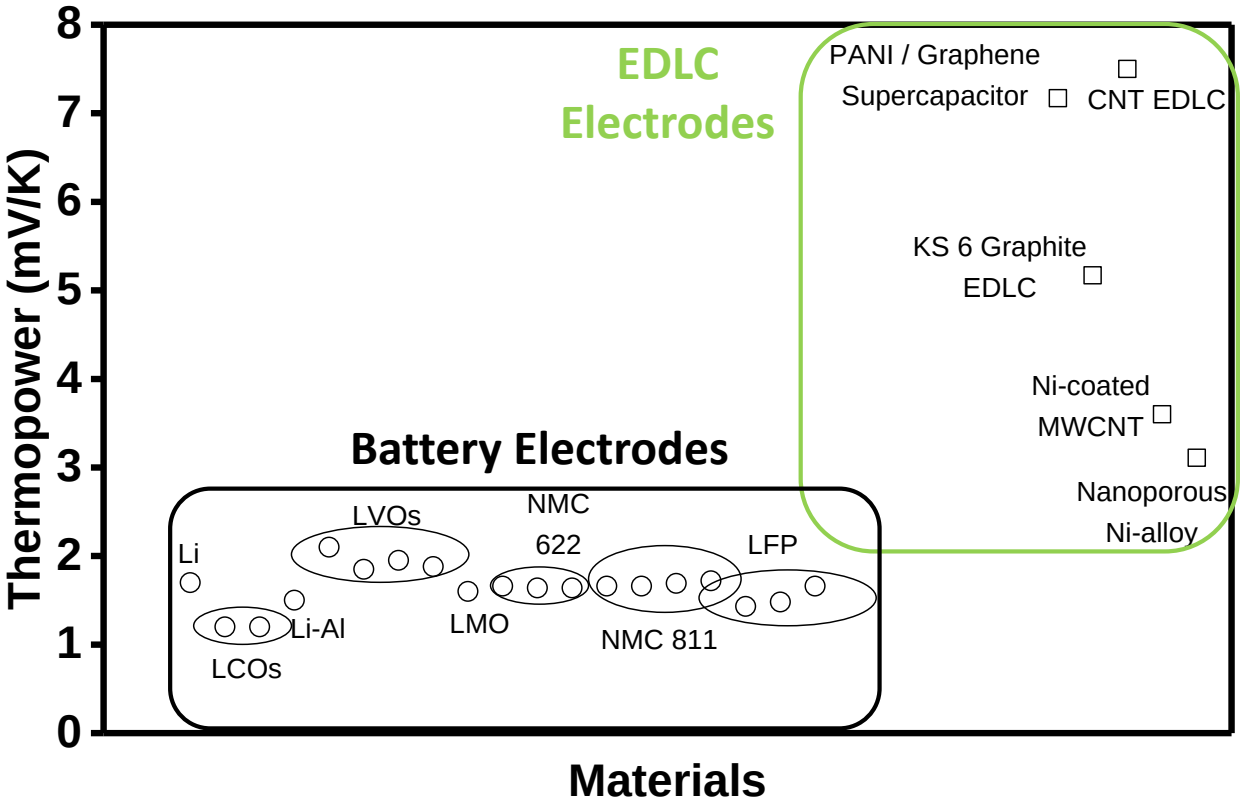

Figure 1.14. Consolidated electrochemical thermopowers at several different rechargeable battery and supercapacitor electrodes. There is a trend that thermopowers of supercapacitor electrodes are generally larger than those of secondary battery electrodes. From the left hand side, identities of the listed materials are as follows. Li[83], LCO: Li_xCoO_2[26,82,84,85], Li-Al: Lithium-Aluminum alloy[86], LVO: $Li_xV_2O_5$[82,87,88], LMO: $Li_xMn_2O_4$[89-91], NMC 622: $Li_xNi_{0.6}Mn_{0.2}Co_{0.2}O_2$[82], NMC 811: $Li_xNi_{0.8}Mn_{0.1}Co_{0.1}O_2$[82], LFP: Li_xFePO_4[82] in 'Battery Electrodes' category. PANI / Graphene Supercapacitor: polyaniline / graphene electrode in supercapacitor[35], CNT EDLC: carbon nanotube electrode in EDLC[33], Ni-coated MWCNT: Nickel-coated multi-walled carbon nanotube in EDLC[92], Nanoporous Ni-alloy: nanoporous Nickel-Copper alloy electrode in EDLC[93] in 'EDLC Electrodes' category, respectively.

1.3.2. Possible Modes of Operations in the Electrochemical Heat Harvesting and Conversion Efficiencies

Figure 1.15 and **Figure 1.16** illustrate two possible modes of operations in the electrochemical heat harvesting. All 3 different origins of electrochemical thermopowers explained in Section 1.3.1 can serve under both modes of operations.

Continuous Mode of Operation under Thermal Gradient

Figure 1.15 (a) – (b) portrays the 'continuous mode of operation under thermal gradient'. This mode is identical to the mode of operation for thermoelectric materials. Even though electrochemical systems have the capability to store charge, this capability is not used at this mode of operation. As a result, the conversion of thermal energy into electrical energy and the consumption of the harvested electricity happen simultaneously. However, the charge storage capacity at the electrodes permits an alternative mode of operation, namely thermodynamic cycling, as will be explained later.

Under this setting, the electrodes are identical at both sides (**Figure 1.15** (a)). The roles of electrodes are current collector and places for the thermogalvanic effect or EDL effect to occur. Electrolyte keeps the thermal gradient and acts as a medium where charged species (ions) carry entropy and electrical current. Assuming that the thermal gradient is steadily maintained, the voltage output should be constant. When the external electrical load is connected to harness the potential difference, Ohmic drop occurs accordingly. The voltage profile under this mode of operation is represented at **Figure 1.15** (b).

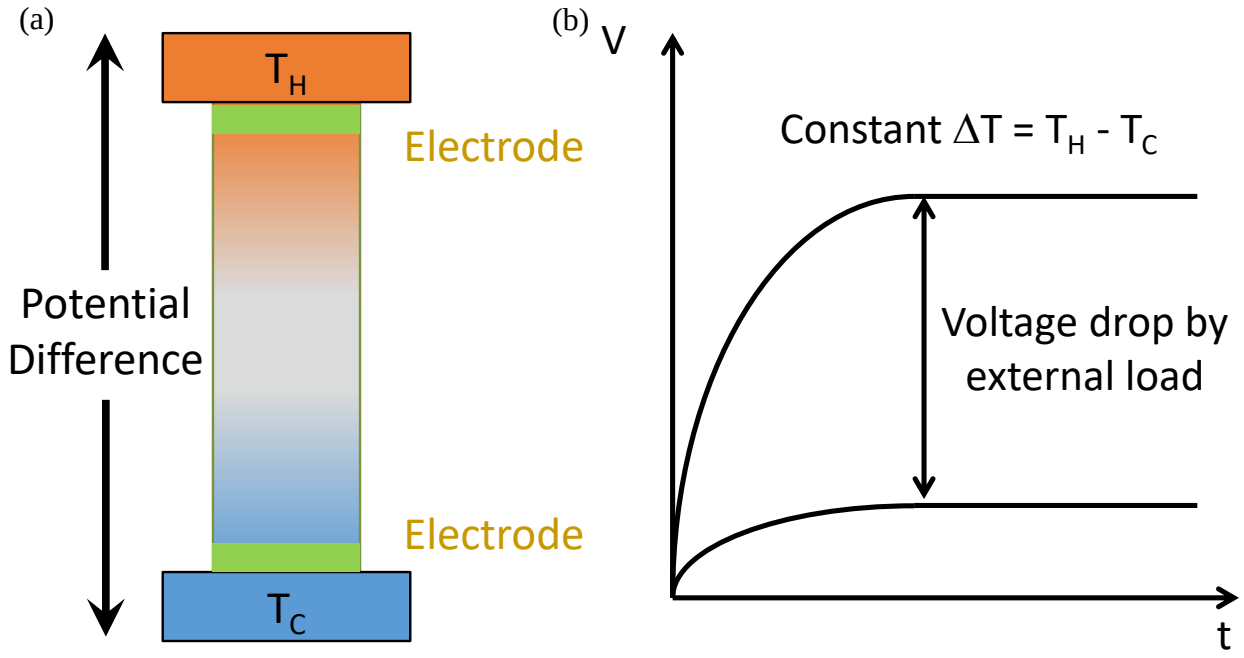

Figure 1.15. (a) Continuous electrochemical heat harvesting under a thermal gradient. This mode is identical to the mode of operation for thermoelectric systems (**Figure 1.5**). (b) When external electrical load is connected, the thermally generated voltage drops. The decreased voltage in turn is utilized to produce work through the external electrical load.

As this mode of operation is exactly the same as thermoelectric operation, the efficiency can be estimated by Equation 1.5. As electrolyte governs the heat and electrical conduction through the electrochemical system, the thermal conductivity and the electrical conductivity terms almost solely rely on the electrolyte properties. For conventional liquid-based electrolytes, the thermal conductivity is low, which is beneficial to ZT. However, its low ionic conductivity range has limited the practicality of this mode of operation. The ionic conductivities of such electolytes are usually lower by 4 – 6 orders of magnitudes than those of state-of-the-art thermoelectric materials. Therefore the resultant ZTs from those different systems can be quickly estimated, by combining 1 or 2 orders of magnitude higher thermopowers. Electrochemical systems under this operation can at best keep the similar ZT with the state-of-the-art thermoelectric materials. More realistically, the ZTs from electrochemical systems are likely less by 1 – 2 orders of magnitude than the state-of-the-art thermoelectric materials.

Thermodynamic Cycles between Two Different Temperatures

In order to address the low projected ZT, an alternative strategy has been developed. This tactics fully exploits the charge storage capability of the electrochemical energy storage systems, by running them under thermodynamic cycles between a hot temperature (T_H) and a cold temperature (T_C). Just like conventional heat engines can store part of the externally supplied heat as internal energy in the system during thermodynamic cycles; this operation enables the collection of part of the heat inflow as the shifted voltage in the electrochemical heat harvester.

In order for the thermodynamic cycles to operate, periodic change of temperature is necessary, rather than temperature gradient within an electrochemical energy storage system (**Figure 1.16** (a)). As a result, the entire electrochemical energy storage system should be transferred from one temperature to another, just like traditional heat engines under thermodynamic cycles. The electrochemical thermodynamic cycle is more clarified in a temperature – entropy change diagram (**Figure 1.16** (b)). The enclosed thermodynamic cycle consists of combination of 4 distinct steps. Step (i): Isothermal discharge to zero voltage at T_C. Step (ii): Thermal recharging at open circuit condition. The entire cell is transferred from T_C to T_H at this step. Step (iii): Isothermal discharge to zero voltage at T_H. This time the polarity of the cell is reversed from that of the step (i). Step (iv): Thermal recharging at open circuit condition. The entire cell is transferred from T_H to T_C at this step. Heat energy is converted into internal electrical energy of the system at step (ii) and step (iv), and the changes in internal energy are expressed as the form of thermally harvested voltage. **Figure 1.16** (c) exemplifies how the thermodynamic cycles can be translated into a real time graph versus voltage.

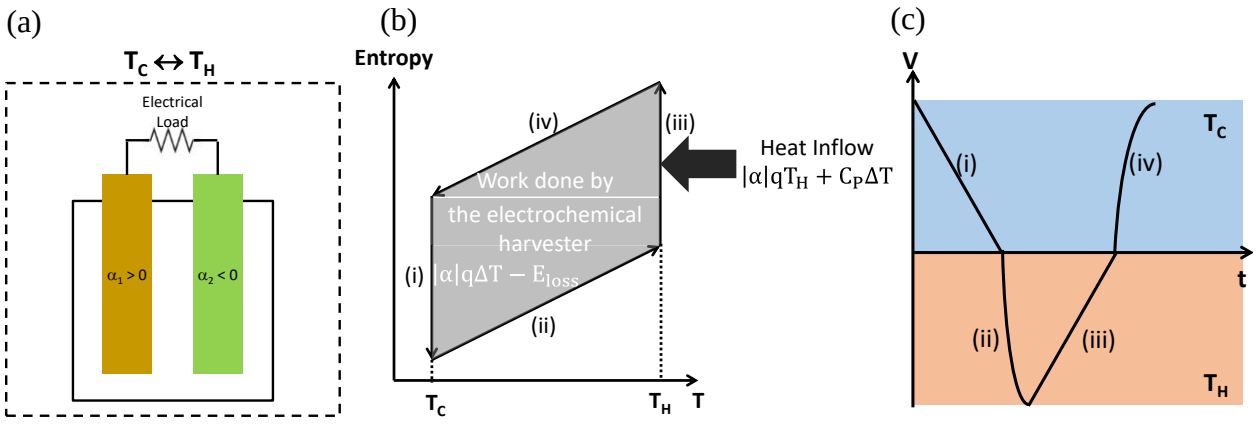

Figure 1.16. (a) Electrochemical heat harvesting via thermodynamic cycling. The entire electrochemical cell undergoes periodic change in the surrounding temperatures, depending on the state of the cell during the thermodynamic cycle. (b) A temperature (T) – entropy (S) diagram represents the concept of electrochemical heat harvesting via thermodynamic cycling. Under this mode of operation, the cell functions as a heat engine. (c) The thermodynamic cycle in (b) is translated into an exemplar voltage – time graph for interpretation.

Efficiency is a ratio between the input and output of energy flow during a single thermodynamic cycle. The energy inflows toward the system as the form of heat at step (ii) and step (iii) (**Figure 1.16** (b)). The inflow of energy at step (ii) is $C_p\Delta T$ (energy required to raise the temperature of the entire system), and the input energy at step (iii) corresponds to $|\alpha|qT_H$ (the heat absorbed into the system at T_H), where $|\alpha|$ is the absolute value of the electrochemical thermopower of the full cell, q is the charge capacity of the system, and C_p is the heat capacity of the system. The work output of the cell per a single thermodynamic cycle corresponds to the area enclosed by the thermodynamic loop in the T – S plane (**Figure 1.16** (b)), and is expressed as $|\alpha|q\Delta T - E_{loss}$. Knowledge about all energy inflow and outflow enables determination of the efficiency, as follows:

$$\eta = \frac{|\alpha|q\Delta T - E_{loss}}{|\alpha|qT_H + C_p\Delta T} \quad (1.13)$$

where η is the conversion efficiency under thermodynamic cycling mode of operation, and E_{loss} is the wasted energy mainly by internal resistance of the electrochemical heat harvester system.

From Equation 1.13, it becomes obvious that heat capacity and charge capacity of the heat harvesting system are importantly considered as well. For the better efficiency, the heat capacity should be suppressed, whereas the charge capacity should be escalated. Following this logic, electrode materials with charge capacity or high loading of the charge-storing electrode materials should be encouraged. However, the gravimetric charge capacity of the material is an innate characteristic of each electrode material, therefore it is difficult to be decoupled from the thermopower term (α). The specific charge capacity (q) is also inherent to the electrode materials. Higher loading of the charge-storing electrode materials may not lead to improved efficiency, because it can also increase the heat capacity term. Hence, the ideal electrode materials for the

electrochemical heat conversion under thermodynamic cycles should have high absolute thermopower, low heat capacity, and high charge capacity at once. Other efforts on design can also be attempted to suppress the heat capacity of the system by minimizing contributions from unnecessary components, such as cases and excessive electrolytes.

The comparison between the expected conversion efficiencies from the two different modes of operations with the identical electrochemical heat harvesting system is shown in **Figure 1.17**. Again, the low ionic conductivity brings about lower conversion efficiency for 'continuous mode of operation under thermal gradient' at all thermopower range. However, as one mode operates under thermal gradient and another one serves under periodic temperature changes, they are not completely exchangeable to each other; Thus, this new mode of operation is not expected to completely replace thermoelectric technology.

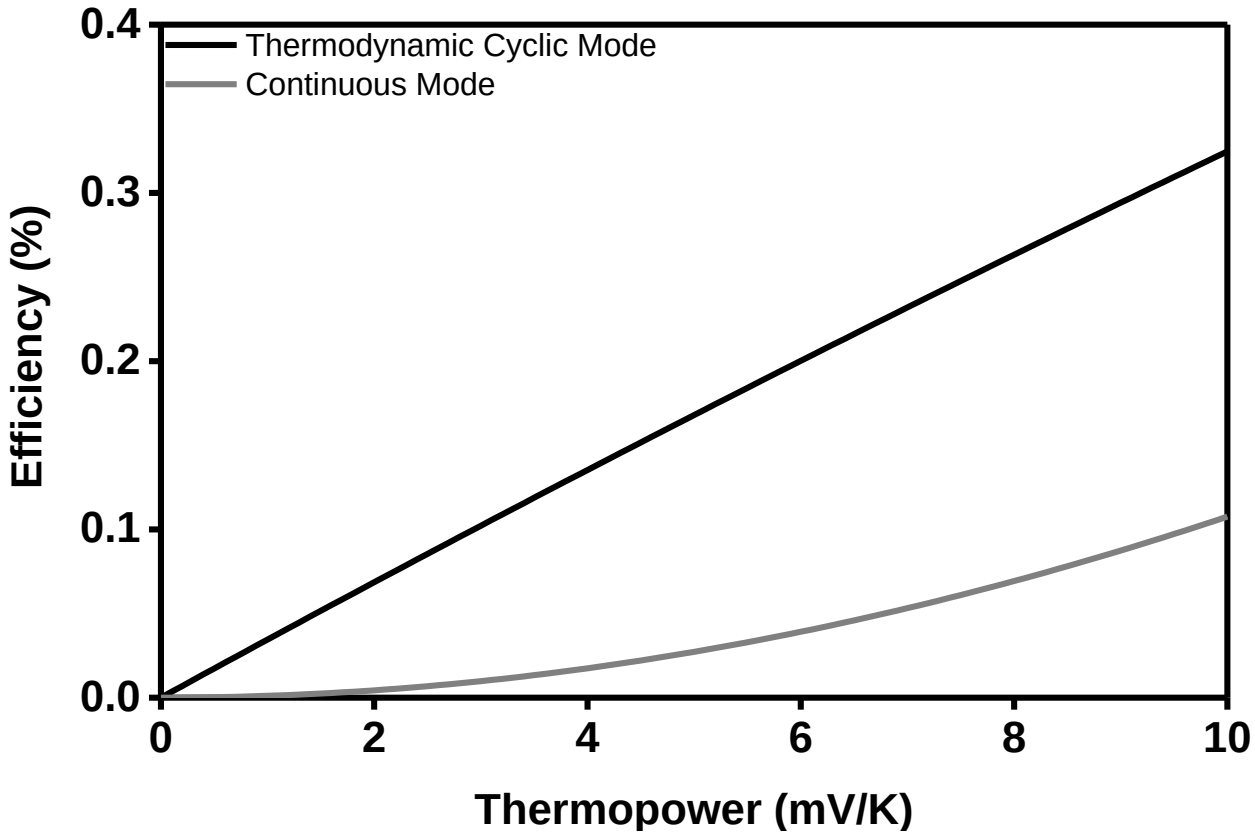

Figure 1.17. An exemplar comparison between the projected efficiencies by the two different modes of operations. Ionic conductivity, thermal conductivity, heat capacity, charge capacity, and operating temperature range used for this estimation were 7.50×10^{-3} S/cm, 0.64 W/m·K, 4.19

J/g·K, 2.84 C/mL, 20 °C – 60 °C, individually. These values are actual physical characteristics of the electrochemical heat harvester investigated in the Chapter 3 of this thesis. Thermodynamic cycling shows monotonically higher efficiency at all thermopowers.

1.3.3. Requirements to Construct Autonomous Heat Harvester Operating under Thermodynamic Cycles

Figure 1.18 (a) graphically explains the requirements to construct autonomous heat harvester operating under thermodynamic cycles. The meaning of autonomy in this case is the electrochemical heat harvesting systems do not involve any recharging step by external electricity supplies during the thermodynamic cycles. The 1st requirement is that the half-cell potentials of redox couple 1 and redox couple 2 composing an electrochemical heat harvester should meet once at a temperature (T_m). This can be a tricky requirement to fulfill, as the half-cell potentials reflect Gibbs free energy changes by redox reactions, and the slopes of half-cell potentials against temperature are proportional to the entropy changes caused by the redox reactions, innate values for each redox couples. It is also difficult to predict electrochemical thermopowers and half-cell potentials of redox coucples before the actual experiments, often due to lack of previous surveys.

Provided that the 1st requirement is conformed, the 2nd requirement is to match the midpoint of the operating temperature range at the intersecting temperature (T_m) of the half-cell potentials of the two redox couples. For example, if the half-cell potentials of redox couple 1 and redox couple 2 cross at 40 °C, the operating temperature range should be tuned accordingly, for example either 20 °C – 60 °C or 10 °C – 70 °C.

The 3rd requirement is that the operating temperature range should not involve malicious side effects on the thermodynamic cycles. For example, if the intersecting temperature is located where self-discharge is severe (reversible self-decomposition of redox couples), or around phase transition of the electrolyte or electrode materials occur, or irreversible thermal decomposition of redox active species becomes active, such designed electrochemical heat harvester would be difficult to be practical.

An optional requirement is large difference between individual half-cell thermopowers of the two constituent redox couples, because the total cell thermopower is defined by the difference between the half-cell thermopowers (Equation 1.14). For instance, when half-cell thermopower of

redox couple 1 is -1 mV/K and half-cell thermopower of redox couple 2 is +3 mV/K, the full cell (total) thermopower equals to -4 mV/K. As demonstrated in Equation 1.13, higher total thermopower can lead to larger conversion efficiency.

$$\alpha_{\text{full cell}} = \alpha_{\text{total}} = \alpha_1 - \alpha_2 \quad (1.14)$$

Other optional requisites are high ionic conductivity of electrolyte, high electronic conductivity of the electrode, and fast kinetics of redox reactions. All of them can contribute to suppress the internal resistance of the electrochemical heat harvester. These in turn assist to minimize E_{loss} term in the efficiency formula, Equation 1.13. Fulfillment of these optional requirements can especially improve device characteristics at high power operation, where loss of the thermally harnessed electricity by the internal resistance is pronounced.

Figure 1.18 (b) schematically displays shift of half-cell potentials of each species at each step in a thermodynamic cycle. Firstly, at step (i), the full cell is discharged until zero voltage is reached at T_C. It means that the half-cell potentials of the two redox couples become equal as a result of the discharge. After this step, the cell is transferred to a different temperature, T_H in this case under open circuit condition (step (ii)). This variation in temperature shifts the half-cell potentials by $\alpha_1(T_H - T_C)$ and $\alpha_2(T_H - T_C)$, respectively. The shifts in the half-cell potentials originate from the reestablishment of electrochemical equilibria of both redox couples. As a result, the full cell potential shifts by $(\alpha_1 - \alpha_2)(T_H - T_C)$, in accordance with Equation 1.14. Then, at step (iii), the cell is discharged until zero voltage is accomplished at T_H. Compared to the step (i), the relative location of redox couple 1 and redox couple 2 becomes inverted, meaning that the full cell voltage sign is flipped at the step (iii). After the half-cell potentials become the same at T_H, the cell is transferred back to T_C under open circuit condition (step (iv)). The half-cell potentials shift again to return back to the original half-cell potential profiles at step (i). Therefore, after the completion of step (iv), the electrochemical heat harvester is ready to repeat the thermodynamic cycle from the start. This dissected explanation offers a more detailed mechanistic description to the thermodynamic process exemplified in **Figure 1.16** (b) – (c).

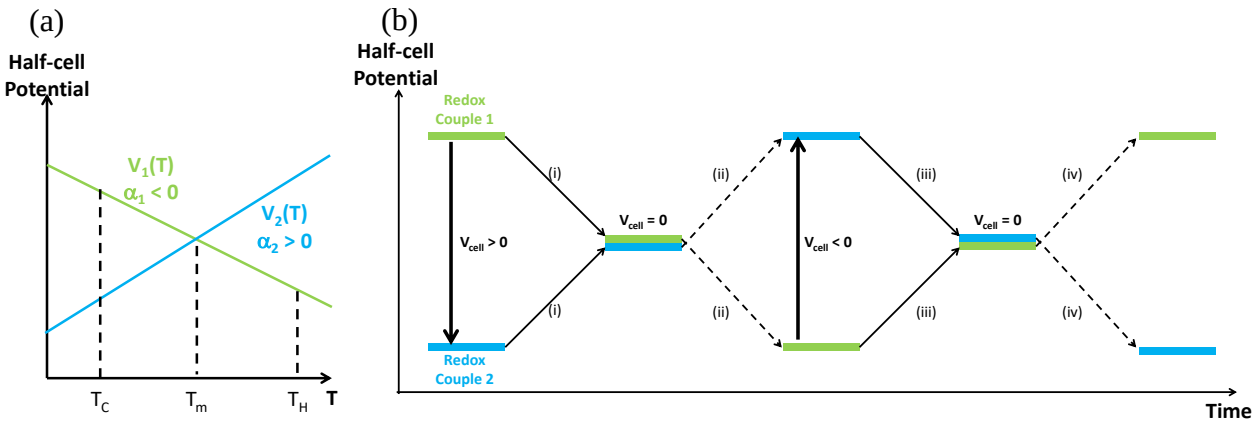

Figure 1.18. (a) The half-cell potentials of the two individual redox couples should meet once at a temperature (T_m), in order to build an autonomous electrochemical heat harvester operating under thermodynamic cycles. The operating temperature range (T_C and T_H) should be set to make T_m the midpoint. (b) Variation of the half-cell potentials under the heat harvesting thermodynamic cycle over time. The full cell potential over time is more clearly shown in **Figure 1.16** (b) – (c). Accordingly, step (i) – step (iv) here are identical to those in **Figure 1.16** (b) – (c).

An exemplar autonomous electrochemical heat harvester was demonstrated in **Figure 1.19** (a) – (b). **Figure 1.19** (a) shows that the 1st requirement to construct autonomous heat harvester operating under thermodynamic cycles was satisfied. Again, the 1st requirement is the half-cell potentials of Prussian blue ($KFe_2(CN)_{6(s)}$) and $Fe(CN)_6^{3-/4-}{}_{(aq)}$ composing the electrochemical heat harvester intersecting only once at a specific temperature (T_{cross}). Here, they intersect around 40 °C. The 2nd requirement on matching the midpoint of the operating temperature range at the intersecting temperature (T_m) of the half-cell potentials of the two redox couples was also fulfilled by setting the operating temperature range from 20 °C to 60 °C. In this temperature range the 3rd requirement is naturally abided, because this operating temperature range does neither cause phase transition of water or redox-active materials nor decomposition of any element in the cell.

Figure 1.19 (b) illustrates time-dependent voltage profiles during the autonomous thermodynamic cycles of the electrochemical heat harvester. The thermodynamic cycles are composed of combination of 4 distinct steps again. Step (i): Isothermal discharge to zero voltage at T_C. Step (ii): Thermal recharging at open circuit condition. The entire cell is transferred from T_C to T_H at this step. Step (iii): Isothermal discharge to zero voltage at T_H. This time the polarity

of the cell is reversed from that of the step (i). Step (iv): Thermal recharging at open circuit condition. The entire cell is transferred from T_H to T_C at this step. Heat energy is converted into internal electrical energy of the system at step (ii) and step (iv), and the changes in the internal energy are expressed as form of thermally harvested voltage.

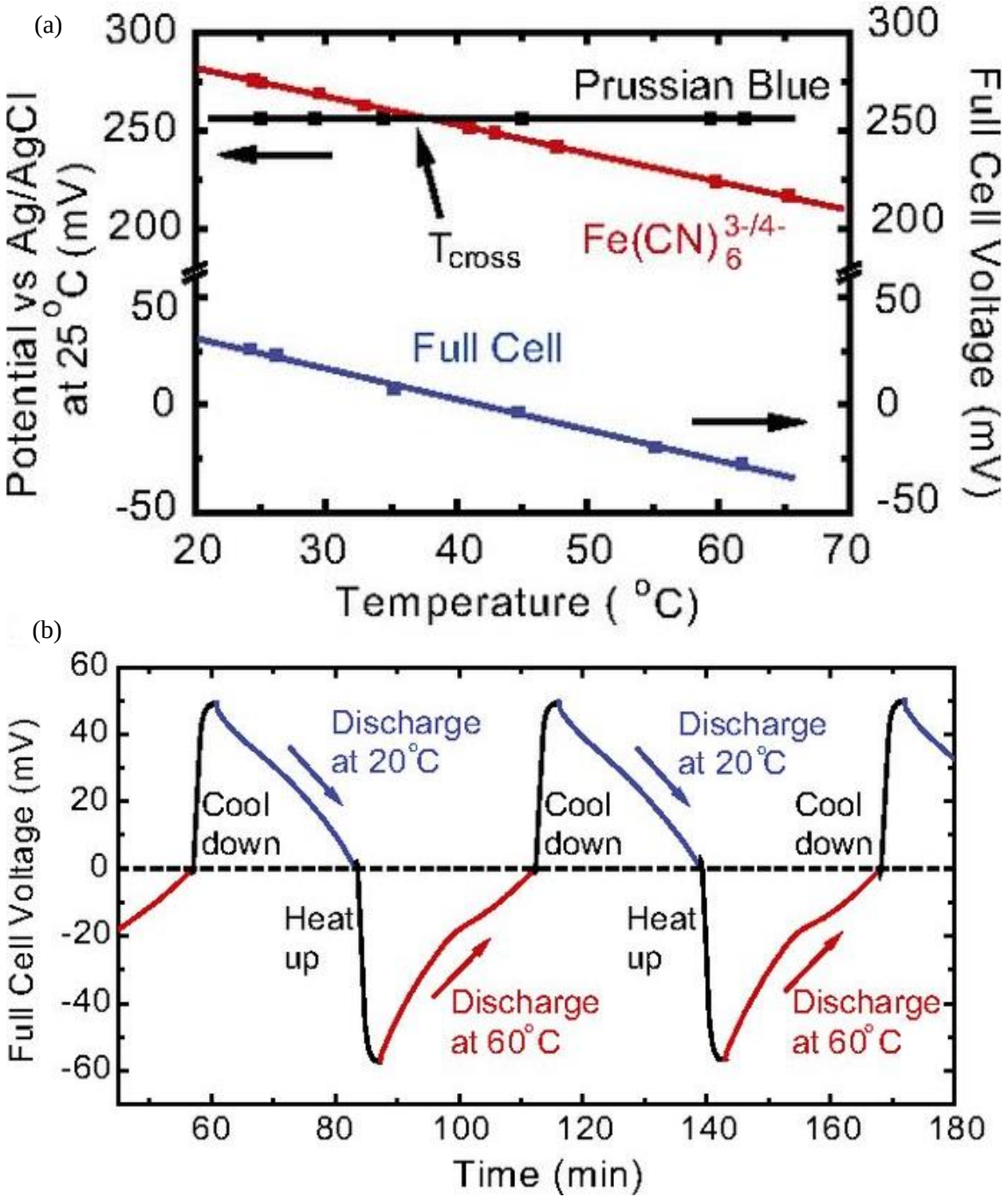

Figure 1.19. (a) Half-cell potentials of Prussian blue ($KFe_2(CN)_{6(s)}$) and $Fe(CN)_6^{3-/4-}$ intersected at 40 °C, fulfilling the requirement for an autonomous electrochemical heat harvester. The temperature range was selected as 20 °C – 60 °C, in order to keep the intersection temperature 40

°C as the midpoint of the operating temperature range. (b) The time-dependent variation of full cell potential of the electrochemical heat harvester. This profile corresponded well with the schematic **Figure 1.16** (c). Figure from *Charging-free electrochemical system for harvesting low-grade thermal energy* and used with permission from the National Academy of Sciences[32].

1.4. Scope of Thesis

Chapter 1 has focused on introducing basic concepts of thermoelectrics, conductive polymers as a category of promising thermoelectric materials, and mechanisms behind thermoelectric power factor improvement in conductive polymer-based nanocomposites. Additionally, electrochemical heat conversion as a novel alternative means to transform heat into electricity was introduced. Thermopowers arising from electrochemical redox reactions usually reach several mV/K, which are one or two orders of magnitude higher than usual solid-state thermoelectric Seebeck coefficients. How to build electrochemical thermodynamic cycles to harness heat without external electrical charging was informed. With these backgrounds, the efforts taken in the following chapters will be clearer to the reader.

Chapter 2 explains the efforts made to design and quantitatively analyze thermoelectric heterostructures based on an earth abundant carbon-based conductive polymer, PEDOT:PSS. We adopted readily available Si and Ge thin films, and increased power factors compared to that of bulk PEDOT:PSS alone. Having thin film heterostructures enabled rigorous understanding on the hole transfer at the interface called modulation doping, which was responsible for the thermoelectric power factor improvement. This chapter is based on *Quantitative Analyses of Enhanced Thermoelectric Properties of Modulation-Doped PEDOT:PSS / Undoped Si (001) Nanoscale Heterostructures* that was published in Nanoscale[60] and *Prediction of Enhanced Thermoelectric Properties via Kraut's Method and 1D Poisson's Equation at PEDOT:PSS / Undoped Ge Thin Film Bilayered Heterostructures* that is ready to be submitted.

Chapter 3 highlights our efforts to develop a flow-battery type electrochemical heat harvester with extended operational lifetime. We first identified two aqueous redox couples which could undergo autonomous thermodynamic cycles to convert heat into electricity, without the need for electrical recharging by external energy. However, this prototype suffered from short operational lifetime less than 4 hours, largely because of Nafion degradation over time. This degradation was attributed to blockage of cation conducting channels in Nafion by large and multivalent $Co(bpy)_3^{2+/3+}$ redox species. We developed a method to resolve this issue, by coating Nafion surface with polyelectrolyte films via layer-by-layer (LbL) deposition. This technique can be further adopted to other fields of practical applications, where selective permeation of ions is desirable.

Chapter 4 describes the development of a more improved version of electrochemical heat harvester using a solid-state redox couple (P2-Na_xCoO_2) and electrical double-layer capacitor (ball-milled Na_xCoO_2). Continuous electrochemical potentials, low heat capacity, and potentially larger electrochemical thermopowers are particular features of solid-state electrode materials, which can realize enable easier design of the electrochemical heat harvester with better conversion efficiency. Electrochemical thermopower could be enhanced by more than an order of magnitude by deliberately disrupting the crystal structure of P2-Na_xCoO_2. It resulted in enhanced heat to electricity conversion efficiency. This correlation between structural disorder and electrochemical thermopowers provided in this chapter may be potentially expanded to offer insights to design more efficient electrochemical heat harvesters in general.

Chapter 5 summarizes the findings from previous chapters and then provides an outlook for the future work in these fields.

References

1 National Academy of Sciences. *Our Energy System*, <http://needtoknow.nas.edu/energy/interactive/our-energy-system/> (2012).

2 LeBlanc, S. Thermoelectric generators: Linking material properties and systems engineering for waste heat recovery applications. *Sustainable Materials and Technologies* **1-2**, 26-35, doi:https://doi.org/10.1016/j.susmat.2014.11.002 (2014).

3 Joo, Y., Agarkar, V., Sung, S. H., Savoie, B. M. & Boudouris, B. W. A nonconjugated radical polymer glass with high electrical conductivity. *Science* **359**, 1391-1395, doi:10.1126/science.aao7287 (2018).

4 Kim, C.-L., Jung, C.-W., Oh, Y.-J. & Kim, D.-E. A highly flexible transparent conductive electrode based on nanomaterials. *Npg Asia Materials* **9**, e438, doi:10.1038/am.2017.177 (2017).

5 Zhao, W., Nugay, I. I., Yalcin, B. & Cakmak, M. Flexible, stretchable, transparent and electrically conductive polymer films via a hybrid electrospinning and solution casting process: In-plane anisotropic conductivity for electro-optical applications. *Displays* **45**, 48-57, doi:https://doi.org/10.1016/j.displa.2016.01.001 (2016).

6 Yoshioka, Y. & Jabbour, G. E. Desktop inkjet printer as a tool to print conducting polymers. *Synthetic Metals* **156**, 779-783, doi:https://doi.org/10.1016/j.synthmet.2006.03.013 (2006).

7 Wang, J. Z., Zheng, Z. H., Li, H. W., Huck, W. T. S. & Sirringhaus, H. Dewetting of conducting polymer inkjet droplets on patterned surfaces. *Nature materials* **3**, 171, doi:10.1038/nmat1073 (2004).

8 Seok-In, N., Seok-Soon, K., Jang, J. & Dong-Yu, K. Efficient and Flexible ITO-Free Organic Solar Cells Using Highly Conductive Polymer Anodes. *Advanced Materials* **20**, 4061-4067, doi:doi:10.1002/adma.200800338 (2008).

9 Nara, K. *et al.* Highly Conductive PEDOT:PSS Nanofibrils Induced by Solution-Processed Crystallization. *Advanced Materials* **26**, 2268-2272, doi:doi:10.1002/adma.201304611 (2014).

10 Kim, G. H., Shao, L., Zhang, K. & Pipe, K. P. Engineered doping of organic semiconductors for enhanced thermoelectric efficiency. *Nature materials* **12**, 719, doi:10.1038/nmat3635 (2013).

11 Vining, C. B. An inconvenient truth about thermoelectrics. *Nature materials* **8**, 83, doi:10.1038/nmat2361 (2009).

12 Zeier, W. G. *et al.* Thinking Like a Chemist: Intuition in Thermoelectric Materials. *Angewandte Chemie International Edition* **55**, 6826-6841, doi:10.1002/anie.201508381 (2016).

13 Vineis, C. J., Shakouri, A., Majumdar, A. & Kanatzidis, M. G. Nanostructured thermoelectrics: big efficiency gains from small features. *Adv Mater* **22**, 3970-3980, doi:10.1002/adma.201000839 (2010).

14 Biswas, K. *et al.* High-performance bulk thermoelectrics with all-scale hierarchical architectures. *Nature* **489**, 414-418, doi:10.1038/nature11439 (2012).

15 Poudel, B. *et al.* High-Thermoelectric Performance of Nanostructured Bismuth Antimony Telluride Bulk Alloys. *Science* **320**, 634-638, doi:10.1126/science.1156446 (2008).

16 Baxter, J. *et al.* Nanoscale design to enable the revolution in renewable energy. *Energy & Environmental Science* **2**, 559-588, doi:10.1039/b821698c (2009).

17 Zebarjadi, M., Esfarjani, K., Dresselhaus, M. S., Ren, Z. F. & Chen, G. Perspectives on thermoelectrics: from fundamentals to device applications. *Energy Environ. Sci.* **5**, 5147-5162, doi:10.1039/c1ee02497c (2012).

18 Hicks, L. D. & Dresselhaus, M. S. Effect of quantum-well structures on the thermoelectric figure of merit. *Physical Review B* **47**, 12727-12731, doi:10.1103/PhysRevB.47.12727 (1993).

19 Dresselhaus, M. S. *et al.* New Directions for Low-Dimensional Thermoelectric Materials. *Advanced Materials* **19**, 1043-1053, doi:10.1002/adma.200600527 (2007).

20 Chum, H. L., Fahlsing, R. F., Jayadev, T. S., Institute, S. E. R. & Institute, M. R. *Analysis of the Application of Thermogalvanic Cells to the Conversion of Low Grade Heat to Electricity*. (Solar Energy Research Institute, 1980).

21 Nichols, A. R. & Langford, C. T. Entropy of the Moving Cuprous Ion in Molten Cuprous Chloride from Thermogalvanic Potentials. *Journal of The Electrochemical Society* **107**, 842-847, doi:10.1149/1.2427524 (1960).

22 Zito, R. THERMOGALVANIC ENERGY CONVERSION. *AIAA Journal* **1**, 2133-2138, doi:10.2514/3.2006 (1963).

23 Tamio, I. Thermoelectric Conversion by Thin-Layer Thermogalvanic Cells with Soluble Redox Couples. *Bulletin of the Chemical Society of Japan* **60**, 1505-1514, doi:10.1246/bcsj.60.1505 (1987).

24 Burrows, B. Discharge Behavior of Redox Thermogalvanic Cells. *Journal of The Electrochemical Society* **123**, 154-159, doi:10.1149/1.2132776 (1976).

25 Quickenden, T. I. & Vernon, C. F. Thermogalvanic conversion of heat to electricity. *Solar Energy* **36**, 63-72, doi:https://doi.org/10.1016/0038-092X(86)90061-7 (1986).

26 Honders, A., der Kinderen, J. M., van Heeren, A. H., de Wit, J. H. W. & Broers, G. H. J. The thermodynamic and thermoelectric properties of Li_xTiS_2 and Li_xCoO_2. *Solid State Ionics* **14**, 205-216 (1984).

27 Dahn, J. R. & Haering, R. R. Entropy measurements on Li_xTiS_2. *Canadian Journal of Physics* **61**, 1093-1098, doi:10.1139/p83-140 (1983).

28 Kuzminskii, Y. V., Zasukha, V. A. & Kuzminskaya, G. Y. Thermoelectric effects in electrochemical systems. Nonconventional thermogalvanic cells. *Journal of Power Sources* **52**, 231-242, doi:https://doi.org/10.1016/0378-7753(94)02015-9 (1994).

29 Hudak, N. S. & Amatucci, G. G. Energy Harvesting and Storage with Lithium-Ion Thermogalvanic Cells. *Journal of The Electrochemical Society* **158**, A572, doi:10.1149/1.3568820 (2011).

30 Lee, S. W. *et al.* An electrochemical system for efficiently harvesting low-grade heat energy. *Nature communications* **5**, 3942, doi:10.1038/ncomms4942 (2014).

31 Yang, Y. *et al.* Membrane-free battery for harvesting low-grade thermal energy. *Nano letters* **14**, 6578-6583, doi:10.1021/nl5032106 (2014).

32 Yang, Y. *et al.* Charging-free electrochemical system for harvesting low-grade thermal energy. *Proceedings of the National Academy of Sciences of the United States of America* **111**, 17011-17016, doi:10.1073/pnas.1415097111 (2014).

33 Wang, J. *et al.* "Thermal Charging" Phenomenon in Electrical Double Layer Capacitors. *Nano letters* **15**, 5784-5790, doi:10.1021/acs.nanolett.5b01761 (2015).

34 Hsu, J.-H., Choi, W., Yang, G. & Yu, C. Origin of unusual thermoelectric transport behaviors in carbon nanotube filled polymer composites after solvent/acid treatments. *Organic Electronics* **45**, 182-189, doi:https://doi.org/10.1016/j.orgel.2017.03.007 (2017).

35 Kim, S. L., Lin, H. T. & Yu, C. Thermally Chargeable Solid-State Supercapacitor. *Advanced Energy Materials* **6**, 1600546-n/a, doi:10.1002/aenm.201600546 (2016).

36 Wang, X. & Feng, S.-P. Thermal Capacitive Electrochemical Cycle on Carbon-Based Supercapacitor for Converting Low-grade Heat to Electricity. *Frontiers in Mechanical Engineering* **3**, doi:10.3389/fmech.2017.00020 (2017).

37 Zhao, D. *et al.* Ionic thermoelectric supercapacitors. *Energy & Environmental Science* **9**, 1450-1457, doi:10.1039/c6ee00121a (2016).

38 Hartel, A., Janssen, M., Weingarth, D., Presser, V. & van Roij, R. Heat-to-current conversion of low-grade heat from a thermocapacitive cycle by supercapacitors. *Energy & Environmental Science* **8**, 2396-2401, doi:10.1039/c5ee01192b (2015).

39 Zhao, D., Fabiano, S., Berggren, M. & Crispin, X. Ionic thermoelectric gating organic transistors. **8**, 14214, doi:10.1038/ncomms14214 (2017).

40 Ail, U. *et al.* Thermoelectric Properties of Polymeric Mixed Conductors. *Advanced Functional Materials* **26**, 6288-6296, doi:10.1002/adfm.201601106 (2016).

41 Gripshover, R. J., VanZytveld, J. B. & Bass, J. Thermopower of Pure Aluminum. *Physical Review* **163**, 598-603, doi:10.1103/PhysRev.163.598 (1967).

42 Blatt, F. J., Schroeder, P. A., Foiles, C. L. & Greig, D. *Thermoelectric Power of Metals. [electronic resource]*. (Boston, MA : Springer US, 1976., 1976).

43 Kasap, S. O. *Principles of electronic materials and devices*. (Boston: McGraw-Hill, 3rd ed., 2006).

44 Chandrasekhar, B. S. The seebeck coefficient of bismuth single crystals. *Journal of Physics and Chemistry of Solids* **11**, 268-273, doi:https://doi.org/10.1016/0022-3697(59)90225-2 (1959).

45 Soni, A. *et al.* Enhanced Thermoelectric Properties of Solution Grown $Bi_2Te_{3-x}Se_x$ Nanoplatelet Composites. *Nano letters* **12**, 1203-1209, doi:10.1021/nl2034859 (2012).

46 Mishra, S. K., Satpathy, S. & Jepsen, O. Electronic structure and thermoelectric properties of bismuth telluride and bismuth selenide. *Journal of Physics: Condensed Matter* **9**, 461 (1997).

47 Boukai, A. I. *et al.* Silicon nanowires as efficient thermoelectric materials. *Nature* **451**, 168-171, doi:10.1038/nature06458 (2008).

48 Tang, J. *et al.* Holey silicon as an efficient thermoelectric material. *Nano letters* **10**, 4279-4283, doi:10.1021/nl102931z (2010).

49 Harman, T. C., Taylor, P. J., Walsh, M. P. & LaForge, B. E. Quantum Dot Superlattice Thermoelectric Materials and Devices. *Science* **297**, 2229-2232, doi:10.1126/science.1072886 (2002).

50 Venkatasubramanian, R., Siivola, E., Colpitts, T. & O'Quinn, B. Thin-film thermoelectric devices with high room-temperature figures of merit. *Nature* **413**, 597, doi:10.1038/35098012 (2001).

51 Abraham, T. J., MacFarlane, D. R. & Pringle, J. M. High Seebeck coefficient redox ionic liquid electrolytes for thermal energy harvesting. *Energy & Environmental Science* **6**, 2639-2645, doi:10.1039/c3ee41608a (2013).

52 Bonetti, M., Nakamae, S., Roger, M. & Guenoun, P. Huge Seebeck coefficients in nonaqueous electrolytes. *The Journal of chemical physics* **134**, 114513, doi:10.1063/1.3561735 (2011).

53 Gao, C., Lee, S. W. & Yang, Y. Thermally Regenerative Electrochemical Cycle for Low-Grade Heat Harvesting. *ACS Energy Letters* **2**, 2326-2334, doi:10.1021/acsenergylett.7b00568 (2017).

54 Rowe, D. M. *CRC handbook of thermoelectrics*. (Boca Raton, FL : CRC Press, c1995., 1995).

55 Sajid, M., Hassan, I. & Rahman, A. An overview of cooling of thermoelectric devices. *Renewable and Sustainable Energy Reviews* **78**, 15-22, doi:https://doi.org/10.1016/j.rser.2017.04.098 (2017).

56 Snyder, G. J. & Toberer, E. S. Complex thermoelectric materials. *Nature materials* **7**, 105-114, doi:10.1038/nmat2090 (2008).

57 Snyder, G. J. & Toberer, E. S. Complex thermoelectric materials. *Nature materials* **7**, 105, doi:10.1038/nmat2090 (2008).

58 Dingle, R., Störmer, H. L., Gossard, A. C. & Wiegmann, W. Electron mobilities in modulation-doped semiconductor heterojunction superlattices. *Applied Physics Letters* **33**, 665-667, doi:10.1063/1.90457 (1978).

59 Takashi, M., Satoshi, H., Toshio, F. & Kazuo, N. A New Field-Effect Transistor with Selectively Doped GaAs/n-$Al_xGa_{1-x}As$ Heterojunctions. *Japanese Journal of Applied Physics* **19**, L225 (1980).

60 Lee, D. *et al.* Quantitative analyses of enhanced thermoelectric properties of modulation-doped PEDOT:PSS/undoped Si (001) nanoscale heterostructures. *Nanoscale*, doi:10.1039/c6nr06950a (2016).

61 Yu, B. *et al.* Enhancement of thermoelectric properties by modulation-doping in silicon germanium alloy nanocomposites. *Nano letters* **12**, 2077-2082, doi:10.1021/nl3003045 (2012).

62 Faleev, S. V. & Léonard, F. Theory of enhancement of thermoelectric properties of materials with nanoinclusions. *Physical Review B* **77**, 214304, doi:10.1103/PhysRevB.77.214304 (2008).

63 Zebarjadi, M. *et al.* Effect of nanoparticle scattering on thermoelectric power factor. *Applied Physics Letters* **94**, 202105, doi:10.1063/1.3132057 (2009).

64 Minnich, A. J., Dresselhaus, M. S., Ren, Z. F. & Chen, G. Bulk nanostructured thermoelectric materials: current research and future prospects. *Energy & Environmental Science* **2**, 466-479, doi:10.1039/b822664b (2009).

65 Minnich, A. J. *et al.* Modeling study of thermoelectric SiGe nanocomposites. *Physical Review B* **80**, 155327, doi:10.1103/PhysRevB.80.155327 (2009).

66 Shen, J.-J. *et al.* Recrystallization induced in situ nanostructures in bulk bismuth antimony tellurides: a simple top down route and improved thermoelectric properties. *Energy & Environmental Science* **3**, 1519-1523, doi:10.1039/c0ee00012d (2010).

67 Yucheng, L., Jerome, M. A., Gang, C. & Zhifeng, R. Enhancement of Thermoelectric Figure-of-Merit by a Bulk Nanostructuring Approach. *Advanced Functional Materials* **20**, 357-376, doi:doi:10.1002/adfm.200901512 (2010).

68 Zebarjadi, M. *et al.* Power factor enhancement by modulation doping in bulk nanocomposites. *Nano letters* **11**, 2225-2230, doi:10.1021/nl201206d (2011).

69 Vashaee, D. & Shakouri, A. Improved thermoelectric power factor in metal-based superlattices. *Physical review letters* **92**, 106103, doi:10.1103/PhysRevLett.92.106103 (2004).

70 Zhang, Y. *et al.* Hot Carrier Filtering in Solution Processed Heterostructures: A Paradigm for Improving Thermoelectric Efficiency. *Advanced Materials* **26**, 2755-2761, doi:10.1002/adma.201304419 (2014).

71 Zhang, Y. *et al.* Silver-based intermetallic heterostructures in Sb_2Te_3 thick films with enhanced thermoelectric power factors. *Nano letters* **12**, 1075-1080, doi:10.1021/nl204346g (2012).

72 Canham, L. T. Silicon quantum wire array fabrication by electrochemical and chemical dissolution of wafers. *Applied Physics Letters* **57**, 1046-1048, doi:10.1063/1.103561 (1990).

73 Wilson, W. L., Szajowski, P. F. & Brus, L. E. Quantum Confinement in Size-Selected, Surface-Oxidized Silicon Nanocrystals. *Science* **262**, 1242-1244, doi:10.1126/science.262.5137.1242 (1993).

74 Takagi, H., Ogawa, H., Yamazaki, Y., Ishizaki, A. & Nakagiri, T. Quantum size effects on photoluminescence in ultrafine Si particles. *Applied Physics Letters* **56**, 2379-2380, doi:10.1063/1.102921 (1990).

75 Wang, Y. & Herron, N. Nanometer-sized semiconductor clusters: materials synthesis, quantum size effects, and photophysical properties. *The Journal of Physical Chemistry* **95**, 525-532, doi:10.1021/j100155a009 (1991).

76 Kittel, C. *Introduction to solid state physics*. (Hoboken, NJ : Wiley, 8th ed., 2005).

77 Zhou, H. & Liu, P. High Seebeck Coefficient Electrochemical Thermocells for Efficient Waste Heat Recovery. *ACS Applied Energy Materials* **1**, 1424-1428, doi:10.1021/acsaem.8b00247 (2018).

78 Lim, H., Zhao, C. & Qiao, Y. Performance of thermally-chargeable supercapacitors in different solvents. *Physical chemistry chemical physics : PCCP* **16**, 12728-12730, doi:10.1039/c4cp01610f (2014).

79 Lim, H., Shi, Y., Wang, M. & Qiao, Y. Effects of work function on thermal sensitivity of electrode potential. *Applied Physics Letters* **106**, 223901, doi:10.1063/1.4921769 (2015).

80 Huang, B. T. *et al.* Thermoelectricity and thermodiffusion in charged colloids. *The Journal of chemical physics* **143**, 054902, doi:10.1063/1.4927665 (2015).

81 Al-zubaidi, A., Ji, X. & Yu, J. Thermal charging of supercapacitors: a perspective. *Sustainable Energy & Fuels* **1**, 1457-1474, doi:10.1039/c7se00239d (2017).

82 Linford, P. A., Lithium ion power generator : a novel system for direct thermal to electric energy conversion. *Thesis from Department of Mechanical Engineering at Massachusetts Institute of Technology* (2017).

83 Schmid, M. J., Xu, J., Lindner, J., Novák, P. & Schuster, R. Concentration Effects on the Entropy of Electrochemical Lithium Deposition: Implications for Li+ Solvation. *The Journal of Physical Chemistry B* **119**, 13385-13390, doi:10.1021/acs.jpcb.5b07670 (2015).

84 Reynier, Y. *et al.* Entropy of Li intercalation in Li_xCoO_2. *Physical Review B* **70**, doi:10.1103/PhysRevB.70.174304 (2004).

85 Viswanathan, V. V. *et al.* Effect of entropy change of lithium intercalation in cathodes and anodes on Li-ion battery thermal management. *Journal of Power Sources* **195**, 3720-3729, doi:https://doi.org/10.1016/j.jpowsour.2009.11.103 (2010).

86 Yao, N. P., Herédy, L. A. & Saunders, R. C. Emf Measurements of Electrochemically Prepared Lithium-Aluminum Alloy. *Journal of The Electrochemical Society* **118**, 1039-1042, doi:10.1149/1.2408242 (1971).

87 Toroshchina, E., Ravdel, B. & Tikhonov, K. Thermodynamic Properties of the Electrochemical-Cell Li / $LiCiO_4$ (Propylene Carbonate) / $Li_xV_2O_5$. *Sov Electrochem* **23**, 1435-1438 (1987).

88 Pereira-Ramos, J. P., Messina, R., Piolet, C. & Devynck, J. A thermodynamic study of electrochemical lithium insertion into vanadium pentoxide. *Electrochimica Acta* **33**, 1003-1008, doi:https://doi.org/10.1016/0013-4686(88)80102-6 (1988).

89 Ravdel, B., Pozin, M. Y., Tikhonov, K. & Rotinyan, A. Thermodynamic Properties of the Electrochemical Cell: Li / $LiClO_4$ (Propylene Carbonate) / Li_xMnO_2. *Sov Electrochem* **23**, 1459-1464 (1987).

90 Lu, W., Belharouak, I., Liu, J. & Amine, K. Thermal properties of $Li_{4/3}Ti_{5/3}O4$ / $LiMn_2O_4$ cell. *Journal of Power Sources* **174**, 673-677, doi:https://doi.org/10.1016/j.jpowsour.2007.06.199 (2007).

91 Takano, K. *et al.* Entropy change in lithium ion cells on charge and discharge. *Journal of Applied Electrochemistry* **32**, 251-258, doi:10.1023/a:1015547504167 (2002).

92 Lim, H., Shi, Y. & Qiao, Y. Thermally chargeable supercapacitor working in a homogeneous, changing temperature field. *Applied Physics A* **122**, 443, doi:10.1007/s00339-016-9981-2 (2016).

93 Qiao, Y., Punyamurtula, V. K. & Han, A. Thermally induced capacitive effect of a nanoporous monel. *Applied Physics Letters* **91**, 153102, doi:10.1063/1.2798245 (2007).

2. Thermoelectrics Performance Enhancements at Si / PEDOT:PSS and Ge / PEDOT:PSS Heterostructures and Their Computational Interpretations

2.1. Introduction

Poly(3,4-ethylenedioxythiophene) poly(styrenesulfonate) (PEDOT:PSS) has high electrical conductivity (~ 10^3 S/cm) when treated with DMSO[1-4], but exhibits low Seebeck coefficient (< 15 μV/K), resulting in low power factor. Mixing PEDOT:PSS with nanostructured semiconductors could enhance Seebeck coefficient and achieve improved thermoelectric power factor[5-14]. However, underlying mechanisms for the composite thermoelectric systems are scarcely understood so far. In this study, quantitative analyses on electrical conductivity and Seebeck coefficient for the heterostructures of nanometer-thick PEDOT:PSS on undoped single-crystal Si (001) on sapphire (SOS) and nanoscale PEDOT:PSS thin films on undoped polycrystalline Ge are reported. The Si / PEDOT:PSS heterostructures have larger Seebeck coefficients up to 7.3 fold and power factors up to 17.5 fold relative to PEDOT:PSS. The maximum power factor and Seebeck coefficient of the Ge / PEDOT:PSS heterostructures are 154 μW/m·K^2 and 398 μV/K respectively, corresponding to 47 fold and 41 fold increases compared to those of bulk PEDOT:PSS and 64 fold increase compared to power factor of the undoped Ge. For both Si / PEDOT:PSS and Ge / PEDOT:PSS heterostructures, electrical conductivity increased with decreasing combined thicknesses of PEDOT:PSS, and Seebeck coefficient increased with decreasing PEDOT:PSS thickness, which can be attributed to modulation doping caused by diffusion of holes from PEDOT:PSS into undoped Si or undoped Ge. This hypothesis is examined by band alignment simulation based on electronic band and transport measurements of individual Si, Ge, and PEDOT:PSS. The valence band offset (i.e. amount of discontinuity of valence band edges at the interfaces) between Si / PEDOT:PSS and Ge / PEDOT:PSS dominantly governs electrical conductivity and Seebeck coefficient of the heterostructures. The agreements between the simulation and experiments for both systems suggest predictability of thermoelectric performances of nanoscale heterostructures with our method. This methodology can further be extended to predict performance of other nanoscale combinations of thermoelectric and other electronic materials in general. This study not only offers mechanistic insights to increase the

power factors of PEDOT:PSS-based composites but also opens a door for strategies to enhance the thermoelectric efficiencies of heterostructured nanocomposite materials in general.

2.2. Experimental and Simulation Methods

2.2.1. Si / PEDOT:PSS Sample Preparation

The sample fabrication starts by preparing the substrates which are 1.8 × 1.8 cm^2 SiO_2 glass coverslips or 1.0 × 1.0 cm^2 silicon on sapphire (SOS). The SOS substrates (Precision Micro-Optics) originally have (001) Si layer on top of $(1\bar{1}02)$ single crystalline bulk sapphire layer. In order to generate different thicknesses of Si from the initial 100 nm SOS, thermal oxidation at 1100 ^oC under dry oxygen flow with different time duration[15] and subsequent oxide strip by hydrofluoric acid (HF) was conducted. The thermally grown SiO_x layer was completely etched by 4.8 wt% HF aqueous solution. X-ray reflectivity (XRR, Cu K-α source) measurements examined thicknesses of the remnant Si layer, using interference pattern of the reflected X-ray.

All glasses and SOS substrates were cleaned with acetone, isopropanol, and distilled water (DI water) in an ultrasonication bath and then piranha-treated in a cleanroom for 10 minutes to completely remove the organic contaminants on the surface. The piranha was mixture of sulfuric acid and hydrogen peroxide with 3:1 volumetric ratio.

Only for SOS wafers, additional steps were applied to control the surface oxidation. After the piranha treatment, the SOS wafers were submerged in 4.8 wt% HF for 3 minutes, then rinsed in DI water to remove the native oxide layer formed by the previous piranha treatment. Since deposition of PEDOT:PSS requires hydrophilic substrate surfaces, HF-etched SOS pieces were treated with 10 vol% aqueous piranha solution (98 wt% H_2SO_4 : 30 wt% H_2O_2 : H_2O = 3 : 1 : 36 v/v) for 5 minutes in order to form sufficiently hydrophilic surfaces with minimal thickness of SiO_x that can accommodate PEDOT:PSS thin film.

Water-dispersed form of conductive polymer PEDOT:PSS (Clevios PH1000) was mixed with solvent dimethyl sulfoxide (DMSO, Sigma-Aldrich, D8418) of 5 wt% mass ratio by ultrasonication for 15 minutes, in order to enhance the electrical conductivity of PEDOT:PSS from 5 S/cm to ~ 10^3 S/cm[1-4]. Ethanol (200 Proof, Koptec) was added to the polymer mixture with 1:5 volumetric ratio and homogenized with horn-ultrasonicator for another 5 minutes. The purpose of ethanol addition is to improve the wettability and surface uniformity of spin-coated PEDOT:PSS.

PEDOT:PSS thin films with various thicknesses were deposited on substrates using spin-coating. To create different PEDOT:PSS layer thickness, spin-coating was repeated without additional time for drying after each round of spin-coating.

2.2.2. Ge / PEDOT:PSS Sample Preparation

Undoped germanium-on-insulator (GeOI) was first cut into 1.0 × 1.0 cm^2 geometry by a dicing saw, and SiO_2 layer was deposited by plasma-enhanced chemical vapor deposition (PECVD) on the back and edges of the resultant square wafer pieces. This PECVD process is introduced to prevent short-circuit by electrical connection between Ge device layer and Si handle layer through spin-coated PEDOT:PSS. Then it was serially washed by acetone (Sigma-Aldrich, 270725, ≥ 99.9 %), ethanol (200 Proof, Koptec), isopropanol (Sigma-Aldrich, I9030, > 99.0%) in ultrasonication bath. The GeOI is briefly rinsed with distilled water (18.2 MΩ·cm) and immersed in 16.7 vol% aqueous hydrochloric acid (Sigma-Aldrich, 258148, 37 %) solution for 10 minutes to remove native oxide. Controlled re-oxidation of the etched Ge surface was carried out by immersing the GeOI in deionized water (18.2 MΩ·cm) for 4 minutes in order to modify the surface more hydrophilic to accommodate the hydrophilic PEDOT:PSS dispersion, while avoiding unnecessarily excessive Ge surface oxidation.

0.5 mL of PEDOT:PSS water-based dispersion (Clevios PH1000) was mixed to 24.0 μL of dimethyl sulfoxide (DMSO, Sigma-Aldrich, D8418) to comply 20 to 1 mass ratio, and 0.50 mL of ethanol (200 Proof, Koptec) was added. They were homogenized by horn-ultrasonicator in ice bath for 30 minutes, to minimize evaporation of liquid contents in the dispersion. 50 μL of the resultant PEDOT:PSS dispersion was spin-coated on GeOI at 6000 RPM with 180 seconds of dwell time. When thicker PEDOT:PSS was needed, the same condition of spin-casting process was repeated for multiple times.

2.2.3. Seebeck Coefficient Measurements

The Seebeck coefficient (S) of all samples was measured with a lab-made setup. In order to determine the Seebeck coefficient, it was necessary to induce the temperature gradient across the sample and measure the voltage change (ΔV) and the temperature difference (ΔT). To accomplish this, a Seebeck measurement device was built (**Figure 2.1**). The device used two

commercially available Peltier modules (TE Technology, Inc.) to heat up one side of the sample and cool down the opposite side. Current was applied through the Peltier heaters in opposite directions using a current source (Keithley 2400 Sourcemeter), which made one Peltier plate a heater and the other a cooler. Under each Peltier heater/cooler was a small heat sink to help conduct heat and create the largest possible temperature difference across the heater or cooler. The sample and alumina support bridged the gap between the heater and cooler.

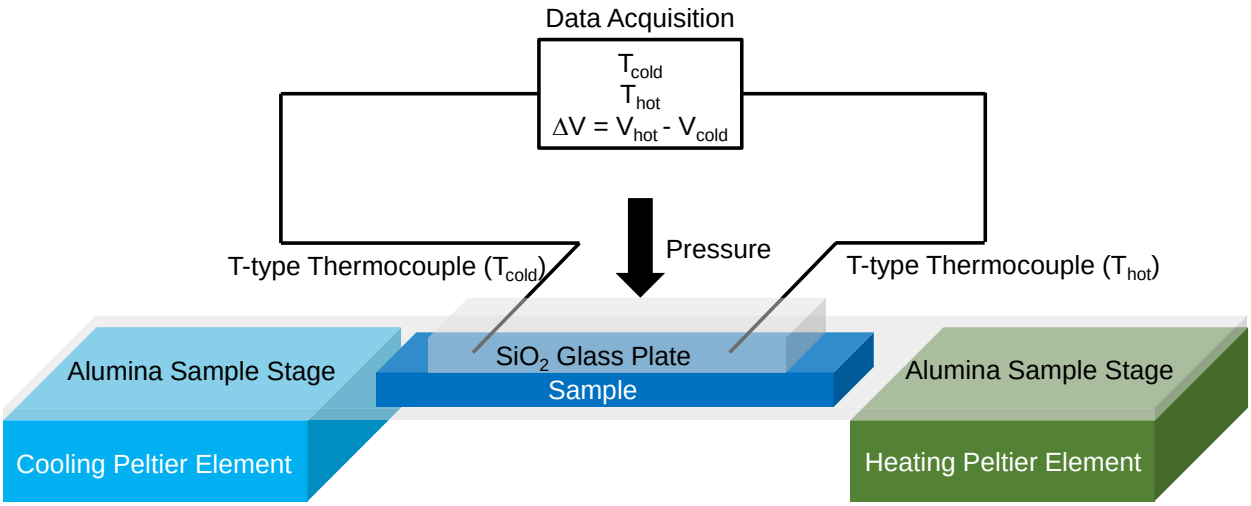

Figure 2.1. Schematic diagram of Seebeck coefficient measurement setup. The Peltier plates provide a temperature gradient across the sample. The temperature and voltage are measured at the same position, by two T-type thermocouples. Mechanical pressure is provided on the thermocouples to maintain firm electrical and thermal contacts with the sample.

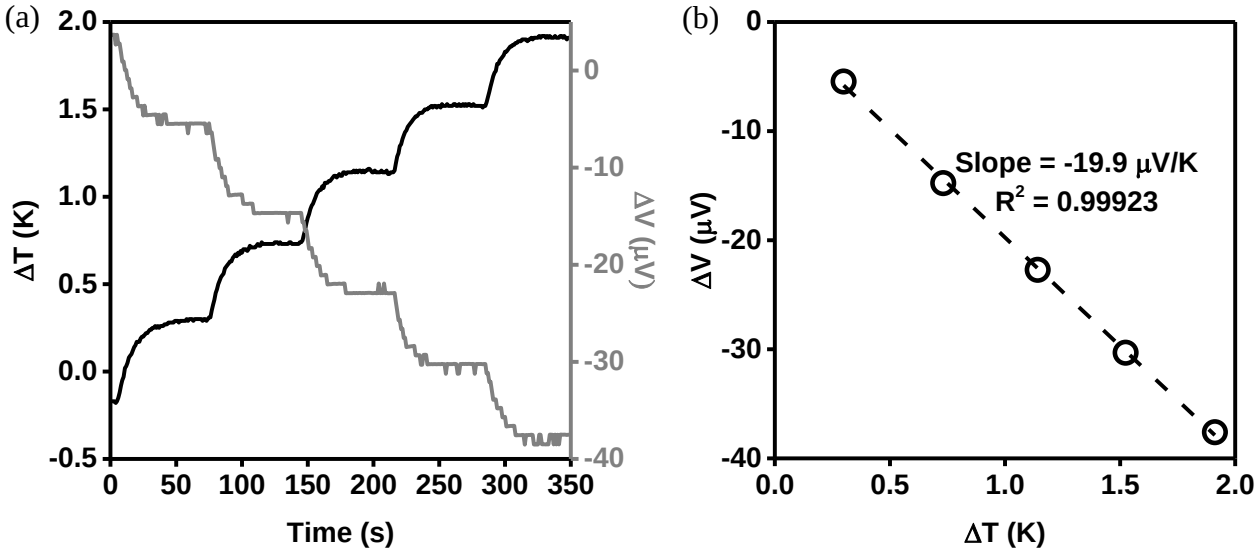

Figure 2.2. An exemplar Seebeck coefficient measurement of a nickel foil. Current through Peltier elements were increased by 0.1 A, every 70 seconds. 70 seconds is enough to allow establish steady-states for both temperature gradient and voltage. As a result, as can be seen at (a), step-wise profile of voltage and temperature difference are observed every 70 seconds, until 350 seconds are reached. (b) The plateaus of voltage and thermal gradient are averaged and plotted against each other. The slope of those dots is Seebeck coefficient. In this case, -19.9 μV/K was measured for the nickel foil, which closely matches with literature value[16].

2.2.4. Electrical Conductivity Measurements by 4-point Probe and Hall Techniques

Electrical conductivity was measured by 4-point probe method (LucasLabs Pro4) for Si / PEDOT:PSS heterostructures. To obtain a more accurate electrical conductivity measurement, 9 individual measurements were taken for each sample. These 9 measurements were averaged to produce experimental electrical conductivity of the samples reported in this thesis.

Hall measurements (LakeShore 7500 Series Hall System) were also carried out to measure electrical conductivity of Ge / PEDOT:PSS samples and to assess thickness-dependent mobility of PEDOT:PSS films on SiO_2. This technique requires Ohmic contacts on each corner of square samples, and detailed schemes are illustrated in **Figure 2.3** and **Figure 2.4**. Those measurements yielded similar results to each other: for instance, electrical conductivity of 2.0 μm thick PEDOT:PSS on SiO_2 was 537.12 S/cm by 4-point probe measurement, and 501.88 S/cm by Hall measurement. The difference between the two measurements is less than 7 %.

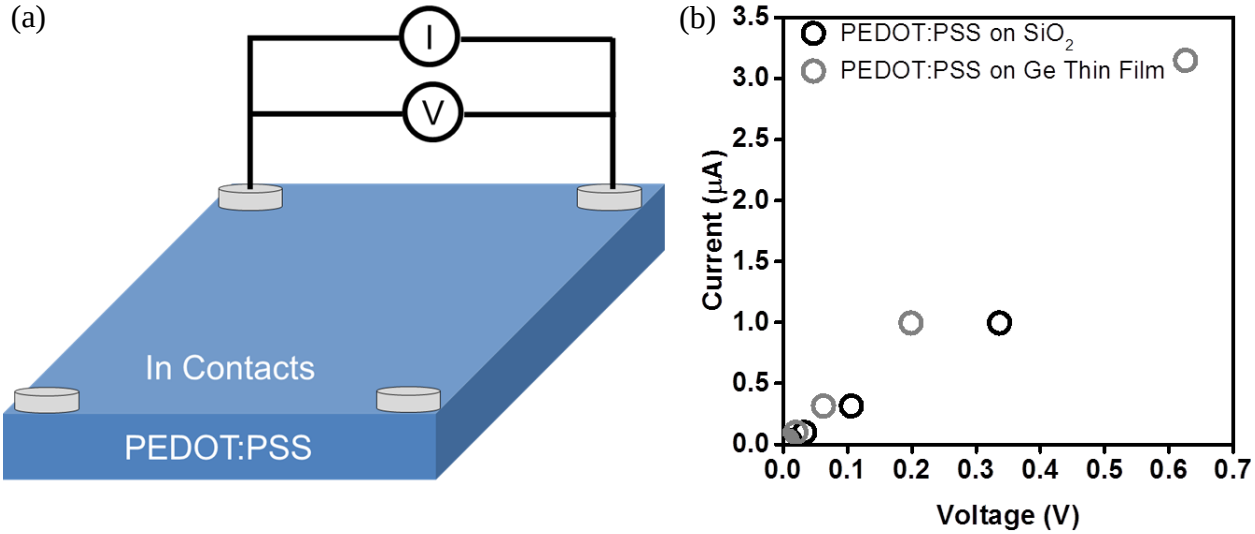

Figure 2.3. (a) Configuration for I-V characteristics measurements and (b) Linear dependence of current on applied voltage indicates In contacts on PEDOT:PSS surface always form Ohmic contacts regardless PEDOT:PSS in on Ge or SiO_2. For both cases, the thicknesses of PEDOT:PSS are 9.4 nm. This Ohmic In contacts were used consistently for Hall measurements of PEDOT:PSS on SiO_2 samples and Ge / PEDOT:PSS heterostructures.

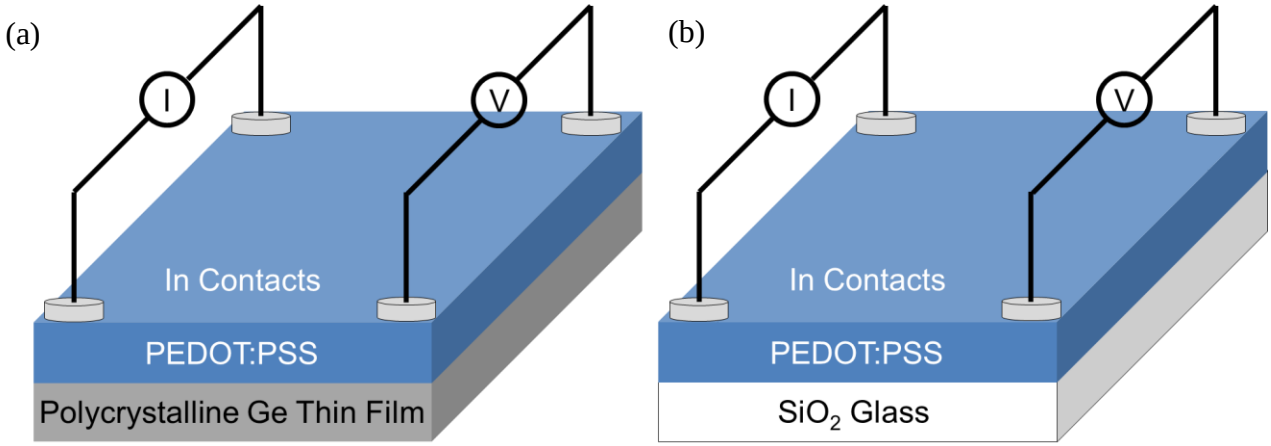

Figure 2.4. (a) – (b) PEDOT:PSS on Ge or SiO_2 glass slides are square-shaped to measure electrical conductivity with van der Pauw method. In contacts are placed on PEDOT:PSS surfaces in order to form Ohmic contacts, and this configuration was constantly employed for all Hall measurements reported in this dissertation.

2.2.5. AFM for PEDOT:PSS Thickness Determination and Thin Film Morphology Observations

The thickness of each sample was measured with AFM using a Veeco NanoScope IV. To obtain an estimate of the thickness, 2 lines were scratched onto the sample using a razor blade, thereby exposing the substrate underneath. The step heights were measured at each of these scratches (**Figure 2.5**), and averaged values were employed as PEDOT:PSS thickness of each sample.

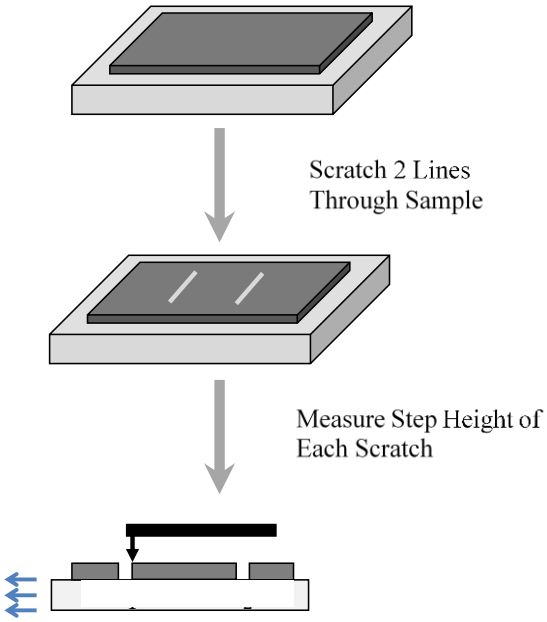

Figure 2.5. Procedure for PEDOT:PSS thickness measurements using the AFM. Figure from *Quantitative analyses of enhanced thermoelectric properties of modulation-doped PEDOT:PSS/undoped Si (001) nanoscale heterostructures*[17]. Reproduced by permission of the Royal Society of Chemistry.

2.2.6. Si, SiO_x, and Ge Thin Film Thickness Measurements by X-ray Reflectivity (XRR)

Thicknesses of SiO_x layers on Si after oxide strip, thermal oxidation, and piranha-based oxidation, were examined by XRR measurements. Thickness of Si layer at SOS after thermal

oxidation and following HF etching was also determined by XRR measurements. Also, undoped Ge layer in the GeOI was characterized. This technique utilizes that the length of interference path depends on incident angle of the electromagnetic wave (X-ray). Therefore, the intensity of the reflected beam will have periodic rise and fall, imposed by boundary conditions, such as wavelength of the incident beam, densities and thicknesses of the films. Since the wavelength of the beam is fixed at that of Cu K α (0.15418 nm), analysis of the periodic interference pattern measured by XRR can inform thickness of the thin film. Beam size was consistently 5×5 mm^2 for all XRR measurements. **Figure 2.6** represents an exemplar XRR pattern of thermally oxidized and then HF etched SOS.

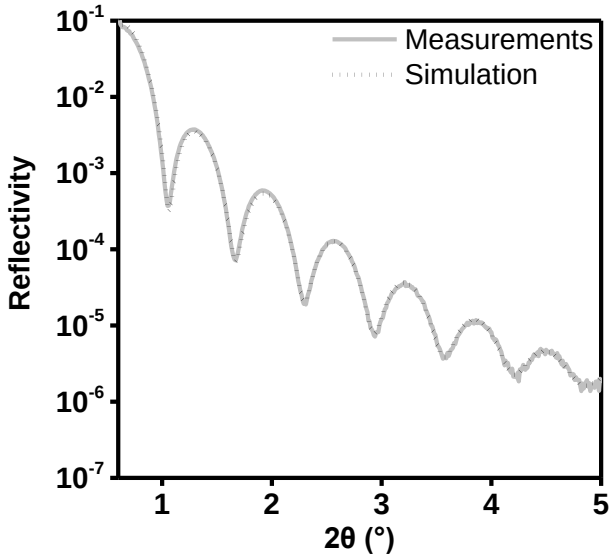

Figure 2.6. An exemplar interference pattern of 14 nm thick Si on sapphire (SOS) measured by XRR. Figure from *Quantitative analyses of enhanced thermoelectric properties of modulation-doped PEDOT:PSS/undoped Si (001) nanoscale heterostructures*[17]. Reproduced by permission of the Royal Society of Chemistry.

2.2.7. Spectroscopic Determination of Valence Band Offsets at Interfaces of Ge / PEDOT:PSS Heterojunctions by Kraut's Method

Kraut's method is a concerted spectroscopic technique to probe band offset by subtracting deconvoluted core level spectra peaks of individual constituent materials from valence band edge locations versus Fermi level[18,19]. This method was validated because energy differences between

the valence band edges and core levels of individual materials are preserved as the same, even after heterojunction between both is formed[18,19]. Therefore, knowing (i) core levels and valence band edges of individual materials without heterojunction and (ii) core levels of individual materials at the heterojunction could lead to band offset of the two materials at the heterojunction. This could be converted to a mathematical formalism:

$$\mathrm{VBO} = \left(\mathrm{E}_{\mathrm{core}}^{\mathrm{A,alone}} - \mathrm{E}_{\mathrm{VB}}^{\mathrm{A,alone}}\right) - \left(\mathrm{E}_{\mathrm{core}}^{\mathrm{B,alone}} - \mathrm{E}_{\mathrm{VB}}^{\mathrm{B,alone}}\right) - \left(\mathrm{E}_{\mathrm{core}}^{\mathrm{A,hetero}} - \mathrm{E}_{\mathrm{core}}^{\mathrm{B,hetero}}\right) \quad (2.1)$$

where $\mathrm{E}_{\mathrm{core}}^{\mathrm{A,alone}}$, $\mathrm{E}_{\mathrm{VB}}^{\mathrm{A,alone}}$, $\mathrm{E}_{\mathrm{core}}^{\mathrm{B,alone}}$, $\mathrm{E}_{\mathrm{VB}}^{\mathrm{B,alone}}$, $\mathrm{E}_{\mathrm{core}}^{\mathrm{A,hetero}}$, and $\mathrm{E}_{\mathrm{core}}^{\mathrm{B,hetero}}$ represented core level of material A alone, valence band edge location versus Fermi level of material A alone, core level of material B alone, valence band edge location versus Fermi level of material B alone, core level of material A at the heterojunction, core level of material B at the heterojunction, respectively. However, when X-ray Photoemission Spectroscopy (XPS) was measured for the core level detection, multiple peaks were superimposed, mainly due to co-existing multiple oxidation states in materials, as shown in **Figure 2.7** (a) – (b). Thus, selection of appropriate core level peaks among superimposed peaks was required for precise interpretation and implementation of Kraut's method.

In order to execute Kraut's method for precise determination of band offset, three criteria should be met: (i) primary XPS peaks of unique elements of each material should be chosen, (ii) the number of deconvoluted peaks should be able to reflect oxidation state of the material, (iii) deconvoluted peaks should correspond to oxidation states of materials that are actually electronically active at the heterojunction. Ge / PEDOT:PSS heterojunction satisfies those requirements, thus this method was selected to measure valence band offset of that heterojunction.

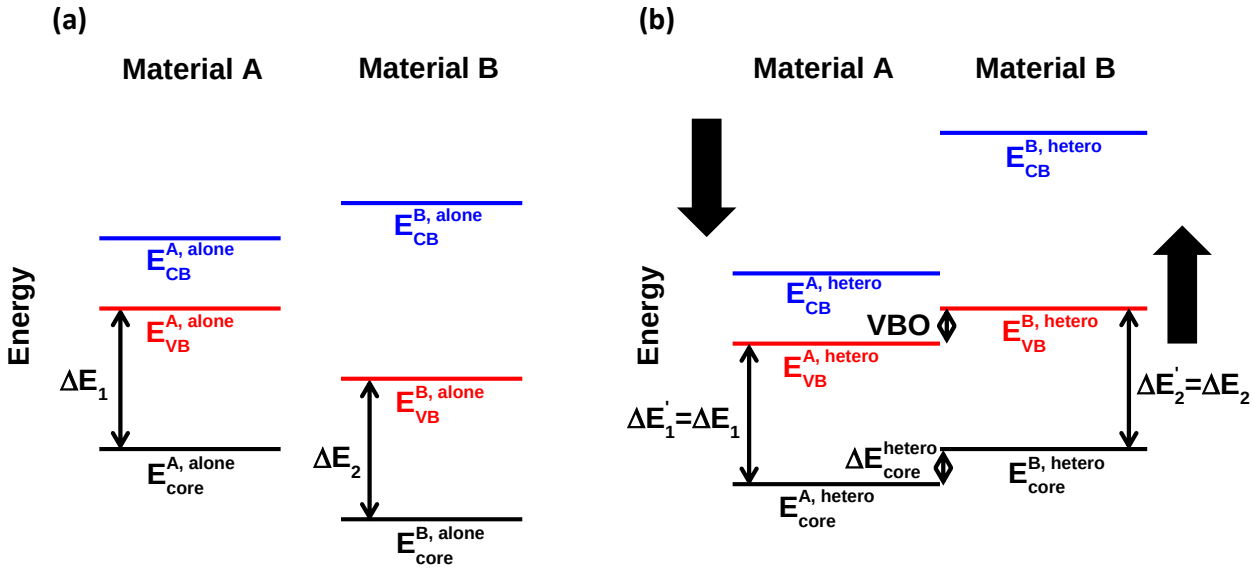

Figure 2.7. Schematic explanation on Kraut's method. (a) Before the heterojunction formation, energy levels of individual materials are shown. (b) Flat band diagram after the heterojunction formation. Because core levels, valence band and conduction band of each material shift the same amount of energy as a result of a heterojunction formation (shown as black wide arrows), $\Delta E_1' = \Delta E_1$ and $\Delta E_2' = \Delta E_2$ can be justified[19]. Thus, if ΔE_{core}^{hetero}, ΔE_1, and ΔE_2 are measured, then it is possible to know the valence band offset (VBO), because VBO can now be expressed as $\Delta E_1 - \Delta E_2 - \Delta E_{core}^{hetero}$, as illustrated at (b).

2.2.8. Purpose of Thermoelectric Properties Simulations and Simulation Tools

By comparing experimental data and simulated data, modulation doping as the working principle can be verified or denied. Also, the simulation can examine if the accuracy is sufficient to predict characteristics of nanoscale heterostructured electronics in general.

Simulation tools for band diagram construction for Si / PEDOT:PSS and Ge / PEDOT:PSS heterojunctions were COMSOL Multiphysics® Modeling Software and Adept 2.1 at Nanohub[20]. The COMSOL Multiphysics® Modeling Software was designed to produce both band diagram and thermoelectric properties of the heterostructures, while Adept 2.1 could only compute band alignments.

2.2.9. 1 Dimensional (1D) Poisson's Equation Solver

The key quantity in evaluating the electrical transport properties was the carrier density distribution ($n_c(x)$), which was obtained by solving the Poisson's equation.

$$\nabla^2\varphi = -\frac{\rho}{\varepsilon} \qquad (2.2)$$

On the left-hand side, φ denotes the electric potential (at each side its energy reference is taken to be the conduction band edge far away from the interface). On the right-hand side, $\rho = N_D - N_A + p - n$ is the net positive charge density (N_D: donor density; N_A: acceptor density; p: hole density; n: electron density), which in turn depends on the electric potential. For example, for electron density, $n = \int_{\text{conduction band}} f(E - e\varphi)D(E)dE$, where $f(E - e\varphi)$ is Fermi-Dirac distribution function at energy $E - e\varphi$ and $D(E)$ is electronic density of states at energy E. The measured valence band offset is inserted into the solver, and the electric potential gradient far away from the interface is assumed to be zero. Solving the Poisson's equation self-consistently for the electric potential φ, one obtains the band alignment profile. Charge transfer across the interface, as well as the electron transport properties, then can be analyzed accordingly.

2.2.10. Simulation of the Seebeck Coefficient and Electrical Conductivity *without Band Bending* under Parallel Resistors Model for Si / PEDOT:PSS

Parallel resistor model was assumed to estimate theoretical Seebeck coefficient and electrical conductivity of the co-planar heterostructures, as validated in previous studies[21,22]. When no band bending upon contact between PEDOT:PSS and Si is assumed, charge distribution within PEDOT:PSS and Si will be unchanged. This means Seebeck coefficient and electrical conductivity of PEDOT:PSS and Si will stay the same. Therefore, theoretical Seebeck coefficient and electrical conductivity of Si / PEDOT:PSS heterostructure can be modeled as shown in **Figure 2.8**, and expressed by following formalisms:

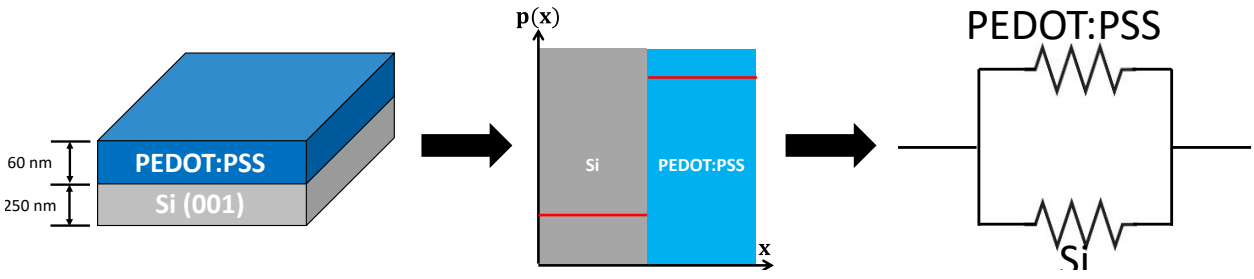

Figure 2.8. Thermoelectric properties simulation procedures *without band bending*. Both Si and PEDOT:PSS are considered as if they are separated without forming heterojunction. Accordingly, the carrier density within each material will not be influenced at all, justifying them to treat as two separate parallel resistors.

$$\frac{1}{\bar{R}} = \frac{1}{R_1} + \frac{1}{R_2} \tag{2.3}$$

$$\bar{\sigma}(d_1 + d_2)\frac{w}{l} = \sigma_1 d_1 \frac{w}{l} + \sigma_2 d_2 \frac{w}{l} \tag{2.4}$$

$$\boldsymbol{\bar{\sigma} = \frac{\sigma_1 d_1 + \sigma_2 d_2}{d_1 + d_2}} \tag{2.5}$$

$$\frac{\bar{S}}{\bar{R}} = \frac{S_1}{R_1} + \frac{S_2}{R_2} \tag{2.6}$$

$$\bar{\sigma}\bar{S}(d_1 + d_2)\frac{w}{l} = \sigma_1 S_1 d_1 \frac{w}{l} + \sigma_2 S_2 d_2 \frac{w}{l} \tag{2.7}$$

$$\boldsymbol{\bar{S} = \frac{S_1 \sigma_1 d_1 + S_2 \sigma_2 d_2}{\sigma_1 d_1 + \sigma_2 d_2}} \tag{2.8}$$

where R_1, R_2, d_1, d_2, σ_1, σ_2, S_1, and S_2 represent resistance, thickness, electrical conductivity, and Seebeck coefficient of Si and PEDOT:PSS respectively. w and l mean width and length of the sample, which always are 1.0 cm. $\bar{\sigma}$ and $\bar{S}$ are electrical conductivity and Seebeck coefficient of Si / PEDOT:PSS heterostructure.

2.2.11. Simulation of the Seebeck Coefficient and Electrical Conductivity *with Band Bending* under Parallel Resistors Model for Both Si / PEDOT:PSS and Ge / PEDOT:PSS

When band bending is assumed, valence band edge at each position changes, as shown in **Figure 2.9**. The band bending causes different hole density at each position. Therefore hole density at each position can be converted to electrical conductivity and Seebeck coefficient at corresponding position. Charge scattering mechanism in PEDOT:PSS and Si were regarded unchanged even after modulation doping, leading to preserved mobility of holes in Si and PEDOT:PSS. Pisarenko relation of PEDOT:PSS[23] and (001) Si[24-27] at room temperature were adopted to evaluate Seebeck coefficient at specific hole density. Detailed mathematical expressions are shown below:

$$\sigma_1(n_1(x)) = n_1(x) e \mu_1 \tag{2.9}$$

$$\sigma_2(n_2(x)) = n_2(x)e\mu_2 \quad (2.10)$$

$$S_1(n_1(x)) = \frac{k_B}{e}\left(\ln\left(\frac{N_{V1}}{n_1(x)}\right) + 3\right) \text{ at room temperature} \quad (2.11)$$

where μ_1 and μ_2 are the mobility of holes in Si and PEDOT:PSS layer, N_{V1} the valence band density of states of Si, k_B the Boltzmann constant, e the elementary charge, respectively. Hole density dependent Seebeck coefficient of PEDOT:PSS, $S_2(n_2(x))$, was taken from Pisarenko relation (i.e. Seebeck coefficient as a function of carrier density in a given material at certain temperatures) in the previous research[23].

In order to evaluate the overall sample thermoelectric properties, averaging the Seebeck coefficient and electrical conductivity over the entire thickness of PEDOT:PSS and Si was needed. Parallel resistor model was applied and each position was regarded as a resistor, as shown in **Figure 2.9**. Detailed mathematical expressions are shown below.

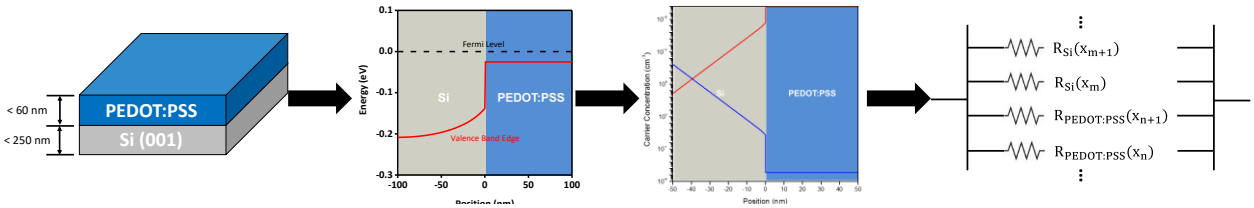

Figure 2.9. Thermoelectric properties simulation procedures *with band bending*. This computation scheme was applied to predict thermoelectric properties of both Si / PEDOT:PSS and Ge / PEDOT:PSS systems. Here, Si / PEDOT:PSS system was taken as an example. These two materials form a heterojunction, and therefore there will be specific band bending. This band bending has information about the distance between the Fermi level and valence band edge at each position within the heterojunction. Thus, it can be converted to yield carrier concentration at each position within the heterojunction. Parallel resistor model can be assumed again, but this time each position should be considered different resistors, because the carrier concentration is not constant. Seebeck coefficients and electrical conductivities of these infinitesimally small resistors are summed up and averaged according to equations below, in order to be compared with experimentally measured ones.

$$\frac{1}{R} = \sum_i \frac{1}{R_i} \quad (2.12)$$

$$\overline{\sigma} = \frac{\int_{-d_1}^{0} n_1(x) e\mu_1 dx + \int_{0}^{d_2} n_2(x) e\mu_2 dx}{d_1 + d_2} \quad (2.13)$$

$$\overline{S} = \frac{\int_{-d_1}^{0} S_1(x) n_1(x) e\mu_1 dx + \int_{0}^{d_2} S_2(x) n_2(x) e\mu_2 dx}{\overline{\sigma}(d_1 + d_2)} \quad (2.14)$$

where R_i is resistance of individual infinitesimal resistors, $\overline{R}$, $\overline{\sigma}$, and $\overline{S}$ represent resistance, thickness, electrical conductivity, and Seebeck coefficient of overall samples, respectively.

2.3. Results and Discussion

2.3.1. Selection Criteria for Si, Ge, and PEDOT:PSS Thin Film Heterostructures

Among conductive polymers deemed appropriate for thermoelectric application, PEDOT:PSS was selected in this study, because it had one of the highest hole densities among conductive polymers, so that it can send holes to an adjacent undoped semiconductor. Another benefit of PEDOT:PSS was its easy processing capability to form thin films and nanoscale composites on various substrates via spin-coating[28], dip-coating[29,30], or drop-casting[30]. Another requirement on band properties for modulation doping was that valence band edge of the modulation dopant PEDOT:PSS should be close to those of the modulation doped materials. Given these requirements, Si and Ge were among candidates.

Undoped Si (001) was selected due to its well-known surface chemistry and band structure, high hole mobility of 450 $cm^2/V{\cdot}s$ at room temperature[31], and high Seebeck coefficients such as 1.3 mV/K at 10^{14} cm^{-3} of undoped hole density[24-27]. Six Si thicknesses of SOS (14 nm, 41 nm, 46 nm, 59 nm, 100 nm, and 250 nm) were used and PEDOT:PSS thickness varied from 5 nm to 60 nm.

Undoped germanium (Ge) was considered as an attractive counterpart for modulation dopant PEDOT:PSS, because it possesses high mobility for holes (up to 1900 $cm^2/V{\cdot}s$ at room temperature)[32] at an intrinsic doping level.

Lastly, thin film bilayered structures of Si / PEDOT:PSS and Ge / PEDOT:PSS were picked for simpler and quantitative analysis. Usually, multiple inadvertent effects arise simultaneously from nanoscale composite materials, especially from inorganic components of such composites. Commonly, they arise from inhomogeneity of the nanoscale mixture, such as preferential ordering between conductive polymer and inorganic semiconductor crystals[33], and percolation[34]. These may affect resultant thermoelectric properties simultaneously, because those effects are not exclusive to each other. Both Si and Ge are commercially available as thin films, and PEDOT:PSS can be spin-coated into thin film down to ~ 10 nm[17] at high rotation speed, making thin film bilayered structures experimentally feasible.

2.3.2. Characterizations on Quality of Germanium on Insulator (GeOI)

Crystallinity, thickness, and layered structure of the undoped germanium-on-insulator (GeOI) were confirmed in **Figure 2.10**. General Area Detector Diffraction System (GADDS) X-ray diffraction (XRD) pattern of the undoped GeOI at **Figure 2.10** (a) proves that polycrystallinity of Ge layer, showing (311) and (400) peaks. Broad background at the low angle region indicates phase of SiO_2 beneath Ge layer is amorphous. X-ray Reflectivity (XRR) spectrum of GeOI at **Figure 2.10** (b) shows that thicknesses of Ge layer and SiO_2 layer are 21.4 nm and 71.9 nm respectively, and the stacking order of GeOI is Ge – SiO_2 – bulk Si, from the top to the bottom. Atomically smooth surface of the Ge layer is shown at **Figure 2.10** (c), demonstrating its suitability for the modulation doped device, where minimal interfacial scattering effect is advantageous. In addition, pinhole-free surface of the undoped GeOI is confirmed, and this is a crucial requirement for spectroscopic detection of band offset.

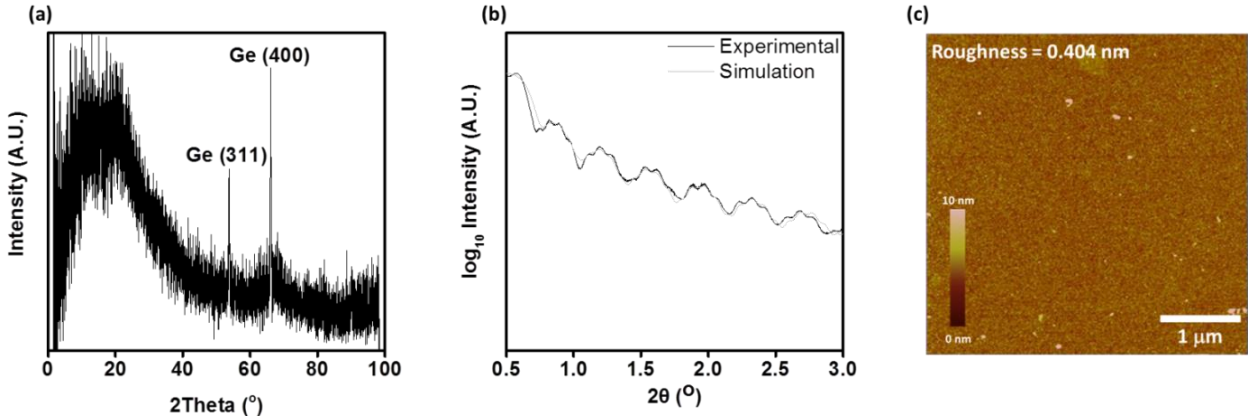

Figure 2.10. (a) GADDS XRD patterns of the undoped GeOI. (b) XRR spectrum of GeOI. (c) AFM image (4 × 4 μm^2) of the undoped GeOI. All measurements are performed at ambient condition.

2.3.3. Dependence of Quality of Spin-coated PEDOT:PSS on Surface Hydrophilicity and Oxidation States

Atomic force microscopy (AFM) was used to monitor spin-coatability by observing morphologies of PEDOT:PSS on SOS with different surface oxidation states. They were compared with morphology of 10-nm-thick PEDOT:PSS deposited on hydrophilic SiO_2 glass substrate (VWR, 48366-045) as a reference, with RMS roughness of 1.48 nm in **Figure 2.11** (a). The Si

(001) of SOS following the hydrofluoric acid etching was hydrophobic and the deposition of PEDOT:PSS was not uniform (**Figure 2.11** (c)), which exhibited a markedly different morphology from that found on SiO_2 glass, suggesting that PEDOT:PSS on HF-treated Si may not intact. This is further supported by the fact that electrical resistivity of the sample represented in **Figure 2.11** (c) is the same as that of bare SOS (4.6×10^3 Ω·cm). In contrast, PEDOT:PSS deposited on the Si (001) following the piranha treatment and 10 vol% diluted piranha treatment (with RMS roughness of 1.48 nm and 1.44 nm in **Figure 2.11** (a) – (b)) was found to have the similar morphologies to that on SiO_2 glass, which were attributed to the formation of subnanometer SiO_x as revealed by X-ray reflectivity (XRR) measurements. Therefore, the electrical conductivity and Seebeck coefficient measurements were made on the Si (001) following the 10 vol% piranha.

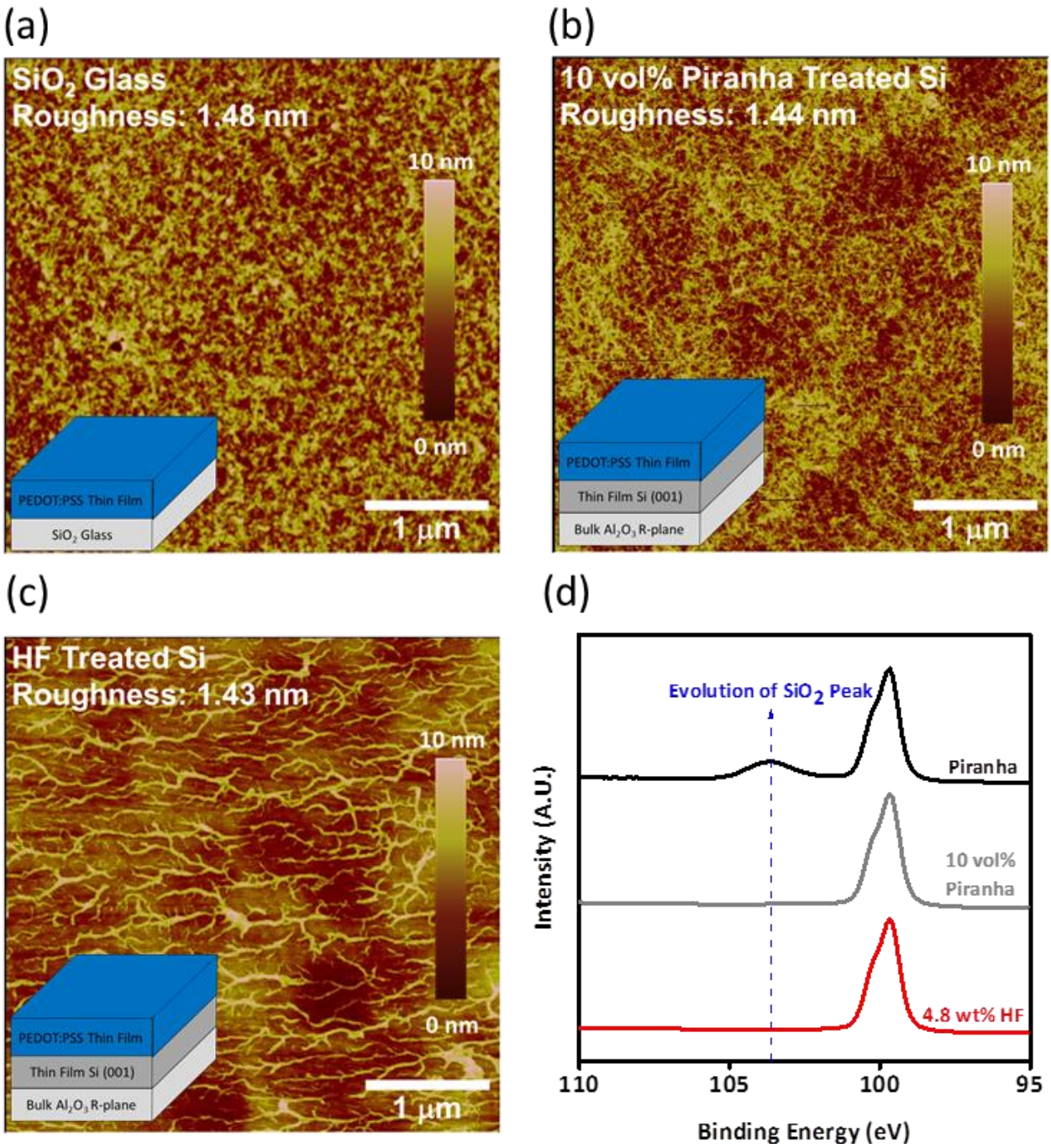

Figure 2.11. Morphologies of PEDOT:PSS measured by AFM. (a) PEDOT:PSS deposited on SiO_2 glass (VWR, 48366-045). (b) Morphology of PEDOT:PSS on hydrophilic Si surfaces of SOS. Si was cleaned with acetone, isopropanol and distilled water serially for 15 minutes for each step and then treated with piranha for 10 minutes. Then PEDOT:PSS was spin-coated. (c) Si was cleaned with acetone, isopropanol and distilled water serially for 15 minutes for each step and then treated

with piranha for 10 minutes. SiO_x was removed by 4.8 wt% HF etching for 3 minutes. Then PEDOT:PSS was spin-coated. All AFM image size is 4 × 4 μm^2. (d) Si 2p XPS spectra of differently oxidized Si surfaces. As oxidation intensifies, distinct SiO_2 peaks[35] at 103.5 eV evolve more apparently, while elemental Si 2p peaks at 99.4 eV are invariant. The light black curve in the middle and red curve at the bottom underwent the same experimental procedures with (b) and (c) respectively, except for the PEDOT:PSS deposition. The black curve at the top represents Si with cleaning by acetone, isopropanol and distilled water serially for 15 minutes for each step and followed piranha treatment for 10 minutes. Figure from *Quantitative analyses of enhanced thermoelectric properties of modulation-doped PEDOT:PSS/undoped Si (001) nanoscale heterostructures*[17]. Reproduced by permission of the Royal Society of Chemistry.

2.3.4. Effect of Chemical Treatments on Thickness of Surface SiO_x on SOS

SiO_x on Si is inevitable in order to accommodate PEDOT:PSS on Si surface. On the other hand, SiO_x thickness should be minimized since SiO_x can impose undesirable energy barrier for charge transfer at the interface between Si and PEDOT:PSS. Exposing the etched surface to 10 vol% piranha satisfies those two conflicting requirements by creating a hydrophilic surface enough to deposit PEDOT:PSS (**Figure 2.11** (c)), as well as generating sub-nanometer thick SiO_x layer (**Figure 2.12**).

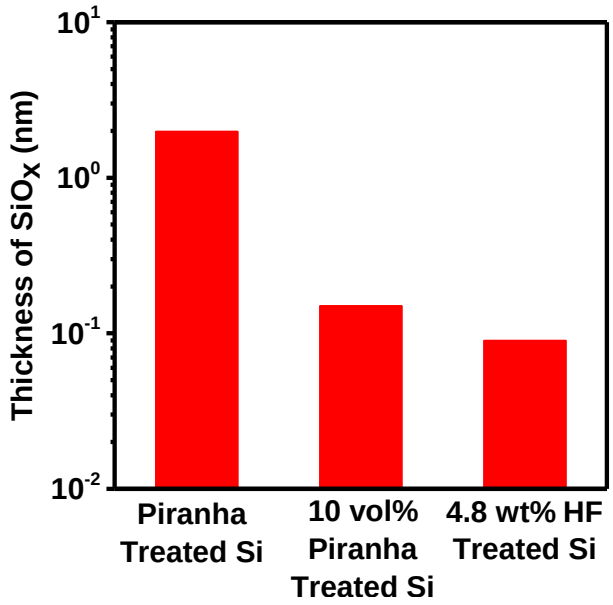

Figure 2.12. Thicknesses of SiO_x on Si by varying chemical treatments on SOS wafers, measured with XRR. Figure from *Quantitative analyses of enhanced thermoelectric properties of modulation-doped PEDOT:PSS/undoped Si (001) nanoscale heterostructures*[17]. Reproduced by permission of the Royal Society of Chemistry.

2.3.5. Thermal Oxidation of SOS to Lessen Silicon Thickness

Thermal oxidation of SOS was implemented in order to decrease the thickness of the Si layer. It converts Si into SiO_2 from the surface at the specific rate under the specific temperature, humidity, and crystalline orientation[15]. Thermally oxidized SiO_2 was removed after thermal oxidation with HF etching.

Before thermal oxidation process, RCA 1 and RCA 2 cleaning procedures were conducted in order to minimize the introduction of metallic elements to Si[15], which can turn into defects after thermal oxidation. For this study, we implemented dry oxidation at 1100 ^oC for varying time durations for (001) SOS under 40 mL/s of dry oxygen flow, as the high temperature, 1100 ^oC ensures quick oxidation, and dry condition tends to produce atomically flat surface[15]. **Figure 2.13** and **Figure 2.14** show morphology of the resultant SOS after thermal oxidation, and resultant resistivity of thinned down SOS, respectively. The thermal growth of SiO_2 layer obeyed Deal-Grove growth model[15], which is summarized at **Figure 2.15**.

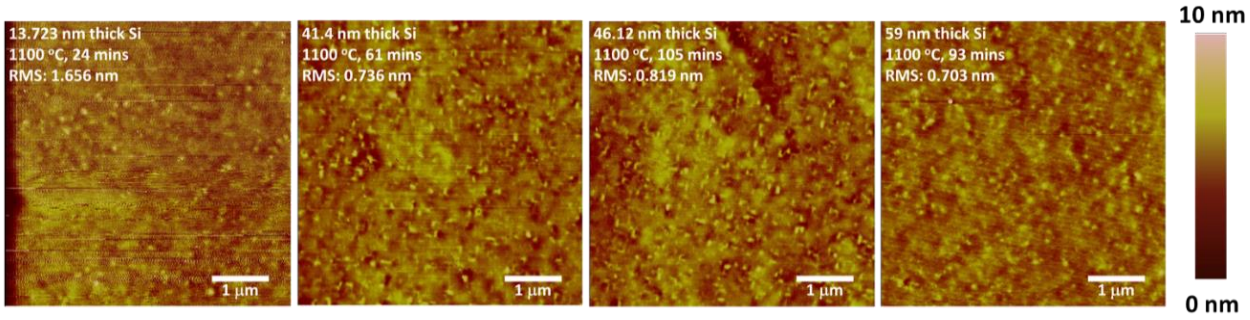

Figure 2.13. Surface roughness of Si was kept flat even after thermal oxidation at 1100 ^oC for varying durations, and following HF removal of thermally grown SiO_x. Figure from *Quantitative analyses of enhanced thermoelectric properties of modulation-doped PEDOT:PSS/undoped Si (001) nanoscale heterostructures*[17]. Reproduced by permission of the Royal Society of Chemistry.

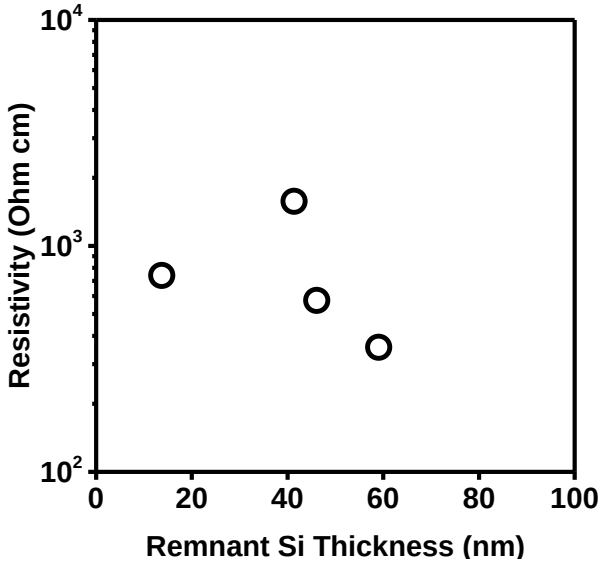

Figure 2.14. Resultant resistivity of SOS after thermal oxidation and subsequent HF etching. Resistivity remained highly intrinsic even after the thermal oxidation. Figure from *Quantitative analyses of enhanced thermoelectric properties of modulation-doped PEDOT:PSS/undoped Si (001) nanoscale heterostructures*[17]. Reproduced by permission of the Royal Society of Chemistry.

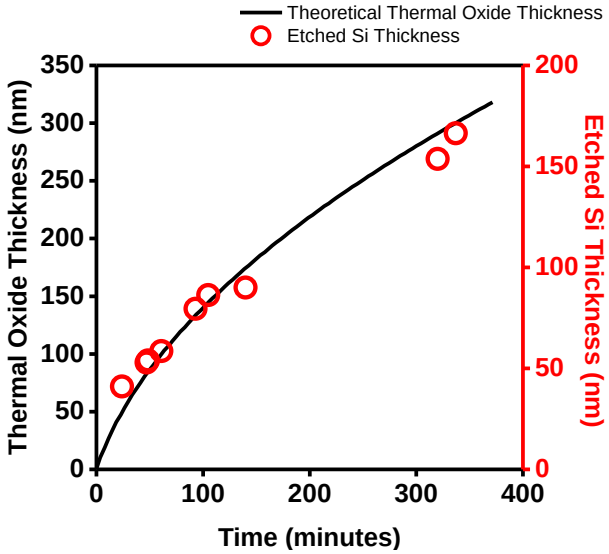

Figure 2.15. Thermal growth of SiO_2 on (001) Si shows agreement with theoretical Deal-Grove model, where oxygen gas diffuses from the outside to the surface, then through the existing oxide layer to the oxide-substrate interface, and then lastly reacts with buried Si atoms[15]. Figure from *Quantitative analyses of enhanced thermoelectric properties of modulation-doped*

PEDOT:PSS/undoped Si (001) nanoscale heterostructures[17]. Reproduced by permission of the Royal Society of Chemistry.

2.3.6. Thermoelectric Properties of PEDOT:PSS Alone for Si / PEDOT:PSS Heterostructures

In order to translate band alignment of Si / PEDOT:PSS heterostructures into their thermoelectric properties, thermoelectric properties of individual consisting materials are necessary.

As thermoelectric characteristics of Si are well-known, most of their properties were excerpted from existing reports[31], and will be summarized later.

Thickness dependency of electrical conductivity of thin films on different insulating substrates is a general phenomenon for various materials[36-38]. Especially for PEDOT:PSS thin films on various insulating substrates, the increase in film thickness accompanies the increase in electrical conductivity[39,40]. Spin-casted PEDOT:PSS films on SiO_2 substrates possess spontaneous phase segregation between conducting PEDOT phase and insulating PSS phase[4,42,43]. It is reported that the electrical connectivity (i.e. percolation) among the conducting PEDOT grains in the PEDOT:PSS matrix is enhanced, when thicknesses of the spin-coated PEDOT:PSS thin films are increased[44,45]. However, an opposite trend is reported for oxidative chemical vapor deposited (oCVD) PEDOT thin films[41]. This contrast in the thickness dependency trends is attributed to the growth in crystallite size with the decreasing thickness of the oCVD PEDOT thin films, unlike typical inorganic thin films[41]. The oCVD PEDOT thin film can orient either face-on or edge-on with respect to the substrate, depending on the thickness of the PEDOT film[41]. This thickness-dependent transition of arrangement among the conducting PEDOT crystallites causes connectivity among them to ameliorate when thickness becomes smaller. The opposite thickness dependencies of electronic conductivity in oCVD PEDOT and spin-casted PEDOT:PSS thin films can be reconciled by this mechanistic comparison.

The measured electrical conductivity of PEDOT:PSS on SiO_2 quartz substrate shows the monotonically increasing trends with the increasing thickness (5 – 60 nm), as shown in **Figure 2.16**. This PEDOT:PSS has the same recipe of PEDOT:PSS dispersion with what was used for fabrication of Si / PEDOT:PSS heterostructures. Thus, this trend was applied only for

thermoelectric simulation of Si / PEDOT:PSS heterostructures. It should be noted that linear fitting of PEDOT:PSS electrical conductivity evolution does not have theoretical basis so far. This linear fitting was adopted only to provide an estimation of PEDOT:PSS electrical conductivity trend within the researched thickness region in this study.

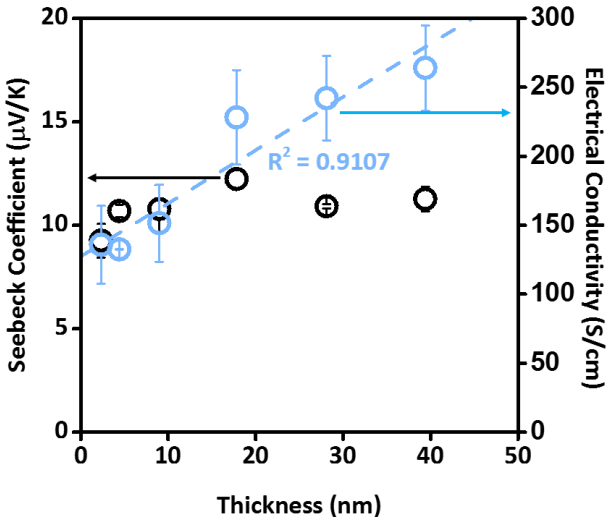

Figure 2.16. Electrical conductivity of PEDOT:PSS on SiO_2 quartz with linear fitting. Note that linear trend does not have theoretical justification yet. Seebeck coefficient of PEDOT:PSS on SiO_2 quartz is constant, which evidences that hole density of PEDOT:PSS is invariant, assuming electronic band structure of PEDOT:PSS is unaffected by its thickness[1,23,46-48]. Figure from *Quantitative analyses of enhanced thermoelectric properties of modulation-doped PEDOT:PSS/undoped Si (001) nanoscale heterostructures*[17]. Reproduced by permission of the Royal Society of Chemistry.

Distinguishing mobility and hole density from electrical conductivity is necessary to solve Poisson's equation. However, it has been widely reported that typically low mobility of PEDOT:PSS[47,49] makes Hall measurement technically difficult[50]. Only for PEDOT:PSS on SiO_2 with micron-scale thickness (6.78 μm), linear relation between Hall voltage and applied external magnetic field could be found, as shown in **Figure 2.17**. PEDOT:PSS with less thickness could not produce clear linear relation, therefore mobility and hole density could not be measured for that range of thickness. Mobility and hole density could be obtained by following formulas, as

indicated below, where n, μ, σ, e, d, and a represent hole density, mobility, electrical conductivity, elementary charge, thickness of PEDOT:PSS, and slope of **Figure 2.17**.

$$n = \frac{1}{aed} \tag{2.15}$$

$$\mu = \frac{\sigma}{ne} \tag{2.16}$$

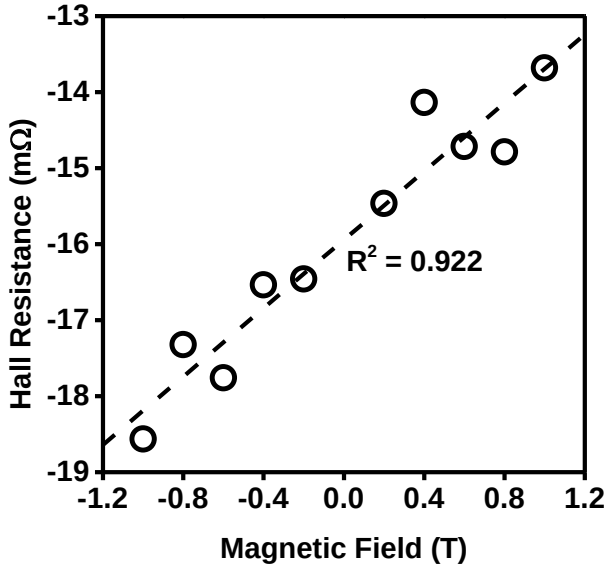

Figure 2.17. Hall resistance showed a linear relationship with applied external magnetic field, only when thickness of PEDOT:PSS on SiO_2 was in micrometer range (6.78 μm). For PEDOT:PSS with less thickness, trends were completely noisy. Figure from *Quantitative analyses of enhanced thermoelectric properties of modulation-doped PEDOT:PSS/undoped Si (001) nanoscale heterostructures*[17]. Reproduced by permission of the Royal Society of Chemistry.

Therefore, it could be concluded that mobility and hole density of 6.78 μm thick PEDOT:PSS are 7.90 $cm^2/V{\cdot}s$ and 4.16×10^{20} cm^{-3}, respectively. The measured hole density of PEDOT:PSS is at similar range with previously reported values[3].

Even though direct measurement of hole density was not possible for PEDOT:PSS with less than μm scale, it was still possible to draw hole density from Seebeck coefficient measurement, because Seebeck coefficient of PEDOT:PSS is a single variable function of hole density, as reported in previous studies[23,40].

Judging from constant Seebeck coefficient trend of PEDOT:PSS at **Figure 2.16**, it can be concluded that hole density of PEDOT:PSS stays the same as well. Given that electrical conductivity of PEDOT:PSS depends on thickness, it is the mobility that varies with thickness. This result was reflected as input parameters for Poisson's equation.

2.3.7. Thermoelectric Properties of PEDOT:PSS Alone for Ge / PEDOT:PSS Heterostructures

In order to translate band alignment of Ge / PEDOT:PSS heterostructures into their thermoelectric properties, thermoelectric properties of individual consisting materials are necessary.

As thermoelectric characteristics of Ge are well-known, most of their properties were excerpted from existing reports[32], and will be tabulated later.

PEDOT:PSS has the dependency of electronic transport and band characteristics on process conditions[51-55]. As PEDOT:PSS used for Ge / PEDOT:PSS thermoelectric study has different mixed ethanol ratio (1:1 v/v) from that of Si / PEDOT:PSS (1:5 v/v), thickness-dependency of PEDOT:PSS thermoelectric properties were separately characterized and mirrored in the consequent thermoelectric simulations distinctly. Even though Seebeck coefficients stays almost the same regardless of the ethanol content, electrical conductivity at thin thickness of PEDOT:PSS exhibits substantially different trend from that of PEDOT:PSS for Si / PEDOT:PSS heterostructures. This time, electrical conductivity dependence on thickness could be best fitted with logistics function, and yielded mobility as a function of thickness. Again, the constant Seebeck coefficient suggests invariant hole density, provided PEDOT:PSS electronic band structure does not change[1,23,46-48].

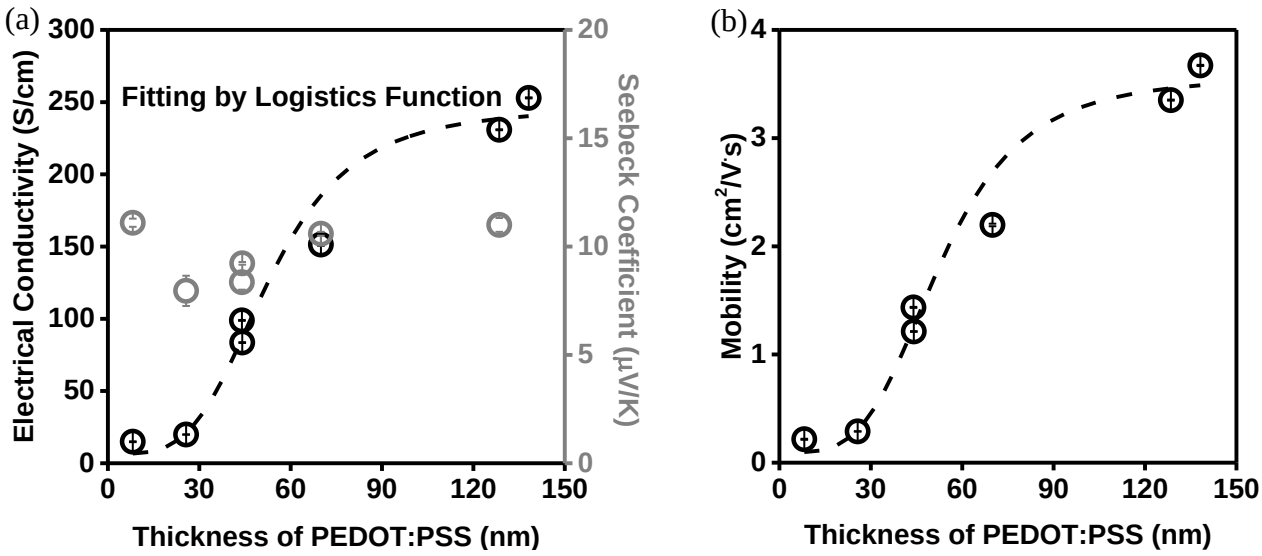

Figure 2.18. (a) Electrical conductivity of PEDOT:PSS on SiO_2 increases as PEDOT:PSS thickness increases. Initial increase in electrical conductivity and eventual convergence to bulk electrical conductivity can be observed. This trend is in line with previous reports on electrical conductivity vs. thickness relations of metal thin films[56,57]. In order to express this trend analytically for the Poisson's equation solver, logistics function was fitted. It is noteworthy that theoretical bases of elemental metal thin film resistivity are available elsewhere[56,57], even though such exploration has not been conducted for PEDOT:PSS thin films. Seebeck coefficient, which is sensitive to hole density change, is invariant. Therefore, it again proves that hole density of PEDOT:PSS is constant. This result is consistent with UPS measurement which shows Fermi level is same as valence band offset of PEDOT:PSS. (b) Mobility of PEDOT:PSS on SiO_2 was obtained by dividing the electrical conductivity trend at (a) with the constant hole density (4.3×10^{20} cm^{-3}). This mobility function is adopted in the Poisson's equation solver, assuming that the effect of PEDOT:PSS thickness on mobility is preserved when substrate beneath PEDOT:PSS thin film is changed.

2.3.8. Determination of Valence Band Offsets of Si / PEDOT:PSS and Ge / PEDOT:PSS

In order to simulate band alignment of Si / PEDOT:PSS and Ge / PEDOT:PSS heterostructures into their thermoelectric properties, determination of the valence band offsets at those interfaces are necessary. Since the electronic band parameters, such as work function[58-60] of

PEDOT:PSS are highly dependent on the sample preparation, the work function of a representative PEDOT:PSS on SiO_2 glass with identical preparation process with PEDOT:PSS for Si / PEDOT:PSS heterostructures was measured using ultraviolet photoemission spectroscopy (UPS), as shown in **Figure 2.19** (a). By reading the x-intercept of spectra, the work function was estimated as 5.03 eV. Valence band offset of Si and PEDOT:PSS, as well as the initial Fermi level of the Si determines the charge transfer direction, hence degree of modulation doping. Energy levels before Si and PEDOT:PSS are in contact are shown in **Figure 2.19** (b). According to Mott-Schottky rule[61], the valence band edge offset was determined. Mott-Schottky rule states the valence band offset of heterojunction is the same as difference between ionization potentials (i.e. difference between the vacuum level and the valence band edge) of neighboring materials. Using the electron affinities and band gaps of Si and PEDOT:PSS, the valence band edge offset was determined to be 0.111 eV, with the valence band edge of PEDOT:PSS upper than that of Si. The measured electronic transport characteristics of PEDOT:PSS, measured work function and other inputs used for Poisson's equation were summarized as a table in the next part.

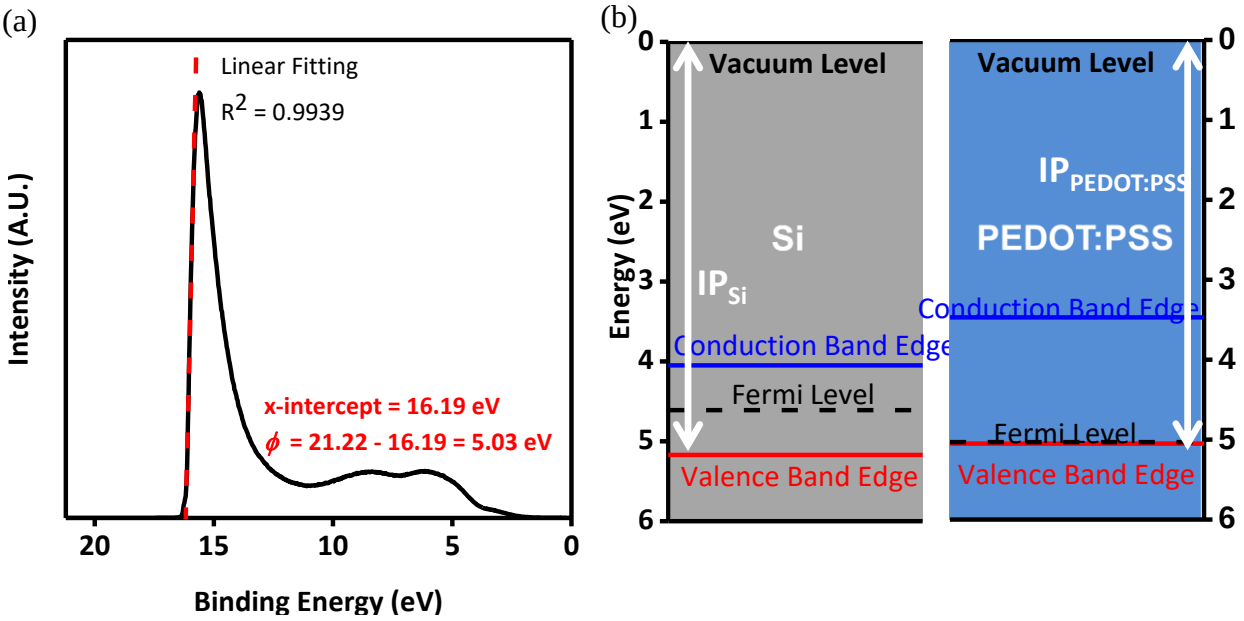

Figure 2.19. Band alignment of Si / PEDOT:PSS heterojunction. (a) UPS spectrum of 10 nm PEDOT:PSS on SiO_2 glass (Axis Ultra from Kratos Analytical, He I α source with 21.22 eV of energy). The x-intercept of the spectra reveals work function of PEDOT:PSS = 5.03 eV. The work function, combined with electrical conductivity of PEDOT:PSS, was applied to simulate band

alignment of Si / PEDOT:PSS heterojunction. (b) Band diagram of Si and PEDOT:PSS bands before contact to form the heterojunction. Applying Mott-Schottky rule predicts the valence band edge offset of 0.111 eV, with the valence band edge of PEDOT:PSS upper than that of Si. Figure from *Quantitative analyses of enhanced thermoelectric properties of modulation-doped PEDOT:PSS/undoped Si (001) nanoscale heterostructures*[17]. Reproduced by permission of the Royal Society of Chemistry.

As Ge / metal heterojunctions are known to experience non-ideality called Fermi level pinning (i.e. valence band offsets between Ge and metals are insensitive to work functions of contact metals), valence band offset at Ge / PEDOT:PSS was determined experimentally. In order to execute Kraut's method for precise determination of band offset, three criteria should be met: (i) primary XPS peaks of unique elements of each material should be chosen, (ii) number of deconvoluted peaks should be able to reflect oxidation state of the material, (iii) deconvoluted peaks should correspond to oxidation states of materials that are actually electronically active at the heterojunction. To follow the condition (i), S 2p peaks of PEDOT:PSS (**Figure 2.20** (a) – (b)) and Ge 3d peaks (**Figure 2.20** (c) – (d)) from the undoped Ge were selected, because those primary regions were often detected with less noise from secondary electron effects[62]. S 2p peaks of PEDOT:PSS was deconvoluted into 4 peaks to reflect spin-split doublets of PEDOT and PSS respectively, in accordance with a previous report[63]. The two deconvoluted peaks (**Figure 2.20** (a) – (b)) at higher binding energy came from PSS, and the lower binding energy ones stemmed from PEDOT. Likewise, Ge 3d peaks of the undoped GeOI were deconvoluted into 2 peaks, in order to distinguish zero oxidation state of Ge device layer and +4 oxidation state of the native oxide on it[64] (**Figure 2.20** (c) – (d)). The highlighted spectra in **Figure 2.20** (a) – (d) offers necessary information on core levels of individual constituent materials and their heterostructures for Kraut's method.

Ultraviolet Photoemission Spectroscopy (UPS) spectrum detected valence band edge location against Fermi level of PEDOT:PSS, as shown at **Figure 2.20** (e). Greater energy resolution of UPS (25 meV) compared to that of XPS (0.1 eV) ensures that Fermi level of PEDOT:PSS overlaps with its valence band edge (**Figure 2.20** (e)). The valence band edge position with respect to Fermi level of the undoped GeOI could not be measured, due to its

electrically insulating nature. This observation is consistent with large electrical resistivity of GeOI (530 Ω·cm), which is nearly intrinsic. Because no precise information about doping state of the undoped GeOI could be known, it is assumed that the undoped GeOI has the intrinsic carrier density of 2.4×10^{13} cm^{-3}. In other words, Fermi level was assumed to be at the midgap of the undoped GeOI (0.33 eV above the valence band edge).

Application of the Kraut's method to the series of spectroscopic data (**Figure 2.20** (a) – (e)) revealed valence band offset 97.4 meV at the heterojunction, indicating valence band edge of PEDOT:PSS is slightly higher by that amount than the valence band edge of Ge (**Figure 2.20** (f) and **Table 2.2**). In addition to this valence band offset value, other information explained earlier is also in need in order to calculate to 1D Poisson's equation for thermoelectric properties simulation: the transport characteristics of individual materials, which will be summarized all together later.

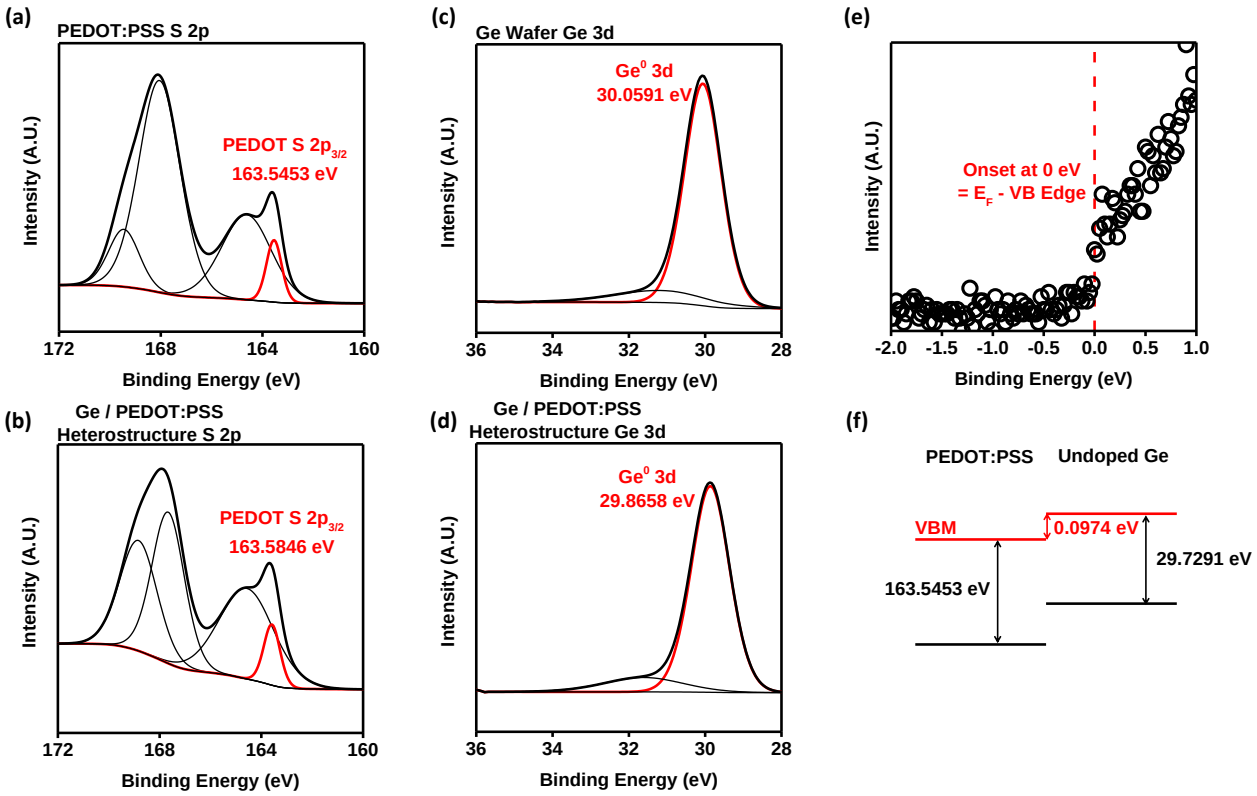

Figure 2.20. XPS and UPS spectra for Ge, PEDOT:PSS and their bilayered structure. (a) S 2p spectrum of 60 nm thick PEDOT:PSS on SiO_2 substrate, (b) S 2p spectrum of 12 nm thick PEDOT:PSS on the 21 nm thick undoped GeOI, (c) Ge 3d spectrum of the bare, undoped GeOI,

(d) Ge 3d spectrum of 12 nm thick PEDOT:PSS on the undoped GeOI. All necessary peak information for Kraut's formula was deconvoluted and marked as red curves in each figure. (e) Magnified UPS spectra for valence band edge of 60 nm thick PEDOT:PSS on SiO_2 glass substrate. Onset of the spectrum at 0 eV of binding energy indicates that Fermi level crosses the valence band edge of PEDOT:PSS. UPS spectrum of the undoped GeOI could not be measured due to its high electrical resistance. (f) Schematic flat band diagram reflecting the measured band offset from Kraut's method (not in scale).

2.3.9. Summary of Band and Thermoelectric Properties of Individual Materials for the Band Diagram Simulation

The listed tables summarize input to calculate band alignments at Si / PEDOT:PSS and Ge / PEDOT:PSS heterojunctions. The calculated band bending in these heterojunctions will be converted into thermoelectric properties by methods explained in **2.2.10** and **2.2.11**, and compared with experimental measurements.

	(001) Si	PEDOT:PSS
Thickness (nm)	14 – 250	1 - 100
Band Gap (eV)	1.12 [a)]	1.57 [c)]
Work Function (eV)	4.61 [b)]	5.03
Ionization Potential (eV)	5.17 [a)]	5.05 [d)]
Acceptor Density (cm^{-3})	0	4.16×10^{20}
Valence Band Density of States (cm^{-3})	1.83×10^{19} [a)]	1.25×10^{21} [e)]
Hole Mobility ($cm^2/V{\cdot}s$)	450 [a)]	1.94 – 7.90 [f)]

Static Dielectric Constant ($\frac{\varepsilon}{\varepsilon_0}$)	11.7 [a)]	1.1 [g)]

Table 2.1. Inputs to simulate band alignment of Si / PEDOT:PSS heterojunction via 1D Poisson's equation solver. a) Bulk values[31]. b) Bulk electron affinity of Si and half of band gap of Si were added up, because Si was undoped[31]. c) Reported in the previous study[65]. d) Difference between Fermi level and valence band maximum were taken from the previous study [66]. e) Calculated from the previous study[23]. f) Dependent to thickness. g) Reported in the previous study[2]. Table from *Quantitative analyses of enhanced thermoelectric properties of modulation-doped PEDOT:PSS/undoped Si (001) nanoscale heterostructures*[17]. Reproduced by permission of the Royal Society of Chemistry.

	Ge	PEDOT:PSS
Thickness (nm)	21	1 - 80
Band Gap (eV)	0.661 [a)]	1.58 [c)]
Valence Band Offset (eV)	0.0974 [b)]	
Acceptor Density (cm^{-3})	2.4×10^{13} [a)]	4.30×10^{20} [b)]
Valence Band Density of States (cm^{-3})	5.0×10^{18} [a)]	1.25×10^{21} [d)]
Hole Mobility ($cm^2/V \cdot s$)	489.84 [b)]	0.0952 - 3.57 [b)]
Static Dielectric Constant ($\frac{\varepsilon}{\varepsilon_0}$)	16.2 [a)]	1.1[e)]

Table 2.2. Inputs to simulate band alignment of Ge / PEDOT:PSS heterojunction via 1D Poisson's equation solver. [a)] Bulk values[32]; [b)] Measured in this study; [c)] Reported in the previous study[67]; [d)] Calculated from the previous study[23]; [e)] Excerpted from the previous research[68].

2.3.10. Simulated Band Diagrams of Si / PEDOT:PSS and Ge / PEDOT:PSS through 1D Poisson's Equation Solver

The numerical simulation of Poisson's equation by COMSOL Multiphysics® Modeling Software analyzed band bending at equilibrium after the heterojunction formation, for various

thicknesses of (001) Si (**Figure 2.21**). Band bending does not happen at PEDOT:PSS layer, as PEDOT:PSS has nearly metallic hole density. At the Si side close to the interface, band bending is upward for all Si thicknesses. This implies no significant change in Seebeck coefficient trend, since the contribution to Seebeck coefficient from the region far from the interface is negligible, as will be demonstrated later.

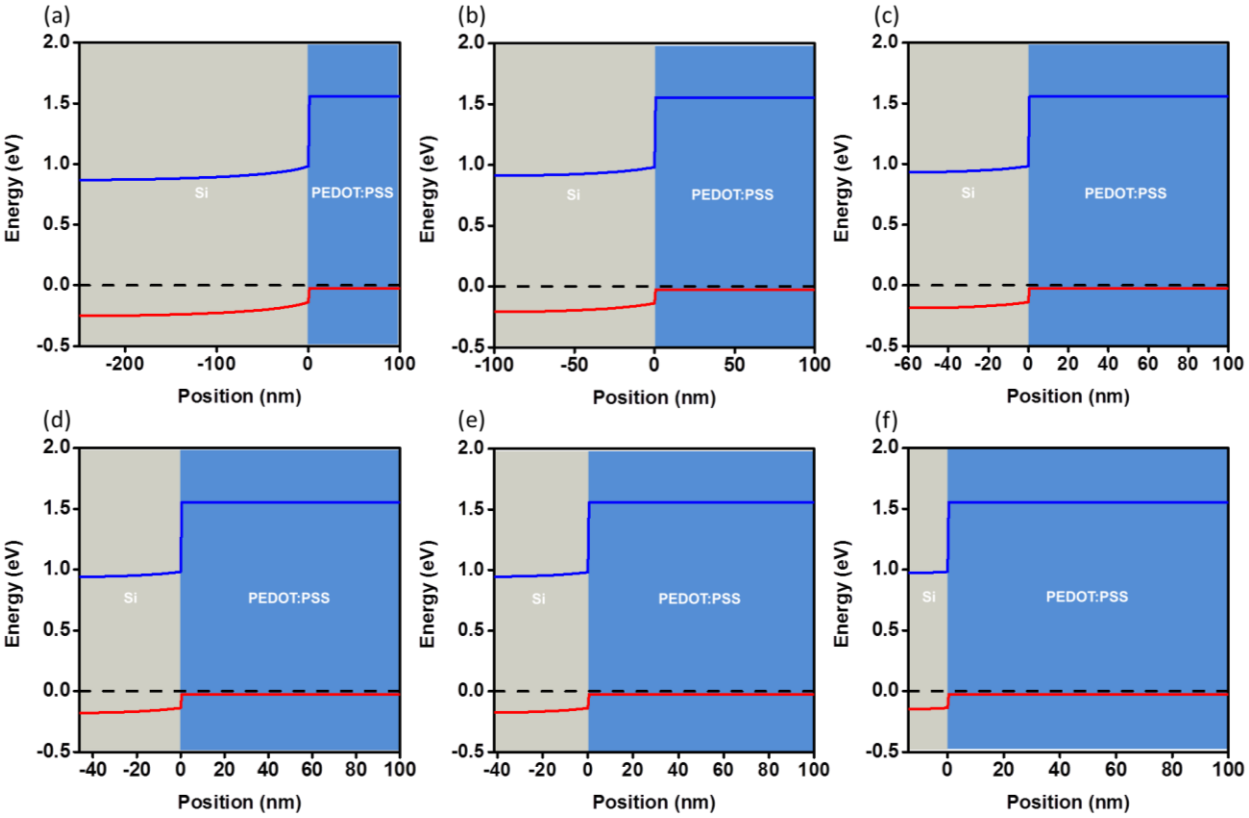

Figure 2.21. (a) – (f) Band diagrams of Si / PEDOT:PSS heterojunction at 250 nm, 100 nm, 59 nm, 46 nm, 41 nm, and 14 nm thick Si. The dashed lines at 0 eV indicate Fermi level. Figure from *Quantitative analyses of enhanced thermoelectric properties of modulation-doped PEDOT:PSS/undoped Si (001) nanoscale heterostructures*[17]. Reproduced by permission of the Royal Society of Chemistry.

For Ge / PEDOT:PSS heterojunctions, because Ge was undoped, only valence band of Ge was strongly influenced by electrical field within the Debye length, resulting in band bending. It is remarkable that Ge closer to the interface also had smaller distance between the Fermi level and the valence band edge compared to Ge farther from the interface, which means that hole transfer

from PEDOT:PSS to Ge is only effective at the interface. In other words, modulation doping became less effective for Ge farther from the interface, because the electric field decayed as a result of carrier screening, as could be seen in the **Figure 2.22**. In the contrast, PEDOT:PSS exhibited a metal-like behavior. As a consequence, Fermi level at PEDOT:PSS side was not shifted at all even after the heterojunction formation with the undoped Ge, reflecting its metallic p-type doping.

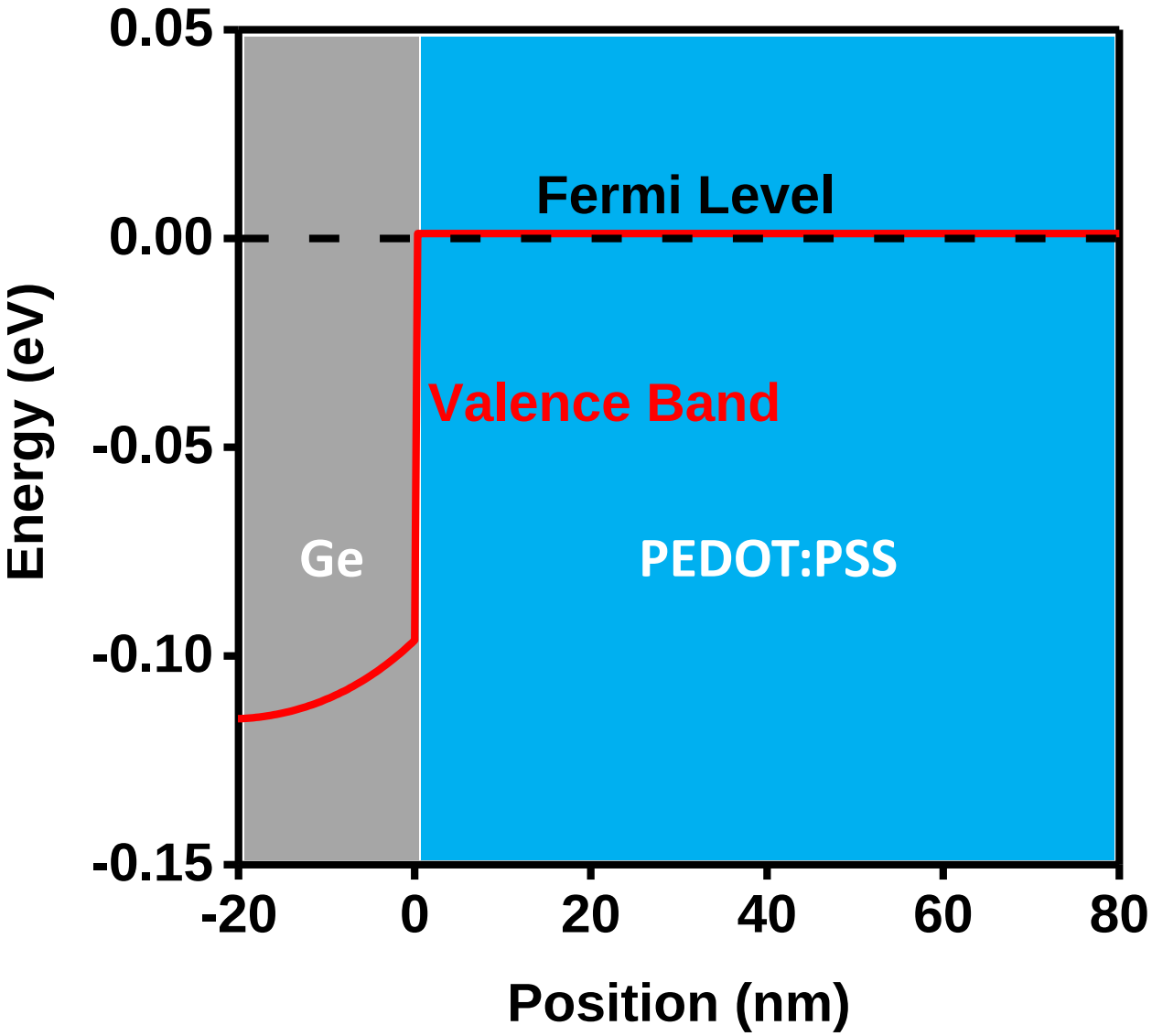

Figure 2.22. Simulated valence band alignment between undoped Ge layer and PEDOT:PSS layer by solving the 1D Poisson's equation.

2.3.11. Agreements between Experimental and Simulated Thermoelectric Properties of Si / PEDOT:PSS and Ge / PEDOT:PSS

The influence of modulation doping by band bending on the electrical conductivity and Seebeck coefficient was further examined. The simulated electrical conductivity and Seebeck coefficient of heterostructures associated with band bending (unbroken curves in **Figure 2.23**) were obtained by the following formulas, assuming parallel resistors model[21,22]:

$$\bar{\sigma}(d_1, d_2) = \frac{e \int_{-d_1}^{d_2} n(x)\mu(x)dx}{d_1+d_2} \quad (2.17)$$

$$\bar{S}(d_1, d_2) = \frac{e \int_{-d_1}^{d_2} n(x)\mu(x)S(x)dx}{\bar{\sigma}(d_1,d_2)\cdot(d_1+d_2)} \quad (2.18)$$

where $n(x)$, $\mu(x)$, and $S(x)$ are hole density, mobility, and Seebeck coefficient of each position x in the Si / PEDOT:PSS heterostructure. When no band bending is assumed at the Si / PEDOT:PSS interface (dashed curves in **Figure 2.23**), the electrical conductivity and Seebeck coefficient of the heterostructures were estimated by following formulas:

$$\bar{\sigma}(d_1, d_2) = \frac{\sigma_1 d_1+\sigma_2(d_2)d_2}{d_1+d_2} \quad (2.19)$$

$$\bar{S}(d_1, d_2) = \frac{S_1\sigma_1 d_1+S_2\sigma_2(d_2)d_2}{\bar{\sigma}(d_1,d_2)\cdot(d_1+d_2)} \quad (2.20)$$

where S_1, σ_1, and S_2, are Seebeck coefficient and electrical conductivity of Si, and Seebeck coefficient of PEDOT:PSS respectively, and kept constants per no band bending assumption. Thickness dependency of electrical conductivity of PEDOT:PSS, $\sigma_2(d_2)$ was taken into account in the simulations. The simulated electrical conductivities regardless of assuming band bending agree well with experimental measurements (**Figure 2.23**), which is in agreement with the lack of band bending in the PEDOT:PSS layer in **Figure 2.21**. Band alignment simulation of the heterostructures with different Si thicknesses consistently shows that transferred holes from PEDOT:PSS into Si mainly stay at the interface (**Figure 2.21**). Therefore, the electrical conductivity rises as thickness of Si decreases as noncontributing Si far from the interface is removed from the electrical conductivity estimation, as seen in **Figure 2.23**. The slight upshift in the electrical conductivity *with band bending* compared to *with band bending* (dotted blue curves and unbroken blue curves in **Figure 2.23**) is a consequence of hole injection from PEDOT:PSS to Si, which slightly elevates the electrical conductivity of Si adjacent to the interface. Although the

comparison of electrical conductivity through experiment and simulation clearly validates the parallel resistor model, the electrical conductivity trends alone could not provide a sufficient evidence in support of modulation doping at the Si / PEDOT:PSS interface.

Only the simulated Seebeck coefficients *under band bending assumption* agree with the experimentally observed enhancement in the Seebeck coefficient with decreasing PEDOT:PSS thickness. In contrast, the simulated Seebeck coefficient of the heterostructures *without band bending assumption* (black dashed curves in **Figure 2.23**) cannot describe the experimental Seebeck coefficients correctly. Therefore, combined results from the experiments and the simulation in **Figure 2.23** support that band bending driven modulation doping is responsible for the enhancement in Seebeck coefficient.

When PEDOT:PSS thickness is less than 10 nm, the Seebeck coefficient changes rapidly, because the influence of PEDOT:PSS with small Seebeck coefficient quickly overwhelms Seebeck coefficient of modulation-doped Si due to its much higher electrical conductivity. This Seebeck coefficient trend does not change by different Si thicknesses down to 14 nm, and this fact experimentally indicates that modulation doping only happens at the interface.

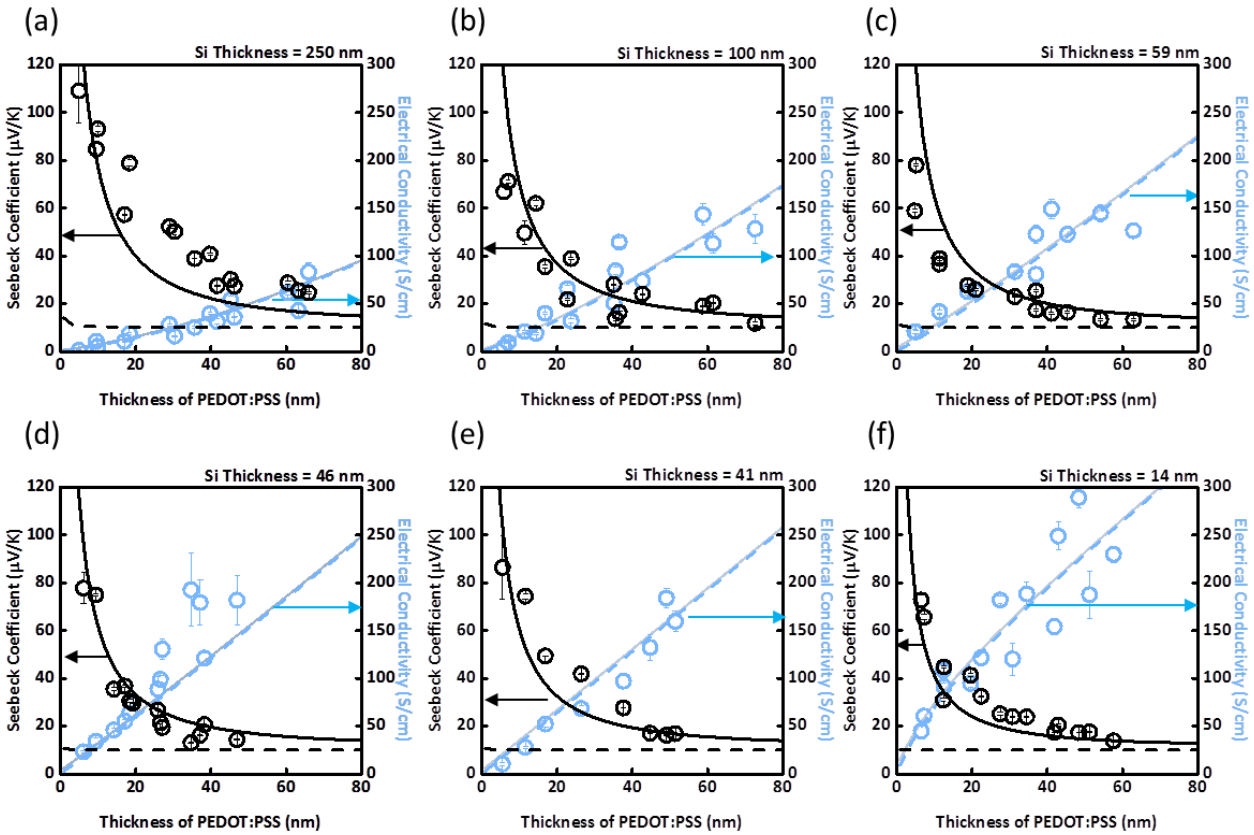

Figure 2.23. Experimental and Simulated electrical conductivity and Seebeck coefficient of Si / PEDOT:PSS heterostructures at different Si thicknesses as a function of PEDOT:PSS thickness. Circles represent experimental data and unbroken and dashed curves show simulation results *with* and *without effect of band alignment*, respectively. As expressed in the main text, The electrical conductivity of the heterostructure ($\overline{\sigma}$) was obtained by normalizing the sheet resistance (R) by the combined thickness of PEDOT:PSS and Si ($d_1 + d_2$), namely $\overline{\sigma} = \frac{1}{R(d_1+d_2)}$. Error bars represent the standard deviation of at least four measurements. Figure from *Quantitative analyses of enhanced thermoelectric properties of modulation-doped PEDOT:PSS/undoped Si (001) nanoscale heterostructures*[17]. Reproduced by permission of the Royal Society of Chemistry.

The band alignment information at the Ge / PEDOT:PSS heterostructures could be transferred to the estimation of electrical conductivity and Seebeck coefficnt, as shown in **Figure 2.24**. It depicts both experimental thermoelectric properties and simulated counterparts. Formalism for experimental electrical conductivity (black dots in **Figure 2.24**) is:

$$\overline{\sigma} = \frac{1}{R(d_1+d_2)} \tag{2.21}$$

where d_1 and d_2 represent the thicknesses of Ge and PEDOT:PSS, respectively, and R represents the sheet resistance. As raw data from the Hall measurements were sheet resistances of the entire Ge / PEDOT:PSS heterostructures, the sheet resistances were normalized by whole thicknesses of PEDOT:PSS and Ge for conservative evaluation of the electrical conductivity.

Quantitative assessment of Seebeck coefficient and electrical conductivity by 1D Poisson's equation matched with experimental measurements, hence further bolstered modulation doping as the operating mechanism behind the enhanced Seebeck coefficient of Ge / PEDOT:PSS heterostructures. Modulation doping was taken into account by the valence band offset when solving the 1D Poisson's equation to simulate electrical conductivity and Seebeck coefficient. The simulated electrical conductivity and Seebeck coefficient of the heterostructures associated with band bending (curves in **Figure 2.24**) followed the formulae below, assuming parallel resistor model[21,22]:

$$\overline{\sigma}(d_1, d_2) = \frac{e\int_{-d_1}^{d_2} n(x)\mu(x)dx}{d_1+d_2} = \frac{e\mu_1\int_{-d_1}^{0} n(x)dx+\sigma_2(d_2)d_2}{d_1+d_2} \tag{2.22}$$

$$\overline{S}(d_1, d_2) = \frac{e\int_{-d_1}^{d_2} n(x)\mu(x)S(x)dx}{\overline{\sigma}(d_1,d_2)\cdot(d_1+d_2)} = \frac{e\mu_1\int_{-d_1}^{0} n(x)S(x)dx+\sigma_2(d_2)S_2d_2}{\overline{\sigma}(d_1,d_2)\cdot(d_1+d_2)} \tag{2.23}$$

where $n(x)$, $\mu(x)$, and $S(x)$ are hole density, mobility, and Seebeck coefficient of each position x in the Ge / PEDOT:PSS heterojunction. Because PEDOT:PSS was predicted to sustain its metal-like transport from its unbent valence band edge (**Figure 2.22**) at the heterojunction, electrical conductivity and Seebeck coefficient of PEDOT:PSS layer at the heterojunction can be considered unaffected. This is why constant S_2 and $\sigma_2(d_2)$ could be justified.

The maximum Seebeck coefficient, 398 μV/K of the heterostructure corresponded at the minimum thickness of PEDOT:PSS 12 nm. This is another experimental indication of modulation doping as the working principle. If there was no hole transfer from PEDOT:PSS to Ge, interfacial Ge would still remain insulating. Therefore, contribution of the still undoped Ge to overall Seebeck coefficient should be almost none, and Seebeck coefficient should also remain that of PEDOT:PSS, ~ 10 μV/K.

As the thickness of PEDOT:PSS increased, Seebeck coefficient diminished and electrical conductivity rose, converging toward the inherent PEDOT:PSS bulk transport properties. Seebeck

coefficient of the bilayered structure shows 18.7 μV/K at 79 nm of PEDOT:PSS thickness (**Figure 2.24**), even though electrical conductivity did not reach saturation toward the bulk electrical conductivity of PEDOT:PSS, ~ 250 S/cm. This could be attributed to the fact that the thickness of PEDOT:PSS was still less than 130 nm, where complete convergence to bulk electrical conductivity required larger thickness (**Figure 2.18** (a)).

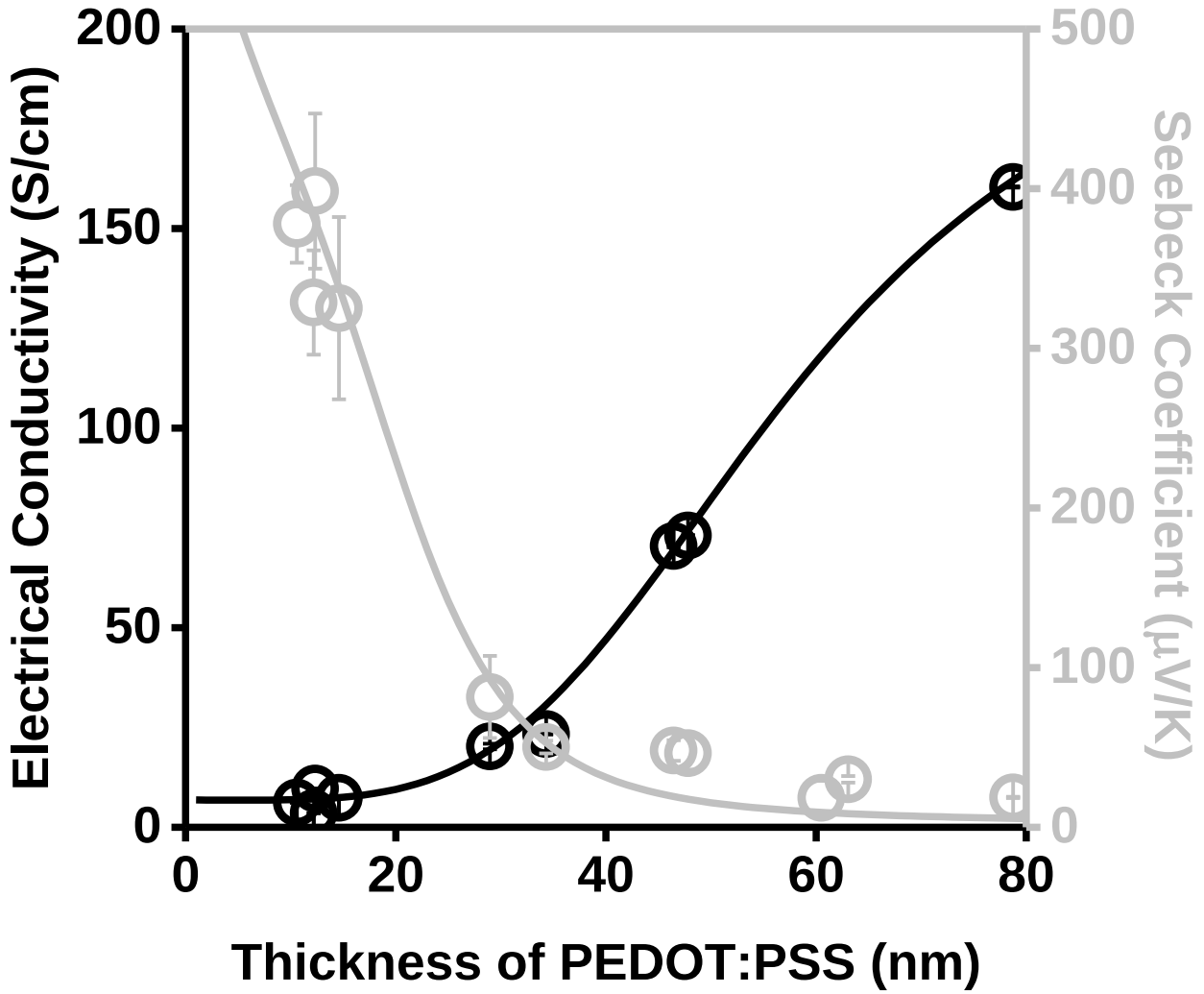

Figure 2.24. Experimental and simulated electrical conductivity (black dots and curve) and Seebeck coefficient (grey dots and curve) of the undoped Ge / PEDOT:PSS heterostructures. Error bars are standard deviations of at least four repeated measurements.

As static dielectric constant of PEDOT:PSS has different values depending on sources[68-70], several possible values of the static dielectric constants were put into the 1D Poisson's equation

solver. The simulated electrical conductivities and Seebeck coefficients under different PEDOT:PSS dielectric constants did not show substantial shift (**Figure 2.25**). All simulated data did not deviate substantially from the experimental thermoelectric properties.

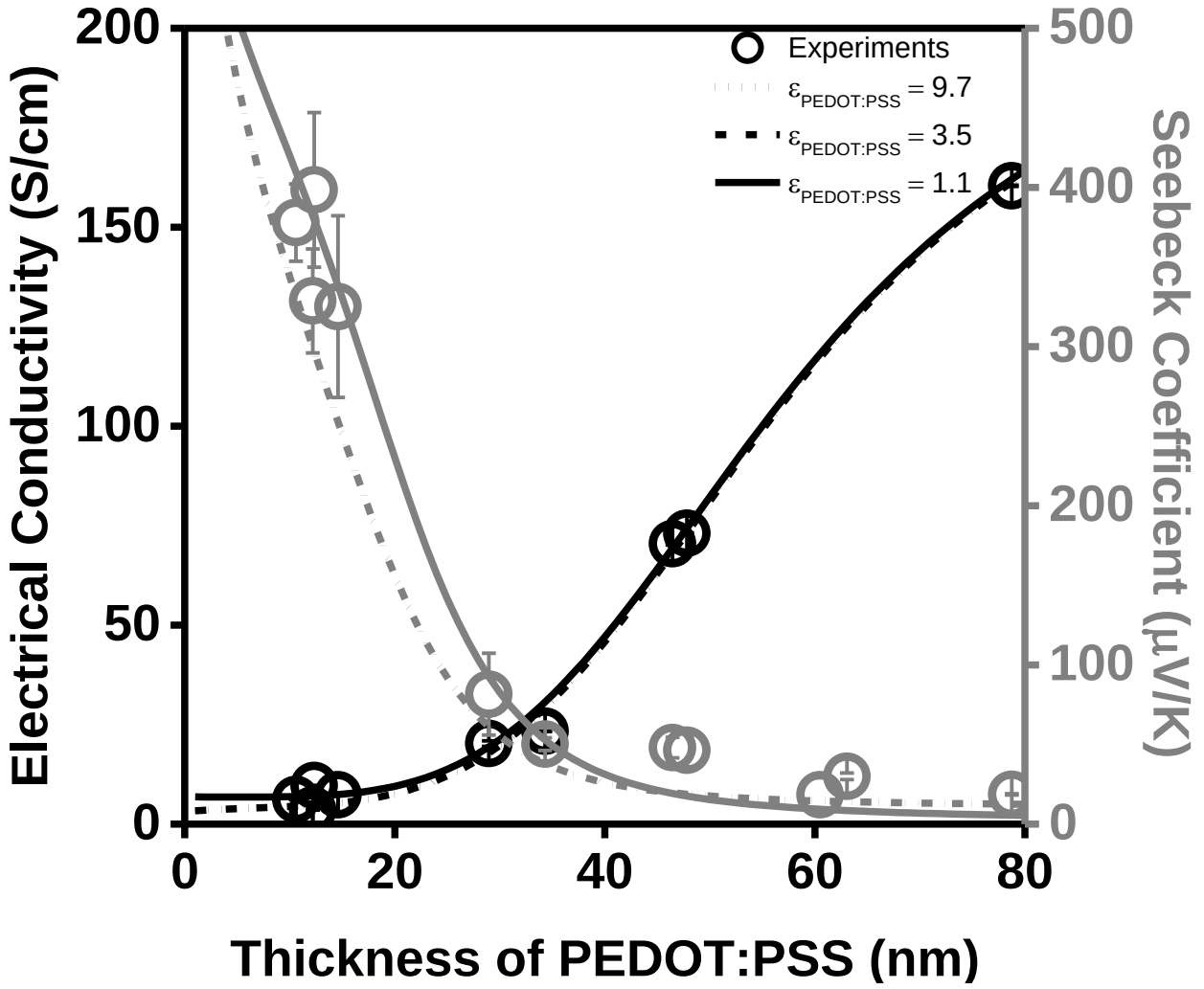

Figure 2.25. Even though dielectric constant of PEDOT:PSS is taken 1.1[68] in the main text, there are also differently reported dielectric constants of PEDOT:PSS[69,70]. Those variations in dielectric constant of PEDOT:PSS are reflected in the thermoelectric properties simulation of the undoped Ge / PEDOT:PSS heterostructures (hollow dots: experimental results, dotted curves: PEDOT:PSS dielectric constant = 9.7[69], broken curves: PEDOT:PSS dielectric constant = 3.5[70], unbroken curves: PEDOT:PSS dielectric constant = 1.1[68]). Even if the dielectric constants of PEDOT:PSS changed, its effect is limited, therefore does not harm the predictability of thermoelectric properties markedly.

2.3.12. Enhanced Thermoelectric Power Factors of Si / PEDOT:PSS and Ge / PEDOT:PSS

A maximum power factor was achieved in the heterostructure with the smallest PEDOT:PSS and Si thickness: 6.5 nm thick PEDOT:PSS on 14 nm thick Si. The Seebeck coefficient was increased from 10 μV/K of PEDOT:PSS on SiO_2 glass to 73 μV/K of the heterostructure, and the power factor was increased from 1.5 $\mu W/m \cdot K^2$ to 26.2 $\mu W/m \cdot K^2$, as shown in **Figure 2.26**. As modulation-doped Si layer is only limited to interfacial area, having interfacial Si layer less than 10 nm thickness is sufficient for modulation doping. In other words, part of Si layer farther from the interface is hardly affected by modulation doping. Rather, this additional Si layer lowers average electrical conductivity, because the electrical conductivity is normalized combined thicknesses of the heterostructures by $\bar{\sigma}(d_1, d_2) = \frac{e\int_{-d_1}^{d_2} n(x)\mu(x)dx}{d_1+d_2}$. Likewise, PEDOT:PSS layer away from the interface with Si does not contribute to modulation doping, as can be seen from no band bending of PEDOT:PSS at the interface. This means even after the hole donation to Si, the hole concentration of PEDOT:PSS is scarcely varied due to metallic hole density of PEDOT:PSS. This also explains why thicker PEDOT:PSS layer on Si incurs the thermoelectric power factor to converge toward that of PEDOT:PSS itself, resulting on lowered power factor of the heterostructures.

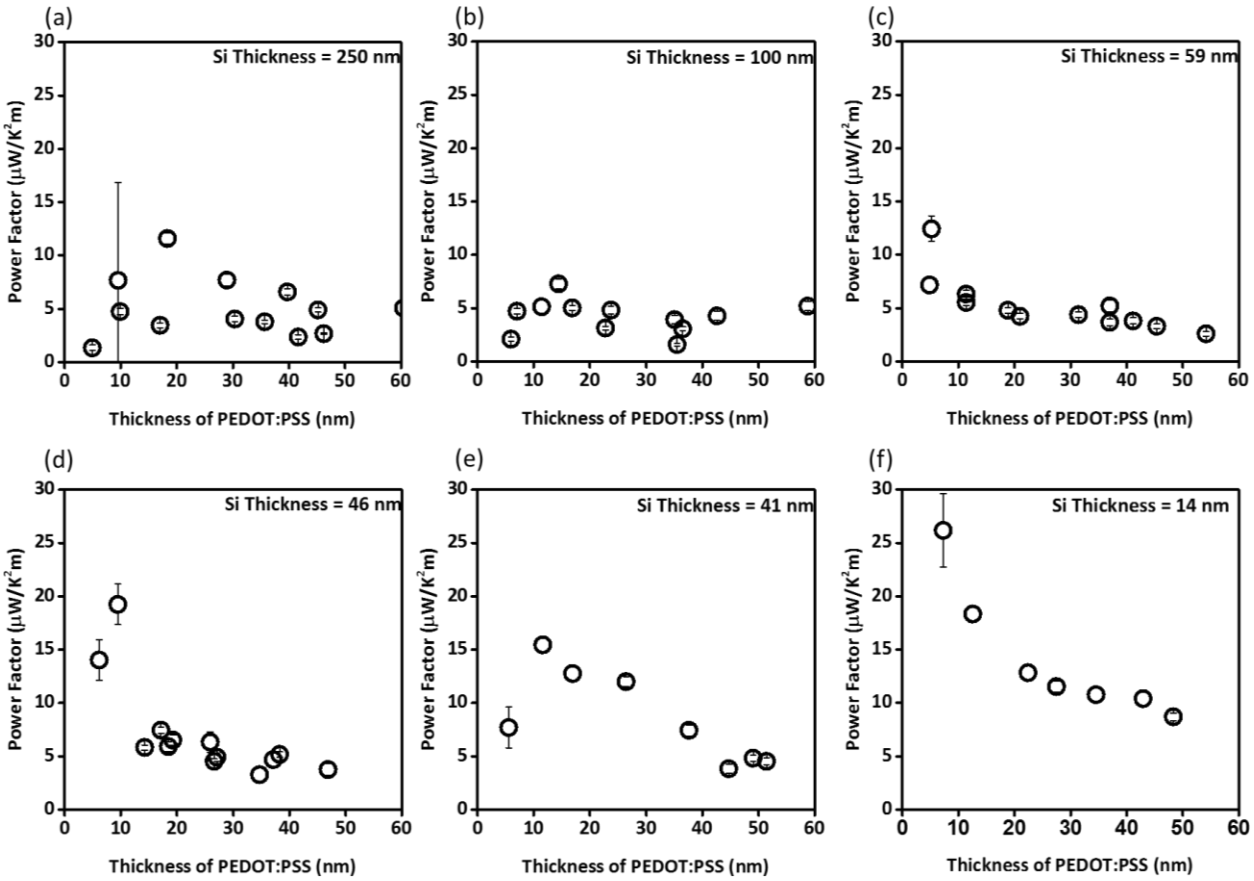

Figure 2.26. (a) – (f) Power factors of PEDOT:PSS films of different thicknesses on 250 nm, 100 nm, 59 nm, 46 nm, 41 nm, and 14 nm thick Si, respectively. These are estimated by multiplying individually square of measured Seebeck coefficients and electrical conductivities. Figure from *Quantitative analyses of enhanced thermoelectric properties of modulation-doped PEDOT:PSS/undoped Si (001) nanoscale heterostructures*[17]. Reproduced by permission of the Royal Society of Chemistry.

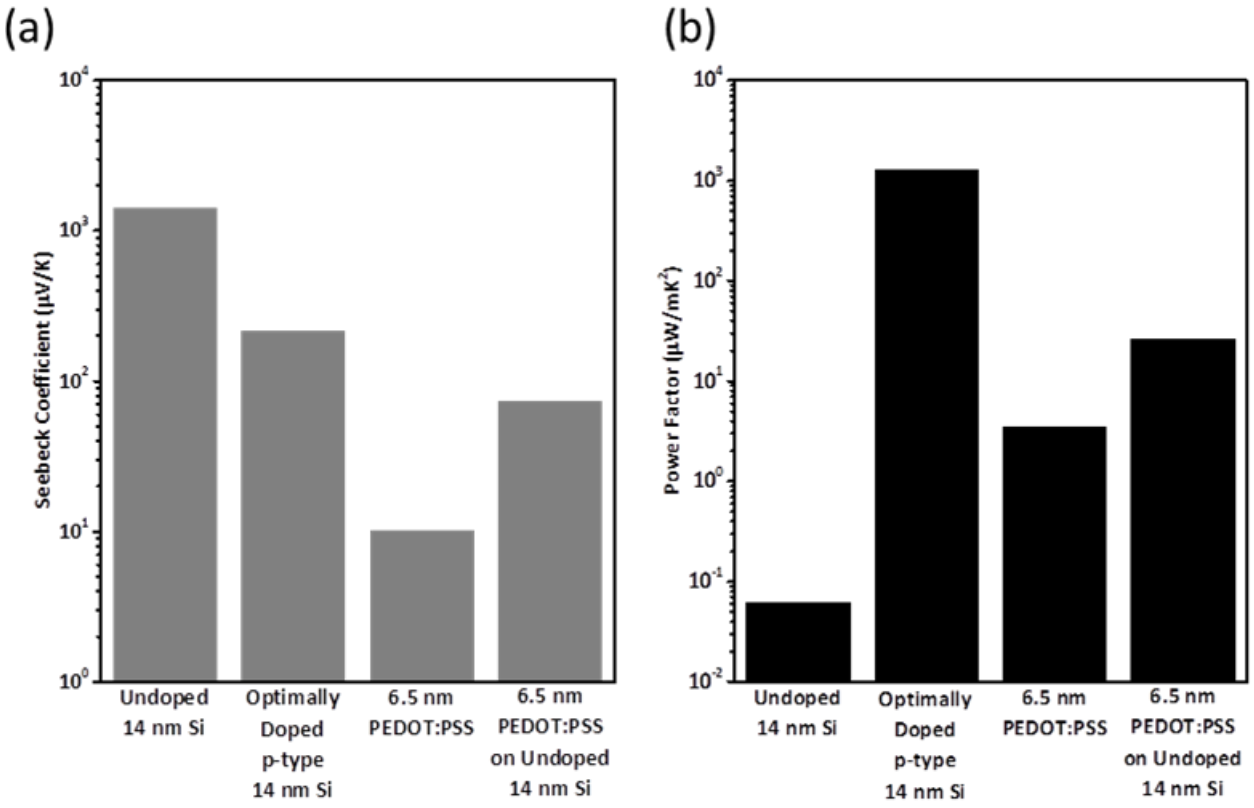

Figure 2.27. (a) Seebeck coefficient and (b) thermoelectric power factor comparison of 6.5-nm-thick PEDOT:PSS film on 14-nm-thick Si (100) on sapphire with respect to 6.5-nm-thick PEDOT:PSS film on SiO_2 glass slide, undoped and optimally doped[71] 14-nm-thick Si (100). These thicknesses of PEDOT:PSS and Si corresponds to the case exhibiting the largest Seebeck coefficient achieved in this study. Figure from *Quantitative analyses of enhanced thermoelectric properties of modulation-doped PEDOT:PSS/undoped Si (001) nanoscale heterostructures*[17]. Reproduced by permission of the Royal Society of Chemistry.

Seebeck coefficients and power factors of PEDOT:PSS, undoped Ge, and their heterostructures are compared in **Figure 2.28**. The maximum power factor appeared when the PEDOT:PSS thickness was minimal (12 nm). The Seebeck coefficient improved from 10 μV/K of PEDOT:PSS on SiO_2 to 398 μV/K in the bilayered structure, and the power factor increased from 3.5 μW/m·K^2 to 154 μW/m·K^2.

As electrical conductivity is normalized combined thicknesses of the heterostructures ($\bar{\sigma}(d_1, d_2) = \frac{e\int_{-d_1}^{d_2} n(x)\mu(x)dx}{d_1+d_2}$), PEDOT:PSS layer away from the interface with Ge does not

contribute to modulation doping, as can be seen from no band bending of PEDOT:PSS at the interface. This means that even after the hole donation to Ge, the hole concentration of PEDOT:PSS is almost unaffected due to metallic hole density of PEDOT:PSS. This also explains why thicker PEDOT:PSS layer on Ge causes the thermoelectric power factor to converge toward that of PEDOT:PSS itself, resulting on lowered power factor of the heterostructures.

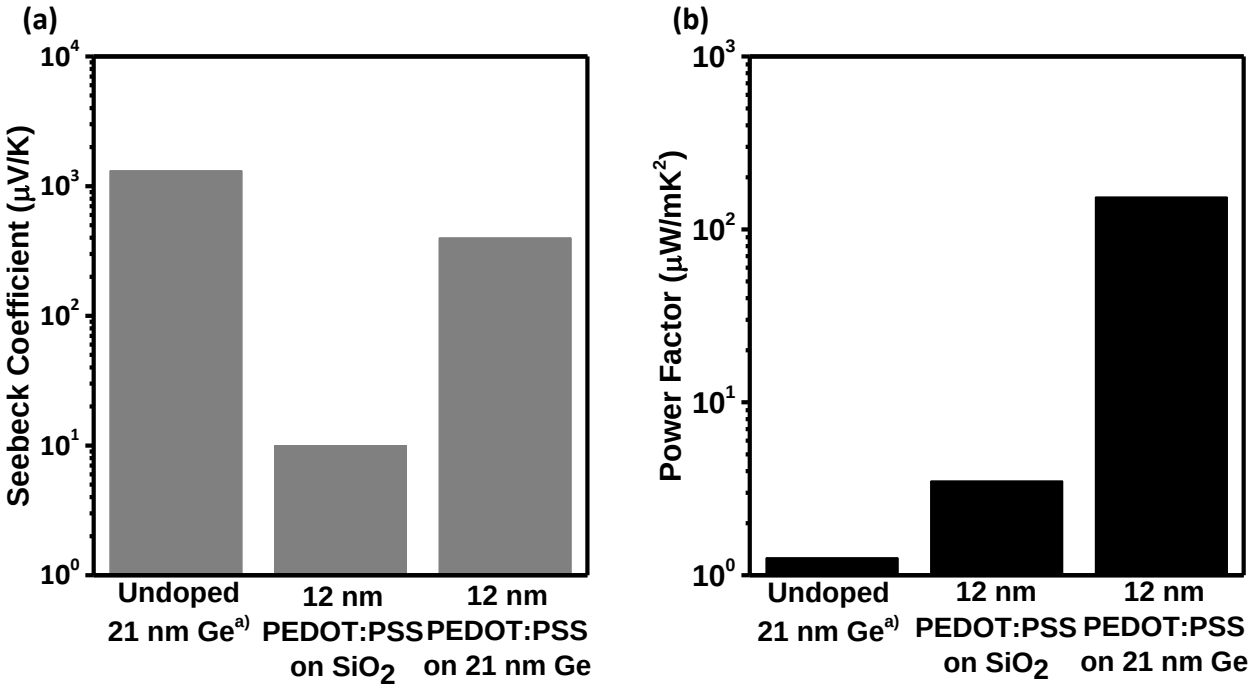

Figure 2.28. (a) Seebeck coefficient and (b) thermoelectric power factor comparison of the 12 nm thick PEDOT:PSS film on 21 nm thick GeOI with respect to the 12 nm thick PEDOT:PSS film on the SiO_2 glass slide and undoped 21 nm thick Ge. The thickness of PEDOT:PSS is where the largest Seebeck coefficient is achieved in this research.

2.4. Conclusion

In this work, we demonstrated that modulation doping at the interfaces of Si / PEDOT:PSS and Ge / PEDOT:PSS heterostructures can lead to enhanced Seebeck coefficients and power factor. The modulation doping at these heterostructures were proven by showing the agreement between the experimental results and simulated thermoelectric properties. Decreasing thickness of PEDOT:PSS can increase the Seebeck coefficient in the expense of electrical conductivity. In the contrast, increase in PEDOT:PSS thickness results in thermoelectric performance converging toward inherent PEDOT:PSS properties, because interfacial contribution from modulation doping becomes relatively smaller by thickened, highly conductive PEDOT:PSS. The power factor was maximized when the thicknesses of PEDOT:PSS and Si were at their minimum, because Seebeck coefficient is more critical to the power factor than electrical conductivity. In Si / PEDOT:PSS system, the Seebeck coefficient was increased from 10 μV/K of PEDOT:PSS on SiO_2 glass to 73 μV/K of the heterostructure, and the power factor was increased from 1.5 $\mu W/m \cdot K^2$ to 26.2 $\mu W/m \cdot K^2$. In Ge / PEDOT:PSS heterostructures, maximum power factor of 154 $\mu W/m \cdot K^2$ and maximum Seebeck coefficient of 398 μV/K were achieved. Simulated electrical conductivities by the 1D Poisson's equation solver with and without equilibrated Si / PEDOT:PSS interfacial band structure agree with experimental electrical conductivities, as the conduction by the modulation doped Si concentrated at the interface only contributes in small portion to the overall electrical conductivity. Thus, examining if modulation doping took place at Si / PEDOT:PSS heterojuncstions cannot be conclusive by simply judging from simulated and experimental electrical conductivity comparisons. However, only the simulated Seebeck coefficients *with band alignment* scenario match well with the experimentally measured Seebeck coefficient, indicating that the hole migration to Si is responsible for the enhancement of the Seebeck coefficient. This simulation technique based on 1D Poisson's equation solver was applied to Ge / PEDOT:PSS heterostructures and displayed matching between the experiment and theoretical prediction as well, hence further demonstrating validity of this simulation technique. The simple sequences of experimental evaluation and follow-up simulation shown in this study can be further extended to other nanoscale heterostructures with different electronic applications, such as solar cells and transistors. Also, proof of modulation doping phenomenon can provide mechanistic insights about

strategies to increase the power factor of PEDOT:PSS-based composites for thermoelectric applications.

In order to further improve power factors of nanoscale heterostructured thermoelectric systems in the future, limitation on valence band position of undoped semiconductors against Fermi level at the heterojunctions should be overcome. When semiconductors form heterojunctions with metals, such as PEDOT:PSS, valence band edge or conduction band edge of such semiconductors can only shift within very narrow ranges, regardless of properties of contacting metal. This phenomenon is called Fermi level pinning, and exists for metal-semiconductor heterojunctions in general, including Si[72] and Ge[73]. As Ge more severely suffers from this issue than Si, techniques to alleviate Fermi-level pinning at Ge-metal heterojunction were developed recently. Typically, nanoscale structuration of metals[74] or deposition of ultrathin oxide layers[75-79] are applied to minimize Fermi level pinning effect, which can be utilized to induce higher degree of modulation doping. Alternatively, replacements of Ge into other inorganic semiconductors that have large carrier mobility and favorable band offsets for modulation doping is expected to lead to large power factors. The determination on the favorable band alignment for heterojunctions can be easily carried out via simple spectroscopic Kraut's method.

References

1 Alemu, D., Wei, H.-Y., Ho, K.-C. & Chu, C.-W. Highly conductive PEDOT:PSS electrode by simple film treatment with methanol for ITO-free polymer solar cells. *Energy & Environmental Science* **5**, 9662, doi:10.1039/c2ee22595f (2012).

2 Gasiorowski, J., Menon, R., Hingerl, K., Dachev, M. & Sariciftci, N. S. Surface morphology, optical properties and conductivity changes of poly(3,4-ethylenedioxythiophene):poly(styrenesulfonate) by using additives. *Thin Solid Films* **536**, 211-215, doi:10.1016/j.tsf.2013.03.124 (2013).

3 Liu, C. *et al.* Highly conducting free-standing poly(3,4-ethylenedioxythiophene)/poly(styrenesulfonate) films with improved thermoelectric performances. *Synthetic Metals* **160**, 2481-2485, doi:10.1016/j.synthmet.2010.09.031 (2010).

4 Lang, U., Müller, E., Naujoks, N. & Dual, J. Microscopical Investigations of PEDOT:PSS Thin Films. *Advanced Functional Materials* **19**, 1215-1220, doi:10.1002/adfm.200801258 (2009).

5 Yee, S. K., Coates, N. E., Majumdar, A., Urban, J. J. & Segalman, R. A. Thermoelectric power factor optimization in PEDOT:PSS tellurium nanowire hybrid composites. *Physical chemistry chemical physics : PCCP* **15**, 4024-4032, doi:10.1039/c3cp44558e (2013).

6 See, K. C. *et al.* Water-processable polymer-nanocrystal hybrids for thermoelectrics. *Nano letters* **10**, 4664-4667, doi:10.1021/nl102880k (2010).

7 Du, Y., Cai, K. F., Chen, S., Cizek, P. & Lin, T. Facile Preparation and Thermoelectric Properties of Bi2Te3 Based Alloy Nanosheet/PEDOT:PSS Composite Films. *ACS Appl Mater Interfaces* **6**, 5735-5743, doi:10.1021/am5002772 (2014).

8 Zhang, B., Sun, J., Katz, H. E., Fang, F. & Opila, R. L. Promising thermoelectric properties of commercial PEDOT:PSS materials and their Bi_2Te_3 powder composites. *ACS applied materials & interfaces* **2**, 3170-3178, doi:10.1021/am100654p (2010).

9 Gao, C. & Chen, G. Conducting polymer/carbon particle thermoelectric composites: Emerging green energy materials. *Composites Science and Technology* **124**, 52-70, doi:http://dx.doi.org/10.1016/j.compscitech.2016.01.014 (2016).

10 Xu, K., Chen, G. & Qiu, D. Convenient construction of poly(3,4-ethylenedioxythiophene)-graphene pie-like structure with enhanced thermoelectric performance. *Journal of Materials Chemistry A* **1**, 12395-12399, doi:10.1039/c3ta12691a (2013).

11 Shakouri, A. Recent Developments in Semiconductor Thermoelectric Physics and Materials. *Annual Review of Materials Research* **41**, 399-431, doi:doi:10.1146/annurev-matsci-062910-100445 (2011).

12 Vashaee, D. & Shakouri, A. Improved Thermoelectric Power Factor in Metal-Based Superlattices. *Physical Review Letters* **92**, 106103 (2004).

13 Shakouri, A., LaBounty, C., Abraham, P., Piprek, J. & Bowers, J. E. Enhanced Thermionic Emission Cooling in High Barrier Superlattice Heterostructures. *MRS Online Proceedings Library Archive* **545**, 449 (410 pages), doi:doi:10.1557/PROC-545-449 (1998).

14 Vashaee, D. & Shakouri, A. Electronic and thermoelectric transport in semiconductor and metallic superlattices. *Journal of Applied Physics* **95**, 1233-1245, doi:doi:http://dx.doi.org/10.1063/1.1635992 (2004).

15 McGuire, G. E. *Semiconductor materials and process technology handbook : for very large scale integration (VLSI) and ultra large scale integration (ULSI)*. (Park Ridge, N.J., U.S.A. : Noyes Publications, c1988., 1988).

16 Burkov, A. T., Heinrich, A., Konstantinov, P. P., Nakama, T. & Yagasaki, K. Experimental set-up for thermopower and resistivity measurements at 100-1300 K. *Measurement Science and Technology* **12**, 264 (2001).

17 Lee, D. *et al.* Quantitative analyses of enhanced thermoelectric properties of modulation-doped PEDOT:PSS/undoped Si (001) nanoscale heterostructures. *Nanoscale*, doi:10.1039/c6nr06950a (2016).

18 Kraut, E. A., Grant, R. W., Waldrop, J. R. & Kowalczyk, S. P. Semiconductor core-level to valence-band maximum binding-energy differences: Precise determination by x-ray photoelectron spectroscopy. *Physical Review B* **28**, 1965-1977 (1983).

19 Kraut, E. A., Grant, R. W., Waldrop, J. R. & Kowalczyk, S. P. Precise Determination of the Valence-Band Edge in X-Ray Photoemission Spectra: Application to Measurement of Semiconductor Interface Potentials. *Physical review letters* **44**, 1620-1623 (1980).

20 Gray, J. *et al.* (2011).

21 Bergman, D. J. & Fel, L. G. Enhancement of thermoelectric power factor in composite thermoelectrics. *Journal of Applied Physics* **85**, 8205, doi:10.1063/1.370660 (1999).

22 Bergman, D. J. & Levy, O. Thermoelectric properties of a composite medium. *Journal of Applied Physics* **70**, 6821, doi:10.1063/1.349830 (1991).

23 Bubnova, O., Berggren, M. & Crispin, X. Tuning the thermoelectric properties of conducting polymers in an electrochemical transistor. *Journal of the American Chemical Society* **134**, 16456-16459, doi:10.1021/ja305188r (2012).

24 Bian, Z., Shakouri, A., Shi, L., Lyeo, H.-K. & Shih, C. K. Three-dimensional modeling of nanoscale Seebeck measurements by scanning thermoelectric microscopy. *Applied Physics Letters* **87**, 053115, doi:doi:http://dx.doi.org/10.1063/1.2008381 (2005).

25 Lyeo, H.-K. *et al.* Profiling the Thermoelectric Power of Semiconductor Junctions with Nanometer Resolution. *Science* **303**, 816-818, doi:10.1126/science.1091600 (2004).

26 Pipe, K. P., Ram, R. J. & Shakouri, A. Bias-dependent Peltier coefficient and internal cooling in bipolar devices. *Physical Review B* **66**, 125316 (2002).

27 Lee, B. *et al.* Quantitative thermopower profiling across a silicon p-n junction with nanometer resolution. *Nano Lett* **12**, 4472-4476, doi:10.1021/nl301359c (2012).

28 Crispin, X. *et al.* The Origin of the High Conductivity of Poly(3,4-ethylenedioxythiophene)−Poly(styrenesulfonate) (PEDOT−PSS) Plastic Electrodes. *Chemistry of Materials* **18**, 4354-4360, doi:10.1021/cm061032+ (2006).

29 Ding, Y., Xu, W., Wang, W., Fong, H. & Zhu, Z. Scalable and Facile Preparation of Highly Stretchable Electrospun PEDOT:PSS@PU Fibrous Nonwovens toward Wearable Conductive Textile Applications. *ACS applied materials & interfaces* **9**, 30014-30023, doi:10.1021/acsami.7b06726 (2017).

30 Liu, J. *et al.* Thermal Conductivity and Elastic Constants of PEDOT:PSS with High Electrical Conductivity. *Macromolecules* **48**, 585-591, doi:10.1021/ma502099t (2015).

31 Hull, R. *Properties of crystalline silicon. [electronic resource]*. (London : The Institution of Electrical Engineers, c2006 (Norwood, Mass. : Books24x7.com [generator]), 2006).

32 Sze, S. M. & Ng, K. K. *Physics of Semiconductor Devices*. Vol. 3rd ed (Wiley-Interscience, 2007).

33 Saxena, N. *et al.* Morphology–Function Relationship of Thermoelectric Nanocomposite Films from PEDOT:PSS with Silicon Nanoparticles. *Advanced Electronic Materials* **3**, 1700181-n/a, doi:10.1002/aelm.201700181 (2017).

34 Bounioux, C. *et al.* Thermoelectric composites of poly(3-hexylthiophene) and carbon nanotubes with a large power factor. *Energy & Environmental Science* **6**, 918-925, doi:10.1039/c2ee23406h (2013).

35 Mitchell, D. F. *et al.* Film thickness measurements of SiO2 by XPS. *Surface and Interface Analysis* **21**, 44-50, doi:10.1002/sia.740210107 (1994).

36 Yoshikatsu, N. Resistivity and Temperature Coefficient of Thin Metal Films with Rough Surface. *Japanese Journal of Applied Physics* **9**, 1326 (1970).

37 Mayadas, A. F. & Shatzkes, M. Electrical-Resistivity Model for Polycrystalline Films: the Case of Arbitrary Reflection at External Surfaces. *Physical Review B* **1**, 1382-1389 (1970).

38 Fuchs, K. The conductivity of thin metallic films according to the electron theory of metals. *Mathematical Proceedings of the Cambridge Philosophical Society* **34**, 100-108, doi:doi:10.1017/S0305004100019952 (1938).

39 Seifert, W., Albrecht, H., Mietke, S., Kohler, T. & Werner, M. 183-190 (SPIE-Int. Soc. Opt. Eng. SPIE SPIE).

40 Yoo, D. *et al.* Gradual thickness-dependent enhancement of the thermoelectric properties of PEDOT:PSS nanofilms. *RSC Advances* **4**, 58924-58929, doi:10.1039/c4ra09587a (2014).

41 Asli, U. *et al.* Low-Dimensional Conduction Mechanisms in Highly Conductive and Transparent Conjugated Polymers. *Advanced Materials* **27**, 4604-4610, doi:doi:10.1002/adma.201502340 (2015).

42 Nardes, A. M. *et al.* Microscopic Understanding of the Anisotropic Conductivity of PEDOT:PSS Thin Films. *Advanced Materials* **19**, 1196-1200, doi:10.1002/adma.200602575 (2007).

43 Kemerink, M., Timpanaro, S., de Kok, M. M., Meulenkamp, E. A. & Touwslager, F. J. Three-Dimensional Inhomogeneities in PEDOT:PSS Films. *The Journal of Physical Chemistry B* **108**, 18820-18825, doi:10.1021/jp0464674 (2004).

44 Greco, F. *et al.* Ultra-thin conductive free-standing PEDOT/PSS nanofilms. *Soft Matter* **7**, 10642-10650, doi:10.1039/c1sm06174g (2011).

45 Rivnay, J. *et al.* Structural control of mixed ionic and electronic transport in conducting polymers. *Nature communications* **7**, 11287, doi:10.1038/ncomms11287 https://www.nature.com/articles/ncomms11287#supplementary-information (2016).

46 Bubnova, O. *et al.* Optimization of the thermoelectric figure of merit in the conducting polymer poly(3,4-ethylenedioxythiophene). *Nature materials* **10**, 429, doi:10.1038/nmat3012 (2011).

47 Rutledge, S. A. & Helmy, A. S. Carrier mobility enhancement in poly(3,4-ethylenedioxythiophene)-poly(styrenesulfonate) having undergone rapid thermal annealing. *Journal of Applied Physics* **114**, 133708, doi:10.1063/1.4824104 (2013).

48 Karagiannidis, P. G. *et al.* Effects of buffer layer properties and annealing process on bulk heterojunction morphology and organic solar cell performance. *Journal of Materials Chemistry* **22**, 14624, doi:10.1039/c2jm31277h (2012).

49 Coehoorn, R., Pasveer, W. F., Bobbert, P. A. & Michels, M. A. J. Charge-carrier concentration dependence of the hopping mobility in organic materials with Gaussian disorder. *Physical Review B* **72**, doi:10.1103/PhysRevB.72.155206 (2005).

50 Eldada, L. A., Lindemuth, J. & Mizuta, S.-I. Hall measurements on low-mobility materials and high resistivity materials. **8110**, 81100I, doi:10.1117/12.893100 (2011).

51 Wei, Q., Mukaida, M., Naitoh, Y. & Ishida, T. Morphological Change and Mobility Enhancement in PEDOT:PSS by Adding Co-solvents. *Advanced Materials* **25**, 2831-2836, doi:10.1002/adma.201205158 (2013).

52 Yamashita, M., Otani, C., Shimizu, M. & Okuzaki, H. Effect of solvent on carrier transport in poly(3,4-ethylenedioxythiophene)/poly(4-styrenesulfonate) studied by terahertz and infrared-ultraviolet spectroscopy. *Applied Physics Letters* **99**, 143307, doi:10.1063/1.3647574 (2011).

53 Lim, K.-G. *et al.* Boosting the Power Conversion Efficiency of Perovskite Solar Cells Using Self-Organized Polymeric Hole Extraction Layers with High Work Function. *Advanced Materials* **26**, 6461-6466, doi:10.1002/adma.201401775 (2014).

54 Kim, S. L., Lin, H. T. & Yu, C. Thermally Chargeable Solid-State Supercapacitor. *Advanced Energy Materials* **6**, 1600546-n/a, doi:10.1002/aenm.201600546 (2016).

55 Ail, U. *et al.* Thermoelectric Properties of Polymeric Mixed Conductors. *Advanced Functional Materials* **26**, 6288-6296, doi:10.1002/adfm.201601106 (2016).

56 Lacy, F. Developing a theoretical relationship between electrical resistivity, temperature, and film thickness for conductors. *Nanoscale Research Letters* **6**, 636, doi:10.1186/1556-276x-6-636 (2011).

57 Liu, H. D., Zhao, Y. P., Ramanath, G., Murarka, S. P. & Wang, G. C. Thickness dependent electrical resistivity of ultrathin (<40 nm) Cu films. *Thin Solid Films* **384**, 151-156, doi:https://doi.org/10.1016/S0040-6090(00)01818-6 (2001).

58 Koch, N., Vollmer, A. & Elschner, A. Influence of water on the work function of conducting poly(3,4-ethylenedioxythiophene)/poly(styrenesulfonate). *Applied Physics Letters* **90**, 043512, doi:10.1063/1.2435350 (2007).

59 Lin, Y.-J. *et al.* Increasing the work function of poly(3,4-ethylenedioxythiophene) doped with poly(4-styrenesulfonate) by ultraviolet irradiation. *Applied Physics Letters* **91**, 092127, doi:10.1063/1.2777147 (2007).

60 Im, S. G., Gleason, K. K. & Olivetti, E. A. Doping level and work function control in oxidative chemical vapor deposited poly (3,4-ethylenedioxythiophene). *Applied Physics Letters* **90**, 152112, doi:10.1063/1.2721376 (2007).

61 Anderson, R. L. Germanium-Gallium Arsenide Heterojunctions [Letter to the Editor]. *IBM Journal of Research and Development* **4**, 283-287, doi:10.1147/rd.43.0283 (1960).

62 Kemeny, P. C. & Shevchik, N. J. Primary XPS spectra of Ni and final state effects. *Solid State Communications* **17**, 255-258, doi:https://doi.org/10.1016/0038-1098(75)90287-2 (1975).

63 Ajimsha, R. S. *et al.* Band offset at TiO_2/MDMO PPV and TiO_2/PEDOT PSS interfaces studied using photoelectron spectroscopy. *RSC Advances* **5**, 97891-97897, doi:10.1039/c5ra21227h (2015).

64 Zhu, Y. *et al.* X-ray photoelectron spectroscopy analysis and band offset determination of CeO2 deposited on epitaxial (100), (110), and (111)Ge. *Journal of Vacuum Science &*

Technology B, Nanotechnology and Microelectronics: Materials, Processing, Measurement, and Phenomena **32**, 011217, doi:10.1116/1.4862160 (2014).

65 Chen, T.-G., Huang, B.-Y., Chen, E.-C., Yu, P. & Meng, H.-F. Micro-textured conductive polymer/silicon heterojunction photovoltaic devices with high efficiency. *Applied Physics Letters* **101**, 033301, doi:10.1063/1.4734240 (2012).

66 Jackle, S. *et al.* Junction formation and current transport mechanisms in hybrid n-Si/PEDOT:PSS solar cells. *Scientific reports* **5**, 13008, doi:10.1038/srep13008 (2015).

67 Chi, D., Qi, B., Wang, J., Qu, S. & Wang, Z. High-performance hybrid organic-inorganic solar cell based on planar n-type silicon. *Applied Physics Letters* **104**, 193903, doi:10.1063/1.4875913 (2014).

68 Gasiorowski, J., Menon, R., Hingerl, K., Dachev, M. & Sariciftci, N. S. Surface morphology, optical properties and conductivity changes of poly(3,4-ethylenedioxythiophene):poly(styrenesulfonate) by using additives. *Thin Solid Films* **536**, 211-215, doi:https://doi.org/10.1016/j.tsf.2013.03.124 (2013).

69 Ke, L. *et al.* Ultrasmooth Silver Thin Film on PEDOT:PSS Nucleation Layer for Extended Surface Plasmon Propagation. *ACS applied materials & interfaces* **4**, 1247-1253, doi:10.1021/am201391f (2012).

70 Abidian, M. R. & Martin, D. C. Experimental and theoretical characterization of implantable neural microelectrodes modified with conducting polymer nanotubes. *Biomaterials* **29**, 1273-1283, doi:https://doi.org/10.1016/j.biomaterials.2007.11.022 (2008).

71 Neophytou, N. & Kosina, H. Large thermoelectric power factor in p-type Si (110)/[110] ultra-thin-layers compared to differently oriented channels. *Journal of Applied Physics* **112**, 024305, doi:doi:http://dx.doi.org/10.1063/1.4737122 (2012).

72 Sankey, O. F., Allen, R. E. & Dow, J. D. Si/transition-metal Schottky barriers: Fermi-level pinning by Si dangling bonds at interfacial vacancies. *Solid State Communications* **49**, 1-5, doi:https://doi.org/10.1016/0038-1098(84)90548-9 (1984).

73 Dimoulas, A., Tsipas, P., Sotiropoulos, A. & Evangelou, E. K. Fermi-level pinning and charge neutrality level in germanium. *Applied Physics Letters* **89**, 252110, doi:10.1063/1.2410241 (2006).

74 Kishore, V. P., Paramahans, P., Sadana, S., Ganguly, U. & Lodha, S. Nanocrystal-based Ohmic contacts on n and p-type germanium. *Applied Physics Letters* **100**, 142107, doi:10.1063/1.3700965 (2012).

75 Kuzmin, M. *et al.* Origin of Fermi-level pinning and its control on the n-type Ge(100) surface. *Physical Review B* **94**, 035421 (2016).

76 Zhou, Y. *et al.* Investigating the origin of Fermi level pinning in Ge Schottky junctions using epitaxially grown ultrathin MgO films. *Applied Physics Letters* **96**, 102103, doi:10.1063/1.3357423 (2010).

77 Masaharu, K., Atsuhiro, K., Saraswat, K., Wong, H. S. P. & Yoshio, N. in *2008 Symposium on VLSI Technology*. 54-55.

78 Tomonori, N., Koji, K. & Akira, T. A Significant Shift of Schottky Barrier Heights at Strongly Pinned Metal/Germanium Interface by Inserting an Ultra-Thin Insulating Film. *Applied Physics Express* **1**, 051406 (2008).

79 Zhou, Y., Ogawa, M., Han, X. & Wang, K. L. Alleviation of Fermi-level pinning effect on metal/germanium interface by insertion of an ultrathin aluminum oxide. *Applied Physics Letters* **93**, 202105, doi:doi:http://dx.doi.org/10.1063/1.3028343 (2008).

3. Development of a Flow-Battery Type Electrochemical Heat Harvester and Elongation of Its Cyclability through Polyelectrolyte Coating on Nafion

3.1. Introduction

Efficient conversion of low grade heat into electricity has been intensively investigated mostly focusing on thermoelectrics. However, state-of-the-art thermoelectric materials in general incorporate rare and expensive elements, hampering their widespread application in daily lives. Electrochemical heat conversion has drawn scientific attention as one of alternatives to thermoelectric technology, largely owing to its capability to easily reach thermopower more than 1 mV/K[1-3]. However, low ionic conductivity has compromised the potential improvement on conversion efficiency due to large thermopower, when the electrochemical heat conversion operated under thermal gradient[1,4,5]. Recent breakthrough addressed the efficiency issue by transitioning the mode of operation into thermodynamic cycles like heat engines[6-10], achieving up to 2.0 % of conversion efficiency between 20 °C and 60 °C[6]. If higher electrochemical thermopowers can be accomplished in addition to this new design, then more advanced efficiency would be achieved.

Here, we report an aqueous redox couple-based autonomous electrochemical heat harvester with full cell thermopower of -2.9 mV/K. This device consisted of two dissimilar redox couples: $Fe(CN)_6^{3-/4-}{}_{(aq)}$ and $Co(bpy)_3^{2+/3+}{}_{(aq)}$. They were chosen because their half-cell electrochemical potentials intersect. Furthermore, the opposite signs of the half-cell thermopowers contributed to the enhanced total thermopower (Equation 1.14). This water-based electrochemical heat harvesting system required ion selective membrane in order to avoid internal short-circuit. Nafion was employed for this function, however it suffered from degradation of ionic conductivity over time because $Co(bpy)_3^{2+/3+}$ species was absorbed into the Nafion. To avert this detrimental phenomenon, polyelectrolyte films were coated by layer-by-layer (LbL) process on Nafion, so that large $Co(bpy)_3^{2+/3+}$ species could be selectively excluded, while remaining permeable to K^+ ions. This coating succeeded in suppressing growth of ionic resistance of the Nafion, hence greatly improved cyclability of the electrochemical heat harvester. The retention of the charge capacity, energy output, and conversion efficiency up to 10 cycles were demonstrated. The average energy, power, and charge capacities during a thermodynamic cycle were 132.1 mJ/mL, 13.95 μW/mL,

and 2.84 C/mL, respectively. The heat to electricity conversion efficiency of this autonomous electrochemical heat harvester was estimated 0.10 % at 20 ºC – 60 ºC operating temperature range. The efficiency was mainly compromised by large heat capacity of the constituent water. This work primarily provides an insight on design principles of electrochemical heat harvesters. Also, using readily available and inexpensive polyelectrolytes, the LbL deposition technique utilized in this research can be further extended into other applications where selective permeation can play as a key merit, such as dialysis, flow batteries, and desalination.

3.2. Experimental Methods

3.2.1. Electrochemical Thermopower Measurements under Thermal Gradient

In order to assess the electrochemical thermopowers of aqueous redox couples, the most straightforward measurements were considered: checking the voltage changes at different temperature gradients. To realize this, steady maintenance of thermal gradient was important, along with chemical stability of the testing cell contacting the aqueous solution specimens. An electrolyte container composed of Teflon was chosen, due to its good mechanical, chemical, thermal stability and electrical insulation. The testing cell was sealed tightly by two Cu plates. They were electronically and thermally conductive, enabling detection of the voltage and thorough conduction of the heat flux. However, because they can be easily corroded in aqueous environment[11], the direct contact of the aqueous solutions should have been avoided. For this purpose, Pt (Alfa Aesar, 99.9 %, 00262) or Au (Alfa Aesar, 99.95 %, 11519) electrodes were introduced, to separate Cu plates from aqueous electrolytes contained in the Teflon body. The electrodes could also offer places for electrochemical reactions to happen without side reactions, as they were chemically inert and resistant to the corrosion.

In order to assemble all parts into an integrated testing cell (**Figure 3.1** (a)), firstly two O-rings composed of a chemically inert fluoropolymer elastomer (Viton rubber) were inserted at the mouths of the Teflon body. Then a piece of Au or Pt electrode was placed on the rubber O-ring, and a Cu plate tightly enclosed one end of the testing cell. Thus, there are one open end and another closed end at the cell. The closed end was put on a flat ground, and electrolyte was carefully poured to fill the internal space completely without any bubble. Then another piece of Au or Pt electrode was put at the open end, and another Cu plate tightly sealed the testing cell. The electrode materials for a single test should be identical in material and size for the symmetry.

Two separate T-type thermocouples (Omega Engineering, 5TC-TT-T-40-36) were firmly attached by electrically conductive Cu tapes (McMaster Carr, 76555A644) on the surface of each Cu plate, in order to observe temperatures at the hot side and the cold side of the cell. Those thermocouples were connected to a temperature data acquisition module (Omega Engineering, TC-08), which converted signals from thermocouples into digital data. Wire leads from each Cu plate were also connected to a Biologic (model SP300 or VSP300) potentiostat to record the voltage

difference between the hot end and the cold end. Peltier plates sandwiched the testing cell, and periodically varied electrical current was supplied. A programmable electrical power source (Tektronix, Keithley 2400 Sourcemeter) regulated the input current to the Peltier plates, hence thermal gradient. The programmed current supply regulated the temperature gradient through the testing cell (**Figure 3.1** (b)). Lastly, a heavy metal block on top of the testing cell ensured thermal conduction from the Peltier plates to the cell by a moderate mechanical pressure (**Figure 3.1** (c)). Once this set of procedures were carried out, then a electrochemical thermopower was ready to be characterized.

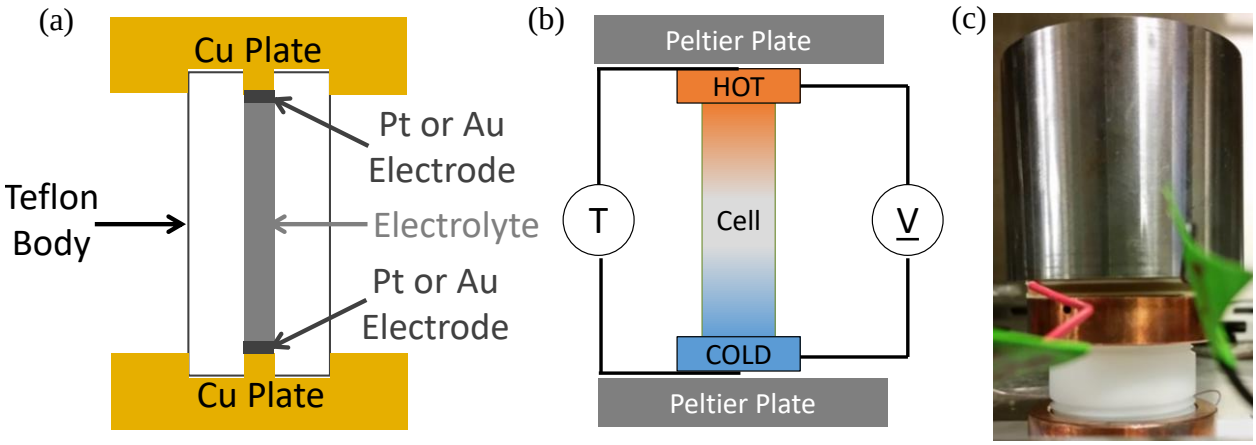

Figure 3.1. (a) Design of the testing cell for electrochemical thermopower characterization under thermal gradient. (b) Schematic representation of the testing cell under a thermal gradient by the two surrounding Peltier plates. Temperatures at the hot end and the cold end, and voltage difference between those ends were recorded. (c) A real photograph of the cell under experiment. A heavy metal block applied mechanical pressure, in order to promote suitable electrical and thermal contacts between the cell, Peltier plates, and thermocouples.

In order to validate this lab-built setup, firstly temperature gradient within the Cu plate was checked. **Figure 3.2** (a) – (b) depict arrangements of the thermocouples to detect temperature differences at inner and outer surfaces of the Cu plates under two different configurations. For both cases shown in **Figure 3.2** (a) – (b), the temperatures of inner surface and outer surface of Cu plates only differed by less than 1 K (**Figure 3.2** (c) – (d)), regardless of the temperature range. These results proved that heat flux losses in the Cu plates were negligible.

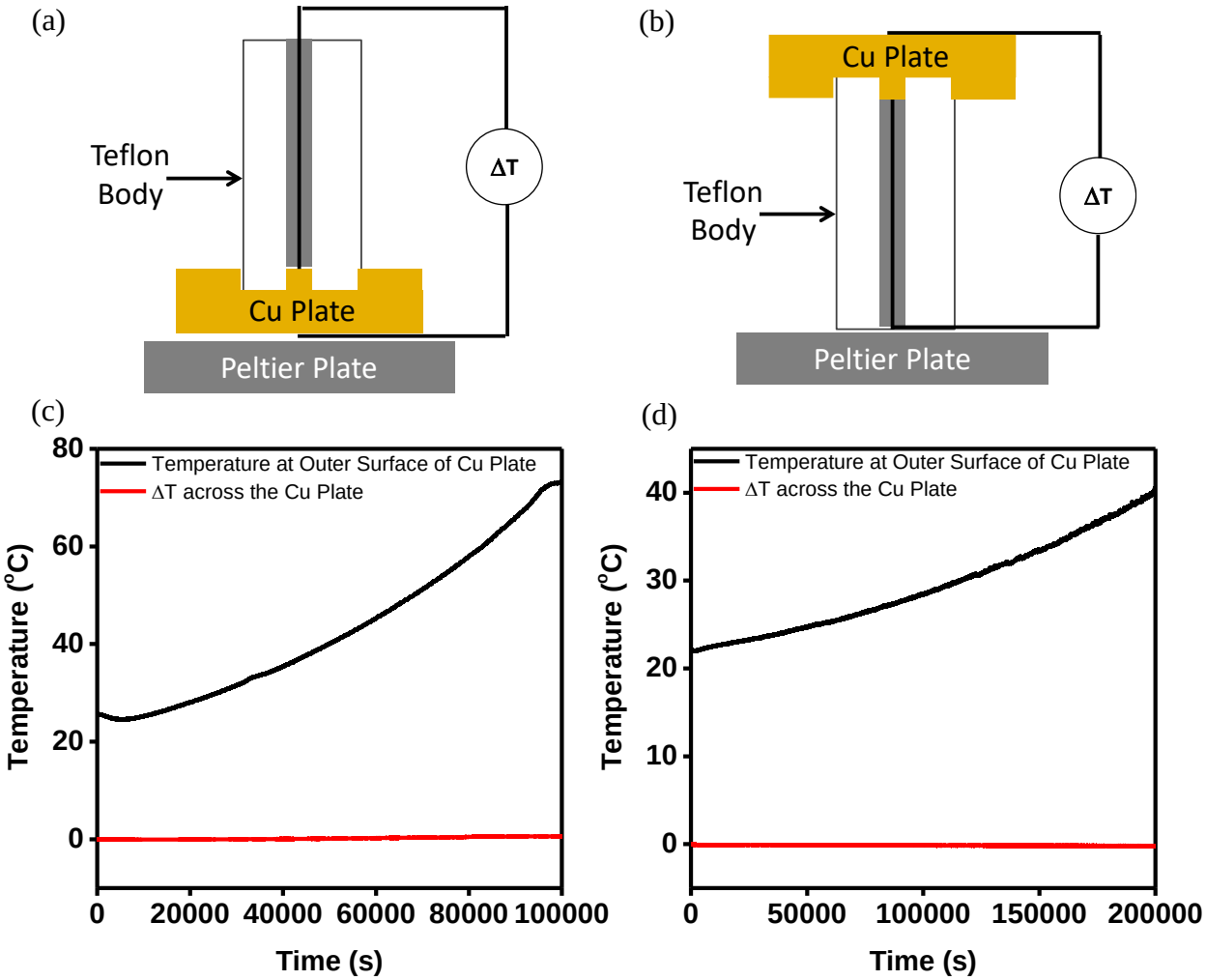

Figure 3.2. Thermal conduction through the Cu plates was measured to ensure temperatures at the surfaces of the testing cell and electrodes are equal. (a) – (b) Arrangements of thermocouples to confirm thermal gradient within the Cu plates. (c) – (d) Confirmation of nearly zero thermal gradient within the Cu plates under both circumstances. (c) corresponds to the configuration at (a) and (d) matches to the configuration at (b).

Because now it was clarified that temperature readings from outer surface of Cu were almost equal to electrode surface temperature, final calibration measurement were ready to be performed. An aqueous solution dissolving both $K_3Fe(CN)_6$ (Sigma-Aldrich, ≥ 99.0 %, 244023) and $K_4Fe(CN)_6{\cdot}3H_2O$ (Sigma-Aldrich, ≥ 99.5 %, 60279) was prepared for the calibration purpose.

For reversible redox reactions, both product and reactant need to be present together in the testing electrolyte. The notation of this solution is 2.0 mM $Fe(CN)_6^{3-/4-}{}_{(aq)}$, which means both $Fe(CN)_6^{3-}$ species and $Fe(CN)_6^{4-}$ have concentration of 2.0 mM in water, individually.

The solution was mounted in the testing cell with Au electrodes at both sides and experienced temperature gradient. **Figure 3.3** (a) – (b) show the variation of temperatures at the hot end and the cold end of the testing cell, along with voltage change over time. The temperature difference was intentionally programmed to rise every 10^4 seconds, in order to permit sufficient time to build steady-states for both voltage and thermal gradient. The successful establishment of the steady-states was evidenced by flat profiles of both the voltage and the two temperatures (**Figure 3.3** (a) – (b)). The entire temperature difference and voltage readings displayed in **Figure 3.3** (a) – (b) were plotted against each other at **Figure 3.3** (c). In comparison, **Figure 3.3** (d) represented the steady-state temperature differences and voltages. **Figure 3.3** (c) – (d) exhibited linearity, yielding the same slope of -1.44 mV/K. The slopes were the electrochemical thermopower of 2.0 mM $Fe(CN)_6^{3-/4-}{}_{(aq)}$ redox couple. Quick build-up of the steady-states caused the agreement between **Figure 3.3** (c) – (d). This fact suggested that reaction kinetics of $Fe(CN)_6^{3-/4-}{}_{(aq)}$ was fast. The measured electrochemical thermopower was compared with the previous report about the electrochemical thermopower of the same redox couple[6], and agreed within 1.39 %.

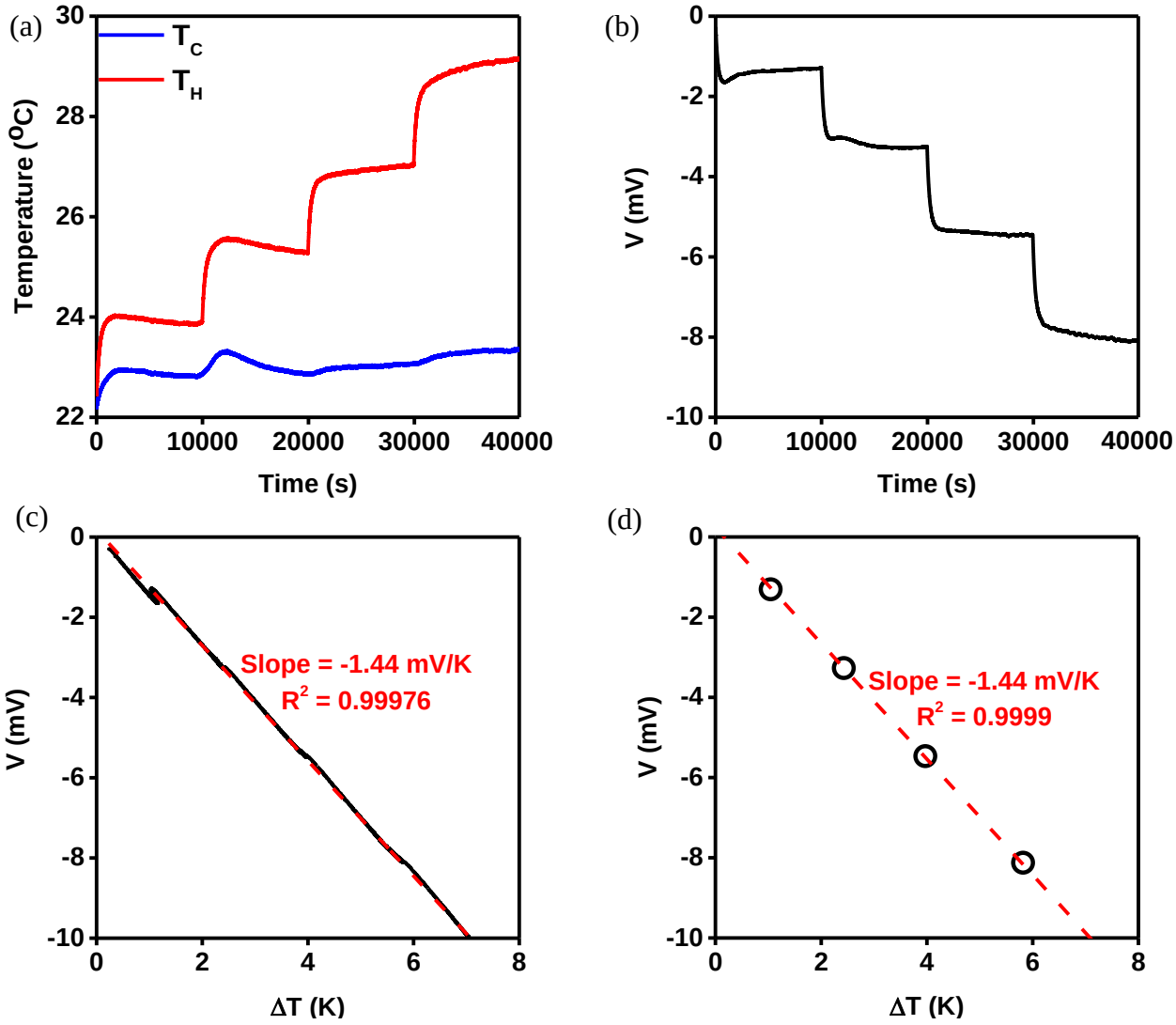

Figure 3.3. Calibration of the electrochemical thermopower characterization setup by 2.0 mM $Fe(CN)_6^{3-/4-}{}_{(aq)}$ redox-active electrolyte. (a) – (b) Time dependent temperature and voltage profiles detected at both ends of the testing cell. (c) Measured voltage as a function of the applied thermal gradient. (d) Relationship between the steady-state thermal gradients and the steady-state voltages. Both (c) and (d) exhibit the same slopes.

3.2.2. Electrochemical Thermopower Measurements under Isothermal Conditions

In order to identify electrochemical thermopowers and redox potentials of aqueous redox couples simultaneously, electrochemical thermopower measurements under isothermal conditions were executed. It could be conducted in two different ways: by monitoring open circuit voltage

(OCV) of the working electrode against a reference electrode or by running cyclic voltammetry (CV) measurements under different temperatures, for instance 20 °C, 30 °C, 40 °C, 50 °C, and 60 °C (**Figure 3.4** (a) – (b)). Both methods required a three electrode setup with a reference electrode (Ag/AgCl), a counter electrode (Pt), and a working electrode (Au) separately. Those 3 separate electrodes were immersed in the testing aqueous electrolyte, where redox-active species were dissolved, and either CV or OCV measurements at different temperatures were performed. Upon transition of a temperature to another, ample time should be permitted in order to match the internal temperature of the cell with the set temperature of the heat circulator pump (Thermo Scientific, model SC100). Then CV or OCV commenced to determine precise electrochemical potentials where redox reactions of the specimen solution occurred, along with the shift of those redox potentials by the temperature.

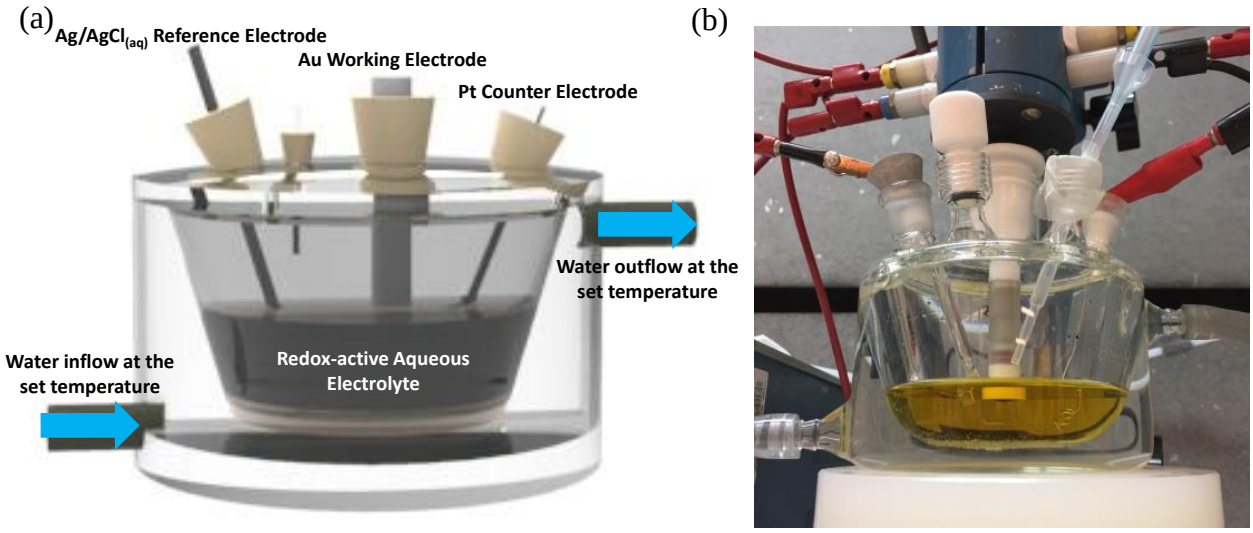

Figure 3.4. (a) A schematic and (b) a photograph of the electrochemical thermopower characterization setup under isothermal conditions. OCVs or redox peaks at CV measurements were monitored at different temperatures, for instance 20 °C, 30 °C, 40 °C, 50 °C and 60 °C. Electrochemical potentials of aqueous redox couples against a reference potential, and their dependencies on temperature were measured with these methods.

3.2.3. Chemical Pretreatments for K^+-Conducting Nafion

Nafion 115 (FuelCellStore.com, 591139) was firstly cut into a 3.5 × ~ 30 cm^2 sized rectangle and soaked in DI water at room temperature longer than 30 minutes. While the Nafion stayed in the DI water, 3 different solutions were prepared: (i) 3 wt% $H_2O_{2(aq)}$ from 30 wt% H_2O_2 aqueous solution (Fisher Chemical, H325-500), (ii) 1.0 M $H_2SO_{4(aq)}$ from concentrated sulfuric acid (Sigma-Aldrich, 95.0 % – 98.0 %, 258105), (iii) 1.0 M $KOH_{(aq)}$ from KOH pellet (Acros Organics, ≥ 99.98 % pellets, AC43713). The Nafion was soaked in the 3 wt% $H_2O_{2(aq)}$ and heated at ~ 100 °C for an hour. After this, it was briefly rinsed with flowing DI water at room temperature, and boiled in DI water at ~ 100 °C for another hour. Then it was transferred to 1.0 M $H_2SO_{4(aq)}$ and heated at ~ 100 °C for 2 hours. Thorough rinsing with DI water followed, and the last step was immersion in 1.0 M $KOH_{(aq)}$ at ~ 100 °C for an hour, succeeded by rinsing with DI water at room temperature. The completely processed K^+-conducting Nafion 115 was entirely submerged and stored in 1.0 M KCl (Sigma-Aldrich, ≥ 99 %, 793590) aqueous solution at room temperature. When the Nafion membrane was mounted in the electrochemical heat harvester, it was cut into ~ 3.5 × 3.5 cm^2 square shape from the 3.5 × ~ 30 cm^2 rectangle. The roles of the Nafion would be preventing internal short-circuit between the catholyte and the anolyte, while permitting ionic conduction necessitated by the redox reactions within the cell.

3.2.4. Characterization of Internal Resistances of the Electrochemical Heat Harvester

As internal resistance of the electrochemical heat harvester is proportional to E_{loss} term (the energy lost or unusable by internal resistance of the cell) the internal resistance can influence the conversion efficiency (Section 1.3.2). Electrochemical impedance spectroscopy (EIS) or galvanostatic discharges for less than 15 seconds were experimental techniques that quantified the internal resistance of the electrochemical heat harvester. EIS could inform individual resistance contributions from different parts of an electrochemical system, while galvanostatic discharge for a short duration could show combined Ohmic resistance of the cell. **Figure 3.5** (a) illustrates a setup to determine the internal resistance of the cell with either EIS or galvanostatic discharge or both. **Figure 3.5** (b) is exemplar overpotential data obtained by regular execution of galvanostatic discharge every hour. The cell assembly for the internal resistance examinations follow the same procedures listed in Section 3.2.7.

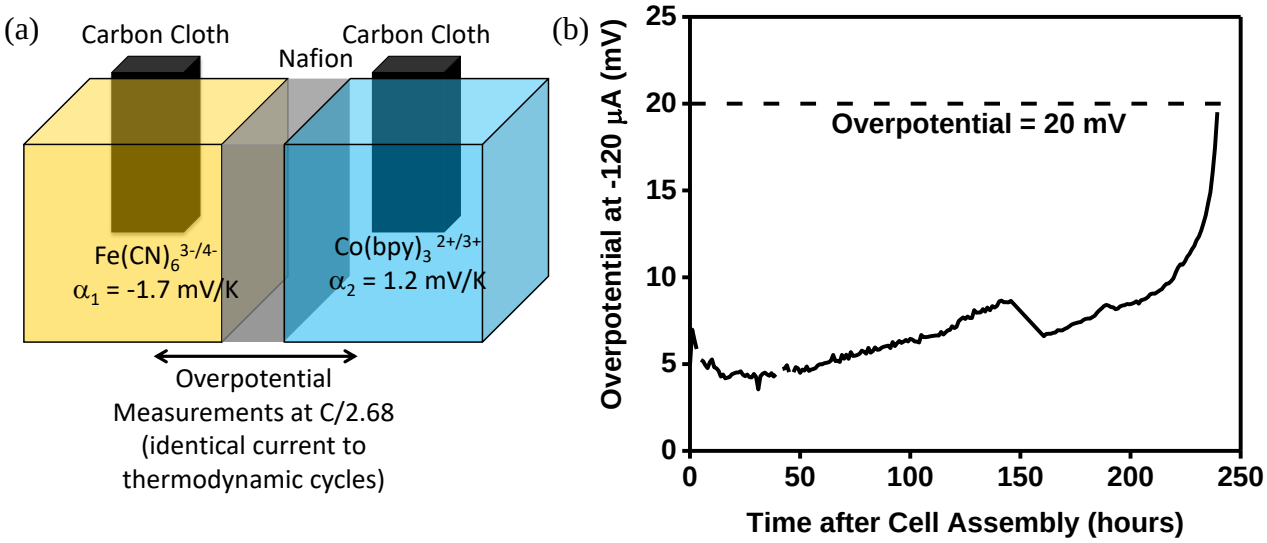

Figure 3.5. (a) The measurement scheme to observe variation of internal resistance of the cell over time. The cell used for this examination was the same as the cell for the thermodynamic cycling experiments. (b) An exemplar measurement result of overpotential (proportional to the internal resistance) of the cell. The internal resistance was checked every hour.

3.2.5. Spectroscopic Characterization Techniques

Both ultraviolet–visible spectroscopy (UV-Vis spectroscopy) and X–ray photoemission spectroscopy (XPS) were employed in order to distinguish of absorption of the aqueous redox-active species into Nafion membrane. An additional function of the UV-Vis spectroscopy was verification of the self-decomposition of the redox-active species.

UV-Vis spectroscopy (Agilent, model Cary 5000) was deemed suitable to determine whether aqueous redox-active species were absorbed into Nafion membranes in a bulk scale. As all of the solutions dissolving redox-active species had distinct colors, they were expected to exhibit absorption within visible light range. Upon absorption of some of those colored chemicals in Nafion, then it would be detectable because pristine Nafion is transparent at visible light region[12]. Also upon chemical degradation of any redox-active chemicals, it would be easily detectable, if the colors of the innate redox-active species mutated as a result of the damage.

XPS (Thermo Scientific, model K-Alpha+) was introduced to identify the remnant chemical species on the surface of Nafion, so that absorption process initiating from the surface of

Nafion membranes could be tracked. Its great sensitivity on the surface chemical species[13] can be helpful for more delicate recognition of absorption of redox active species into the Nafion. Especially when the diffusion is limited only at the surface, XPS becomes necessary.

3.2.6. Polyelectrolyte Film Deposition on Nafion via LbL Process

The polyelectrolyte deposition procedures were conducted by LbL process throughout this study. This procedure involves repetitive dips of a substrate into two separate solutions dissolving two oppositely charged polyelectrolytes respectively. The LbL processes often exploit Coulombic binding between two oppositely charged polymeric ions[14]. Polarity of surface charge is reversed after each immersion step, enabling adsorption of the oppositely charged polyelectrolyte[15]. This adsorption-based process can serve as a thin film coating technique on a surface. Because Nafion is negatively charged[16-18], the LbL process always began with cationic polyelectrolyte adsorption on the bare surfaces of the Nafion membranes.

The polyelectrolyte species in this study have different mechanisms of dissociation; for a weak polyelectrolyte poly(allylamine hydrochloride) cation (PAH^+), it needs to accept proton from the LbL solution in order to dissociate and have the positive charge. Therefore, pH of the LbL solution is an important factor to determine effectiveness of coatings using PAH^+. However, for other polyelectrolytes such as poly(diallyldimethylammonium chloride) cation ($PDADMAC^+$) and polystyrene sulfonate anion (PSS^-) do not require any acceptance of H^+ or OH^- from the solution. Thus, they are categorized as strong polyelectrolytes, because their dissociation is not affected by pH[19-22].

For this reason, for deposition of a film composed of PAH^+ and PSS^-, control variables included pH, supporting salt concentration, and repetition of the LbL process (**Figure 3.6**). For deposition of a film composed of $PDADMAC^+$ and PSS^- (**Figure 3.7**), control parameters were only supporting salt concentration and repetition of the LbL process, because dissociation of both $PDADMAC^+$ and PSS^- would hardly be affected by pH.

LbL process began with preparation of the deposition solution. PAH^+ (Aldrich, average M_w ~17,500, 283215), PSS^- (Aldrich, average M_w ~70,000, 243051), $PDADMAC^+$ (Aldrich, average M_w 200,000 – 350,000 20 wt% in water, 409022) polysalts were mixed with DI water (18.2 MΩ·cm at room temperature) in 20 mM concentrations, respectively. Then supporting salt,

anhydrous NaCl (Sigma-Aldrich, ≥ 99 %, 793566) was added with a desired amount into the aqueous polyelectrolyte solutions. After this step, pH was adjusted by adding HCl (Sigma Aldrich, 37 %, 258148) or anhydrous NaOH (Sigma Aldrich, ≥ 97 %, 795429). After thorough stirring for more than 10 minutes at room temperature, pH was checked by a pH meter prior to the very first dip of Nafion membrane.

As-prepared Nafion membrane (Section 3.2.3) was dipped firstly in a polycation solutions (PAH^+ solution or $PDADMAC^+$ solution) for 5 minutes and washed for 30 seconds in DI water to remove the residual polycations from the surface. Then the Nafion was immersed into PSS^- solution for 5 minutes again, and rinsed again in DI water. This set of processes was repeated until desired number of repetitions was reached. After the last washing in DI water at the end of all LbL procedures, water on the surface of the Nafion was removed by shaking and it was mounted between the two rubber sheets (Section 3.2.7).

In order to convey the film composition more simply, a special notation was introduced. It clarifies sequences of the polyelectrolyte film deposition. For example, if a notation was represented as $(PAH^+/PSS^-)_{3.5}$, then the process of (PAH^+ coating – DI water washing – PSS^- coating – DI water washing) was repeated for 3 times and finalized by PAH^+ coating – DI water washing. Therefore, the termination of the film composition would be PAH^+, because the last step was deposition of the PAH^+ layer.

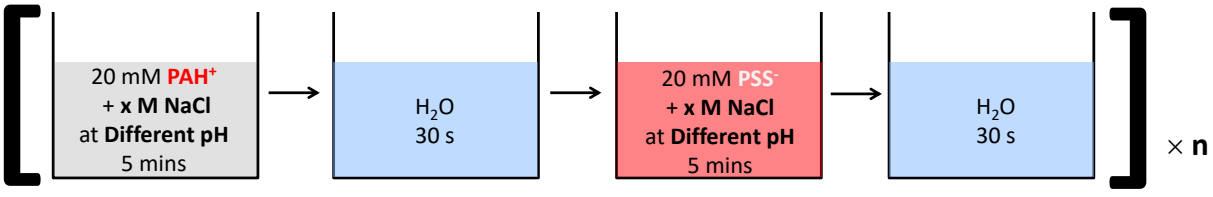

Figure 3.6. Procedures for coating of PAH^+ cation and PSS^- anion on Nafion membrane through LbL deposition. pH, number of repetition and supporting salt concentration (concentration of NaCl, denoted as [NaCl]) were selected control variables to optimize the $(PAH^+/PSS^-)_n$ film on the Nafion for selective filtration of $Co(bpy)_3^{2+/3+}$ species.

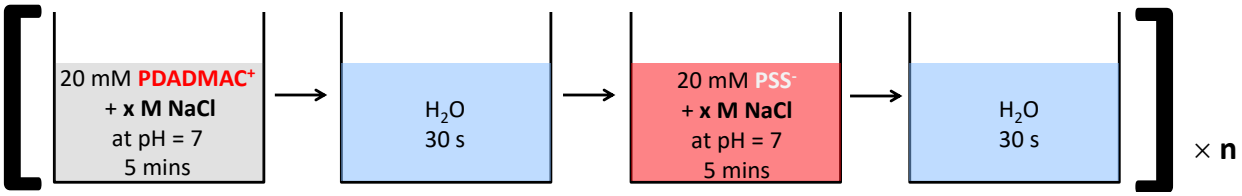

Figure 3.7. Procedures for coating of $PDADMAC^+$ cation and PSS^- anion on Nafion membrane through LbL deposition. Number of repetition and supporting salt concentration (concentration of NaCl, denoted as [NaCl]) were chosen as control variables to optimize the $(PDADMAC^+/PSS^-)_n$ coating for selective exclusion of $Co(bpy)_3^{2+/3+}$ species.

3.2.7. Fabrication of the Electrochemical Heat Harvester

The catholyte and the anolyte composed of 1:1 60 mM equimolar concentrations were prepared. Thus, $Co(bpy)_3Cl_2{\cdot}5H_2O$ (Dyenamo, DN-C15) along with $Co(bpy)_3Cl_3{\cdot}4H_2O$ (Dyenamo, DN-C16) were dissolved in DI water with 60 mM concentrations each. This means that both 60 mmol of $Co(bpy)_3^{2+}$ and 60 mmol of $Co(bpy)_3^{3+}$ coexist in 1.0 L of the anolyte. The notation for this solution is $Co(bpy)_3^{2+/3+}{}_{(aq)}$ throughout this article. Likewise, $K_3Fe(CN)_6$ salt together with $K_4Fe(CN)_6{\cdot}3H_2O$ powder were dissolved in DI water in 60 mM concentrations each, within a single solution. This means that both 60 mmol of $Fe(CN)_6^{3-}$ and 60 mmol of $Fe(CN)_6^{4-}$ coexist in 1.0 L of the catholyte. $Fe(CN)_6^{3-/4-}{}_{(aq)}$ is the notation for this solution in this article. Unless noted otherwise, the concentrations of both the anolyte and the catholyte were consistently 60 mM during this study. Those two separate electrolytes were homogenized in an ultrasound sonication bath for 5 minutes at room temperature.

Carbon cloth electrodes were selected in this work as a current collector and a template to foster fast electrochemical reactions simultaneously (**Figure 3.8** (b)). As the carbon cloth is light, inexpensive, electronically conductive, chemically stable, and owns a high surface area, it was considered an optimal electrode material. A carbon fabric (FuelCell.com, model EC-CC1-060) was cut into a shape with 1.0 × 1.0 cm^2 square active area with an attached 0.5 × 3.0 cm^2 rectangular tale. The 1.0 × 1.0 cm^2 square active area was intended as a place for the redox reactions, while the adherent 0.5 × 3.0 cm^2 rectangular tale served as a current collector. Only the square active areas were oxidized by oxygen plasma at 200 W for a minute (Glow Research,

AutoGlow Plasma Cleaner and Asher) or briefly contacting flame from burning butane gas, to facilitate wetting by the electrolytes. As the tales at carbon electrodes were purely dedicated to electrical conduction, thus hydrophobic coating by polystyrene dissolved in toluene (Sigma-Aldrich, 244511) on the tail area were carried out. By this process, wetting by the electrolytes could be only restricted to the 1.0 × 1.0 cm^2 active area.

A chemically inert fluoropolymer elastomer, Viton rubber sheets were chosen to accommodate carbon cloth electrodes and a Nafion membrane (**Figure 3.8** (b)). A square hole (1.0 × 1.0 cm^2) per a sheet at the center was perforated. This square hole offered a place for carbon electrodes and the electrolyte to contact each other. For the watertight assembly of the cell, holes were penetrated.

Transparent covers, cut from a polypropylene plastic sheet (McMaster Carr, product 8742K131) with holes for the electrolyte injection were also prepared. Injection holes had diameters less than 3 mm. The transparency allowed confirming if the oxidized carbon electrode surface was wet by the inserted electrolytes. For the watertight assembly of the cell, holes to accommodate bolts and nuts were penetrated.

After all parts for the cell were prepared, then both carbon cloth electrodes were placed in the square voids in the Viton rubber sheets. Then the transparent plastic covers capped each rubber sheet with carbon electrode at the center hole. Nafion was then put in between the rubber sheets, so that it can separate a carbon electrode from the other. After sandwiching all the parts, they were fixed tightly together by the bolts and nuts. Lastly, the prepared electrolytes were injected (**Figure 3.8** (c)), and airtight tape was attached to prevent evaporation through the injection holes.

(a)

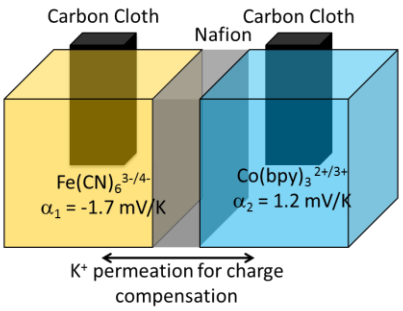

(b)

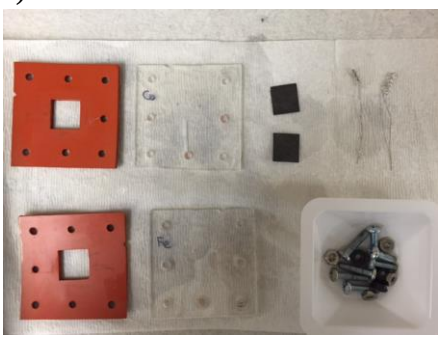

(c)

Figure 3.8. (a) Schematics of the designed aqueous redox couple-based electrochemical heat harvester. (b) The parts for fabrication of the watertight electrochemical heat harvester. (c) A front view of the completely assembled electrochemical heat harvester.

3.2.8. Thermodynamic Cycling Measurements

The measurement started with putting the assembled cell (shown in **Figure 3.8** (c)) in a watertight, opaque, electrically insulating, but thermally conductive heat-sealable plastic bag (Aldrich, Z183385). No light and water from the heat circulator pump were allowed to invade the cell, while the cell could be promptly affected by the surrounding temperature.

Firstly, the cell in the bag was immersed in a water tank, of which temperature was set at 20 °C (**Figure 3.9** (a)). + terminal of a Biologic (model SP300 or VSP300) potentiostat was connected to $Fe(CN)_6^{3-/4-}{}_{(aq)}$ side, and – terminal was assigned to $Co(bpy)_3^{2+/3+}{}_{(aq)}$ side. The initial OCV of the cell typically ranged around +100 mV at 20 °C. Then it firstly underwent a galvanostatic (constant current) discharge with a current density corresponding to C/2.68, until the cell voltage became zero at 20 °C (step (i) in **Figure 3.9** (b) – (c)). The C/2.68 notation means 2.68 hours are needed to fully discharge or charge the theoretical charge capacity of the cell. Then the cell in the bag was transferred to a 60 °C environment controlled by the heat circulator pump at open circuit condition. By this step, the cell could absorb heat from the surroundings and convert part of the heat input into electrical energy (step (ii) in **Figure 3.9** (b) – (c)). The conversion of the heat could be confirmed by shift of OCV of the cell at this step toward the negative direction. This phenomenon was caused by shift in electrochemical equilibrium by the temperature variation, which led to thermally harnessed voltage. Step (iii) in **Figure 3.9** (b) – (c) was another galvanostatic discharge at 60 °C under the same absolute current density with opposite sign as step (i). This step lasted until the cell voltage became zero again. It is remarkable that the polarity of the cell was flipped during the thermodynamic cycle. The last step (step (iv) in **Figure 3.9** (b) – (c)) was another thermal recuperation stage. Therefore, the entire cell was turned back to 20 °C at open circuit condition, and the cell voltage was recovered to positive. The end of step (iv) returned the thermodynamic state of the cell into onset of step (i). Thus, step (i) – step (iv) successfully consisted a complete thermodynamic cycle.

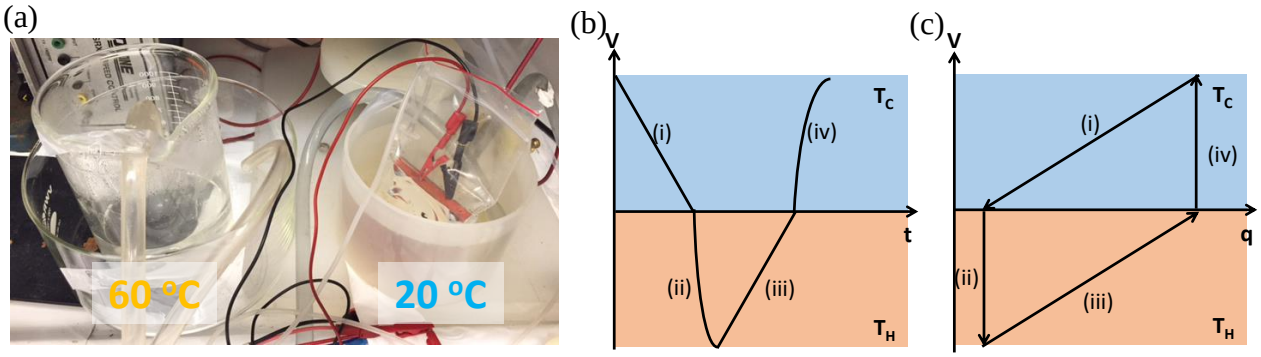

Figure 3.9. (a) A photograph of the setup for the heat harvesting thermodynamic cycle experiments. The entire cell was transferred between two different temperatures regularly, in this case between 20 °C and 60 °C. (b) – (c) Schematic illustrations indicate how the state of the electrochemical heat harvester would vary, during an exemplar thermodynamic cycle.

3.3. Results and Discussion

3.3.1. Electrochemical Potential Dependence on Temperature for Aqueous Redox Couples for Electrochemical Heat Harvester Application

In order to find aqueous redox couples which satisfy the requirements offered in Section 1.3.3, electrochemical redox potentials of several candidate redox couples and their dependency on temperature were measured. As can be seen **Figure 3.10** (a), the only redox pairs with half-cell potential crossing in the examined temperature range were $Fe(CN)_6^{3-/4-}{}_{(aq)}$ and $Co(bpy)_3^{2+/3+}{}_{(aq)}$, among the 6 tested aqueous redox couples. Their half-cell potentials were enlarged in **Figure 3.10** (b), indicating intersection happened around 40 °C. In order to match this meeting point as the midpoint of operating temperature range of the electrochemical heat harvester, the operating temperature range was selected as 20 °C – 60 °C. This temperature range was largely free from unwanted side effects, such as volatile evaporation of water. The opposite signs of electrochemical thermopowers (**Figure 3.10** (b)) were synergistic, enhancing the electrochemical thermopower of the full cell to addition of both, -2.9 mV/K (Equation 1.14). In sum, all requisites listed in Section 1.3.3 for design of an autonomous electrochemical heat harvester were fulfilled.

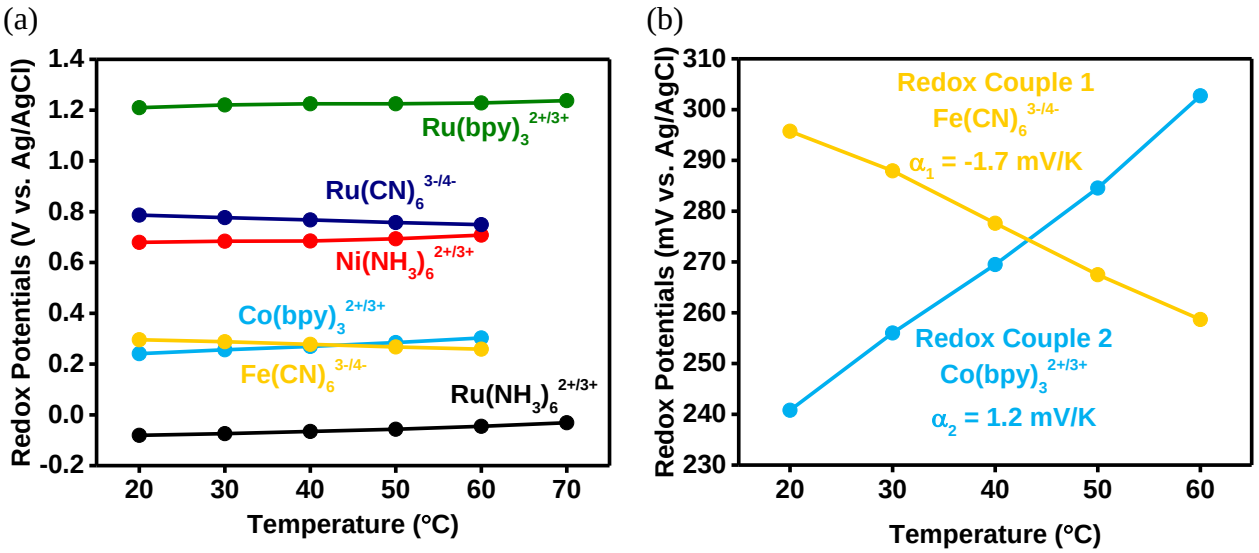

Figure 3.10. (a) Temperature-dependent electrochemical potentials of several aqueous redox couples vs. Ag/AgCl reference electrode. The counter electrode consistently used for these measurements was cleaned Pt wire. (b) A magnified view of temperature-dependent half-cell

electrochemical potentials of $Fe(CN)_6^{3-/4-}{}_{(aq)}$ and $Co(bpy)_3^{2+/3+}{}_{(aq)}$. The slopes of half-cell potentials are electrochemical thermopowers: -1.7 mV/K for $Fe(CN)_6^{3-/4-}{}_{(aq)}$ and +1.2 mV/K for $Co(bpy)_3^{2+/3+}{}_{(aq)}$. Because their half-cell potentials meet around 40 °C, 20 °C to 60 °C were selected as the operating temperature range.

3.3.2. Nafion as an Indispensable Component of the Electrochemical Heat Harvester

As aqueous $Co(bpy)_3^{2+/3+}{}_{(aq)}$ and $Fe(CN)_6^{3-/4-}{}_{(aq)}$ species were chosen to build the electrochemical heat harvester, it became critical to prevent the internal short-circuit by mixing the catholyte and the anolyte. In order to accomplish this requirement, the watertight separator would be needed. On the other hand, such separator should be able to transport non-redox active species through it, in order to compensate change in charge states during the redox reactions. As the designed electrochemical heat harvester would contain K^+, Cl^-, $Co(bpy)_3^{2+}$, $Co(bpy)_3^{3+}$, $Fe(CN)_6^{3-}$ and $Fe(CN)_6^{4-}$, either only K^+ cation or only Cl^- anion should be transported across the separator. If redox-active species would be transported across the separator, then it would lead to short-circuit or serious decay in the charge capacity over time.

Such requirement may be fulfilled by two categories of materials: ion exchange membrane, and ceramic ionic conductors. The ceramic ionic conductors include a wide range of crystals, such as NASICON[23,24], β-alumina[25,26], or inorganic solid Li ion conductors[27,28]. However, their ionic conductivity would be low, of which maximum ranges around 10^{-2} S/cm[27,29-33]. This low ionic conductivity in turn would increase the internal resistance of the cell, leading to larger E_{loss} term, hence drag down efficiency by Equation 1.13.

Alternative candidates are cationic or anionic selective membranes. Among them, Nafion was deemed best, not only because of its cation selective conduction[17,18], but also because of its high ionic conductivity reaching up to 10^{-1} S/cm[34]. Especially this high cationic conductivity was expected to minimize additional internal resistance of the cell, thereby limiting E_{loss} term in Equation 1.13. However, usage of Nafion also created a concern; whether cationic $Co(bpy)_3^{2+/3+}{}_{(aq)}$ species would be conducted through it to lead to short-circuit or decay in charge capacity overtime. Thus, this potential issue and solution to it will be explored.

3.3.3. Solubility Limit of $Co(bpy)_3^{2+3/+}$ Species in Water

For this flow-battery type electrochemical heat harvester explored in this research, solubility of the redox-active species would govern how much charge can be stored in the cell. This would in turn influence charge and energy density of the device. A previous investigation suggested that solubility limit of $Fe(CN)_6^{3-/4-}$ could reach beyond 0.3 M in water[6]. In comparison, the solubility limit for $Co(bpy)_3^{2+/3+}{}_{(aq)}$ turned out to be around 60 mM in water at room temperature. For this reason, the concentration of $Fe(CN)_6^{3-/4-}{}_{(aq)}$ was also restricted to 60 mM; otherwise, the temperature where half-cell redox potentials met would be shifted significantly[6]. This would cause shift in operating temperature range, and the new temperature range may be impractical for the waste heat harnessing purpose.

3.3.4. Degradation of Ionic Conductivity of Nafion by $Co(bpy)_3^{2+/3+}$ Absorption

All the key components of the electrochemical heat harvester were chosen. Thus, examinations if their combination would not bring issues were necessary. One of the concerned aspects was interaction among the catholyte, the anolyte and Nafion membrane in unwanted manners. Firstly, issues from combinations of the anolyte and Nafion, and the catholyte and Nafion were checked respectively. The possible issues of the selected redox-couples themselves will be explored later. Symmetric cells were fabricated with Nafion membranes in them, having configurations of 60 mM $Co(bpy)_3^{2+/3+}{}_{(aq)}$ | K^+-conducting Nafion 115 | 60 mM $Co(bpy)_3^{2+/3+}{}_{(aq)}$ and 60 mM $Fe(CN)_6^{3-/4-}{}_{(aq)}$ | K^+-conducting Nafion 115 | 60 mM $Fe(CN)_6^{3-/4-}{}_{(aq)}$, individually (**Figure 3.11** (a)). The architecture and assembly process followed the procedures explained in Section 3.2.7. EIS was adopted to characterize internal resistance of the cell over time at room temperature.

Figure 3.11 (b) demonstrates that internal resistance of the cell containing $Co(bpy)_3^{2+/3+}{}_{(aq)}$ and Nafion grows over time with, whereas the other cell incorporating $Fe(CN)_6^{3-/4-}{}_{(aq)}$ and Nafion keeps low and constant internal resistance profile for at least 24 hours. The invariant resistance of the $Fe(CN)_6^{3-/4-}{}_{(aq)}$ cell indicate that interaction between the Nafion and $Fe(CN)_6^{3-/4-}{}_{(aq)}$ did not incur any ionic conductivity degrading mechanism. In the contrast, the higher initial and increasing resistance from the combination of $Co(bpy)_3^{2+/3+}{}_{(aq)}$ and Nafion can be attributed to either (i) malignant interactions between $Co(bpy)_3^{2+/3+}{}_{(aq)}$ and Nafion, or (ii) sluggish ionic conduction of

$Co(bpy)_3^{2+/3+}$ species through cation conducting channels within Nafion[16-18] or (iii) slow diffusion of large and heavy $Co(bpy)_3^{2+/3+}$ cation in water. However, there was only one combination of the redox-active species which fulfilled the criteria to build the autonomous electrochemical harvester (**Figure 3.10** (a) – (b)). Because the replacement of $Co(bpy)_3^{2+/3+}$ is impossible in this case, possibility (ii) and (iii) were not regarded; instead, only the possibility (i) will be focused.

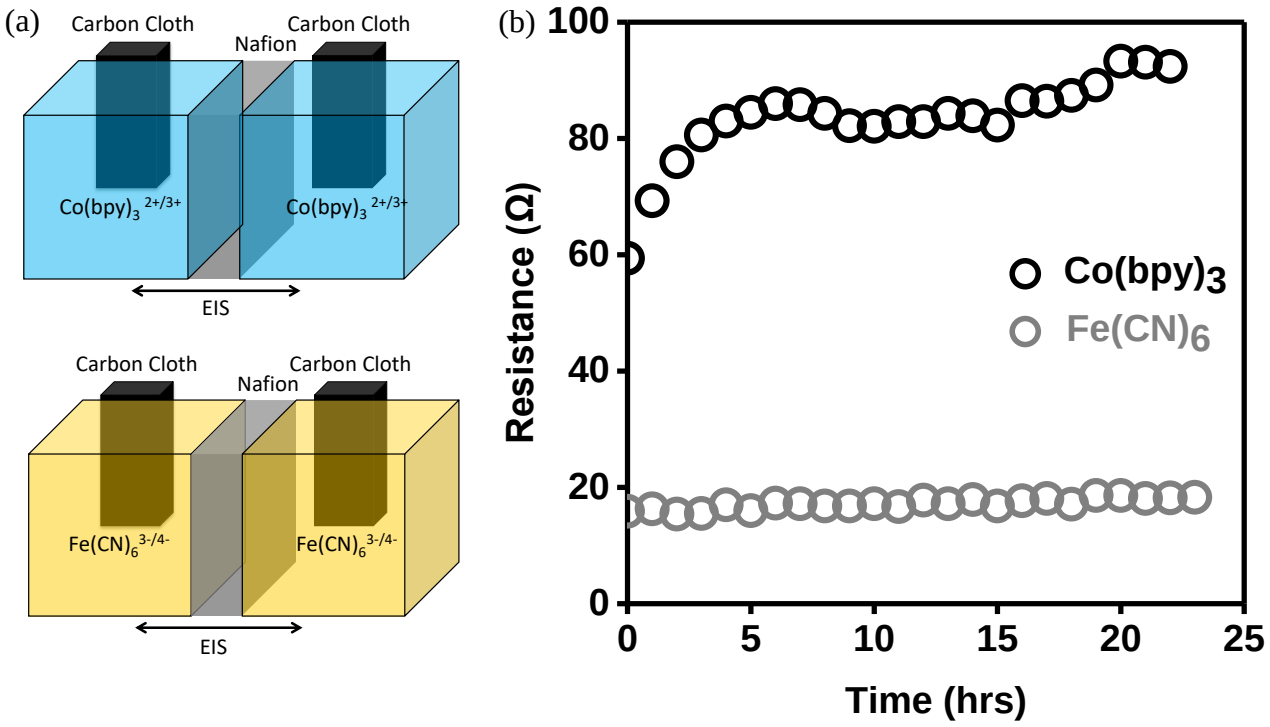

Figure 3.11. (a) An experimental scheme to identify origin of increase in internal resistance. (a) Cells consist of the pure catholyte or the pure anolyte separated by Nafion membranes in between the identical compartments. (b) Growth of internal resistance of the symmetric cells over time.

The distinction on true origins of degradation in ionic conductivity among $Co(bpy)_3^{2+/3+}{}_{(aq)}$ and Nafion became necessary. Also, sorting out if the ionic conductivity damaging mechanism was chemical or electrochemical would be helpful to develop countermeasures for this drawback.

For this reason, the K^+-permeating Nafion membranes were thoroughly immersed into 60 mM $Fe(CN)_6^{3-/4-}{}_{(aq)}$ and 60 mM $Co(bpy)_3^{2+/3+}{}_{(aq)}$ solutions respectively for 24 hours at room temperature, under dark condition, in order to avoid possible photodecomposition or thermal

decomposition of the redox-active species (**Figure 3.12**). As can be seen from **Figure 3.12**, only the Nafion membrane soaked in the $Co(bpy)_3^{2+/3+}{}_{(aq)}$ solution exhibited discoloration, while the one stored in the $Fe(CN)_6^{3-/4-}{}_{(aq)}$ solution stayed transparent. The discoloration of $Co(bpy)_3^{2+/3+}{}_{(aq)}$–soaked Nafion could not be reversed even by a vigorous washing with DI water for several minutes. These observations imply either (i) $Co(bpy)_3^{2+/3+}$ species were tightly bound to the Nafion or (ii) $Co(bpy)_3^{2+/3+}$ species and the Nafion underwent chemical reactions to produce wholly new chemical compounds.

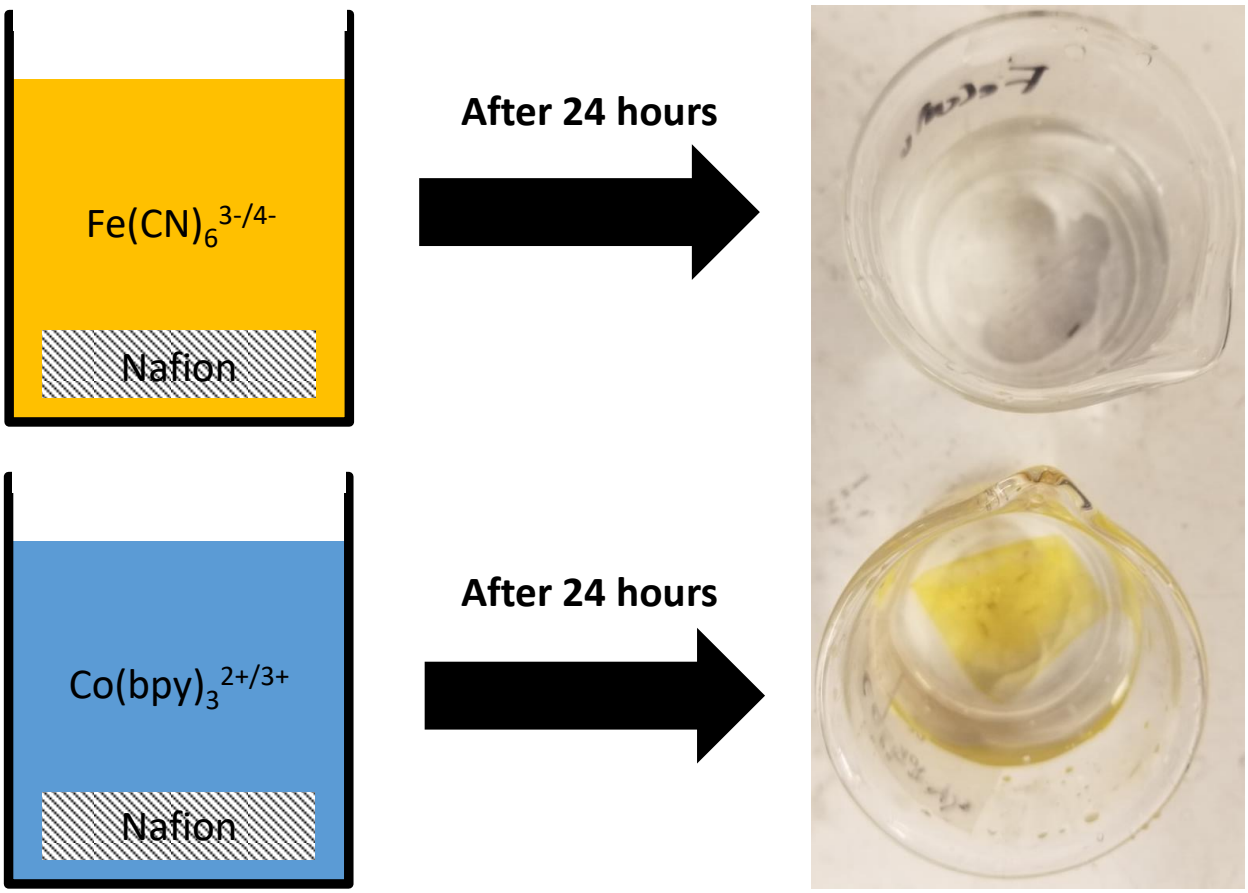

Figure 3.12. Colors of Nafion after 24 hours of dipping into 60 mM $Fe(CN)_6^{3-/4-}{}_{(aq)}$ and 60 mM $Co(bpy)_3^{2+/3+}{}_{(aq)}$, respectively. Even subsequent washing by DI water could not revert the discoloration from the $Co(bpy)_3^{2+/3+}{}_{(aq)}$ solution-soaked Nafion membrane. $Fe(CN)_6^{3-/4-}{}_{(aq)}$ solution-soaked Nafion membrane maintained its initial transparency.

The Nafion membranes shown in **Figure 3.12** were further examined with EIS technique. By this, the relation between the discoloration phenomenon and the electrochemical resistance could be tracked in **Figure 3.13**. In order to exclude side effects from $Fe(CN)_6^{3-/4-}{}_{(aq)}$ and $Co(bpy)_3^{2+/3+}{}_{(aq)}$, the anolyte and the catholyte was replaced into $KCl_{(aq)}$ with the same 60 mM concentration (the inset of **Figure 3.13**). Other cell configurations were preserved the same.

Figure 3.13 clarified the origin of the impaired ionic conductance. The K^+-conducting Nafion membranes dipped in the anolyte and the catholyte for a short period of time (5 minutes) maintained high ionic conductivity profile, similar to that of a pristine K^+-conducting Nafion membrane. However, Nafion membranes dipped for 24 hours exhibited largely differed ionic conductivity. The $Co(bpy)_3^{2+/3+}{}_{(aq)}$–soaked Nafion membrane exhibited much worse ionic conduction property, whereas the $Fe(CN)_6^{3-/4-}{}_{(aq)}$–soaked Nafion was virtually unaffected. This means the rises in the internal resistance of the cell was triggered due to the irreversible discoloration of the Nafion by $Co(bpy)_3^{2+/3+}{}_{(aq)}$. The mechanism for this process was chemical, not electrochemical.

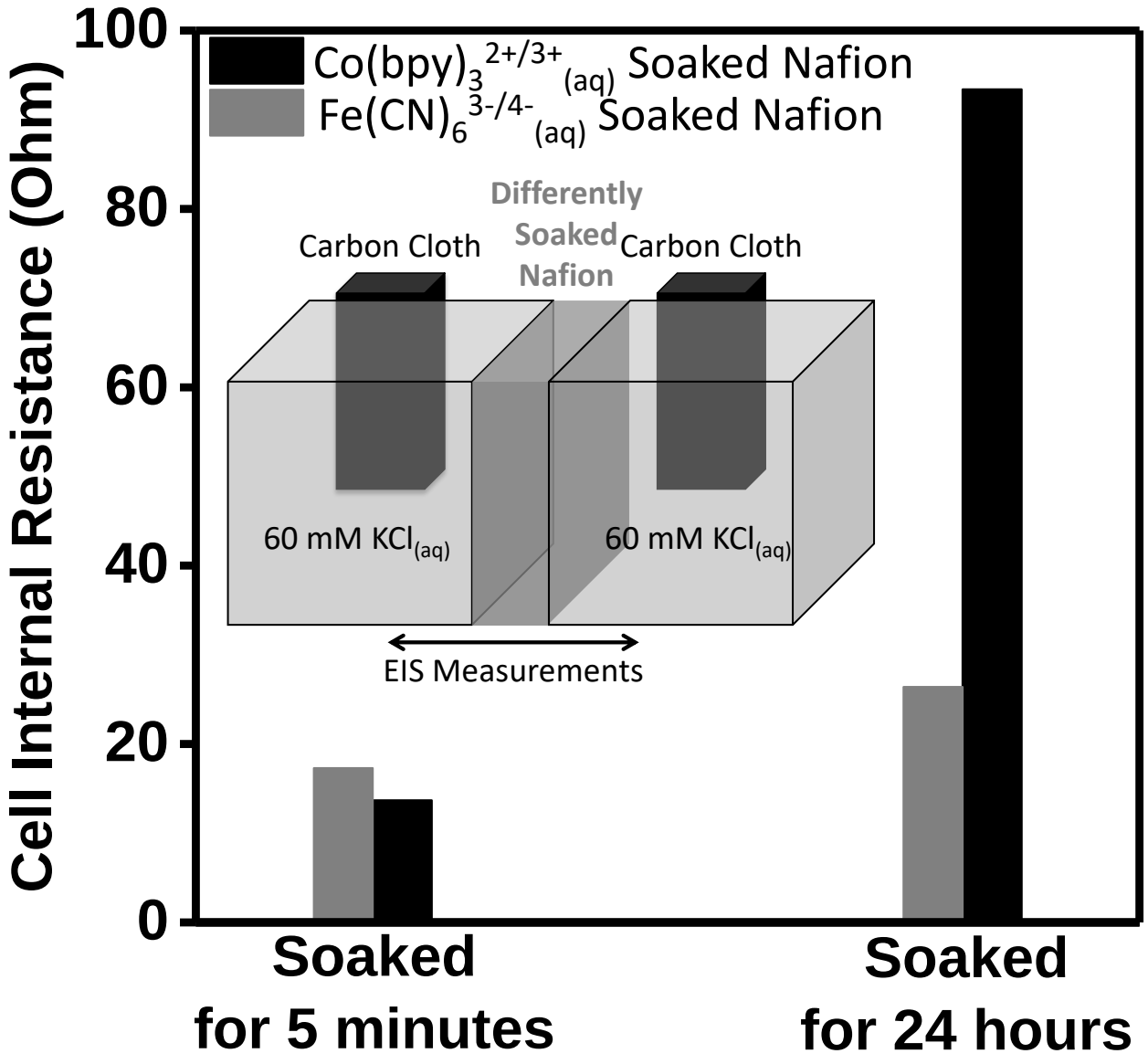

Figure 3.13. Internal resistances of the symmetric cells consisting of differently soaked Nafion membranes and 60 mM $KCl_{(aq)}$ solution.

The chemical aspects of the discoloration mechanism were explored deeper through the UV-Vis spectroscopy, as all of the aqueous solutions of the individual redox chemicals, namely $Co(bpy)_3Cl_2$, $Co(bpy)_3Cl_3$, $K_3Fe(CN)_6$, and $K_4Fe(CN)_6$ displayed distinct colors. Therefore, strong absorptions of visible light range were expected for all of the solutions dissolving them. Intensities of absorption and onsets of the absorption wavelength can serve as fingerprints of each redox-active chemical species in water. Therefore, if $Co(bpy)_3^{2+/3+}$ were absorbed into Nafion intactly,

the absorption pattern of $Co(bpy)_3^{2+/3+}{}_{(aq)}$–soaked Nafion would be very similar to those of $Co(bpy)_3Cl_{2(aq)}$ or $Co(bpy)_3Cl_{3(aq)}$ solutions. Moreover, if onset or the intensity the absorption shift, chemical deformation of either $Co(bpy)_3Cl_2$ or $Co(bpy)_3Cl_3$ species or both can be suggested. Different chemical species often possess different discrete quantum mechanical energy levels, and therefore the energy gaps between them would be also dissimilar. This in turn would result in modification in light-induced transition behaviors, including the light absorption.

Figure 3.14 (a) displays reference absorption spectra of $Co(bpy)_3Cl_{2(aq)}$, $Co(bpy)_3Cl_{3(aq)}$, $K_3Fe(CN)_{6(aq)}$, and $K_4Fe(CN)_{6(aq)}$, all with 60 mM concentrations in water. These solutions were contained in zero absorption cuvettes, in order to solely perceive the absorption by the solutions. Disparate onsets of the absorption for all reference spectra within visible light range were confirmed, proposing that the outsets can function as unique fingerprints of each chemical. These absorption patterns were compared with the absorption behaviors of differently soaked Nafion membranes (**Figure 3.14** (b)). Noises in the absorption spectra around 250 nm – 500 nm were likely due to the scratches on the surfaces of testing cuvettes. Only the $Co(bpy)_3^{2+/3+}{}_{(aq)}$–soaked Nafion absorbed the incident light at violet to near UV range, while both the pristine K^+-conducting Nafion and the $Fe(CN)_6^{3-/4-}{}_{(aq)}$–soaked Nafion were transparent between 250 nm – 800 nm wavelength range. This is in accordance to the results in **Figure 3.12**, but this time more quantifiable. It is remarkable that the beginning of the absorption for the $Co(bpy)_3^{2+/3+}{}_{(aq)}$–soaked Nafion differed from those of $Co(bpy)_3Cl_{2(aq)}$ and $Co(bpy)_3Cl_{3(aq)}$. This indicates $Co(bpy)_3Cl_{2(aq)}$ or $Co(bpy)_3Cl_{3(aq)}$ underwent chemical changes that shifted the onset of absorption.

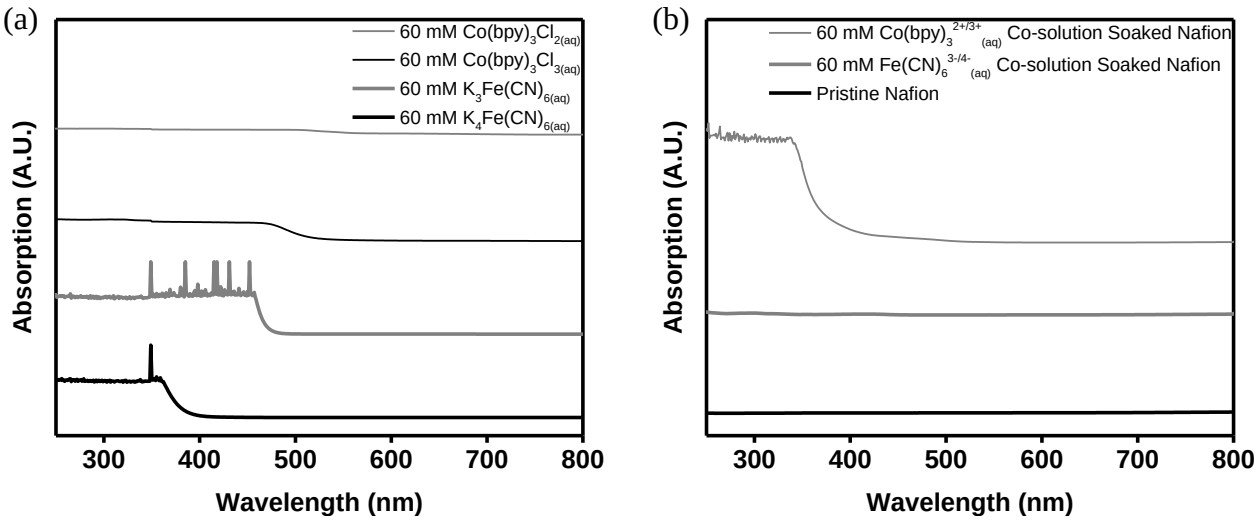

Figure 3.14. (a) Reference absorption spectra of 60 mM solutions of individual redox active species, namely 60 mM $Co(bpy)_3Cl_{2(aq)}$, 60 mM $Co(bpy)_3Cl_{3(aq)}$, 60 mM $K_3Fe(CN)_{6(aq)}$, and 60 mM $K_4Fe(CN)_{6(aq)}$ in UV-Vis wavelength range. (b) Absorption patterns of Nafion membranes with different soaking conditions in UV-Vis wavelength range. Discoloration of $Co(bpy)_{3(aq)}$ solution-immersed Nafion was qualitatively demonstrated.

In order to supplement the bulk-sensitive UV-Vis spectroscopy, surface sensitive XPS measurements were carried out on the same samples. XPS could offer greater sensitivities about the existence and oxidation states of the chemical species on the surface of Nafion. As a prerequisite for absorption is diffusion, and the diffusion begins from the surface of Nafion, the $Co(bpy)_3^{2+/3+}$ species would leave signature on the Nafion surface. Even though XPS alone could not specify what chemical compounds were produced during the $Co(bpy)_3^{2+/3+}{}_{(aq)}$ absorption into Nafion, it could affirm if $Co(bpy)_3^{2+/3+}$ and their damaged forms shifted oxidation states. Whether Co-containing species truly discolored Nafion could be also checked by XPS, as all elements possess characteristic binding energy ranges, which could serve as their unique identifications.

Figure 3.15 (a) – (b) represent reference XPS spectra of $Co(bpy)_3Cl_2$, $Co(bpy)_3Cl_3$, $K_3Fe(CN)_6$, and $K_4Fe(CN)_6$, all in powder form. Those powders were thoroughly ground with mortar and pestle before mounting, and tightly affixed to the sample stage by conductive carbon tapes, so that they do not displace during the vacuuming process. Fe 3s and Co 3s were selected, because their primary XPS regions (Fe 2p and Co 2p) exhibit multiple emissions from a single oxidation state[35]. This phenomenon was deemed to complicate the analyses of the spectra. Weak intensities from those non-primary photoemission ranges were compensated by slower scan rate and larger numbers of repeated scans. The reference spectra from the powder samples were compared with XPS spectra of 60 mM $Co(bpy)_3^{2+/3+}{}_{(aq)}$–soaked Nafion and 60 mM $Fe(CN)_6^{3-/4-}{}_{(aq)}$–soaked Nafion at **Figure 3.14** (a) – (b). Only the $Co(bpy)_3^{2+/3+}{}_{(aq)}$–soaked Nafion showed remnant Co species on the surface, while the $Fe(CN)_6^{3-/4-}{}_{(aq)}$–soaked Nafion did not contain any residual Fe species on its surface. These data were consistent with remarks from **Figure 3.12** and **Figure 3.14**. The slight shift in the peak from Co species on the Nafion surface was observed, compared to the reference spectra of $Co(bpy)_3Cl_2$ and $Co(bpy)_3Cl_3$.

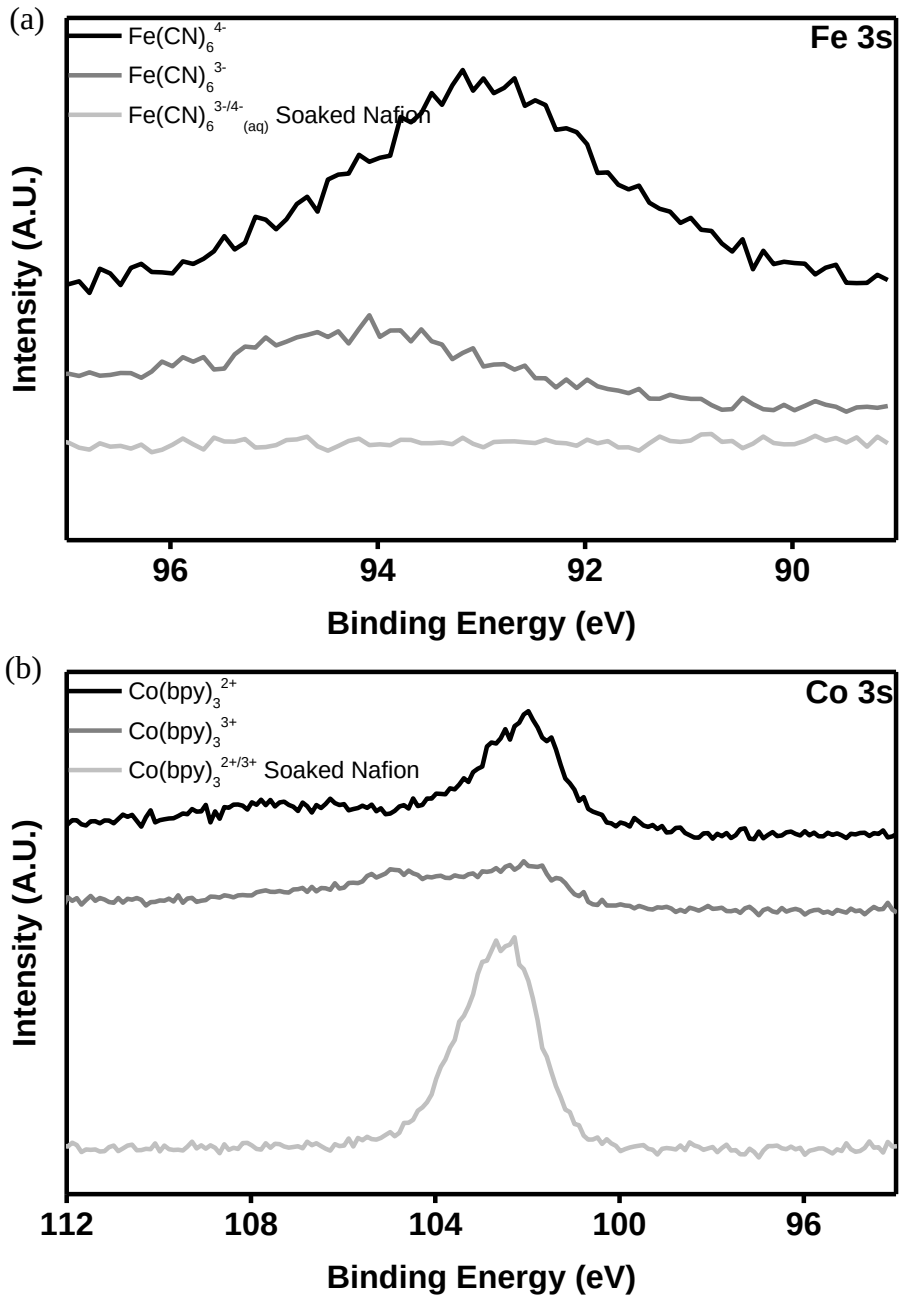

Figure 3.15. As absorption began from the surface of Nafion, surface sensitive XPS could be considered a valid technique to prove the trace of the absorption, if any. 3s peaks of Fe and Co were selected despite the relatively weak intensities, because the primary Fe 2p and Co 2p regions emit multiple peaks from each oxidation state[6], potentially complicating the follow-up analysis. (a) – (b) display respective reference spectra of $Co(bpy)_3Cl_2$, $Co(bpy)_3Cl_3$, $K_3Fe(CN)_6$, and $K_4Fe(CN)_6$ powders, along with 60 mM $Co(bpy)_3^{2+/3+}{}_{(aq)}$-soaked Nafion and 60 mM $Fe(CN)_6^{3-/4-}$

$_{(aq)}$-soaked Nafion. While no Fe element remained on the surface of Nafion, a fingerprint of Co element was detected.

Based on the evidences obtained so far, a detailed mechanism on degradation on ionic conductivity of Nafion can be proposed, as shown in **Figure 3.16**. At this point, it was proven that (i) $Co(bpy)_3^{2+/3+}$ species and their decomposed products strongly and irreversibly bound to Nafion via a chemical process, (ii) there is a strong positive correlation between the absorption of $Co(bpy)_3^{2+/3+}$-derived species into the Nafion and the deteriorated ionic conduction through it. Combined with those observations, it should be additionally considered that the cation conductive channels of Nafion are negatively charged. SO_3^- groups are mainly populated on walls of the channels[16-18], whereas $Co(bpy)_3^{2+/3+}$-originated species are positively charged and multivalent. Therefore, (i) the multivalent $Co(bpy)_3^{2+/3+}$ species in water would first diffuse into negatively charged conducting channels of Nafion, and (ii) they would form ionic strong bonding with the channels by Coulombic attraction. At the same time, self-decomposition of $Co(bpy)_3^{2+/3+}$ species into another multivalent Co-based cations[36-38], and their binding with the Nafion conduction channels would be also possible. After these processes, removal of those highly charged cations from Nafion would become irreversible, because of the strong binding. The fixation of Co-based cations is likely to clog the cation conducting channels, because K^+ ions would be repelled by the sessile $Co(bpy)_3^{2+/3+}$-derived cations. This proposed model can couple the absorption of $Co(bpy)_3^{2+/3+}$-originated species with the serious compromise in ionic conductivity through the Nafion.

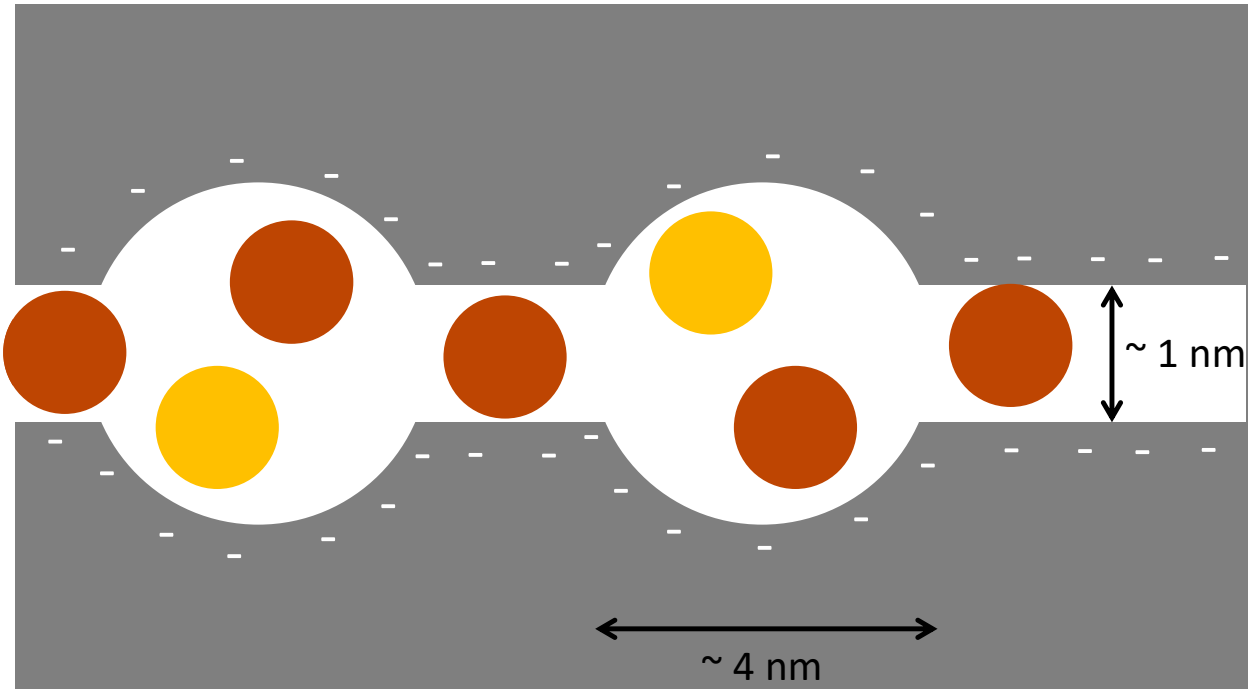

Figure 3.16. Nafion conducts cations through interconnected negatively charged channels[16-18]. In this model, the multivalent $Co(bpy)_3^{2+/3+}$ cations (red circles) or their decomposed products with positive charge (orange circles) were strongly bound by Coulombic attraction in the negatively charged cation conducting channels within the Nafion. This in turn would hamper diffusion of K^+ ions through the channels, because the 'stuck' cobalt-based ions in the channels would repulse the entering K^+ ions by Coulombic repulsion force. Figure redrawn based on *Thermocontrolled benzylimine–benzaldimine rearrangement over Nafion-H catalysts for efficient entry into α-trifluoromethylbenzylamines* and used with permission from Elsevier[39].

3.3.5. Self-Decomposition of $Co(bpy)_3^{2+}{}_{(aq)}$ as Another Limiting Factor for Lifetime of the Electrochemical Heat Harvester

As shown in **Figure 3.14** (a) – (b), the UV-Vis absorption spectra of $Co(bpy)_3^{2+/3+}$–soaked Nafion were unequal to the reference spectra. This strongly suggested $Co(bpy)_3^{2+/3+}$ chemical reactions with Nafion or self-decomposition of $Co(bpy)_3^{2+/3+}$ influenced the UV-Vis absorption pattern. To narrow down the possibilities, UV-Vis measurements were implemented to discover existence of self-decomposition. In order to allow abundant time for possible self-decomposition reaction, the 60 mM solutions of redox-species ($Co(bpy)_3Cl_{2(aq)}$, $Co(bpy)_3Cl_{3(aq)}$, $K_3Fe(CN)_{6(aq)}$,

and $K_4Fe(CN)_{6(aq)}$) were stored for 2.5 months. Dark and ambient environment was consistently maintained during the storage to exclude potential side effects by heat and light. To minimize unwanted effects from evaporation of water during the storage, the solution containing scintillation vials were further sealed by parafilm wrapping. The absorption spectra of the aged specimen solutions will be cross-checked by reference UV-Vis spectra from the fresh solutions with nominally identical compositions.

Figure 3.17 (a) – (d) display variations in the UV-Vis spectra during the 2.5 months of storage. All characterized solutions were contained in zero absorption cuvettes, in order to accept the absorption patterns purely from the specimen solutions. Whereas $Co(bpy)_3Cl_{3(aq)}$, $K_3Fe(CN)_{6(aq)}$, and $K_4Fe(CN)_{6(aq)}$ solutions preserved the UV-Vis absorption patterns after the aging, only the absorption spectra of the $Co(bpy)_3Cl_{2(aq)}$ solution significantly transformed over time. The fresh $Co(bpy)_3Cl_{2(aq)}$ solution had particularly weak absorption, but after 2.5 months of storage, the absorption intensified at an altered outset. This fact suggests that $Co(bpy)_3Cl_2$ in water experienced fundamental change in chemical state without external stimuli. This can be alternatively indicated as self-decomposition. As possibilities that the decomposition processes were driven by heat and light were circumvented by stocking the specimen solutions at room temperature under dark circumstance, one of the last candidates that may have catalyzed the self-decomposition was oxygen in the air.

An additive which may delay the self-decomposition of the $Co(bpy)_3^{2+}$ species[36-38], 2,2'-bipyridine (bpy) was added to the 60 mM $Co(bpy)_3Cl_{2(aq)}$ solution. However, this additive could not bring any difference in the UV-Vis absorption spectra, which means the co-existent bpy could not inhibit or at least hardly reverted the self-decomposition reaction of $Co(bpy)_3Cl_2$ in water. This conclusion may be extended to suggestions on the decomposition mechanism of $Co(bpy)_3Cl_2$ in water: either (i) the self-decomposition reaction is not relevant to splitting of bpy from the $Co(bpy)_3^{2+}$ ion or (ii) detachment of bpy is thermodynamically irreversible, or (iii) influence by small amount of bpy is limited due to its tiny solubility in water at room temperature (64 mg/mL)[40].

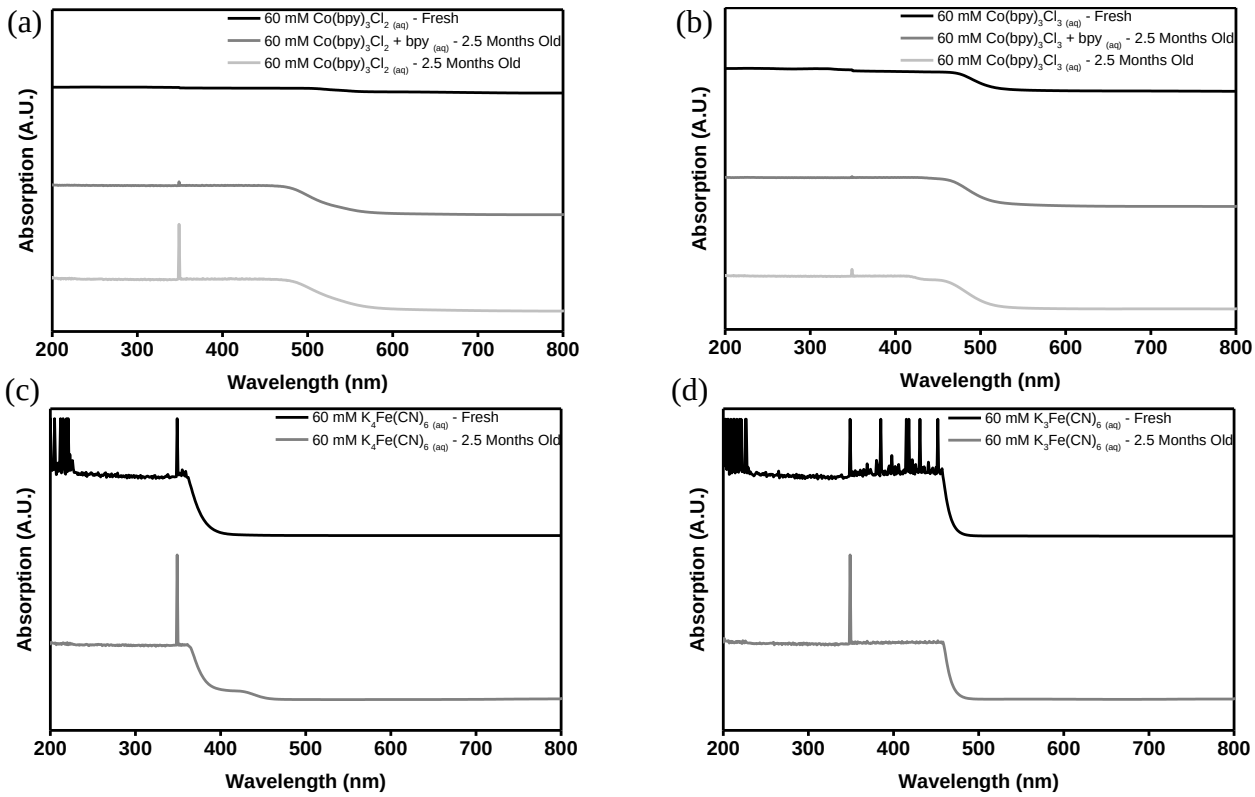

Figure 3.17. (a) – (d) UV-Vis absorption spectra of fresh and aged 60 mM solutions of the redox active species, namely $Co(bpy)_3Cl_{2(aq)}$, $Co(bpy)_3Cl_{3(aq)}$, $K_3Fe(CN)_{6(aq)}$, and $K_4Fe(CN)_{6(aq)}$. 2,2'-bipyridine (bpy) neutral molecule was deliberately added to $Co(bpy)_3Cl_{2(aq)}$ and $Co(bpy)_3Cl_{3(aq)}$ solutions, to examine if they could delay the self-decomposition of $Co(bpy)_3^{2+}$ or $Co(bpy)_3^{3+}$ species, if there existed such chemical degradation.

Effects of the self-decomposition of $Co(bpy)_3Cl_{2(aq)}$ along with $Co(bpy)_3^{2+/3+}{}_{(aq)}$ absorption into Nafion were reflected as gradual decrease of OCV at a cell comprised of 60 mM $Co(bpy)_3^{2+/3+}{}_{(aq)}$ | K^+-conducting Nafion | 60 mM $Fe(CN)_6^{3-/4-}{}_{(aq)}$ (**Figure 3.18**). In order to remove unexpected side effects, the temperature was kept at room temperature and light was shielded. As the OCV of the cell relies on molar concentration ratios among all redox-active species, both the self-decomposition $Co(bpy)_3Cl_{2(aq)}$ and immobilization of $Co(bpy)_3^{2+/3+}{}_{(aq)}$ due to the absorption into the Nafion led to change of OCV (**Figure 3.18**). Both mechanisms serve as 'sinks' for $Co(bpy)_3^{2+/3+}{}_{(aq)}$ species from the aqueous anolyte. This also implies that charge capacity of the electrochemical heat harvester would decay as time elapses, as will be demonstrated later.

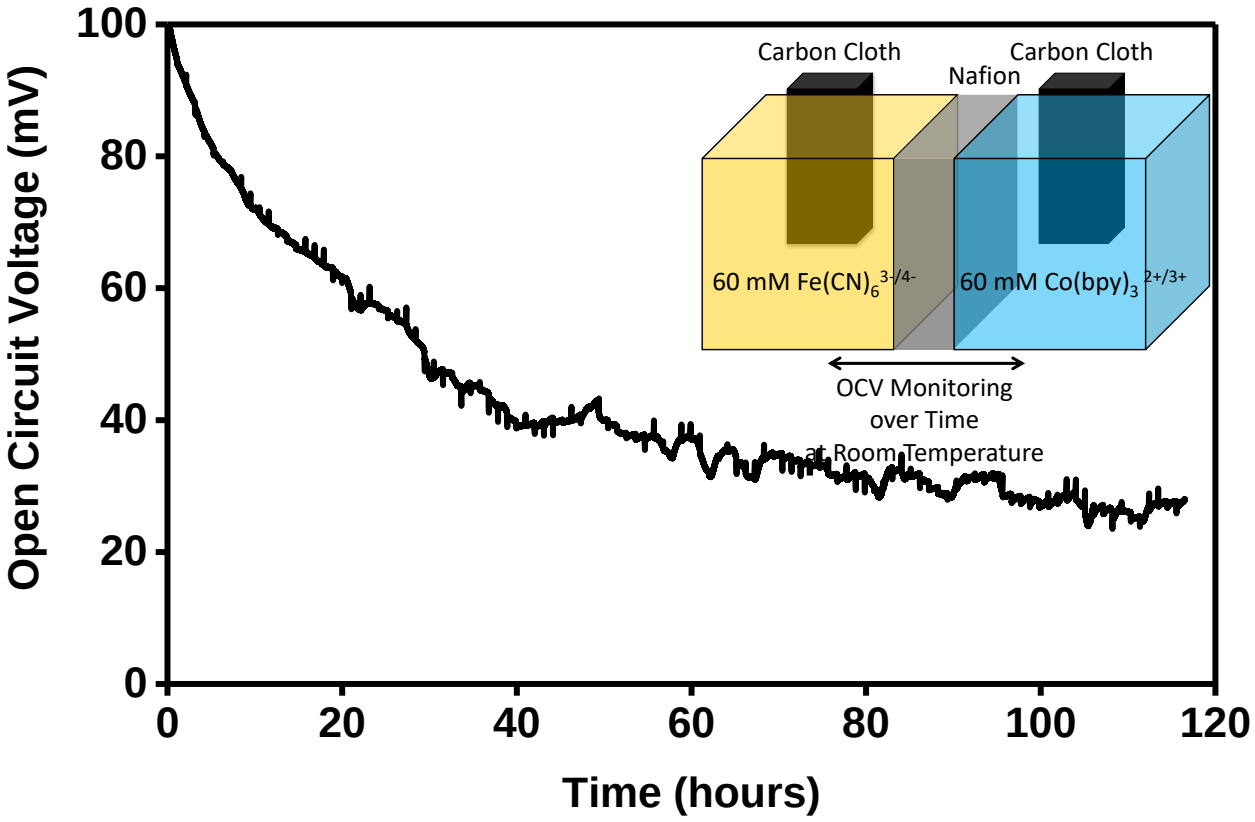

Figure 3.18. Degradation of OCV of the cell (shown as inset) over time, under dark and room temperature condition.

3.3.6. Polyelectrolyte Coatings on the Nafion as a Countermeasure to Its Ionic Conductivity Deterioration

Degradation of the Nafion membrane by absorption of $Co(bpy)_3^{2+/3+}{}_{(aq)}$ species was confirmed by XPS and UV-Vis spectroscopy. However, in order for the cell to operate, K^+ ion should still remain permeable while $Co(bpy)_3^{2+/3+}{}_{(aq)}$ species should be blocked and stay in the electrolyte. It is difficult to replace Nafion into other material, because superionic conductivity of Nafion[34] cannot be easily matched by other materials; which contribute to the minimization of the cell internal resistance.

Instead, plans were considered in order to augment Nafion, so that it may not be contacted by the $Co(bpy)_3^{2+/3+}{}_{(aq)}$ species. Accordingly, several filtration mechanism could be proposed to exclude $Co(bpy)_3^{2+/3+}{}_{(aq)}$ selectively, focusing on the main differences between K^+ and

$Co(bpy)_3^{2+/3+}{}_{(aq)}$ species. The major differences between those two species were valency and ionic size.

The selection among two differently charged cations is often feasible by ion exchange membranes. The ion exchange membranes are mostly polymers[41,42], to which Nafion belongs. From this hint, it can be drawn that solely relying on valency is not applicable to resolve this issue, because the any ion exchange membrane will result in fixation of $Co(bpy)_3^{2+/3+}{}_{(aq)}$ species from the electrolyte, similar to the Nafion. Both $Co(bpy)_3^{2+/3+}{}_{(aq)}$ species and the newly introduced ion exchange membrane would be 'consumed' together, because it would absorb multivalent ions from the solution by definition. This process is irreversible, unless the cell is opened and special desorption procedures are performed. In other words, without dissecting the electrochemical heat harvester, the membranes would not be recovered to the initial pristine state. Furthermore, their ionic conductivity is likely to be much less than that of the Nafion. Therefore, valency-based exclusion of $Co(bpy)_3^{2+/3+}{}_{(aq)}$ would be impractical.

When size-based exclusion is chosen as a tactics to prohibit contact of Nafion by $Co(bpy)_3^{2+/3+}{}_{(aq)}$ species, relatively wider options become available. They can be zeolite-class materials coating on Nafion or free standing membranes[43-48], polyelectrolyte coating[49-53] on Nafion, or self-standing cellulose-type polymeric membranes, such as cellophane[42,54]. Among them, zeolite materials were firstly removed from the list, because they are brittle crystalline ceramics. It also means they can be easily fractured during the handling, and through which $Co(bpy)_3^{2+/3+}{}_{(aq)}$ can diffuse readily. Moreover, when they are coated on Nafion, the process would involve expensive deposition techniques to ensure conformity (i.e. pinhole free coating), such as chemical vapor deposition (CVD)[55].

For this reason, cheap polyelectrolyte coatings on Nafion via inexpensive layer-by-layer (LbL) processes were decided, as they were proven capable of realizing size-based exclusion[56-58]. Polyelectrolytes are polymers attaching dissociable groups, which can be viewed as combination of polymer and salt in a single molecule[59]. Hence, they become to have charge when they are dissolved in solvents, such as water. LbL process is a deposition technique, where alternating layers of oppositely charged polyelectrolytes are stacked step-by-step, with washing steps in between. After the deposition, nanopores spontaneously formed in the polyelectrolyte film have particular range of the pore size, which can be controlled by selection of polyelectrolyte species.

Figure 3.19 (a) – (b) demonstrate why selection of polyelectrolyte species affects the nanopore size[56,57], and selectivity between two dissimilar species based on size. First, the descriptor that determines nanopore size of the polyelectrolyte films should be defined:

Charge density of a polyelectrolyte ≡ Charge that each monomer has when dissociated / Number of carbon atoms in a monomer of each polyelectrolyte (3.1)

The charge density and polyelectrolyte species cannot be decoupled, because it is an innate characteristic of each polyelectrolyte. In other words, if the polyelectrolyte species are substituted from one to another, then it is possible to alter the resultant nanopore size.

Polyelectrolyte films fabricated only with high charge polyelectrolytes are illustrated schematically as **Figure 3.19** (a), and only with low charge polyelectrolytes are depicted schematically as **Figure 3.19** (b). When polyelectrolytes with high charge densities are combined as a film, it results in small mean nanopore size. On the contrary, when polyelectrolytes with low charge densities are built as a film, it leads to large average nanopore size. **Figure 3.19** (a) – (b) reflect these facts very intuitively. Medium nanopore size is expected when a polyelectrolyte with low charge density and another polyelectrolyte with high charge density are LbL deposited together. Ideally, for the selective permeation, the size of nanopores should be larger than the ions that should be conducted. The nanopore size should be smaller than the ions that should be impermeable. It is noteworthy that polyelectrolyte films are not selective for the valency and the signs of the species in the solution (+ or – or 0). Therefore, neutral molecules can also be selectively filtered via this 'molecular sieve'[56,57,60].

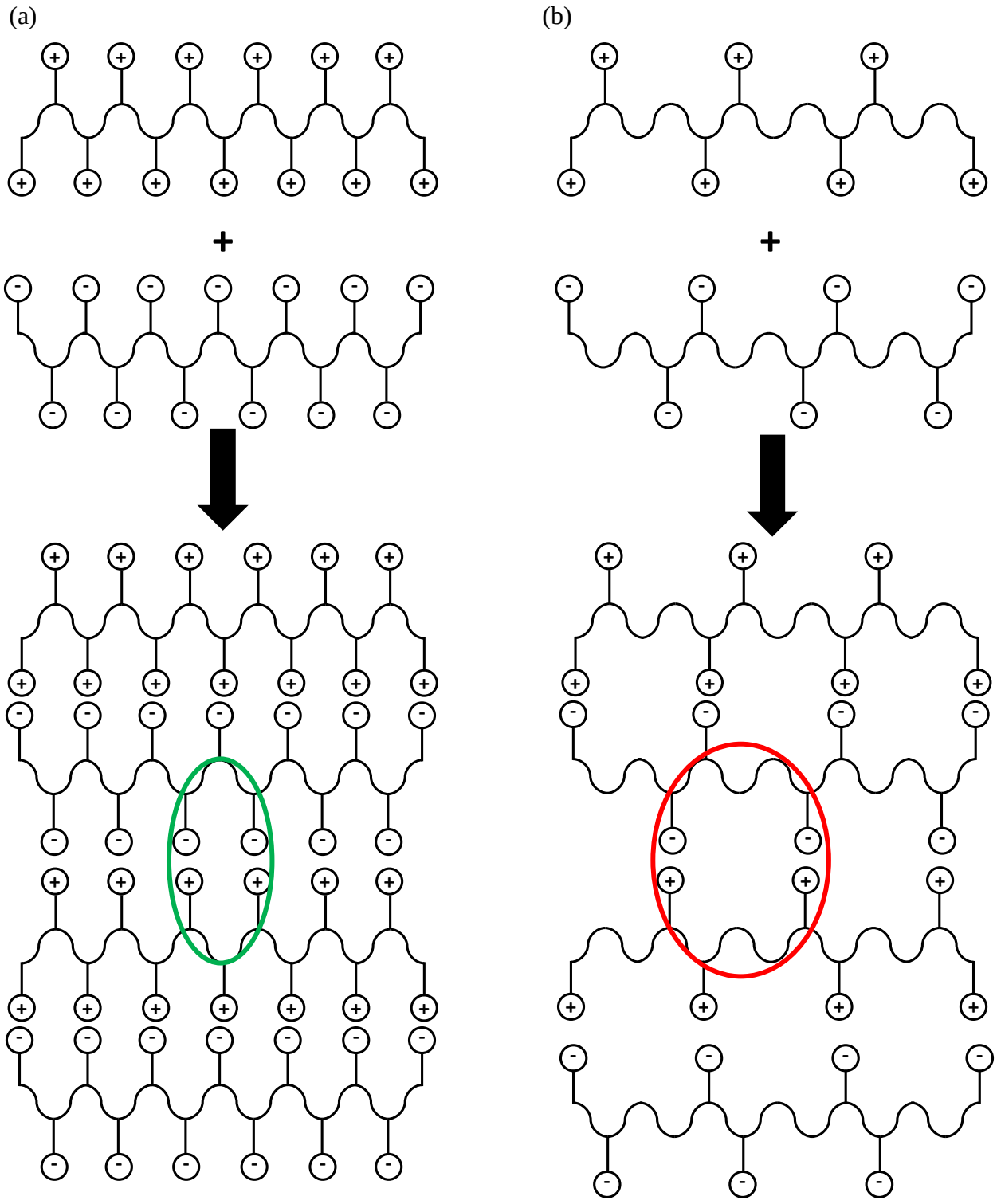

Figure 3.19. Charge densities of polyelectrolytes lead to different sizes of nanopores in their resultant polyelectrolyte films. (a) Combination of polyelectrolytes with high charge densities concludes in smaller nanopore sizes. (b) Combination of polyelectrolytes with low charge densities

causes smaller nanopore sizes. Figure redrawn based on *Selective transport of ions and molecules across layer-by-layer assembled membranes of polyelectrolytes, p-sulfonato-calix[n]arenes and Prussian Blue-type complex salts* and used with permission from Elsevier[56].

Another important factor that can influence the quality of selective filtration would be the thickness of the polyelectrolyte film. Thickness growth of polyelectrolyte coating can be tuned by (i) repetition of LbL processes, (ii) ionic strength (i.e. supporting salt concentration) of the solutions used in the LbL processes, and (iii) pH of the solutions used in the LbL processes.

The repetition of LbL process monotonically increases the thickness of the polyelectrolyte coating. However, solely relying on this mechanism to grow polyelectrolyte films would be time consuming.

For this reason, the growth rate of the polyelectrolyte films is usually increased by higher ionic strength (supporting salt concentration). As explained earlier, the polyelectrolyte has properties of both polymer and salt. The polymeric nature induces the entanglement of the polyelectrolyte chains, due to hydrophobic attraction among the chains. On the contrary, the salt-like nature of the polyelectrolytes fosters repulsion among the chains with the same sign of charges. The role of supporting salt is providing ions which functions as electrostatic shields. Hence, when the ionic strength is low, the repulsion among a single species of polyelectrolyte chains is more pronounced, as the Coulombic repulsion is not shielded. This circumstance leads to disentanglement of the polyelectrolytes (Left hand side of **Figure 3.20**). When the ionic strength is high in the LbL solution, the ions from ionization of the supporting salt buffer the Coulombic repulsion among the same charged functional groups, promoting the coiling of polyelectrolytes (Right hand side of **Figure 3.20**). As can be intuitively understood from **Figure 3.20**, the higher ionic strength fosters growth rate of the polyelectrolyte film during the LbL procedures.

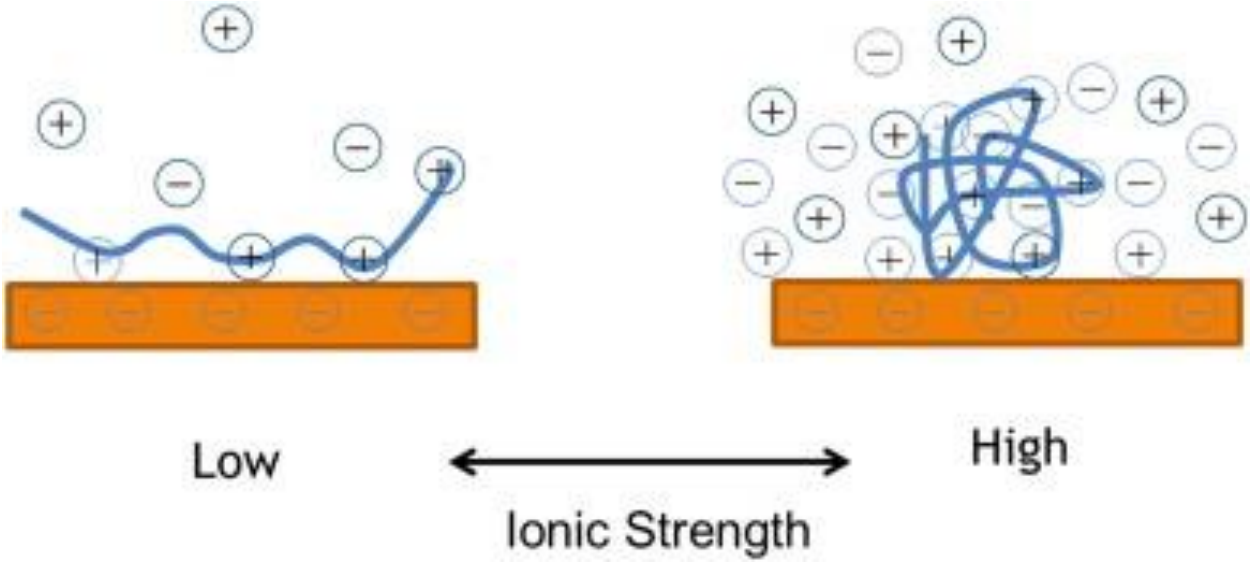

Figure 3.20. Illustration on the effect of ionic strength on polyelectrolyte entanglement. At low ionic strength, charged functional groups at polyelectrolyte repel each other, fostering disentanglement. At higher ionic strength, the presence of ions weakens the electrostatic repulsion between the charged segments, thereby promoting the entanglement. Figure from *Dynamics of polyelectrolyte adsorption and colloidal flocculation upon mixing studied using mono-dispersed polystyrene latex particles* and used with permission from the Elsevier[61].

The last factor is pH of the LbL solutions. pH is expected to influence only the weak polyelectrolytes, because the weak polyelectrolytes need H^+ or OH to dissociate and have charge[19-22]. In comparison, strong polyelectrolytes dissociate regardless of pH, because their dissociation mechanism does not participate H^+ or OH^- in the process[19-22]. When weak polyelectrolytes are incorporated in the film, then they can construct stable coatings only if they can dissociate under appropriate pH. It is noteworthy that concept of weak / strong polyelectrolyte is different from the concept of charge density.

It was already proven that a polyelectrolyte coating composed of PAH^+ and PSS^- on Nafion can selectively permeate K^+, while hindering Mg^{2+} transport across the Nafion membrane in water[58], because size of Mg^{2+} is larger. This feature is particularly favorable for this electrochemical heat harvester system, because the requirement for this study is same as this previous report: only K^+ should be permeable, while larger $Co(bpy)_3^{2+/3+}{}_{(aq)}$ species should be

excluded, just like Mg^{2+}. For this reason, selective filtration by polyelectrolyte coatings with similar compositions on Nafion membrane will be examined, together with optimization on the coatings.

3.3.7. Optimization of the Polyelectrolyte Coatings on Nafion for Prevention of the $Co(bpy)_3^{2+/3+}$ Absorption

Degradation of ionic conductivity of Nafion is a grave issue which would restrict effectiveness of the electrochemical heat harvester (Equation 1.13). The reason for this phenomenon was modeled to be absorption of highly charged $Co(bpy)_3^{2+/3+}$-derived species into negatively charged cation conducting channels in the Nafion membrane, thereby blocking passage of K^+ cations through the Nafion. In order to resolve this issue, polyelectrolyte coatings on the Nafion membrane was proposed as a countermeasure. They would selectively pass K^+ cation to the Nafion surface, while selectively hampering the passage of $Co(bpy)_3^{2+/3+}$ species. Moreover, the polyelectrolyte films on the Nafion are proven conformal[62,63], so that $Co(bpy)_3^{2+/3+}$ species cannot bypass the coatings.

As informed earlier, there are three important factors which govern growth of polyelectrolyte coating: (i) number of repetitions on the polyelectrolyte coating procedures, (ii) supporting salt concentration, and (iii) pH for weak polyelectrolytes such as PAH^+. For the firstly examined polyelectrolyte coating, $(PAH^+/PSS^-)_n$, all of those 3 variables were expected to influence its growth and performance. Their effects were investigated one by one, while holding other two variables constant. The following serial experiments were oriented toward optimization of the polyelectrolyte coating with best selective filtration of $Co(bpy)_3^{2+/3+}{}_{(aq)}$ species. This capability was characterized by how much time was required to reach 20 mV of overpotential, because overpotential higher than 20 mV would bring about considerably deteriorated energy output and conversion efficiency of the electrochemical heat harvester (Equation 1.13). More detailed information about the measurements can be found in Section 3.2.4.

The effect of number of repetitions on the $(PAH^+/PSS^-)_n$ coating procedures were illustrated in **Figure 3.21**. The LbL deposition was consistently performed in pH = 1 and [NaCl] = 1.0 M solutions. Time to reach the 20 mV overpotential line could be most delayed when the LbL coating procedure was repeated for 3.5 times (n = 3.5 at the $(PAH^+/PSS^-)_n$ notation). The short

life expectancy of $(PAH^{+}/PSS^{-})_{1.5}$ was attributed to excessively thin thickness of the coating, therefore the coating hardly could block $Co(bpy)_3^{2+/3+}{}_{(aq)}$. Otherwise, there still were huge enhancements on the life expectancy of the Nafion by $(PAH^{+}/PSS^{-})_n$ coating; 3 hours of life expectancy of the bare Nafion improved to more than 50 hours by the $(PAH^{+}/PSS^{-})_n$ coating. These results propose that $(PAH^{+}/PSS^{-})_n$ coating could at least substantially postpone the diffusion of $Co(bpy)_3^{2+/3+}{}_{(aq)}$ species through the coating.

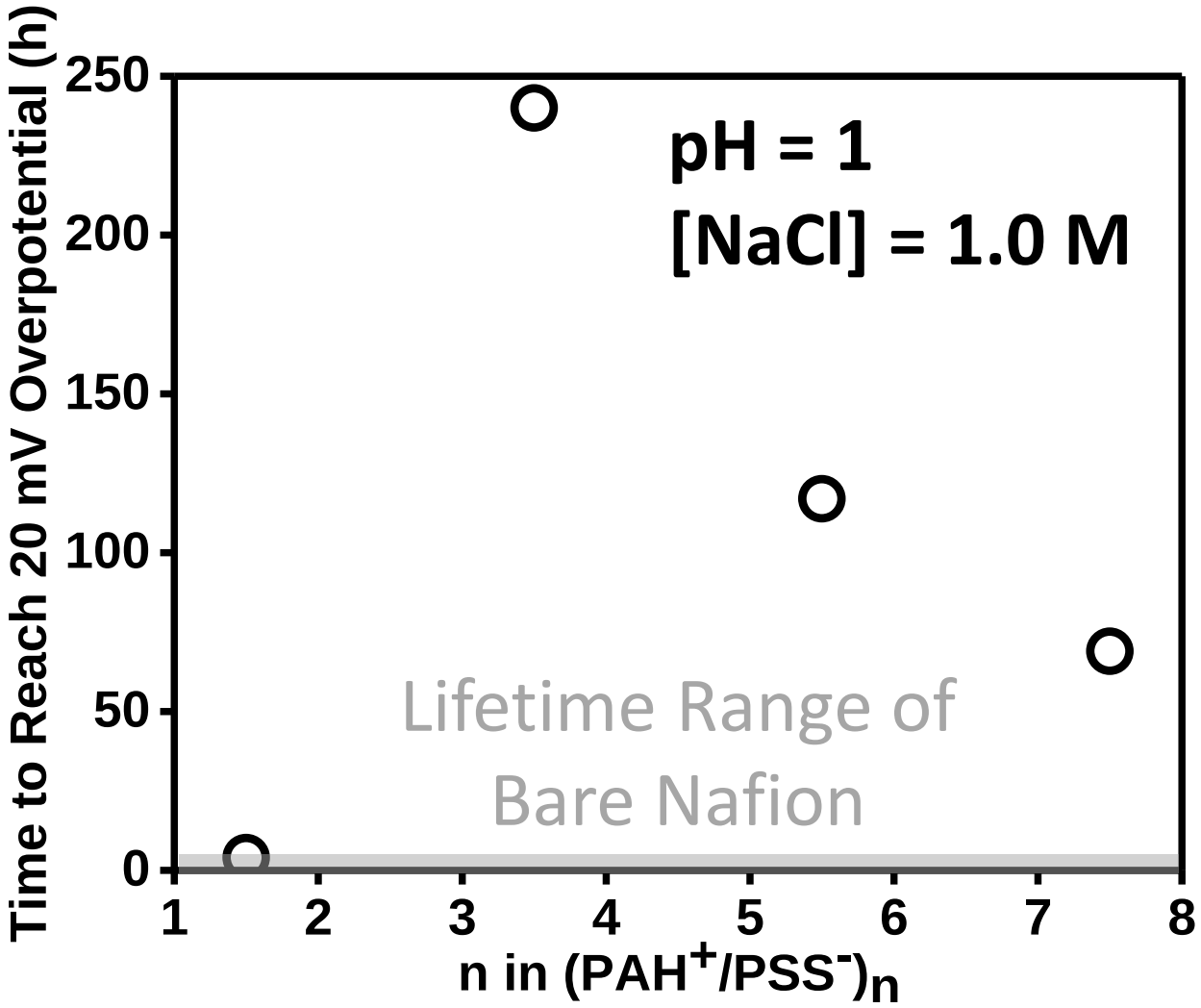

Figure 3.21. Lifetime of the $(PAH^{+}/PSS^{-})_n$-coated Nafion membranes as a function of different repetitions of the LbL deposition. The LbL polyelectrolyte deposition procudures were consistently carried out at pH = 1 and [NaCl] = 1.0 M environments. 20 mV overpotential was adopted as a criterion to determine if the cell would be still usable practically, because

overpotential higher than 20 mV would result in critical decrease in the conversion efficiency (Equation 1.13).

As the number of repetitions on the $(PAH^{+}/PSS^{-})_n$ coating was optimized, another parameter, pH was optimized in **Figure 3.22**. This time, pH of the LbL deposition solution was tuned, while keeping the number of repetitions on the $(PAH^{+}/PSS^{-})_n$ coating as 3.5 and supporting NaCl concentration at 1.0 M. **Figure 3.22** indicates that $(PAH^{+}/PSS^{-})_n$ coatings with higher lifetime of Nafion were generally formed in acidic environments of the LbL coating solutions. This result is consistent with the theory, because the weak polyelectrolyte, PAH^{+} requires proton in order to dissociate and possess positive charge; otherwise, it cannot dissociate and would remain neutral, so that Coulombic attraction-reliant LbL coating cannot be effective. The optimal condition of pH ranges between 1 and 2.

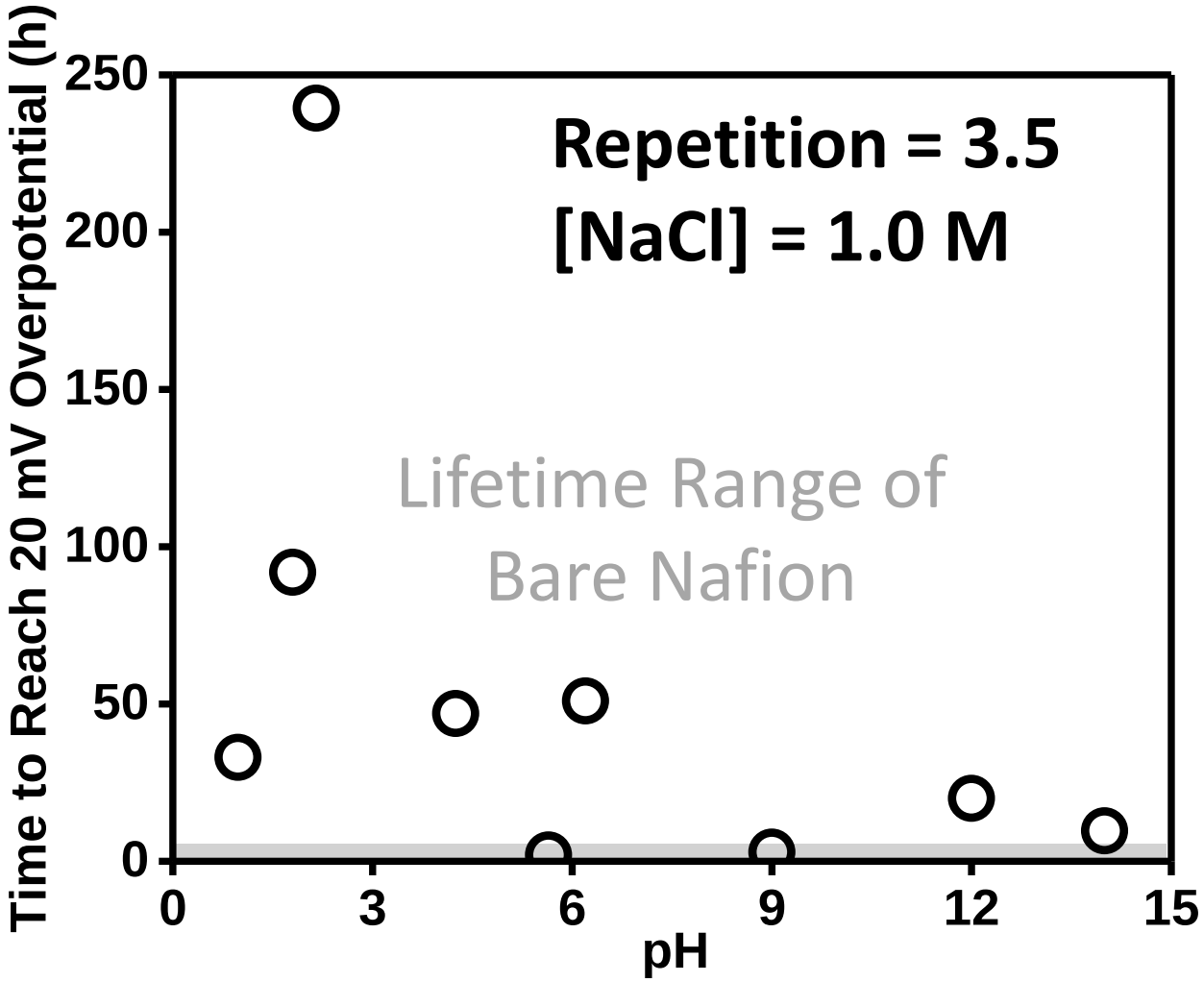

Figure 3.22. Lifetime of the $(PAH^{+}/PSS^{-})_n$-coated Nafion membranes as a function of pH during the LbL deposition solutions. The LbL polyelectrolyte deposition was consistently repeated for 3.5 times and the supporting NaCl concentration was fixed at 1.0 M. 20 mV overpotential was adopted as a criterion to determine if the cell would be still usable practically, because overpotential higher than 20 mV would result in critical decrease in the conversion efficiency (Equation 1.13).

Figure 3.23 (a) – (b) reflect peculiar observations during the optimization of $(PAH^{+}/PSS^{-})_n$ coating by NaCl concentration ([NaCl]). At this set of experiments, both pH and the number of repetitions on the $(PAH^{+}/PSS^{-})_n$ coating were kept 1 and n = 3.5 respectively. When [NaCl] = 0 M, $(PAH^{+}/PSS^{-})_n$ on Nafion behaved as if the film did not exist, because the Nafion degraded as

quick as the bare Nafion. In the contrast, under another [NaCl] = 5.0 M, very close to the solubility limit[64] in water at room temperature, the overpotential exceeded 12 V from the start, and stayed there. The OCV readings of the cell at the room temperature were unstable (**Figure 3.23** (b)), as if the catholyte and the anolyte were separated by an ionic insulator. In comparison, the cells with the same configurations except for the coating exhibited very steady OCV readings, as hinted in **Figure 3.18**. As Nafion is a superionic conductor at room temperature[34], $(PAH^{+}/PSS^{-})_{n}$ coated at [NaCl] = 5.0 M would be solely responsible for the vibrating OCV readings and very high overpotentials captured in **Figure 3.23** (a) – (b).

The particularities at the two extreme NaCl concentrations could be explained within the framework stated in Section 3.3.6. The polyelectrolytes possess both properties of polymers and salts; therefore they experience two contradictory driving forces on their structures. The first one is attraction among the carbon backbones by hydrophobic attractions, while opposite one is Coulombic repulsion among the ionized functional groups with identical charges in the same polyelectrolyte species[65-67]. The supporting salt concentration regulates priority of one driving force over another. When the supporting salt concentration is high, then the repulsion between the identically charged functional groups can be moderated due to the screening effect. Therefore, the polyelectrolytes tend to coil under that circumstance, promoting the growth rate of the LbL deposited polyelectrolyte film. On the contrary, at low supporting salt concentration, the polyelectrolyte chains disentangle and the growth of polyelectrolyte layer becomes slower correspondingly.

According to this logic, the quick compromise on ionic conductivity for the $(PAH^{+}/PSS^{-})_{3.5}$ deposited at [NaCl] = 0 M could be understood due to almost nearly zero film thickness. The unstable OCV and very high overpotential for $(PAH^{+}/PSS^{-})_{3.5}$ deposited at [NaCl] = 5.0 M could be attributed to extremely large thickness, virtually impermeable to any ions. Hence, the Nafion with such coating became an ionic insulator.

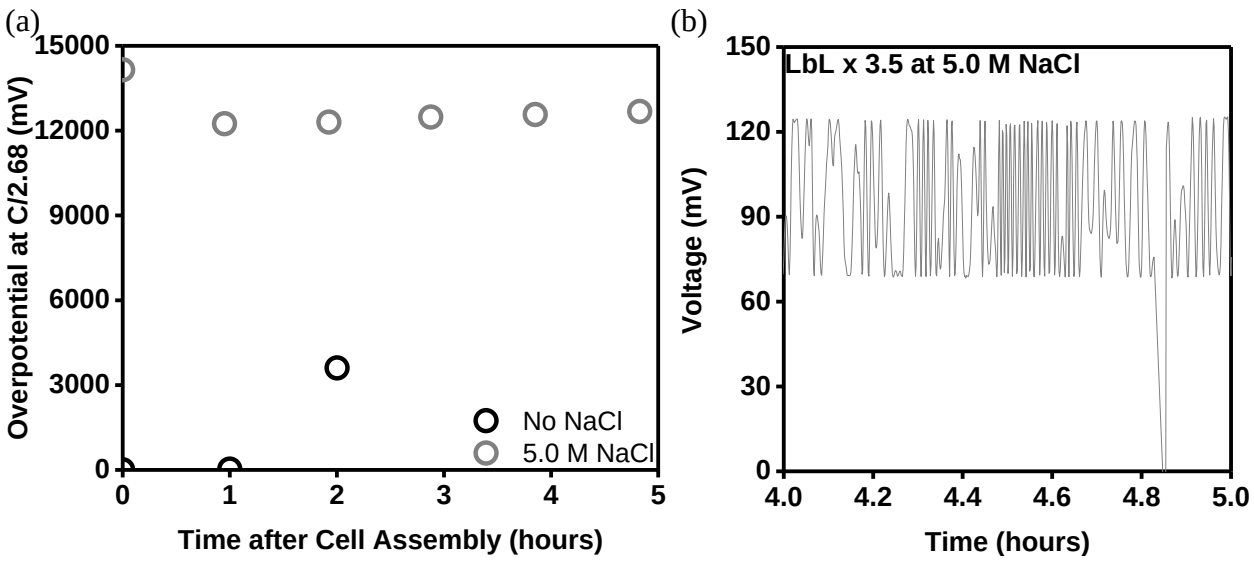

Figure 3.23. (a) Overpotential at C/2.68 of current when $(PAH^{+}/PSS^{-})_{3.5}$ coating was deposited at pH = 1 at two extreme supporting NaCl concentrations: 0 M and 5.0 M. (b) OCV of the testing cell with $(PAH^{+}/PSS^{-})_{3.5}$-coated Nafion, of which deposition was carried out at pH = 1 and [NaCl] = 5.0 M. OCV fluctuated, even though no stimuli like mechanical vibration, temperature swing, or light was applied to the cell. The Nafion with the coating acted as if it was an ionic insulator separating the catholyte and the anolyte.

Other [NaCl] conditions for the LbL deposition were also tested, following the same experimental steps. The results were summarized in **Figure 3.24**, showing that higher [NaCl] monotonically led to better selective filtering capability of $Co(bpy)_3^{2+/3+}{}_{(aq)}$ species, except for the highest [NaCl] = 5.0 M. The optimal $(PAH^{+}/PSS^{-})_n$ coating was formed at the second highest [NaCl] = 1.0 M, adequately thick to exclude $(PAH^{+}/PSS^{-})_n$, while still permeating K^{+} cations, so that the Nafion coated with the $(PAH^{+}/PSS^{-})_n$ could remain ionically conductive.

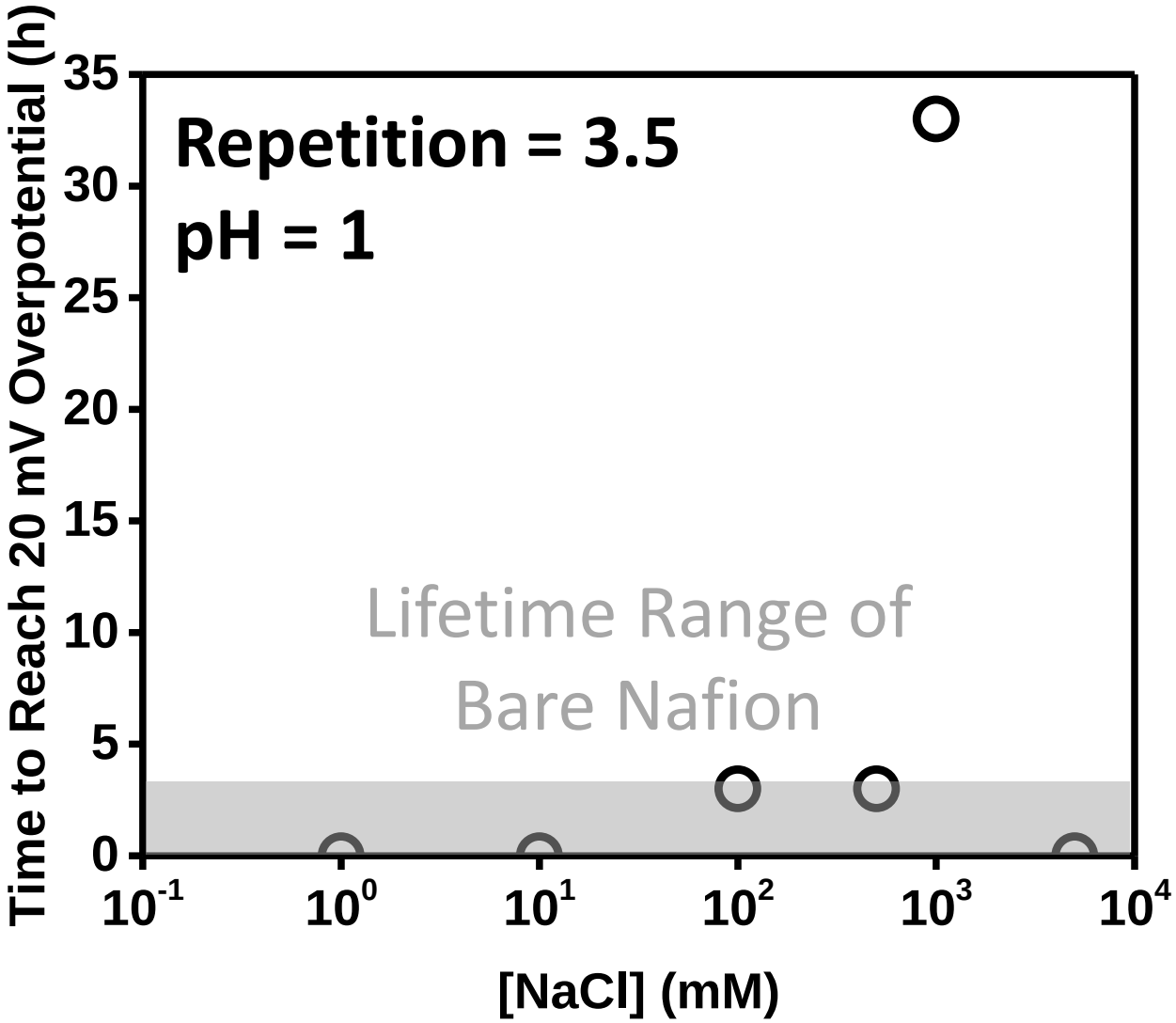

Figure 3.24. Lifetime of the $(PAH^{+}/PSS^{-})_n$-coated Nafion membranes as a function of supporting NaCl concentration during the LbL deposition. The LbL polyelectrolyte deposition was repeated for 3.5 times and the pH was fixed at 1.0 M during the deposition process. 20 mV overpotential was adopted as a criterion to determine if the cell would be still usable practically, because overpotential higher than 20 mV would result in critical decrease in the conversion efficiency (Equation 1.13).

3.3.8. $(PDADMAC^{+}/PSS^{-})_n$ Coating on Nafion for Prevention of the $Co(bpy)_3^{2+/3+}$ Absorption

As $(PDADMAC^{+}/PSS^{-})_n$ is only comprised of strong polyelectrolytes of which dissociation should be independent from pH, effect of only two parameters were investigated for the optimization: [NaCl] and number of repetitions during the polyelectrolyte coating procedures (i.e. n in $(PDADMAC^{+}/PSS^{-})_n$). $(PDADMAC^{+}/PSS^{-})_n$ could only result in little increase on life expectancy of the Nafion. Even if the growth rate was maximized by employing a NaCl concentration near the solubility limit ([NaCl] = 5.0 M) and by repeating the LbL for 7.5 times, such $(PDADMAC^{+}/PSS^{-})_n$ coating could not protect the Nafion from contacting $Co(bpy)_3^{2+/3+}{}_{(aq)}$ species. This means that both $K^{+}_{(aq)}$ and $Co(bpy)_3^{2+/3+}{}_{(aq)}$ penetrated through the $(PDADMAC^{+}/PSS^{-})_n$ film without considerable restriction. In comparison, $(PAH^{+}/PSS^{-})_{3.5}$ deposited at the same [NaCl] environment was so thick to prevent all passage of ions (**Figure 3.23** (a) – (b)). This gap between the selectivity of $(PAH^{+}/PSS^{-})_n$ coatings and $(PDADMAC^{+}/PSS^{-})_n$ coatings will be explained later, from a mechanistic viewpoint.

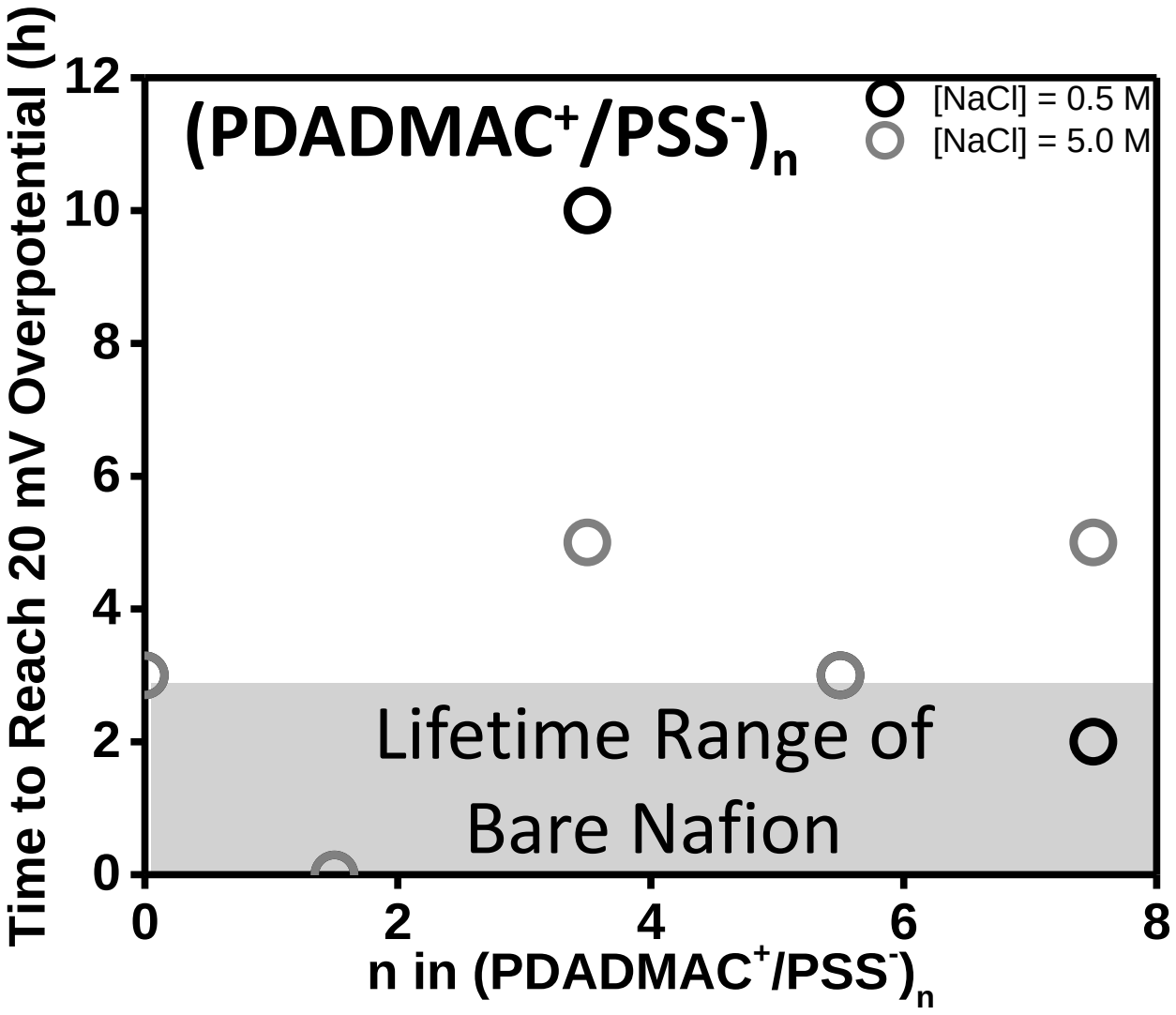

Figure 3.25. Lifetime of the $(PDADMAC^+/PSS^-)_n$-coated Nafion membranes as a function of repetitions of the LbL process and supporting NaCl concentrations. Because dissociation processes of both $PDADMAC^+$ and PSS^- do not involve H^+ or OH^-, influence by pH was expected minimal, therefore its effect was not investigated. 20 mV overpotential was adopted as a criterion to determine if the cell would be still usable practically, because overpotential higher than 20 mV would result in critical decrease in the conversion efficiency (Equation 1.13).

3.3.9. Origins of the Selective Permeation through the Polyelectrolyte Coatings

Origin of selectivity in polyelectrolyte coatings are often size-based exclusion[56-58], as described in the Section 3.3.6. It clearly indicated that charge densities of polyelectrolytes used in

LbL process determine mean sizes of nanopores[56,57] in the resultant film, thereby influencing the selectivity (**Figure 3.19**).

In order to apply this principle for analysis of different selectivity of $(PAH^+/PSS^-)_n$ and $(PDADMAC^+/PSS^-)_n$, the number of carbons in each monomer of respective polyelectrolytes were counted and summarized in **Table 3.1**. Only PAH^+ has high charge density (Equation 3.1) owing to small number of carbon atoms in its monomer unit, whereas both $PDADMAC^+$ and PSS^- possess small charge densities. As a result, $(PAH^+/PSS^-)_n$ film would have smaller sizes of nanopores than those of $(PDADMAC^+/PSS^-)_n$. This would cause dissimilar size-based filtration capability.

	Carbons in a monomer per unit charge	**Charge Density**
PAH^+	3	**High**
$PDADMAC^+$	8	**Low**
PSS^-	10	**Low**

Table 3.1. Number of carbon atoms in monomers and consequent charge densities of the individual polyelectrolytes.

Figure 3.26 (a) – (b) graphically depict the origins of the selectivity difference between $(PAH^+/PSS^-)_n$ and $(PDADMAC^+/PSS^-)_n$. Given that hydrated ionic radii of K^+ and $Co(bpy)_3^{2+/3+}$ are 0.28 nm[68] and 0.68 nm[69] respectively, the 0.67 nm-large nanopores[56] in $(PAH^+/PSS^-)_n$ can only permeate much smaller K^+ ions, while blocking major portion of marginally larger $Co(bpy)_3^{2+/3+}$ ions. The eventual increase in overpotential over time at the electrochemical heat harvester can be because small portion of the nanopores in $(PAH^+/PSS^-)_n$ is wider than the hydrated $Co(bpy)_3^{2+/3+}$ ionic size. In the contrast, the mean size of nanopores in $(PDADMAC^+/PSS^-)_n$ film (0.82 nm[56]) is slightly larger than $Co(bpy)_3^{2+/3+}$ ions, hence this film allow passage of all ions indiscriminately. This explains why $(PDADMAC^+/PSS^-)_n$–coated Nafion does not have meaningfully improved lifetime over that of the bare Nafion.

The best polyelectrolyte coating on the Nafion to counter the ionic conductivity degradation is $(PAH^+/PSS^-)_{3.5}$ film, deposited under pH = 1 – 2 and [NaCl] = 1.0 M conditions.

This optimized coating on Nafion will be further examined under thermodynamic cycling, to check if this coating would be still effective even at the elevated temperature 60 °C.

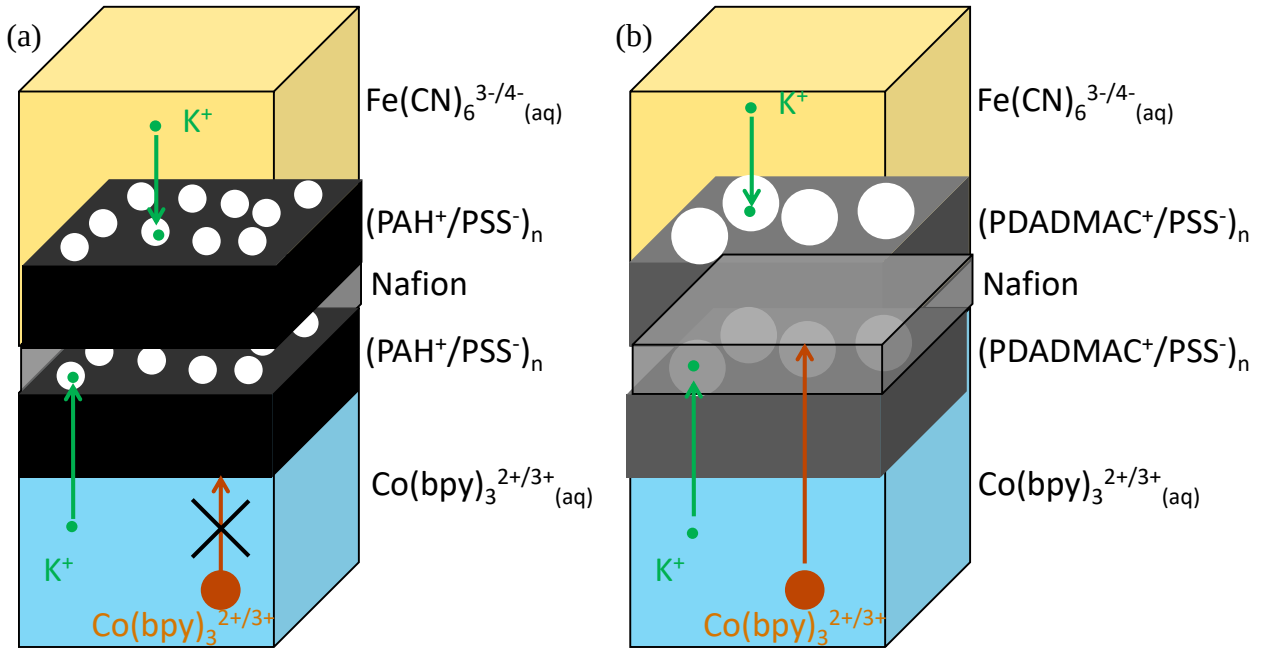

Figure 3.26. A suggested model to interpret difference between $Co(bpy)_3^{2+/3+}$ filtering capabilities of $(PAH^+/PSS^-)_n$ and $(PDADMAC^+/PSS^-)_n$ coatings on Nafion membranes. Dissimilar sizes of nanopores in those coatings are regarded the determinant.

3.3.10. Effect of $(PAH^+/PSS^-)_n$ on Cyclability of the Electrochemical Heat Harvester

Cyclability of two different electrochemical harvesters with and without the optimal $(PAH^+/PSS^-)_n$ film on the Nafion membranes were inspected. Except for this difference in the coating on the Nafion, the cell configurations were identical, as shown in **Figure 3.8** (a). They went through heat harvesting thermodynamic cycles composed of 4 distinct steps (**Figure 3.27** (a) – (d)). Step (i) was a galvanostatic discharge process at 20 °C until the cell voltage becomes zero. This stage was carried out as soon as the electrochemical heat harvester was completely assembled. Step (ii) was thermal recharging process at open circuit condition. This process utilized shift in electrochemical equilibrium by the elevation of the surrounding temperature to 60 °C, which was expressed as variation in the OCV from 0 mV to ~ -80 mV. Step (iii) was another galvanostatic

discharge process at 60 °C until the cell voltage became zero again. The signs of the voltage and the applied current were inverted from step (i), while preserving the absolute values. Lastly, the electrochemical heat harvester was thermally recharged by returning the surrounding temperature back to 20 °C under open circuit condition at step (iv). This process brought the electrochemical heat harvester to a state identical to the very initial state.

Figure 3.27 (a) – (b) compares the very first time-dependent heat harvesting thermodynamic cycles from the two cells incorporating Nafion membranes *with and without the optimal* $(PAH^{+}/PSS^{-})_n$ *coating*. Their profiles were similar to each other due to the almost identical cell configurations, and the same thermodynamic cycling conditions. However, at the outset of the 2^{nd} thermodynamic cycle, for the cell with bare Nafion, the overpotential right after the step (iv) became markedly higher. The overpotential was even larger than the thermally harvested voltage, + 80 mV (**Figure 3.27** (a)). On the contrary, the cell incorporating the optimally coated $(PAH^{+}/PSS^{-})_n$ on Nafion could transit to the 2^{nd} cycle without hugely grown overpotential. This demonstrated the merit of the polyelectrolyte coating under the real thermodynamic cycles.

Figure 3.27 (c) – (d) depict relationship between cell voltage and charge at each step forming the heat harvesting thermodynamic cycle. These plots displayed the roles of each constituting steps more clearly. Moreover, they proved that the four steps formed nearly enclosed loops, a characteristic of thermodynamic cycles.

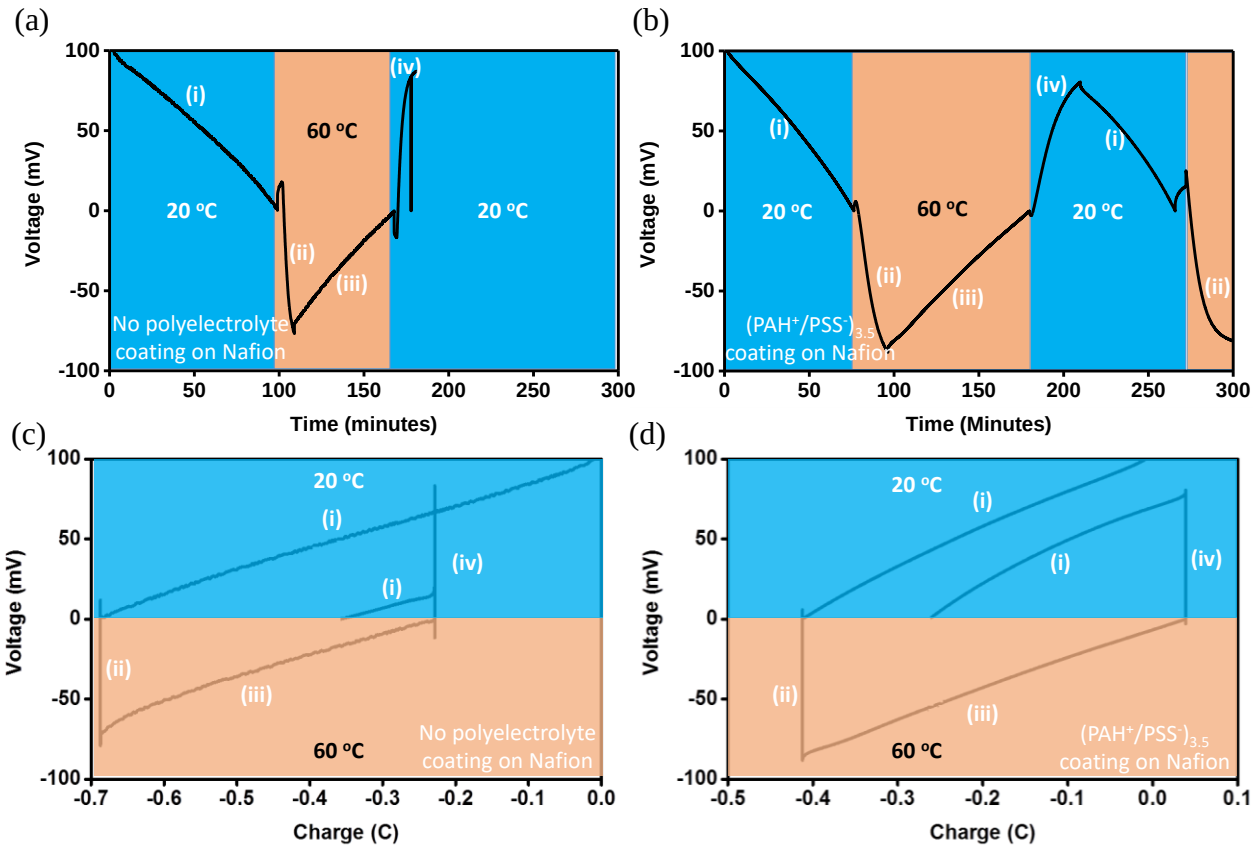

Figure 3.27. The initial autonomous heat harvesting thermodynamic cycles of the cells with the 60 mM $Co(bpy)_3^{2+/3+}{}_{(aq)}$ anolyte and the 60 mM $Fe(CN)_6^{3-/4-}{}_{(aq)}$ catholyte in equal volumes. However, the cells include Nafion with different conditions: (a), (c) Nafion with the optimal $(PAH^+/PSS^-)_{3.5}$ coating and (b), (d) Nafion without any polyelectrolyte coating. (a) – (b) depicts change in voltage over real time, while (c) – (d) shows relation between the cell voltage and charge at each stage of the heat harvesting thermodynamic cycle. Significantly grown overpotential at the beginning of the 2nd cycle was observed at only at (a), where bare Nafion was in the cell.

Figure 3.28 demonstrates the enhanced cyclability of the electrochemical heat harvester with the optimal $(PAH^+/PSS^-)_n$ coating on Nafion. The cell and testing conditions were entirely identical to the thermodynamic cycles represented in **Figure 3.27** (b) and (d). During more than 10 thermodynamic cycles, overpotential could be retained less than 5 mV out of ±80 mV thermally harvested voltages. However, the gradual decomposition of $Co(bpy)_3^{2+}$ species discussed in Section 3.3.5 caused slowly fading charge capacity after the repeated thermodynamic cycles.

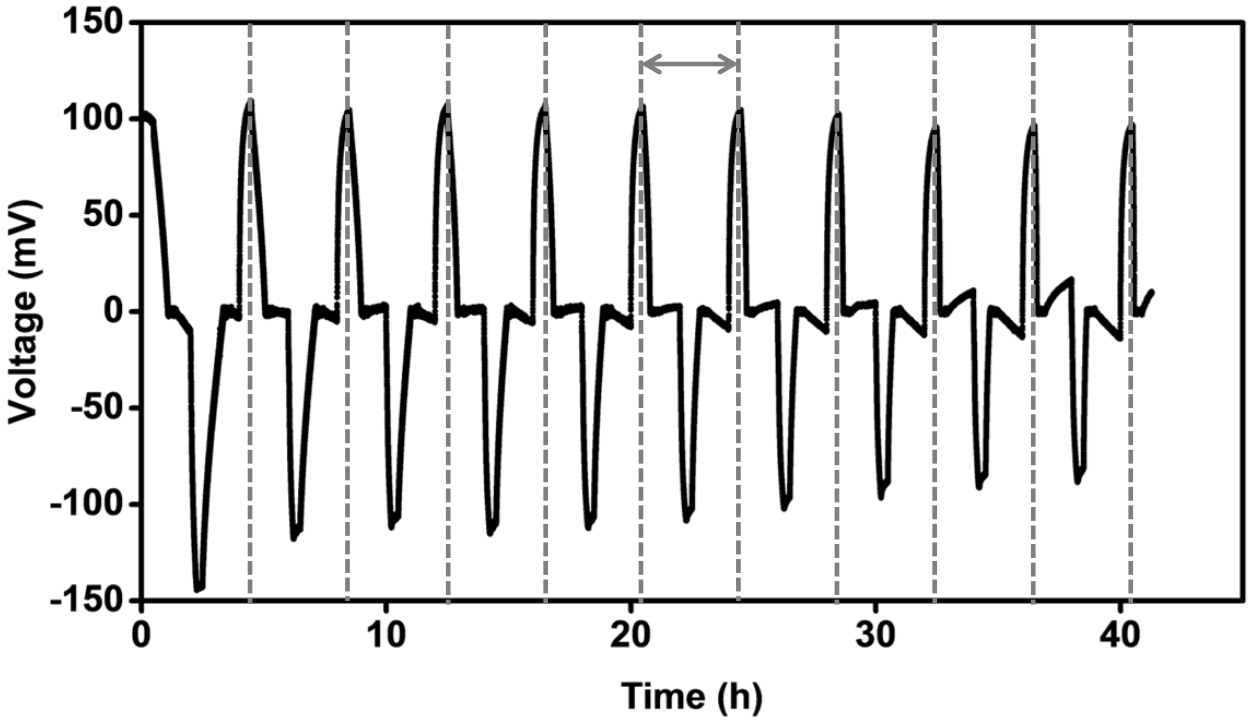

Figure 3.28. 10 consecutive autonomous heat harvesting thermodynamic cycles of a cell configured with 60 mM $Co(bpy)_3^{2+/3+}{}_{(aq)}$ | the optimal $(PAH^+/PSS^-)_{3.5}$-coating on Nafion | 60 mM $Fe(CN)_6^{3-/4-}{}_{(aq)}$. Each grey dashed vertical line corresponds to end of a thermodynamic cycle and onset of the new one. The grey arrow represents a time period for a single thermodynamic cycle.

3.3.11. Effect of Concentrations of the Redox Couples on Energy, Power, and Charge Output

As explained in Section 3.3.3, the solubility limit of $Co(bpy)_3^{2+/3+}{}_{(aq)}$ in water (60 mM maximum) is the major reason for this concentration dependency tests. As can be easily expected, when the concentrations of the redox-active species were tuned, energy, power, and charge capacities exhibited approximate proportionality with the concentrations, until 60 mM concentration was reached (**Figure 3.29** (a) – (c)). It is noteworthy that concentrations and volumes of both $Co(bpy)_3^{2+/3+}{}_{(aq)}$ and $Fe(CN)_6^{3-/4-}{}_{(aq)}$ in the cell were equal consistently throughout the entire examinations. When the concentration was aimed at 70 mM, the $Co(bpy)_3^{2+/3+}{}_{(aq)}$ solution started to precipitate. This observation was helpful to understand a sudden decrease of all 3 performances,

because water may have preference among those two. If this was the case, the molar amount of $Co(bpy)_3^{2+}$ and $Co(bpy)_3^{3+}$ in the anolyte would not be equal anymore, hence the cell would deviate from the optimal configuration, leading to a compromise in all performances. When the concentrations of both $Co(bpy)_3^{2+/3+}{}_{(aq)}$ and $Fe(CN)_6^{3-/4-}{}_{(aq)}$ were 60 mM, the average volumetric energy, power, and charge capacities during a thermodynamic cycle were optimized to 132.1 mJ/mL, 13.95 μW/mL, and 2.84 C/mL, respectively.

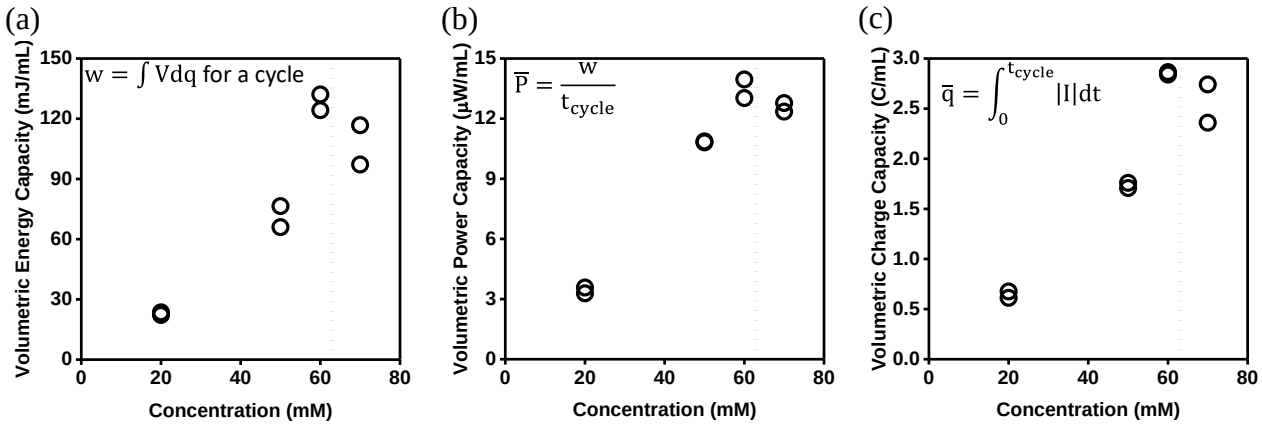

Figure 3.29. The dashed vertical line represents the solubility limit of $Co(bpy)_3^{2+/3+}$ species in water at room temperature. (a) Volumetric energy capacity harnessed by the electrochemical heat harvester during a thermodynamic cycle. (b) Volumetric power density produced by the electrochemical heat harvester during a thermodynamic cycle. (c) Volumetric charge capacity exchanged during a thermodynamic cycle. The inset formulae inform how the performances in the graphs were calculated. The normalization into volumetric capacities accounted combined volumes of the catholyte and the anolyte all together. All 3 performances showed maxima at 60 mM concentration.

3.3.12. Conversion Efficiency of the Electrochemical Heat Harvester

The conversion efficiency is defined as ratio between the output electrical energy and the input heat energy during a thermodynamic cycle[70]. As a result, the conversion efficiency can be expressed as Equation 1.13 in Section 1.3.2.

At the optimal concentration of 60 mM, the volumetric energy output capacity for a thermodynamic cycle was 132.1 mJ/mL ($|\alpha|q\Delta T - E_{loss}$ term). Multiplication of heat capacity of the system and the temperature difference was projected 130.9 J/mL ($C_p\Delta T$ term), and $|\alpha|qT_H$ term was estimated 2.74 J/mL. Thus, the ratio between these values produced a relatively low conversion efficiency, 0.10 %. This low efficiency was mainly attributed to high heat capacity of water. When additional contributions from the Nafion membrane and the redox-active species to the total heat capacity of the system (C_p), the actual efficiency can become even less than 0.10 %. However, the mass of water content in the system could not be easily discarded, as it would be also proportional to the charge capacity term (q) of the system. Decreasing the electrolyte amount of the system would diminish the charge capacity (q) and the heat capacity (C_p) simultaneously.

However, this efficiency under the thermodynamic cycles is still much larger than heat conversion efficiency under thermal gradient operating in a continuous mode (**Figure 1.15** in Section 1.3.2, and Equation 1.5). Assuming the same electrochemical thermopower ($|\alpha|$ = 2.9 mV/K) and ionic conductivity (7.50×10^{-3} S/cm, measured by EIS technique), the efficiency is projected as low as 9.42×10^{-3} %. For this assessment, the thermal conductivity of such system was presumed same as that of liquid water (0.63 W/m·K[71]) under the atmospheric pressure and the average temperature 40 °C. This efficiency is more than an order of magnitude less than the achieved efficiency in this study, under the thermodynamic cycling operation. This conclusion can be extended to other potential electrochemical heat harvesting systems which have similar degree of ionic conductivities; for such electrochemical systems, thermodynamic cyclic operation can better harness heat into electricity.

3.4. Conclusion

In this chapter, we characterized electrochemical potentials and their dependencies on temperature of several aqueous redox couples for electrochemical heat harvesting application. Only $Co(bpy)_3^{2+/3+}{}_{(aq)}$ and $Fe(CN)_6^{3-/4-}{}_{(aq)}$ were determined to fulfill the requirements to build an autonomous electrochemical heat harvester, without need for recharging by external electrical power source during heat harvesting thermodynamic cycles. As half-cell potentials of those two redox couples intersect around 40 °C, operating temperature range of the electrochemical heat harvester was designated as 20 °C – 60 °C, to match the midpoint of the operating temperature range to the intersecting temperature. Carbon cloth was elected as electrodes for the system to guarantee the high electronic conductivity and best power capability by its high surface area. Nafion membrane was adopted in order to prevent internal short-circuit by mixing between the anolyte and the catholyte or direct contact between the carbon cloth electrodes, while still enabling permeation of K^+ cations for charge balance accompanied by the redox reactions. It was identified by XPS and UV-Vis spectroscopy that absorption of $Co(bpy)_3^{2+/3+}{}_{(aq)}$ species into Nafion brought serious damage in ionic conduction. The sustainability of the ionic conductance through the Nafion membrane was critical to maintain the energy output and efficiency performances of the electrochemical heat harvester over long duration. The optimal $(PAH^+/PSS^-)_n$ coating on Nafion deposited via LbL procedures turned out to cure this issue by selective exclusion of $Co(bpy)_3^{2+/3+}{}_{(aq)}$ species. This film on Nafion was composed of PAH^+ and PSS^- polyelectrolytes, and possessed spontaneously formed nanopores in it. Because the average size of the nanopores were smaller than that of $Co(bpy)_3^{2+/3+}{}_{(aq)}$ species, the nanopores could substantially suspend the diffusion of $Co(bpy)_3^{2+/3+}{}_{(aq)}$ species through the $(PAH^+/PSS^-)_n$. By this coating, the heat harvesting thermodynamic cycles without high overpotential could run for 10 cycles, because degradation of Nafion ionic conductivity by $Co(bpy)_3^{2+/3+}{}_{(aq)}$ species could be suppressed for an extended time period. However, the charge capacity of the electrochemical heat harvester gradually faded over time, due to self-decomposition of a redox-active species, $Co(bpy)_3^{2+}$. The projected conversion efficiency of this electrochemical heat harvester was around 0.10 %. The relatively low efficiency was mostly attributed to the high heat capacity of water, of which mass could not be decoupled with the charge capacity and energy output of this prototype. The next chapter will address this issue by an alternatively designed electrochemical heat harvester.

References

1 Hu, R. *et al.* Harvesting Waste Thermal Energy Using a Carbon-Nanotube-Based Thermo-Electrochemical Cell. *Nano letters* **10**, 838-846, doi:10.1021/nl903267n (2010).

2 Salazar, P. F., Stephens, S. T., Kazim, A. H., Pringle, J. M. & Cola, B. A. Enhanced thermo-electrochemical power using carbon nanotube additives in ionic liquid redox electrolytes. *Journal of Materials Chemistry A* **2**, 20676-20682, doi:10.1039/c4ta04749d (2014).

3 Salazar, P. F., Kumar, S. & Cola, B. A. Nitrogen- and Boron-Doped Carbon Nanotube Electrodes in a Thermo-Electrochemical Cell. *Journal of The Electrochemical Society* **159**, B483-B488, doi:10.1149/2.043205jes (2012).

4 Hudak, N. S. & Amatucci, G. G. Energy Harvesting and Storage with Lithium-Ion Thermogalvanic Cells. *Journal of The Electrochemical Society* **158**, A572, doi:10.1149/1.3568820 (2011).

5 S., R. M. *et al.* Carbon Nanotube – Reduced Graphene Oxide Composites for Thermal Energy Harvesting Applications. *Advanced Materials* **25**, 6602-6606, doi:doi:10.1002/adma.201303295 (2013).

6 Yang, Y. *et al.* Charging-free electrochemical system for harvesting low-grade thermal energy. *Proceedings of the National Academy of Sciences of the United States of America* **111**, 17011-17016, doi:10.1073/pnas.1415097111 (2014).

7 Lee, S. W. *et al.* An electrochemical system for efficiently harvesting low-grade heat energy. *Nature communications* **5**, 3942, doi:10.1038/ncomms4942 (2014).

8 Kim, S. L., Lin, H. T. & Yu, C. Thermally Chargeable Solid-State Supercapacitor. *Advanced Energy Materials* **6**, 1600546-n/a, doi:10.1002/aenm.201600546 (2016).

9 Zhao, D. *et al.* Ionic thermoelectric supercapacitors. *Energy & Environmental Science* **9**, 1450-1457, doi:10.1039/c6ee00121a (2016).

10 Ail, U. *et al.* Thermoelectric Properties of Polymeric Mixed Conductors. *Advanced Functional Materials* **26**, 6288-6296, doi:10.1002/adfm.201601106 (2016).

11 Szakálos, P., Hultquist, G. & Wikmark, G. Corrosion of Copper by Water. *Electrochemical and Solid-State Letters* **10**, C63-C67, doi:10.1149/1.2772085 (2007).

12 De Almeida, S. H. & Kawano, Y. Ultraviolet-visible spectra of Nafion membrane. *European Polymer Journal* **33**, 1307-1311, doi:https://doi.org/10.1016/S0014-3057(96)00217-0 (1997).

13 Powell, C. J. & Jablonski, A. Surface sensitivity of X-ray photoelectron spectroscopy. *Nuclear Instruments and Methods in Physics Research Section A: Accelerators, Spectrometers, Detectors and Associated Equipment* **601**, 54-65, doi:https://doi.org/10.1016/j.nima.2008.12.103 (2009).

14 Decher, G. Fuzzy Nanoassemblies: Toward Layered Polymeric Multicomposites. *Science* **277**, 1232-1237, doi:10.1126/science.277.5330.1232 (1997).

15 Gero, D. & Jong-Dal, H. Buildup of ultrathin multilayer films by a self-assembly process, 1 consecutive adsorption of anionic and cationic bipolar amphiphiles on charged surfaces. *Makromolekulare Chemie. Macromolecular Symposia* **46**, 321-327, doi:doi:10.1002/masy.19910460145 (1991).

16 D., G. T., E., M. G. & C., W. F. The morphology in nafion perfluorinated membrane products, as determined by wide- and small-angle x-ray studies. *Journal of Polymer Science: Polymer Physics Edition* **19**, 1687-1704, doi:doi:10.1002/pol.1981.180191103 (1981).

17 Heitner-Wirguin, C. Recent advances in perfluorinated ionomer membranes: structure, properties and applications. *Journal of Membrane Science* **120**, 1-33, doi:https://doi.org/10.1016/0376-7388(96)00155-X (1996).

18 Mauritz, K. A. & Moore, R. B. State of Understanding of Nafion. *Chemical reviews* **104**, 4535-4586, doi:10.1021/cr0207123 (2004).

19 Wu, B. *et al.* Reorganization of hydrogen bond network makes strong polyelectrolyte brushes pH-responsive. *Science Advances* **2**, doi:10.1126/sciadv.1600579 (2016).

20 Stuart, M. A. C. *et al.* Emerging applications of stimuli-responsive polymer materials. *Nature materials* **9**, 101, doi:10.1038/nmat2614 (2010).

21 Mura, S., Nicolas, J. & Couvreur, P. Stimuli-responsive nanocarriers for drug delivery. *Nature materials* **12**, 991, doi:10.1038/nmat3776 (2013).

22 Cobo, I., Li, M., Sumerlin, B. S. & Perrier, S. Smart hybrid materials by conjugation of responsive polymers to biomacromolecules. *Nature materials* **14**, 143, doi:10.1038/nmat4106 (2014).

23 Anantharamulu, N. *et al*. A wide-ranging review on Nasicon type materials. *Journal of Materials Science* **46**, 2821-2837, doi:10.1007/s10853-011-5302-5 (2011).

24 Fergus, J. W. Ion transport in sodium ion conducting solid electrolytes. *Solid State Ionics* **227**, 102-112, doi:https://doi.org/10.1016/j.ssi.2012.09.019 (2012).

25 Whittingham, M. S. & Huggins, R. A. Measurement of Sodium Ion Transport in Beta Alumina Using Reversible Solid Electrodes. *The Journal of chemical physics* **54**, 414-416, doi:10.1063/1.1674623 (1971).

26 Yung-Fang Yu, Y. & Kummer, J. T. Ion exchange properties of and rates of ionic diffusion in beta-alumina. *Journal of Inorganic and Nuclear Chemistry* **29**, 2453-2475, doi:https://doi.org/10.1016/0022-1902(67)80301-4 (1967).

27 Bachman, J. C. *et al.* Inorganic Solid-State Electrolytes for Lithium Batteries: Mechanisms and Properties Governing Ion Conduction. *Chemical reviews* **116**, 140-162, doi:10.1021/acs.chemrev.5b00563 (2016).

28 Knauth, P. Inorganic solid Li ion conductors: An overview. *Solid State Ionics* **180**, 911-916, doi:10.1016/j.ssi.2009.03.022 (2009).

29 Deng, Y. *et al.* Structural and Mechanistic Insights into Fast Lithium-Ion Conduction in Li4SiO4–Li3PO4 Solid Electrolytes. *Journal of the American Chemical Society* **137**, 9136-9145, doi:10.1021/jacs.5b04444 (2015).

30 Murayama, M. *et al.* Synthesis of New Lithium Ionic Conductor Thio-LISICON—Lithium Silicon Sulfides System. *Journal of Solid State Chemistry* **168**, 140-148, doi:https://doi.org/10.1006/jssc.2002.9701 (2002).

31 Tachez, M., Malugani, J.-P., Mercier, R. & Robert, G. Ionic conductivity of and phase transition in lithium thiophosphate Li3PS4. *Solid State Ionics* **14**, 181-185, doi:https://doi.org/10.1016/0167-2738(84)90097-3 (1984).

32 Kanno, R. & Murayama , M. Lithium Ionic Conductor Thio-LISICON: The Li2 S - GeS2 - P 2 S 5 System. *Journal of The Electrochemical Society* **148**, A742-A746, doi:10.1149/1.1379028 (2001).

33 Kamaya, N. *et al.* A lithium superionic conductor. *Nature materials* **10**, 682, doi:10.1038/nmat3066 (2011).

34 Colomban, P. *Proton conductors : solids, membranes, and gels--materials and devices*. (Cambridge ; New York : Cambridge University Press, 1992., 1992).

35 Biesinger, M. C. *et al.* Resolving surface chemical states in XPS analysis of first row transition metals, oxides and hydroxides: Cr, Mn, Fe, Co and Ni. *Applied Surface Science* **257**, 2717-2730, doi:https://doi.org/10.1016/j.apsusc.2010.10.051 (2011).

36 Yang, W., Hao, Y., Ghamgosar, P. & Boschloo, G. Thermal Stability Study of Dye-Sensitized Solar Cells with Cobalt Bipyridyl–based Electrolytes. *Electrochimica Acta* **213**, 879-886, doi:https://doi.org/10.1016/j.electacta.2016.07.112 (2016).

37 Gao, J., Bhagavathi Achari, M. & Kloo, L. Long-term stability for cobalt-based dye-sensitized solar cells obtained by electrolyte optimization. *Chemical Communications* **50**, 6249-6251, doi:10.1039/c4cc00698d (2014).

38 Jiang, R. *et al.* 2000 hours photostability testing of dye sensitised solar cells using a cobalt bipyridine electrolyte. *Journal of Materials Chemistry A* **2**, 4751-4757, doi:10.1039/c4ta00402g (2014).

39 Prakash, G. K. S. *et al.* Thermocontrolled benzylimine–benzaldimine rearrangement over Nafion-H catalysts for efficient entry into α-trifluoromethylbenzylamines. *Tetrahedron Letters* **53**, 607-611, doi:https://doi.org/10.1016/j.tetlet.2011.11.088 (2012).

40 Burgess, J. & Haines, R. I. Solubility of 2,2'-bipyridyl in binary aqueous solvent mixtures. *Chemistry & Industry*, 289-289 (1980).

41 Logette, S., Eysseric, C., Pourcelly, G., Lindheimer, A. & Gavach, C. Selective permeability of a perfluorosulphonic membrane to different valency cations. Ion-exchange isotherms and kinetic aspects. *Journal of Membrane Science* **144**, 259-274, doi:https://doi.org/10.1016/S0376-7388(98)00062-3 (1998).

42 Irvine, G. J., Rajesh, S., Georgiadis, M. & Phillip, W. A. Ion Selective Permeation Through Cellulose Acetate Membranes in Forward Osmosis. *Environmental Science & Technology* **47**, 13745-13753, doi:10.1021/es403581t (2013).

43 Piera, E. *et al.* Separation of alcohols and alcohols/O2 mixtures using zeolite MFI membranes. *Journal of Membrane Science* **142**, 97-109, doi:https://doi.org/10.1016/S0376-7388(97)00321-9 (1998).

44 McLeary, E. E., Jansen, J. C. & Kapteijn, F. Zeolite based films, membranes and membrane reactors: Progress and prospects. *Microporous and Mesoporous Materials* **90**, 198-220, doi:https://doi.org/10.1016/j.micromeso.2005.10.050 (2006).

45 Brinker, C. J. *et al.* Sol-gel strategies for controlled porosity inorganic materials. *Journal of Membrane Science* **94**, 85-102, doi:https://doi.org/10.1016/0376-7388(93)E0129-8 (1994).

46 Nishiyama, N., Gora, L., Teplyakov, V., Kapteijn, F. & Moulijn, J. A. Evaluation of reproducible high flux silicalite-1 membranes: gas permeation and separation characterization. *Separation and Purification Technology* **22-23**, 295-307, doi:https://doi.org/10.1016/S1383-5866(00)00152-0 (2001).

47 M., v. d. G. J., Freek, K. & A., M. J. Modeling permeation of binary mixtures through zeolite membranes. *AIChE Journal* **45**, 497-511, doi:doi:10.1002/aic.690450307 (1999).

48 Zhu, W., Kapteijn, F., Moulijn, J. A., den Exter, M. C. & Jansen, J. C. Shape Selectivity in Adsorption on the All-Silica DD3R. *Langmuir : the ACS journal of surfaces and colloids* **16**, 3322-3329, doi:10.1021/la9914007 (2000).

49 Cheng, C., Yaroshchuk, A. & Bruening, M. L. Fundamentals of Selective Ion Transport through Multilayer Polyelectrolyte Membranes. *Langmuir : the ACS journal of surfaces and colloids* **29**, 1885-1892, doi:10.1021/la304574e (2013).

50 Liu, X. & Bruening, M. L. Size-Selective Transport of Uncharged Solutes through Multilayer Polyelectrolyte Membranes. *Chemistry of Materials* **16**, 351-357, doi:10.1021/cm034559k (2004).

51 L., B. M. & M., S. D. Enhancing the Ion-Transport Selectivity of Multilayer Polyelectrolyte Membranes. *Chemistry – A European Journal* **8**, 3832-3837, doi:doi:10.1002/1521-3765(20020902)8:17<3832::AID-CHEM3832>3.0.CO;2-8 (2002).

52 Manning, G. S. Limiting laws and counterion condensation in polyelectrolyte solutions. 8. Mixtures of counterions, species selectivity, and valence selectivity. *The Journal of Physical Chemistry* **88**, 6654-6661, doi:10.1021/j150670a030 (1984).

53 Hoshi, T. *et al.* Selective Permeation of Hydrogen Peroxide through Polyelectrolyte Multilayer Films and Its Use for Amperometric Biosensors. *Analytical Chemistry* **73**, 5310-5315, doi:10.1021/ac010605t (2001).

54 Tiara, P., Haizhou, Y. & Klaus-Viktor, P. Charge- and Size-Selective Molecular Separation using Ultrathin Cellulose Membranes. *ChemSusChem* **9**, 2908-2911, doi:doi:10.1002/cssc.201600791 (2016).

55 Li, J. *et al.* Preparation and properties of ZSM-5 zeolite membrane obtained by low-temperature chemical vapor deposition. *Desalination* **147**, 321-326, doi:https://doi.org/10.1016/S0011-9164(02)00559-3 (2002).

56 Tieke, B., Toutianoush, A. & Jin, W. Selective transport of ions and molecules across layer-by-layer assembled membranes of polyelectrolytes, p-sulfonato-calix[n]arenes and Prussian Blue-type complex salts. *Advances in Colloid and Interface Science* **116**, 121-131, doi:https://doi.org/10.1016/j.cis.2005.05.003 (2005).

57 Jin, W., Toutianoush, A. & Tieke, B. Size- and charge-selective transport of aromatic compounds across polyelectrolyte multilayer membranes. *Applied Surface Science* **246**, 444-450, doi:https://doi.org/10.1016/j.apsusc.2004.11.067 (2005).

58 White, N., Misovich, M., Yaroshchuk, A. & Bruening, M. L. Coating of Nafion Membranes with Polyelectrolyte Multilayers to Achieve High Monovalent/Divalent Cation Electrodialysis Selectivities. *ACS applied materials & interfaces* **7**, 6620-6628, doi:10.1021/am508945p (2015).

59 Budd, P. M. in *Comprehensive Polymer Science and Supplements* (eds Geoffrey Allen & John C. Bevington) 215-230 (Pergamon, 1989).

60 Kilduff, J. E., Karanfil, T., Chin, Y.-P. & Weber, W. J. Adsorption of Natural Organic Polyelectrolytes by Activated Carbon: A Size-Exclusion Chromatography Study. *Environmental Science & Technology* **30**, 1336-1343, doi:10.1021/es950547r (1996).

61 Feng, L., Stuart, M. C. & Adachi, Y. Dynamics of polyelectrolyte adsorption and colloidal flocculation upon mixing studied using mono-dispersed polystyrene latex particles. *Advances in Colloid and Interface Science* **226**, 101-114, doi:https://doi.org/10.1016/j.cis.2015.09.004 (2015).

62 Wilson, J. T., Cui, W. & Chaikof, E. L. Layer-by-Layer Assembly of a Conformal Nanothin PEG Coating for Intraportal Islet Transplantation. *Nano letters* **8**, 1940-1948, doi:10.1021/nl080694q (2008).

63 Krogman, K. C., Lowery, J. L., Zacharia, N. S., Rutledge, G. C. & Hammond, P. T. Spraying asymmetry into functional membranes layer-by-layer. *Nature materials* **8**, 512, doi:10.1038/nmat2430 (2009).

64 Pinho, S. P. & Macedo, E. A. Solubility of NaCl, NaBr, and KCl in Water, Methanol, Ethanol, and Their Mixed Solvents. *Journal of Chemical & Engineering Data* **50**, 29-32, doi:10.1021/je049922y (2005).

65 Seyrek, E., Hierrezuelo, J., Sadeghpour, A., Szilagyi, I. & Borkovec, M. Molecular mass dependence of adsorbed amount and hydrodynamic thickness of polyelectrolyte layers. *Physical Chemistry Chemical Physics* **13**, 12716-12719, doi:10.1039/c1cp20654k (2011).

66 Netz, R. R. & Andelman, D. Neutral and charged polymers at interfaces. *Physics Reports* **380**, 1-95, doi:https://doi.org/10.1016/S0370-1573(03)00118-2 (2003).

67 Claesson, P. M., Poptoshev, E., Blomberg, E. & Dedinaite, A. Polyelectrolyte-mediated surface interactions. *Advances in Colloid and Interface Science* **114-115**, 173-187, doi:https://doi.org/10.1016/j.cis.2004.09.008 (2005).

68 Marcus, Y. Ionic radii in aqueous solutions. *Chemical reviews* **88**, 1475-1498, doi:10.1021/cr00090a003 (1988).

69 Hupp, J. T. & Weaver, M. J. Solvent, ligand, and ionic charge effects on reaction entropies for simple transition-metal redox couples. *Inorganic Chemistry* **23**, 3639-3644, doi:10.1021/ic00190a042 (1984).

70 Howell, J. R. & Buckius, R. O. *Fundamentals of engineering thermodynamics*. (New York : McGraw-Hill, 2nd ed., 1992).

71 Huber, M. L. *et al.* New International Formulation for the Thermal Conductivity of H2O. *Journal of Physical and Chemical Reference Data* **41**, 033102, doi:10.1063/1.4738955 (2012).

4. Design of P2-Na_xCoO_2 Based Na-ion Battery-type Electrochemical Heat Harvester

4.1. Introduction

Efficient conversion of low grade heat into electricity has been intensively investigated mostly focusing on thermoelectrics. However, state-of-the-art thermoelectric materials in general incorporate rare and expensive elements, hampering their widespread application in daily lives. Electrochemical heat conversion has drawn scientific attention as one of alternatives to thermoelectric technology, largely owing to its capability to easily reach thermopower more than 1 mV/K[1-3]. However, low ionic conductivity has compromised the potential improvement on conversion efficiency due to large thermopower, when the electrochemical heat conversion operated under thermal gradient[1,4,5]. Recent breakthrough addressed the efficiency issue by transitioning the mode of operation into thermodynamic cycles like heat engines[6-10], achieving up to 2.0 % of conversion efficiency between 20 °C and 60 °C[6]. If higher electrochemical thermopowers can be accomplished in addition to this new design, then more advanced efficiency would be achieved.

In this study, we invented a novel solid-state electrochemical heat harvesting system, in order to address several issues discovered in the previous aqueous redox couple-based electrochemical heat harvester. The first issue on coupling between the high heat capacity and the charge capacity was resolved by replacing the aqueous redox couples into solid-state electrodes. This new electrochemical heat harvester based on solid-state electrode did not need pricey Nafion. Lastly, the electrochemical potentials of solid-state electrodes could be tuned continuously, so that broader selection of candidate materials could be permitted for the electrochemical heat harvesting application. As the growth of overpotential turned out the most critical drawback of the aqueous redox couple-based electrochemical heat harvester, Na_xCoO_2 was chosen as an electrode material with both high electronic and ionic conductivity to minimize overpotential. Ball-milling on as-synthesized P2-Na_xCoO_2 led to complete disorder of the material. This process transformed the crystal structure of Na_xCoO_2 from P2-phase crystal into amorphous phase. The disruption of the crystal structure resulted in loss of redox activity and eventually, huge enhancement on electrochemical thermopower from -0.65 mV/K to 9.50 mV/K at 2.3 V vs. Na/Na^+. In order to fully exploit electrochemical thermopowers from both P2-Na_xCoO_2 and BM-Na_xCoO_2, dual cell

stack was designed. The dual cell stack required a cell consisting P2-Na_xCoO_2 cathode, Na metal anode in 1 M $NaClO_4$ in PC electrolyte, and another cell composed of BM-Na_xCoO_2 cathode, Na metal anode in 1 M $NaClO_4$ in PC electrolyte. Both cells were set at equal electrochemical potential of 2.3 V vs. Na/Na^+ at the midpoint temperature (30 °C) of the intended temperature range (20 °C – 40 °C), and they were serially connected in opposite directions. The voltages from each cell canceled out, while adding up for the increased total thermopower of the dual cell stack. Up to 6.30 % of the conversion efficiency is expected, provided that the heat capacity of this electrochemical harvester can be minimized. Such efforts can include minimization of the mass of PC-based liquid electrolyte or alternative usage of solid-state electrolyte in thin films. This research paved an exemplar framework for the more efficient future autonomous electrochemical heat harvesters without need for external electrical power source.

4.2. Experimental Methods

4.2.1. Synthesis of P2-Na_xCoO_2 and Its Ball-milling Process

For synthesis of P2-Na_xCoO_2, anhydrous Na_2CO_3 (Sigma-Aldrich, 222321, ≥ 99.5 %) and Co_3O_4 (Beantown Chemical, 215780, 99.5 %) were thoroughly ground together by mortar and pestle. The initial molar ratio of Na element to Co element was adjusted to 0.8. The mixture was pressed into a 1-inch diameter pellet at 10 metric tons of uniaxial force for 30 minutes. The typical mass of this pellet ranged between 2.0 g and 2.5 g. The pellet was firstly calcined at 850 °C for 24 hours under dry oxygen environment (Airgas, 99.5 %). This process enabled a solid-state reaction between Na and Co precursors, thereby producing P2-Na_xCoO_2[11,12]. After the first calcination, the pellet was ground with mortar and pestle again and pressed into a 1-inch diameter pellet at the same condition. The pellet was sintered at 850 °C for 24 hours under dry oxygen environment once more, in order to encourage thorough chemical reaction among the residual precursors so that the resultant pellet became purely composed of P2-Na_xCoO_2. After this second sintering process, the pellet was ground with mortar and pestle and the resultant powder was stored in Ar-filled dry glove box to prevent undesirable intercalation of water molecules into P2-Na_xCoO_2 crystal by humidity[13].

In order to induce structural disorder to the as-synthesized P2-Na_xCoO_2, ball-milling process was carried out. Zirconia (ZrO_2) balls with 1.0 mm diameter and P2-Na_xCoO_2 powder were mixed in 10 to 1 mass ratio and put inside a zirconia ball-milling jar. The entire jar with the balls and the powder was transferred into the Ar-filled, dry glove box and sealed inside a heat-sealable plastic bag (Aldrich, Z183385). As a result, the ball-milling process could be executed in an inert condition without unintended chemical reactions, such as intercalation of water from ambient air. Ball-milling was performed at 550 RPM for 48 hours, in order to guarantee minimal particle size and maximal disruption in the crystal structure. The notation of the consequent material from the ball-milling procedure in this article is BM-Na_xCoO_2.

4.2.2. Material Characterization of P2-Na_xCoO_2 and Ball-milled Na_xCoO_2

In order to determine crystallinity of the two forms of Na_xCoO_2 and possible impurity phases in them, powder X-ray diffraction (XRD) technique was carried out. The measurements

were executed in a Panalytical X'Pert Pro with Cu K α source (wavelength 0.15418 nm). The powder was mounted on a silicon zero-background diffraction holder for the measurement.

Field emission scanning electron microscopy (FESEM, Zeiss, Ultra55) observed morphologies and particle sizes of P2-Na_xCoO_2 and BM-Na_xCoO_2. The acceleration voltage was 20 kV, and metallic coating on the surface of powders were not conducted. In-lens detector collected the micrograph images, by capturing backscattering of the incident electron beam.

4.2.3. Electrode Preparation

P2-Na_xCoO_2 electrode was generated by mixing the as-synthesized P2-Na_xCoO_2 powder, KS6 synthetic graphite (TIMCAL), carbon black Super P (TIMCAL), and polyvinylidene fluoride (PVDF, Kynar) binder under 80:5:5:10 mass ratio. BM-Na_xCoO_2 electrode was fabricated from 9:1 w/w mixture of BM-Na_xCoO_2 powder and PVDF. KS6 and Super P conducted electrons necessary for redox reactions, while PVDF held the electronically conductive carbon and P2-Na_xCoO_2 on Al foil.

During the fabrication of both P2-Na_xCoO_2 and BM-Na_xCoO_2 electrodes, mortar and pestle firstly homogenized the powder. Then N-methyl-2-pyrrolidone (NMP, Sigma-Aldrich 328634) was applied into the mortar and pestle generate uniform slurry. The slurry was casted on cleaned Al foil with a doctor blade. The residual NMP was completely dried firstly at 70 °C in air for 2 hours and secondly at 80 °C under vacuum overnight.

After the thorough evaporation of NMP and water from the electrodes, they were punched into 10 mm-diameter disks and pressed with uniaxial force of 5 metric tons for about 10 minutes. The purpose of pressing was to improve electronic connection between the Al foil substrates and active materials. These fully processed electrodes were kept in Ar-filled dry glove box.

4.2.4. Cell Preparation

As-prepared P2-Na_xCoO_2 and BM-Na_xCoO_2 cathodic electrodes were weighed to estimate the theoretical charge capacities and placed in 2016 coin cell cases. 2016 coin cell has 20 mm of diameter and 1.6 mm of height after the completion. This is composed of passivated stainless steel so that unintended electrochemical side reactions may not happen. GF/A Whatman® glass microfiber filters (Aldrich, Z242152) were sliced into 19 mm-diameter disks in order to serve as

separators preventing internal short-circuit. The separator was put on top of the cathode, and sufficient volume of 1 M anhydrous $NaClO_4$ (Alfa Aesar, 98.0 - 102.0%) in propylene carbonate (PC, BASF, Selectilyte) electrolyte was applied. Na metal (Sigma-Aldrich, 28206) stored in the Ar-filled dry glove box was comprehensively scratched with brush in order to strip native oxide on the surface. The brushed Na metal was placed on the wet separator and then the lid was closed. The assembly was finalized by a crimper, which realized airtight sealing, so that consequent electrochemical characterizations could be implemented in air.

4.2.5. Characterization of Electrochemical Thermopowers under Isothermal Condition

The electrochemical thermopowers of the solid-state electrodes were measured under isothermal conditions (**Figure 4.1**). This means a full cell with a anode and a cathode were placed at open circuit condition and put under different temperatures periodically, such as 10 °C, 20 °C, 30 °C, 40 °C for an hour at each temperature. The duration was empirically decided for stable formation of steady-states. 2016 coin cell turned out suitable for this setup because its thin and small geometry could facilitate thermal conduction through the cell, so that steady-states could be founded readily.

Figure 4.1 (a) shows a photograph of the actual electrochemical thermopower measurement setup. On the left, a programmable power source (Keithley 2400 SourceMeter), which provided and controlled electrical power to the Peltier plates is shown. The Peltier plates regulated the temperature of the enclosed coin cell periodically. The temperatures of the both sides of the coin cell surfaces were monitored by two different branches of thermocouples (**Figure 4.1** (b)). The thermal contacts between the cell surfaces and thermocouples were maintained by thin Cu tape. The open circuit voltage (OCV) of the cell was recorded by a Biologic (model SP300 or VSP300) potentiostat. The most notable feature of this thermopower measurement was that it could detect the electrochemical thermopowers at specific state of charge (SoC) of the cathode materials.

(a)

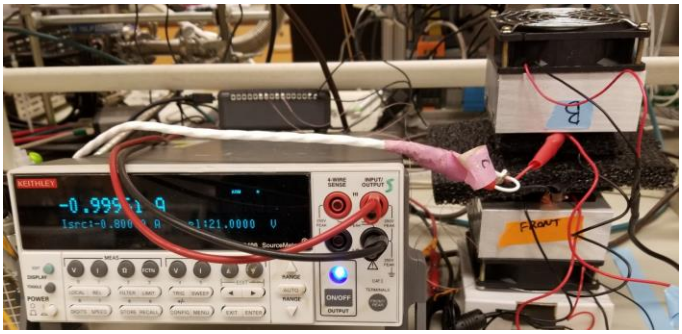

(b)

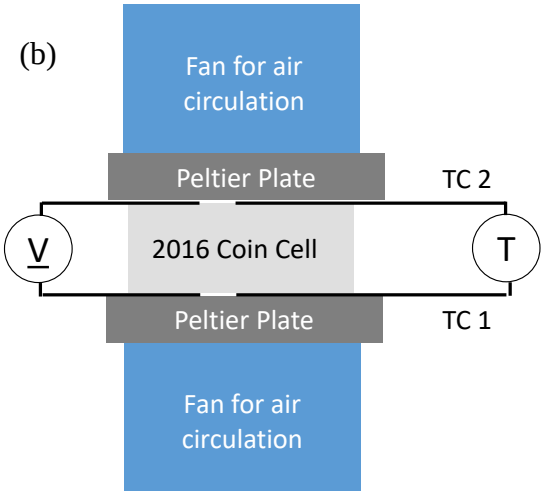

Figure 4.1. A lab-customized equipment for electrochemical thermopower characterization under isothermal conditions. At this setup, temperature of the cell is varied periodically, after steady-states were established in the cell. (a) a photograph, and (b) schematics of the setup. Peltier plates enveloping a 2016 coin cell controlled the heat flow toward/out of the cell. The temperature and voltage responses were recorded by two independent thermocouples (TC 1 and TC 2) and a potentiostat, respectively.

Figure 4.2 depicts a calibration measurement by a 2016 coin cell composed of Li_xCoO_2 cathode, Li metal anode, and 1 M $LiPF_6$ in a 3:7 w/w ethylene carbonate (EC):ethyl methyl carbonate (EMC) electrolyte (LP57, BASF, Selectilyte). The coin cell underwent a cycle of galvanostatic (constant current) charge and discharge at C/20 rate (i.e. 20 hours were required to remove or provide 1 mole of electrons from 1 mole of cobalt in Li_xCoO_2) between 3.6 V and 4.2 V vs. Li/Li^+. By this procedure, it could be confirmed whether the cell performed normally. After this performance-checking galvanostatic cycle, the cell was heated to 40 °C, and galvanostatically charged to the desired SoC (3.9 V vs. Li/Li^+ in this case). 3.9 V vs. Li/Li^+ was deliberately selected because this electrochemical potential corresponded to the plateau potential of Li_xCoO_2. As self-discharge effect is also pervasive in Li-ion batteries[14,15] just like other categories of batteries, it lowers voltage over time. By adjusting the voltage of the cell at the plateau potential, effect of self-discharge on voltage could be minimized, because change in SoC could affect voltage only very limitedly. After these steps, the temperature was decreased by 10 °C every hour at open circuit

condition. The OCV during this stage were recorded and compared with temperature profile. The comparison between steady-state OCVs and temperatures show linear relationship, and the slope of this line was the electrochemical thermopower of Li_xCoO_2 against Li metal, at 3.90 V vs. Li/Li^+. The measured thermopower -0.4796 mV/K matched well with the previous report at the same electrochemical potential[16-18]. As the measured thermopower contained two separate thermopower contributions from both Li_xCoO_2 and Li (Equation 1.14), it could be further distinguished by another thermopower measurement under thermal gradient, as will be clarified later.

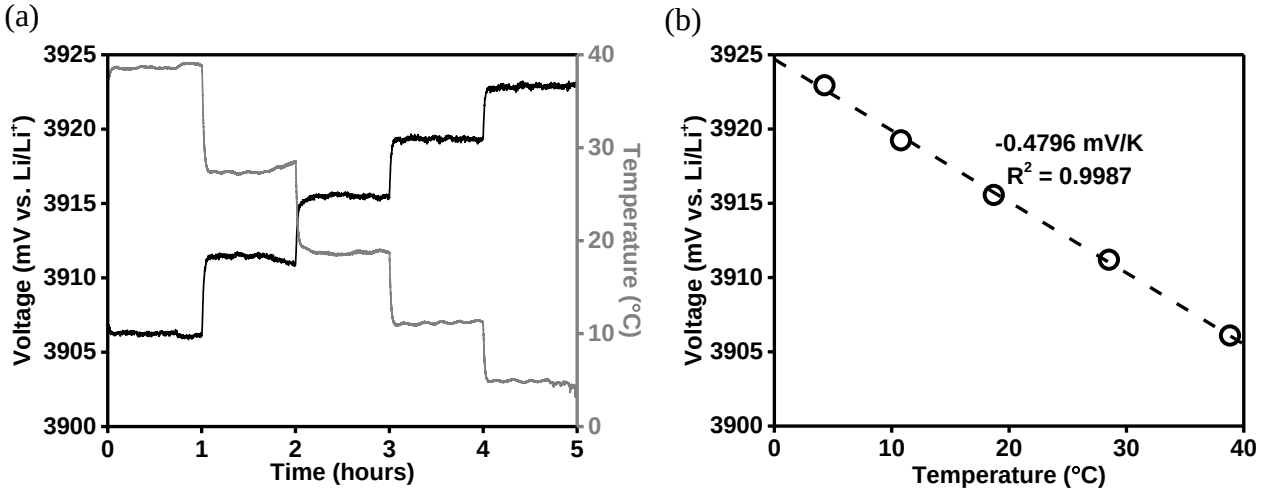

Figure 4.2. Calibration of the electrochemical thermopower measurement setup shown in **Figure 4.1**, using a 2016 coin cell containing Li_xCoO_2 cathode | LP57 electrolyte | Li metal anode. The SoC of Li_xCoO_2 cathode was set at 3.90 V vs. Li/Li^+. (a) Temperature and OCV profiles during periodically accustomed current through the Peltier plates. One hour was permitted per step in order to create steady-states for both OCV and temperature. The steady-states were confirmed by flat profiles for both OCV and temperature. (b) OCV and temperature at steady-states exhibited linearity, yielding -0.4796 mV/K electrochemical thermopower of Li_xCoO_2 at 3.90 V vs. Li/Li^+. This thermopower represented the combined contributions of two electrochemical thermopowers from Li metal anode and Li_xCoO_2 cathode (Equation 1.14)[18].

4.2.6. Characterization of Electrochemical Thermopowers under Thermal Gradient

In order to assess the electrochemical thermopowers of solid-state redox couples, the most straightforward measurements were considered: checking the voltage changes at different

temperature gradients. To realize this, steady maintenance of thermal gradient was important, along with chemical stability of the testing cell contacting the aqueous solution specimens. An electrolyte container composed of Teflon was chosen, due to its good mechanical, chemical, thermal stability and electrical insulation. The testing cell was sealed tightly by two Cu plates. They were electronically and thermally conductive, enabling detection of the voltage and thorough conduction of the heat flux.

In order to assemble all parts into an integrated testing cell (**Figure 4.3** (a)), firstly two O-rings composed of a chemically inert fluoropolymer elastomer (Viton rubber) were inserted at the mouths of the Teflon body. Pieces of malleable and sticky Na metal and Li metal were cut in the dry, Ar-filled glove box. They were fixed on the inner surfaces of Cu plates, and native surface oxide layer was removed by brush. Then a Cu plate with the attached Li or Na metal was tightly enclosed on the Teflon body. The closed end was put on a flat ground in the glove box, and electrolyte was poured so that it could fill the internal space completely without any bubble. The applied electrolyte was LP57 for Li metal and 1 M $NaClO_4$ in PC for Na metal. Then another Cu plate attaching either Li metal or Na metal was tightly closed to seal the testing cell. The completely assembled testing cell was taken out of the glove box for measurements.

Two separate T-type thermocouples (Omega Engineering, 5TC-TT-T-40-36) were firmly attached by electrically conductive Cu tapes (McMaster Carr, 76555A644) on the surface of each Cu plate, in order to observe temperatures at the hot side and the cold side of the cell. Those thermocouples were connected to a temperature data acquisition module (Omega Engineering, TC-08), which converted signals from thermocouples into digital data. Wire leads from each Cu plate were also connected to a Biologic (model SP300 or VSP300) potentiostat to record the voltage difference between the hot end and the cold end. Peltier plates sandwiched the testing cell, and periodically varied electrical current was supplied. A programmable electrical power source (Tektronix, Keithley 2400 Sourcemeter) regulated the input current to the Peltier plates, hence thermal gradient. The programmed current supply regulated the temperature gradient through the testing cell (**Figure 4.3** (b)). Lastly, a heavy metal block on top of the testing cell ensured thermal conduction from the Peltier plates to the cell by a moderate mechanical pressure (**Figure 4.3** (c)). Once this set of procedures were carried out, then a electrochemical thermopower was ready to be characterized.

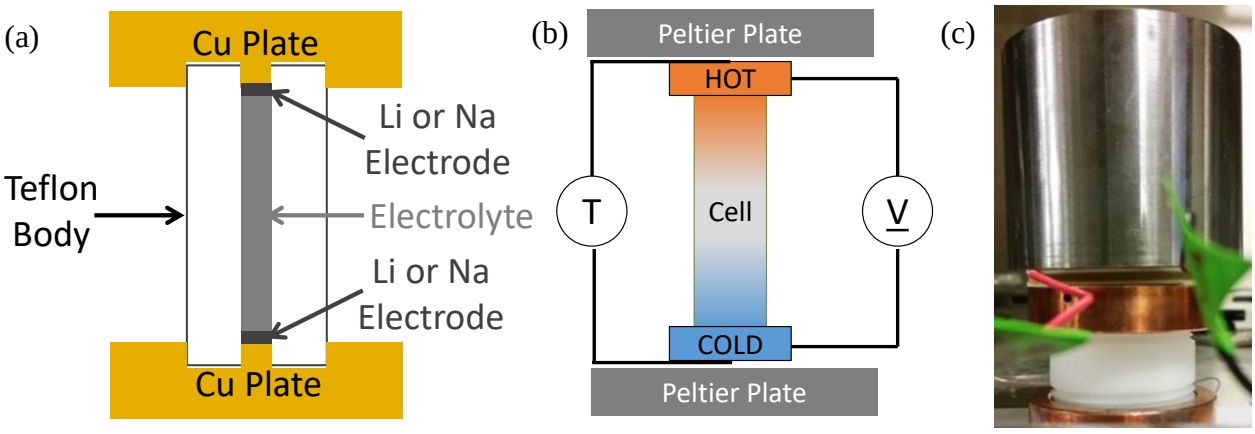

Figure 4.3. (a) Design of the testing cell for electrochemical thermopower characterization under thermal gradient. (b) Schematic representation of the testing cell under a thermal gradient by the two surrounding Peltier plates. Temperatures at the hot end and the cold end, and voltage difference between those ends were recorded. (c) A real photograph of the cell under experiment. A heavy metal block applied mechanical pressure, in order to promote suitable electrical and thermal contacts between the cell, Peltier plates, and thermocouples.

This setup for electrochemical thermopower characterization under thermal gradient is proven effective for solid-state redox couples as well. Thermal gradient and voltage over time profiles were represented at **Figure 4.4** (a) – (b) for Li | LP57 | Li symmetric cell and (c) – (d) for Na | 1 M $NaClO_4$ in PC | Na symmetric cell, respectively. As can be seen at **Figure 4.4** (a) and (c), both temperature difference and voltage successfully formed steady-states as evidenced by the plateaus. Also, steady-states of voltage and temperature difference corresponded to each other. This means that the voltage responses were prompt upon the thermal gradient stimuli, suggesting their kinetics were not sluggish. Again, the slopes of those steady-state voltages and temperature differences were electrochemical thermopowers of Li in LP57 and Na in 1 M $NaClO_4$ in PC, respectively. From the half-cell electrochemical thermopower of Li in LP57 and the full cell thermopower of Li | LP57 | Li_xCoO_2 shown in **Figure 4.2**, pure thermopower of Li_xCoO_2 can be obtained using Equation 1.14.

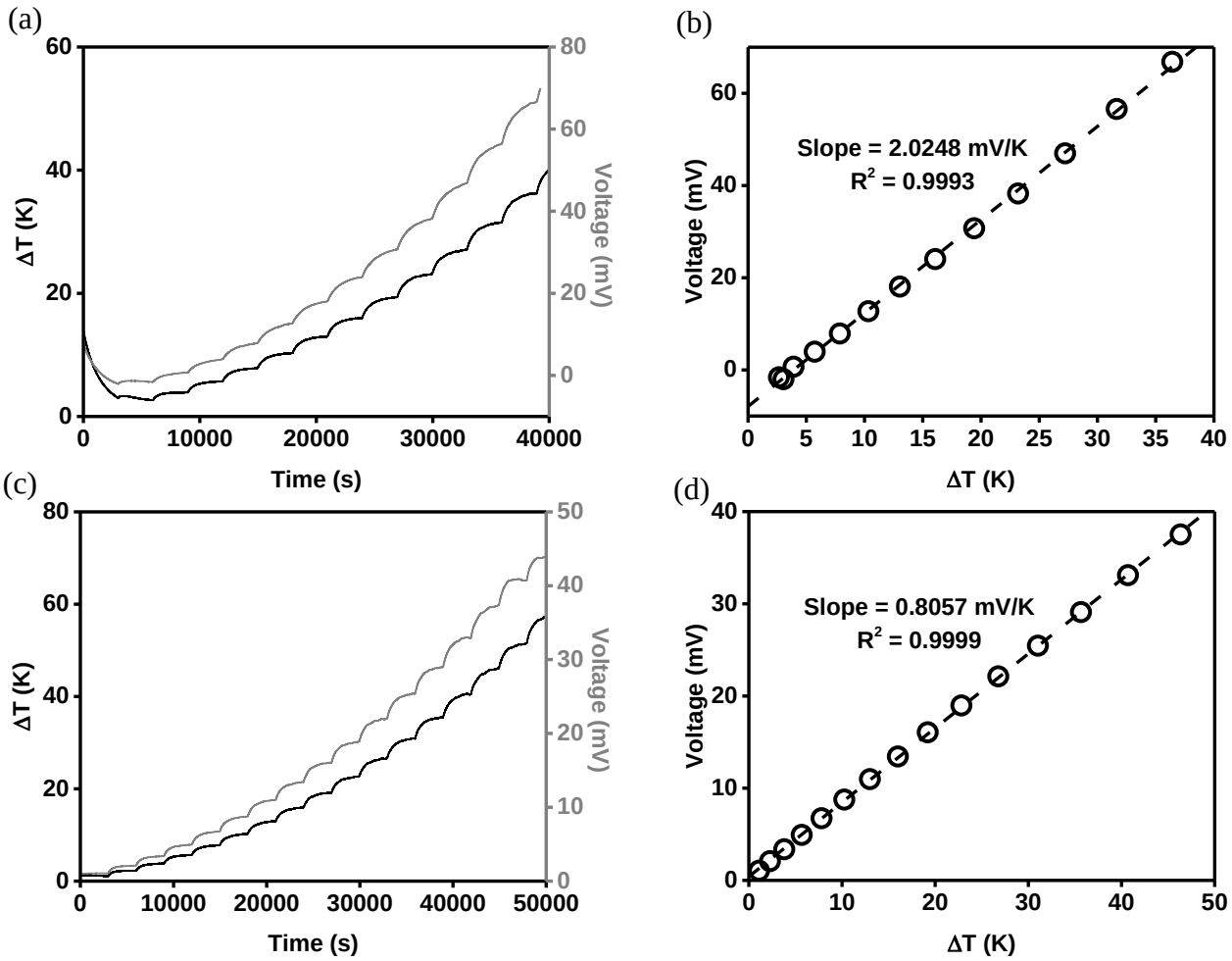

Figure 4.4. Time-dependent ΔT and voltage profiles of (a) Li | LP57 | Li and (c) Na | 1 M $NaClO_4$ in PC | Na symmetric cells under non-isothermal electrochemical thermopower measurements. Currents flowing through the Peltier plates (**Figure 4.3** (b)) were adjusted periodically to create distinct steady-state plateaus of both ΔT and voltage. The time period for each plateau was empirically determined to allow steady-states for both ΔT and voltage. Each steady-state values of ΔT and voltage were averaged, and drawn against each other in (b) and (d) for Li | LP57 | Li symmetric cell and Na | 1 M $NaClO_4$ in PC | Na symmetric cell, respectively. Both symmetric cells exhibited completely linear relations to each other. The slopes of those lines were pure electrochemical thermopowers of Li metal in LP57 and Na metal in 1 M $NaClO_4$ in PC, without influences of any cathode materials.

4.2.7. Other Electrochemical Measurement Techniques

Cyclic voltammetry (CV) was carried out in a 2016 coin cell at room temperature. The purpose of this examination was detection of the redox activities at working electrodes: P2-Na_xCoO_2 and BM-Na_xCoO_2 in this study. Hence, testing cells consisting of Na metal as the counter and reference electrode and P2-Na_xCoO_2 and BM-Na_xCoO_2 as working electrodes, and 1 M $NaClO_4$ in PC were assembled and connected to a Biologic (SP300 or VSP300) potentiostat. A single sheet of separator (19 mm diameter, GF/A Whatman® glass microfiber filter, Aldrich, Z242152) was inserted in between the Na metal and the working electrodes. The scan rate was set at 0.1 mV/s in order to ensure clear detection of redox phenomena at the working electrodes, and potential range was selected as 1.8 V – 3.6 V or 2.0 V – 3.4 V vs. Na/Na^+.

For the galvanostatic charge and discharge cycling tests, the potentiostat and cell configuration were the same as CV measurements. The cutoff voltage was selected as 2.0 V – 3.4 V vs. Na/Na^+, and the constant currents for these experiments were adjusted by the phase and mass loading of the cathode materials. Airtight cells were utilized for both electrochemical characterizations.

4.3. Results and Discussion

4.3.1. Advantages of Solid State Electrode Materials over Aqueous Redox Couples for Electrochemical Heat Harvester Application

Several serious drawbacks at the previous electrochemical heat harvester based on the aqueous redox couples could be resolved by moving its basis to solid-state electrode materials. Aqueous redox couples needed costly ion selective membranes, such as Nafion, which were expensive and eventually led to significantly increased overpotential by absorption of $Co(bpy)_3^{2+/3+}$ species inside the membranes. Moreover, $Co(bpy)_3^{2+}$ species in the electrolyte self-decomposed over time, restricting shelf life of the electrochemical heat harvesters. Furthermore, the charge capacity and heat capacity of the aqueous redox couple-based electrochemical heat harvesters could not be decoupled, dragging down the conversion efficiency by the high heat capacity of the indispensable electrolytes. Final issue at the aqueous redox couple-based electrochemical heat harvesters was that there only existed limited redox couples with close potentials to each other, therefore only a few aqueous redox couples could be utilized for electrochemical heat harvesting applications.

Solid-state electrodes for the heat harvesting application can resolve most of these problems, by shifting the electrochemical system design. In place of ion selective membrane, only separator is needed in order to prevent the internal short-circuit. The separator can be almost any materials that are porous and electronically insulating, but ionically permeating. Hence, cotton or glass fiber, or chemically inert polymers can serve as separator component for this reason. Also, it can allow a possibility to lower the heat capacity of the system, because the heat capacity from liquid electrolyte can be reduced by minimization of the mass of liquid electrolyte or alternative solid-state electrolytes with less heat capacity. Lastly, because the electrochemical potentials become continuous, half-cell potentials can be tuned to meet the requirements for the electrochemical heat harvester (refer to Section 1.3.3).

4.3.2. Selection Criteria of Solid State Electrode Material for Electrochemical Heat Harvester Application

As overpotential was the most serious issue that limited cyclability of the previous flow battery-type electrochemical heat harvester (Section 3.3.4), it was primarily considered in the selection of solid-state electrode material for this new version of electrochemical heat harvester. P2-Na_xCoO_2 is chosen by considering this aspect, because it possesses both high electronic[19,20] and ionic conductivity[21] simultaneously. Among various co-existent phases of Na_xCoO_2 at the room temperature[12], P2-phase is particularly favorable, because this phase has the highest reversibility during repeated electrochemical sodiation / desodiation[22]. Moreover, P2-phase in general allows higher diffusivity of Na^+ ions in the crystal compared to the polymorphic O3-phases[21], which means P2-phase has higher Na^+ ionic conductivity than O3-phases. This in turn can suppress the E_{loss} term in the efficiency formula (Equation 1.13), therefore can contribute to an improved conversion efficiency. As usage of a lighter element Li is not expected to bring advantages, usage of Na instead of more expensive Li can be more advantageous on cost.

A drawback of P2-Na_xCoO_2 is that it has multiple voltage plateaus, of which widths are often small[11] (**Figure 4.5**). The distribution of narrow plateaus over multiple electrochemical potential range is a particular characteristic of all phases of Na_xCoO_2 materials[11,12], due to (i) spontaneous clustering between Na^+ ions and Na^+ vacancies[11], and (ii) phase transition during the charge and discharge[12,21]. Each transition in the clustering structures of Na^+ ions in those crystals or phases of those crystals correspond to the step-like feature in **Figure 4.5**[11,12,21]. As explained earlier in this chapter, the self-discharge effect is persistent at battery systems in general and makes it more difficult to sustain the electrochemical potential of a cell the same over time[14,15]. However, by placing the electrochemical potential at a plateau potential, effect of self-discharge on voltage can be lessened, because change in SoC can influence voltage only very limitedly. For this reason, the widest plateau at the electrochemical potential vs. SoC of P2-Na_xCoO_2 was selected for operation of the electrochemical heat harvester, namely 2.1 V – 2.3 V vs. Na/Na^+ (**Figure 4.5**).

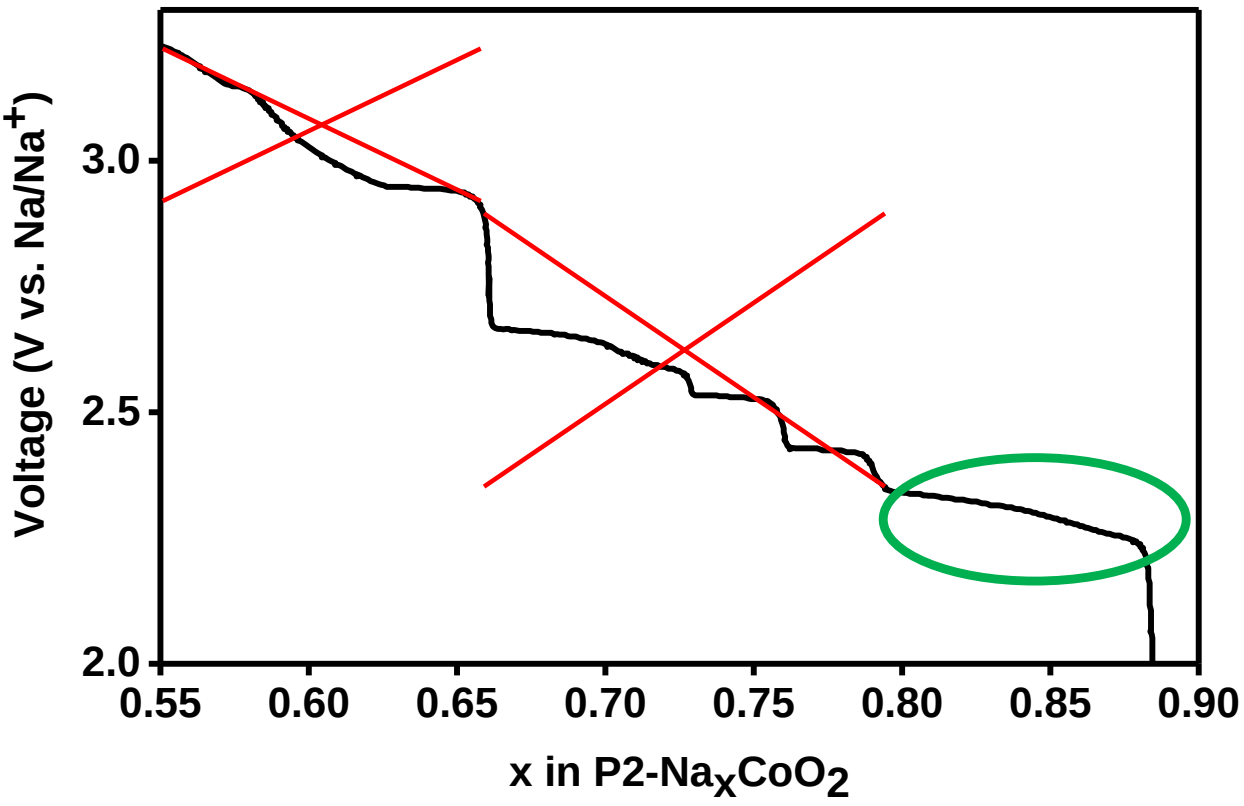

Figure 4.5. Equilibrium electrochemical potentials of P2-Na_xCoO_2 as a function of Na content, x[11]. The self-discharge effect is a grave engineering issue when constructing electrochemical heat harvesters with solid-state electrodes. It constantly shifts the electrochemical potential, disabling to keep the accurately defined electrochemical potential over time. The broadest plateau can minimize the inevitable self-discharge on the potential. The widest plateau is located at 2.1 V – 2.3 V vs. Na/Na^+. Figure from *Electrochemical investigation of the P2–Na_xCoO_2 phase diagram* and used with permission from the Nature Publishing Group[11].

4.3.3. Phase Transition of Na_xCoO_2 from P2- Phase into Amorphous by Ball-Milling

Figure 4.6 shows diffracted X-ray patterns of P2-Na_xCoO_2 and its ball-milled product, BM-Na_xCoO_2. These data informed crystallinity and phase purity of these two powders. XRD pattern of P2-Na_xCoO_2 indicated that the as-synthesized P2-Na_xCoO_2 was polycrystalline and free from any detectable crystalline impurities. Also, the widths of all diffracted peaks from the P2-Na_xCoO_2 sample were narrow and their intensities were high, suggesting that as-synthesized P2-Na_xCoO_2 had good crystallinity and large grain size. In the contrast, BM-Na_xCoO_2 utterly lacked

any diffracted X-ray signals. This transformation was the consequence of the high energy ball-milling implemented in this study. The ball-milling process was strong enough to completely diminish the crystallinity and transform the material into an entirely disordered phase.

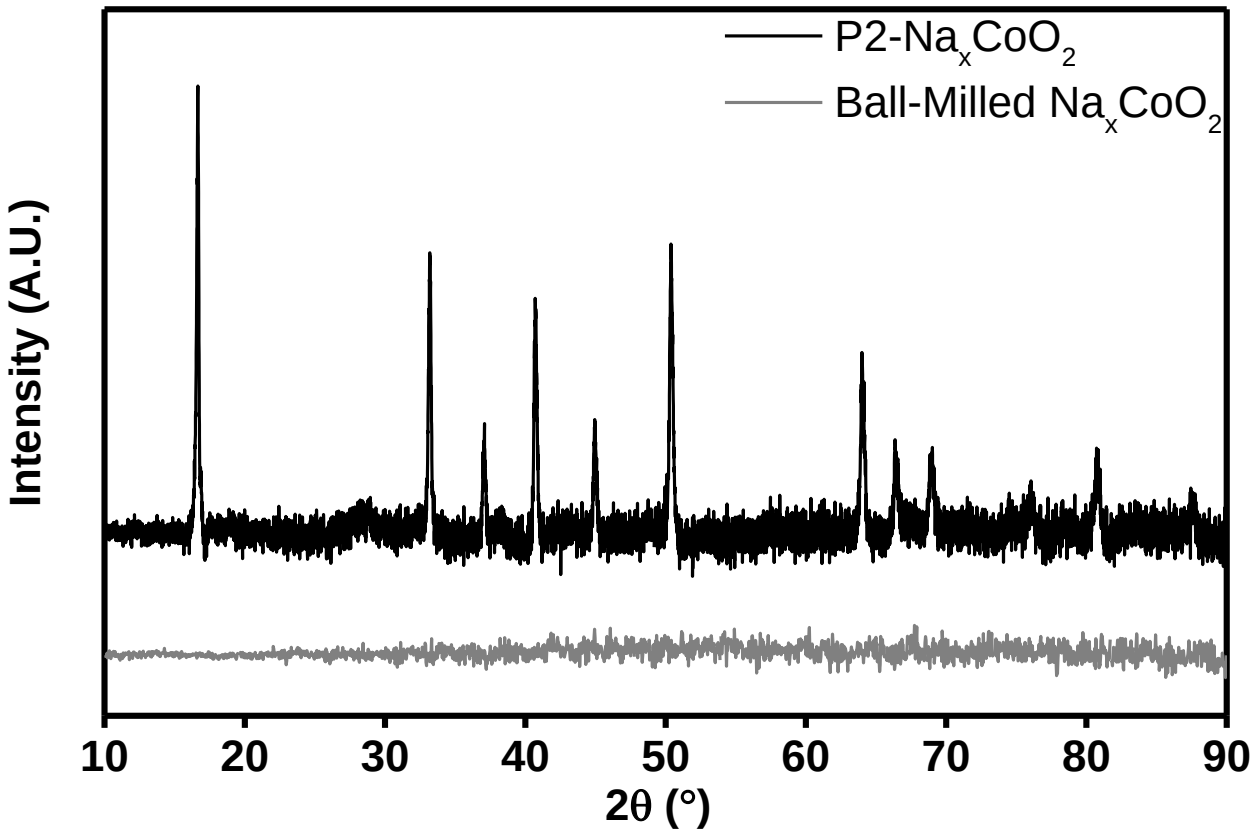

Figure 4.6. Powder X-ray diffraction (XRD) patterns of as-synthesized P2-Na_xCoO_2 and BM-Na_xCoO_2.The P2-Na_xCoO_2 diffraction pattern matched well with the previous study on the same material[12]. The ball-milling process proved effective on thoroughly removing crystallinity entirely from P2-Na_xCoO_2, as BM-Na_xCoO_2 was deprived of any diffracted peaks.

Effect of the high energy ball-milling procedure was also pronounced on particle size and morphology of Na_xCoO_2 before and after the process. **Figure 4.7** illustrates morphology and particle size of as-synthesized P2-Na_xCoO_2 and BM-Na_xCoO_2, respectively, measured by FESEM technique. P2-Na_xCoO_2 presented plate-like morphology and lateral particle size well above 5 μm

on average, consistent with the previous studies[23,24]. In comparison, the shape of BM-Na_xCoO_2 transformed into porous and globular microstructures with particle size ranging around sub-μm.

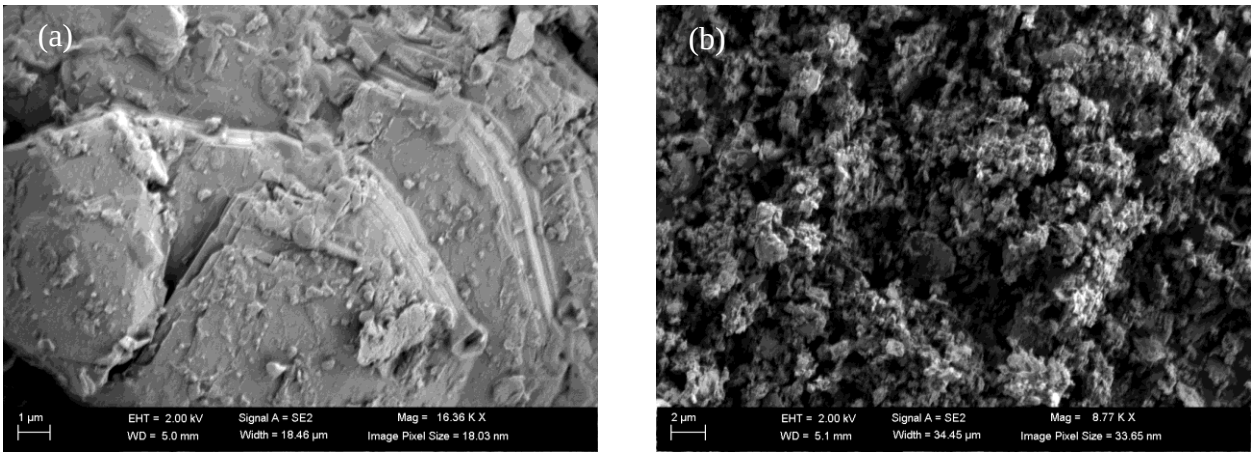

Figure 4.7. Morphologies and particle sizes of (a) as-synthesized P2-Na_xCoO_2, and (b) BM-Na_xCoO_2. Particle size diminished and morphology transformed from plate-like shape into globular and porous geometry after the high energy ball-milling process.

It is well-known that P2-Na_xCoO_2 chemically reacts with either liquid or vapor water to intercalate the water molecules in the gallery[13,25], staying there with pre-existent Na^+ ions. **Figure 4.8** reveals the corresponding changes in the crystal structure through XRD measurements. The weakened amplitudes of the diffracted peaks were pronounced at 2θ = ~ 15°, ~ 32° and evolution of a new peak at 2θ = ~ 60° were observed. These obvious variations in the diffraction patterns point out that chemical processes on P2-Na_xCoO_2 occurred during the storage in air. This observation justified why P2-Na_xCoO_2 should have been stored in dry Ar-filled glove box, in order to inhibit such unwanted side reactions.

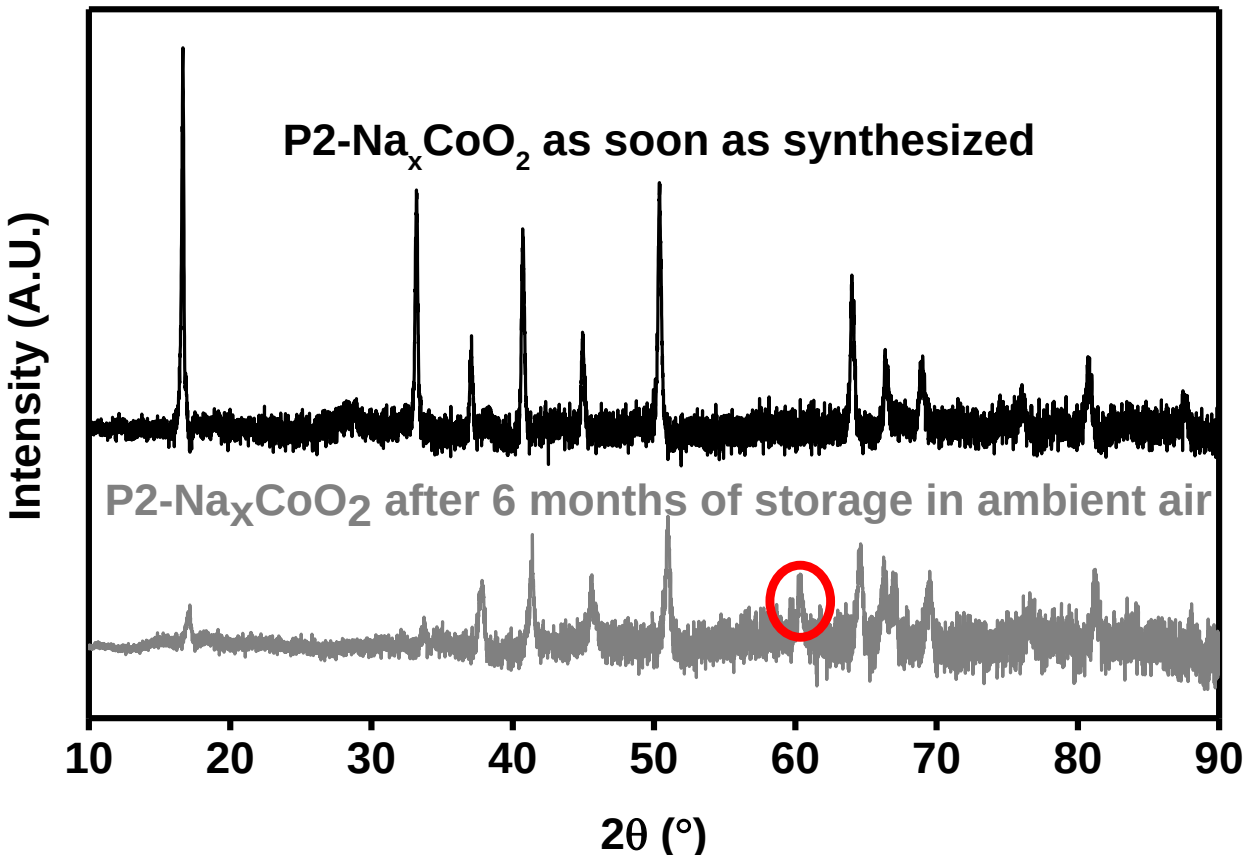

Figure 4.8. Effect of long term exposure to ambient humid air on phase purity of P2-Na_xCoO_2. Shrinkage of intensities of the peaks at 2θ = ~ 15 ° and ~ 32 ° were observed. An unforeseen peak in the red circle at 2θ = ~ 60 ° indicates that new distinct phase appeared as a possible result of chemical reaction during storage in air.

4.3.4. Modification of Electrochemical Charge Storage Mechanism of Na_xCoO_2 from Battery to EDLC by the Phase Transition

The phase transition from P2-phase to amorphous phase of Na_xCoO_2 removed redox activity from P2-Na_xCoO_2. **Figure 4.9** compares CV of P2-Na_xCoO_2 and BM-Na_xCoO_2 working electrodes, of which role is identification of redox activity at working electrodes under particular electrochemical potentials. If there are reversible redox reactions at the working electrodes at the particular electrochemical potential, corresponding peaks (surge of current) should appear both at oxidation stage (current > 0) and reduction stage (current < 0) almost symmetrically at that potential. If a redox peak is detected only at the oxidation stage, the corresponding redox reaction

is irreversible. When there is no redox reaction at a specific potential, then no redox peak appears at all at that potential. The currents flowing through the working electrodes were normalized by their geometric area.

P2-Na_xCoO_2 displayed multiple and fully reversible redox reactions between 1.8 V – 3.6 V vs. Na/Na^+. On the contrary, BM-Na_xCoO_2 did not show any redox peaks stemming from redox reactions between 2.0 V – 3.4 V vs. Na/Na^+. This clarifies that BM-Na_xCoO_2 was totally deprived of redox activity anymore. Hence, if there is still remaining electrochemical charge storage mechanism in this material, the mechanism would not be redox-based intercalation of Na^+ ions, but rather electrical double layer capacitance (EDLC). In addition, it can be concluded that thorough loss of crystallinity via ball-milling led to complete lack of redox capability as well.

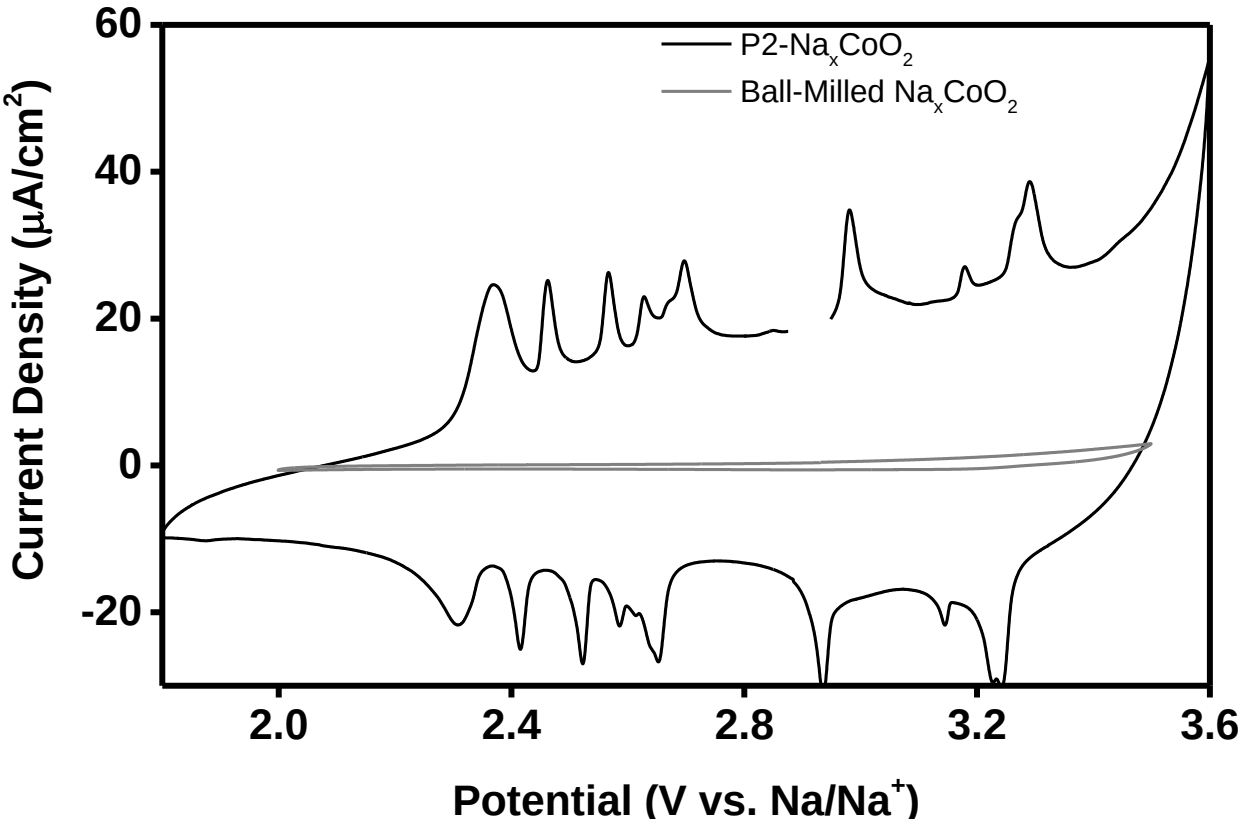

Figure 4.9. Cyclic voltammetry (CV) of P2-Na_xCoO_2 and BM-Na_xCoO_2 working electrodes at room temperature. Both employed 1 M $NaClO_4$ in PC as electrolyte, and Na metal as reference and counter electrode. A slow scan rate, 0.1 mV/s was consistently used for CV. The

electrochemical potential ranges were set as 1.8 V – 3.6 V vs. Na/Na^+ for the P2-Na_xCoO_2 working electrode, and 2.0 V – 3.4 V vs. Na/Na^+ for the BM-Na_xCoO_2 working electrode.

This change in redox activity was also reflected to charge capacities. In order to reveal charge capacities of two different forms of Na_xCoO_2, galvanostatic cycling measurements were performed between 2.0 V – 3.4 V vs. Na/Na^+. Small current was passed through the cells to clearly discern steps and plateaus during the galvanostatic cycles. **Figure 4.10** (a) evidently shows voltage vs. capacity curve of P2-Na_xCoO_2 with multiple steps and plateaus, precisely matching with previous measurements from multiple research groups[11,24]. The gravimetric charge capacity of P2-Na_xCoO_2 also showed agreement with previous reports in the same electrochemical potential range[26,27]. This agreement indirectly confirmed that the material was P2-phase. However, redox-deficient BM-Na_xCoO_2 did not behave like P2-Na_xCoO_2. The galvanostatic charge-discharge curve wholly lost the peculiar steps and plateaus of P2-Na_xCoO_2. The almost straight charge-discharge curve of BM-Na_xCoO_2 reflected a particular property of supercapacitors. As another consequence to the absence of redox activity, the capacity of the BM-Na_xCoO_2 shrank by nearly 2 orders of magnitude. However, this material did store charge electrochemically, strongly suggesting that the charge storage at BM-Na_xCoO_2 solely relied on the electrical double layer (EDL) effect. Thus, application of voltage would not intercalate or de-intercalate Na^+ ions from the material; instead it would polarize the surface of BM-Na_xCoO_2 electrode and adsorb ions from the electrolyte. Another notable point here would be whether the coupled transitions in crystallinity and redox activity would lead to enhancement on the thermopower, following the same trend shown in **Figure 1.14**. This will be clarified next.

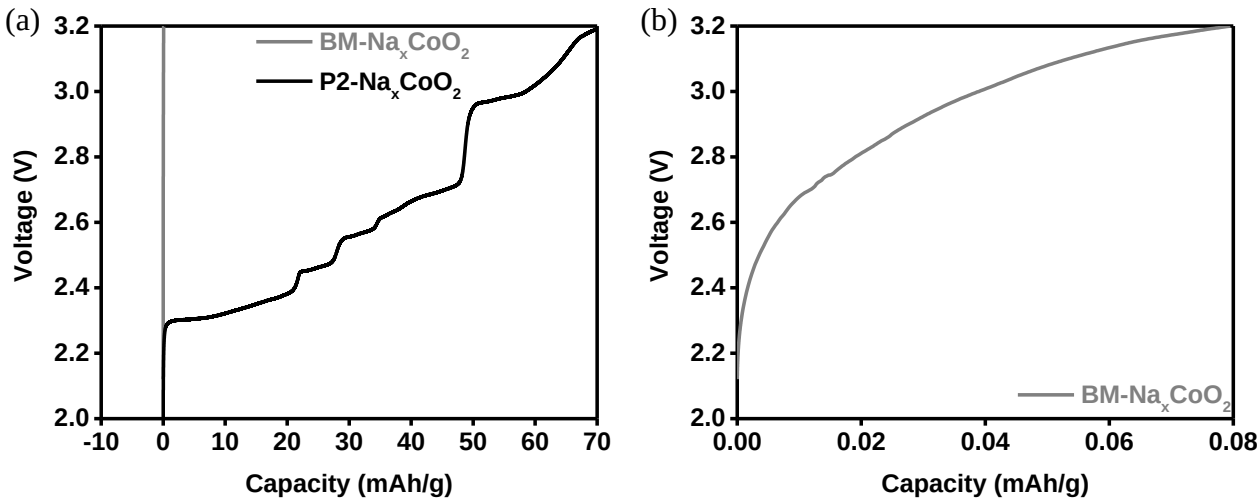

Figure 4.10. (a) Galvanostatic (constant current) charge curves of P2-Na_xCoO_2 and BM-Na_xCoO_2 at room temperature. (b) The enlarged galvanostatic charge curve of BM-Na_xCoO_2 at room temperature. The grey curves in (a) and (b) reflect the same experimental result. The anode was Na metal and the electrolyte was 1 M $NaClO_4$ in PC for both cells. For P2-Na_xCoO_2, current corresponding to C/100 (100 hours were required to remove or provide 1 mole of electrons from 1 mole of cobalt in P2-Na_xCoO_2) were used. For BM-Na_xCoO_2, ±1 μA was used, because C-rate would be only valid for redox-active materials.

4.3.5. Enhancement of Electrochemical Thermopowers by the Phase Transition and the Modified Electrochemical Charge Storage Mechanism

Electrochemical thermopowers of P2-Na_xCoO_2 and BM-Na_xCoO_2 were characterized, in order to determine the effect of the transitions in phase and electrochemical behaviors. Because 2.3 V vs. Na/Na^+ was chosen as the operating electrochemical potential due to widest plateau profile, SoCs of P2-Na_xCoO_2 and BM-Na_xCoO_2 were tuned accordingly, abiding to the procedures described in Section 4.2.5.

Figure 4.11 (a) – (b) illustrates how OCVs and temperatures varied over time for different cells. Basically, the temperatures were controlled stimuli, and the corresponding OCVs were reaction to them. As intended, stable steady-state profiles of both temperatures and OCVs were obtained for all tested 2016 coin cells, enveloping P2-Na_xCoO_2 and BM-Na_xCoO_2 with Na metal

anode in 1 M $NaClO_4$ in PC electrolyte. Those steady-state values were charted against each other in **Figure 4.11** (c).

Figure 4.11 (c) demonstrates that electrochemical thermopower measurements were reproducible at multiple P2-Na_xCoO_2 | 1 M $NaClO_4$ in PC | Na cells. The electrochemical thermopower of Na_xCoO_2 evolved from -0.65 mV/K of the P2-Na_xCoO_2 to 9.50 mV/K of the BM-Na_xCoO_2. Thus, it can be concluded that enhancement in electrochemical thermopowers was closely correlated to transformation in charge electrochemical storage mechanism, invoked by the phase transition. This observation is also consistent with the trend in electrochemical thermopowers in **Figure 1.14**, which displayed that supercapacitors in general possess much larger thermopower than conventional Li-ion battery materials.

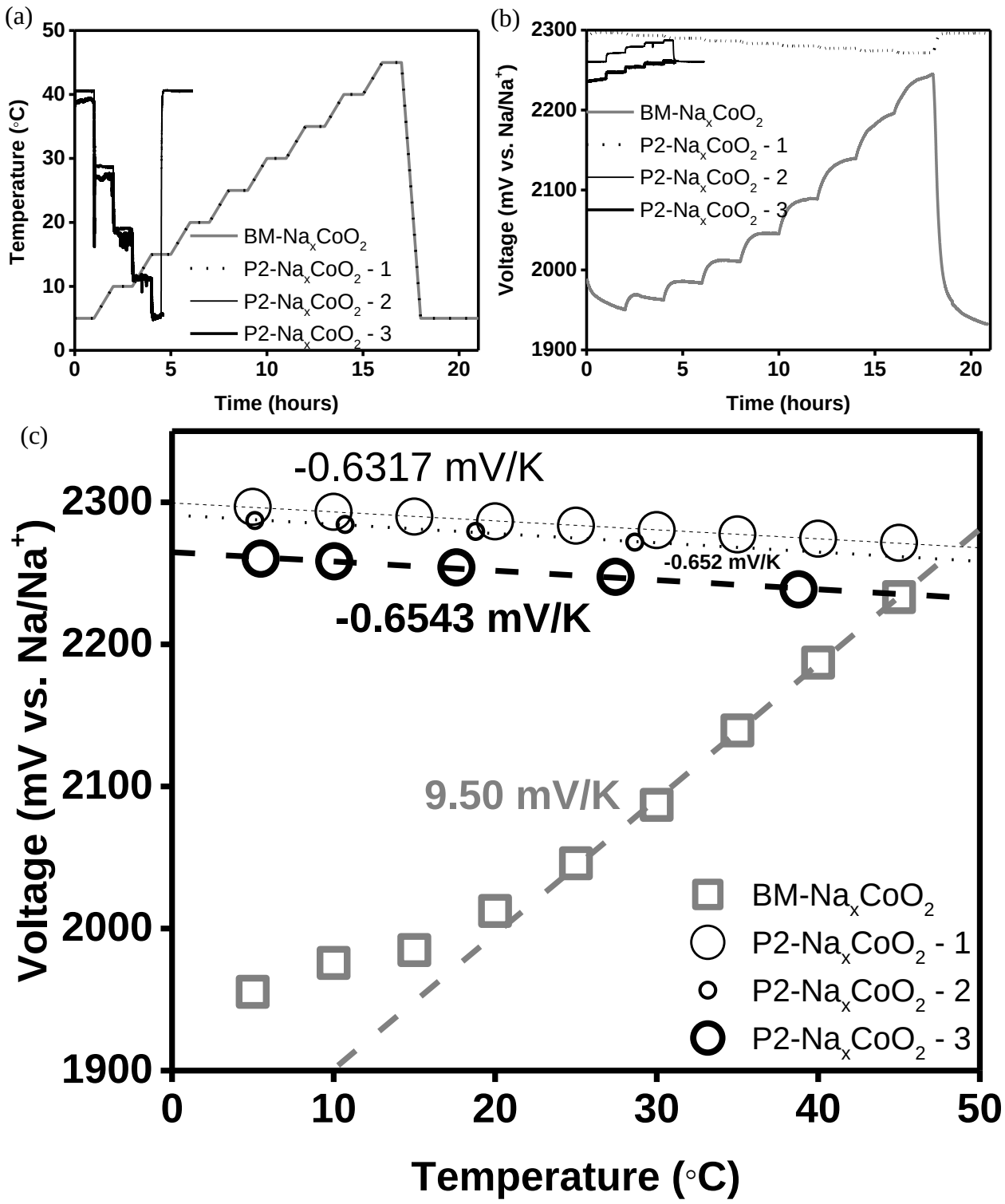

Figure 4.11. Time dependence of (a) temperature and (b) open circuit voltage (OCV) of the 2016 coin cells composed of P2-Na_xCoO_2 | 1 M $NaClO_4$ in PC | Na, and BM-Na_xCoO_2 | 1 M $NaClO_4$ in PC | Na, respectively. The purpose of periodic temperature control was to observe the

corresponding OCV variation. Electrochemical thermopowers of P2-Na_xCoO_2 and BM-Na_xCoO_2 were measured at the premeditated electrochemical potential, 2.3 V vs. Na/Na^+. (c) Dependencies of steady-state OCVs on steady-state temperatures. Again, the slopes represented the electrochemical thermopowers.

4.3.6. Heat Harvesting Thermodynamic Cycles of the Na_xCoO_2-based Dual Cell Stack

As BM-Na_xCoO_2 proved large electrochemical thermopower reaching 9.50 mV/K, the next step was to determine how to operate the Na_xCoO_2-based system under autonomous thermodynamic cycles (no need for recharging by external electricity in any stage of the thermodynamic cycles). First requirement would be that the electrochemical heat harvester should be freely maneuverable to set the SoC of P2-Na_xCoO_2 at 2.3 V vs. Na/Na^+. For this reason, the electrochemical heat harvester was obliged to have two independent cells, composed of P2-Na_xCoO_2 and BM-Na_xCoO_2, respectively. However, independent cell may sacrifice another requirement for the autonomous electrochemical heat harvesting, because OCV of the electrochemical harvester should be zero at the midpoint of operating temperature range.

In order to reconcile seemingly conflicting requirements, a dual cell stack was designed (**Figure 4.12** (a)), inspired by the previous work[18]. The constituent cells for the dual cell stack were (i) P2-Na_xCoO_2 | 1 M $NaClO_4$ in PC | Na, and (ii) BM-Na_xCoO_2 | 1 M $NaClO_4$ in PC | Na. These two cells were set at the same electrochemical potentials, 2.3 V vs. Na/Na^+. The serial connection of these two cells toward the opposite direction could shift the voltage of the dual cell stack to zero, fulfilling one of the requirements for designing the autonomous electrochemical heat harvester (Section 1.3.3). This architecture operated as intended, consistent with the previous report[18]. It demonstrated that likewise stacked cells in serial connection could undergo heat harvesting thermodynamic cycles[18]. Furthermore, according to Equation 1.14, the dual cell stack possessed synergized thermopower around 10 mV/K.

Figure 4.12 (b) summarized the preparation procedures for the thermodynamic cycles of the dual cell stack. Firstly, SoC of each cell was adjusted to correspond to 2.3 V vs. Na/Na^+ at the midpoint of the intended operating temperature. Here, the operating temperature range corresponded to 20 °C – 40 °C, and the midpoint was 30 °C. Then the cells were stacked together

according to **Figure 4.12** (a), and transferred to 20 °C environment under open circuit condition. After the dual cell stack found thermal equilibrium with the surrounding, the thermodynamic cycle described in Section 1.3.3 were initiated.

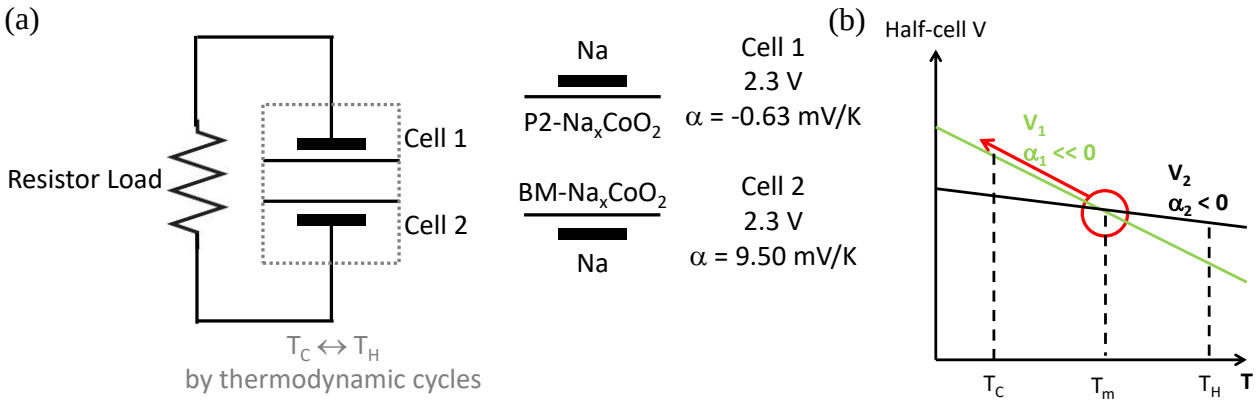

Figure 4.12. (a) Finalized design of the dual cell stack for the electrochemical heat harvesting application incorporating different forms of Na_xCoO_2. The voltages of each cell (2.3 V in this case) should nullify each other due to their opposite directions; therefore the combined voltage of the dual cell stack can become 0. On the contrary, electrochemical thermopowers from each of them can become enhanced, by following Equation 1.14. (b) Preparation to initiate the thermodynamic cycles of the dual cell stack. At the midpoint of the chosen temperature range (T_m = 30 °C), the open-circuit potentials of the constituent cells are set as 2.3 V vs. Na/Na^+ and stacked to face against each other. Then the stack is transferred to pre-selected T_C = 20 °C under open circuit condition, so that the heat harvesting thermodynamic cycle between T_C = 20 °C and T_H = 40 °C can be initiated.

4.3.7. Energy Harvested during a Single Heat Harvesting Thermodynamic Cycle and Projected Conversion Efficiency

As explained earlier, conversion efficiency is defined as the ratio of the produced useful energy to total heat inflow into the conversion system, as shown in the Equation 1.13 in Section 1.3.2. Using the Equation 1.13, the efficiency of this system was estimated as a function of heat capacity of the system (**Figure 4.13**). The lower bound and the upper bound were also projected at **Figure 4.13**. Operating temperature range of 20 °C – 40 °C was used for the estimation, and the

upper bound corresponded to the Carnot efficiency = 6.30 %. The lower bound was calculated by presuming the two 2016 coin cells were totally filled with the most heat capacitive component, PC. It should be noted that other cell parts were not regarded in the lower bound calculation. The actual efficiency would be closer to the lower bound because most, but not all of the internal space in the 2016 coin cells were occupied with PC.

However, if electrolyte materials with lower heat capacities, such as polymeric[28] and ceramic[29,30] electrolytes are utilized in thin film arrangements in the future for faster ionic passage and minimization of unnecessary heat capacity, the conversion efficiency is expected to shift toward Carnot efficiency.

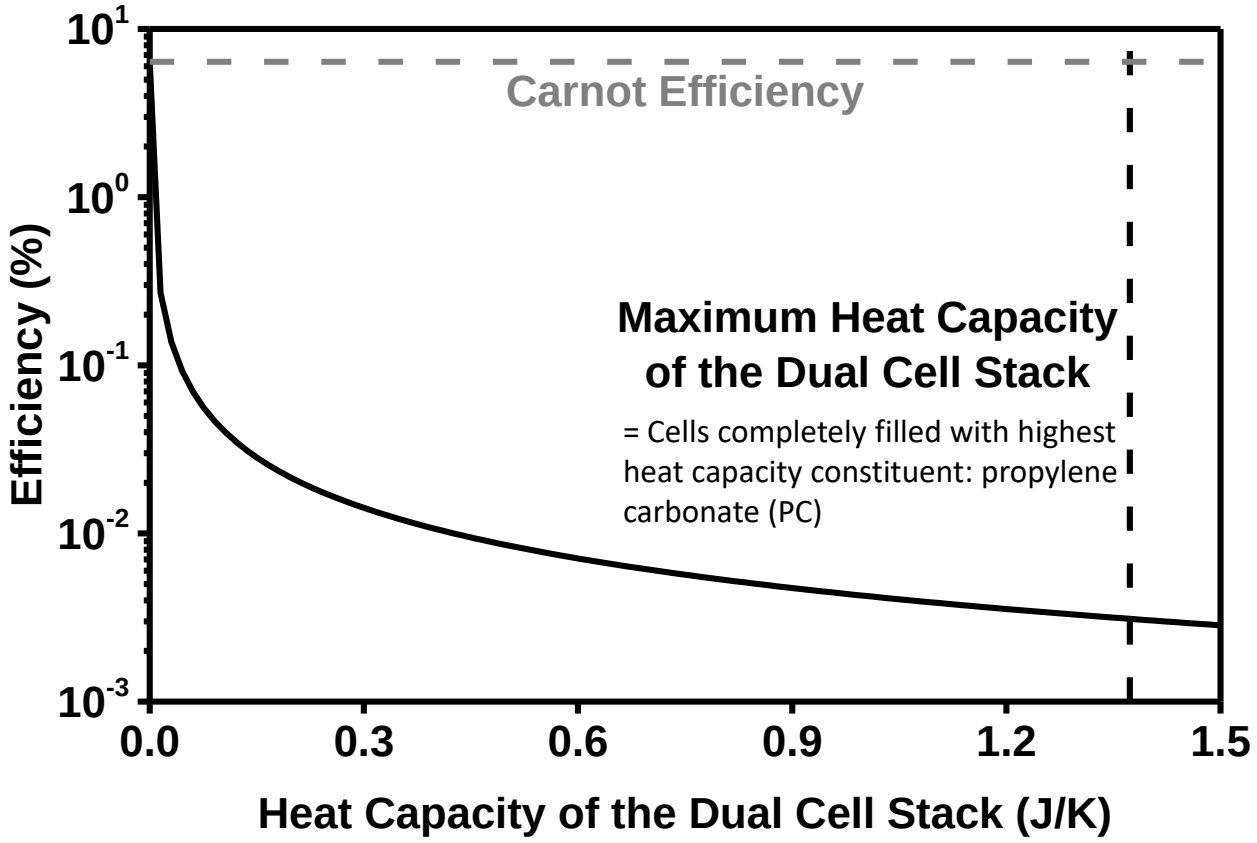

Figure 4.13. Projected heat conversion efficiency of the electrochemical heat harvester. The upper bound for the efficiency was Carnot efficiency = 6.30 % under operating temperature range of 20 °C – 40 °C. The lower bound for the efficiency was determined by assuming two 2016 coin cells in the dual cell stack were completely filled with PC. The lower bound can be improved in more

optimized future designs, where the highly heat capacitive PC is minimally contained, or PC is replaced into a thin film, solid-state electrolyte.

4.4. Conclusion

We fabricated an autonomous Na_xCoO_2-based electrochemical heat harvester which operated without need for supply of external electricity. This device successfully addressed majority of issues in the previous aqueous redox couple-based electrochemical heat harvester: cost, overpotential, heat capacity, and limited number of active materials for electrochemical heat harvesting. Ball-milling on as-synthesized P2-Na_xCoO_2 led to complete disorder of the material. This process transformed the crystal structure of Na_xCoO_2 from P2-phase crystal into amorphous phase. The disruption of the crystal structure resulted in loss of redox activity and eventually, huge enhancement on electrochemical thermopower from -0.65 mV/K to 9.50 mV/K at 2.3 V vs. Na/Na^+. A dual cell stack consisting of a rechargeable battery incorporating P2-Na_xCoO_2 cathode, and an EDLC containing amorphous Na_xCoO_2 cathode was built for electrochemical heat harvesting. This dual cell stack has the high thermopower reaching 10 mV/K, enabling efficiency up to 6.30 % under working temperature range of 20 °C – 40 °C. To approach toward the maximum efficiency, the heat capacity of the system should be strictly limited. This research presented an example, from which more efficient autonomous electrochemical heat harvesters can be stemmed.

References

1 Hu, R. *et al.* Harvesting Waste Thermal Energy Using a Carbon-Nanotube-Based Thermo-Electrochemical Cell. *Nano letters* **10**, 838-846, doi:10.1021/nl903267n (2010).

2 Salazar, P. F., Stephens, S. T., Kazim, A. H., Pringle, J. M. & Cola, B. A. Enhanced thermo-electrochemical power using carbon nanotube additives in ionic liquid redox electrolytes. *Journal of Materials Chemistry A* **2**, 20676-20682, doi:10.1039/c4ta04749d (2014).

3 Salazar, P. F., Kumar, S. & Cola, B. A. Nitrogen- and Boron-Doped Carbon Nanotube Electrodes in a Thermo-Electrochemical Cell. *Journal of The Electrochemical Society* **159**, B483-B488, doi:10.1149/2.043205jes (2012).

4 Hudak, N. S. & Amatucci, G. G. Energy Harvesting and Storage with Lithium-Ion Thermogalvanic Cells. *Journal of The Electrochemical Society* **158**, A572, doi:10.1149/1.3568820 (2011).

5 S., R. M. *et al.* Carbon Nanotube – Reduced Graphene Oxide Composites for Thermal Energy Harvesting Applications. *Advanced Materials* **25**, 6602-6606, doi:doi:10.1002/adma.201303295 (2013).

6 Yang, Y. *et al.* Charging-free electrochemical system for harvesting low-grade thermal energy. *Proceedings of the National Academy of Sciences of the United States of America* **111**, 17011-17016, doi:10.1073/pnas.1415097111 (2014).

7 Lee, S. W. *et al.* An electrochemical system for efficiently harvesting low-grade heat energy. *Nature communications* **5**, 3942, doi:10.1038/ncomms4942 (2014).

8 Kim, S. L., Lin, H. T. & Yu, C. Thermally Chargeable Solid-State Supercapacitor. *Advanced Energy Materials* **6**, 1600546-n/a, doi:10.1002/aenm.201600546 (2016).

9 Zhao, D. *et al.* Ionic thermoelectric supercapacitors. *Energy & Environmental Science* **9**, 1450-1457, doi:10.1039/c6ee00121a (2016).

10 Ail, U. *et al.* Thermoelectric Properties of Polymeric Mixed Conductors. *Advanced Functional Materials* **26**, 6288-6296, doi:10.1002/adfm.201601106 (2016).

11 Berthelot, R., Carlier, D. & Delmas, C. Electrochemical investigation of the P2–Na_xCoO_2 phase diagram. *Nature materials* **10**, 74-80 (2011).

12 Lei, Y., Li, X., Liu, L. & Ceder, G. Synthesis and Stoichiometry of Different Layered Sodium Cobalt Oxides. *Chemistry of Materials* **26**, 5288-5296, doi:10.1021/cm5021788 (2014).

13 Ohta, H., Michioka, C., Itoh, Y. & Yoshimura, K. Novel Phase Diagram of Superconductor $Na_xCoO_2 \cdot yH_2O$ in 75% Relative Humidity. *Journal of the Physical Society of Japan* **74**, 3147-3150, doi:10.1143/jpsj.74.3147 (2005).

14 Yazami, R. & Reynier, Y. F. Mechanism of self-discharge in graphite–lithium anode. *Electrochimica Acta* **47**, 1217-1223, doi:https://doi.org/10.1016/S0013-4686(01)00827-1 (2002).

15 Verma, P., Maire, P. & Novák, P. A review of the features and analyses of the solid electrolyte interphase in Li-ion batteries. *Electrochimica Acta* **55**, 6332-6341, doi:https://doi.org/10.1016/j.electacta.2010.05.072 (2010).

16 Schmid, M. J., Xu, J., Lindner, J., Novák, P. & Schuster, R. Concentration Effects on the Entropy of Electrochemical Lithium Deposition: Implications for Li+ Solvation. *The Journal of Physical Chemistry B* **119**, 13385-13390, doi:10.1021/acs.jpcb.5b07670 (2015).

17 Reynier, Y. *et al.* Entropy of Li intercalation in Li_xCoO_2. *Physical Review B* **70**, doi:10.1103/PhysRevB.70.174304 (2004).

18 Linford, P. A., Lithium ion power generator : a novel system for direct thermal to electric energy conversion. *Thesis from Department of Mechanical Engineering at Massachusetts Institute of Technology* (2017).

19 Molenda, J., Delmas, C., Dordor, P. & Stokłosa, A. Transport properties of Na_xCoO_{2-y}. *Solid State Ionics* **12**, 473-477, doi:https://doi.org/10.1016/0167-2738(84)90180-2 (1984).

20 Molenda, J., Delmas, C. & Hagenmuller, P. Electronic and electrochemical properties of Na_xCoO_{2-y} cathode. *Solid State Ionics* **9-10**, 431-435, doi:https://doi.org/10.1016/0167-2738(83)90271-0 (1983).

21 Mo, Y., Ong, S. P. & Ceder, G. Insights into Diffusion Mechanisms in P2 Layered Oxide Materials by First-Principles Calculations. *Chemistry of Materials* **26**, 5208-5214, doi:10.1021/cm501563f (2014).

22 Ding, J. J. *et al.* Electrochemical properties of P2-phase $Na_{0.74}CoO_2$ compounds as cathode material for rechargeable sodium-ion batteries. *Electrochimica Acta* **87**, 388-393, doi:https://doi.org/10.1016/j.electacta.2012.09.058 (2013).

23 Xia, X. & Dahn, J. R. A Study of the Reactivity of De-Intercalated P2-Na_xCoO_2 with Non-Aqueous Solvent and Electrolyte by Accelerating Rate Calorimetry. *Journal of The Electrochemical Society* **159**, A647-A650, doi:10.1149/2.102205jes (2012).

24 Rami Reddy, B. V., Ravikumar, R., Nithya, C. & Gopukumar, S. High performance Na_xCoO_2 as a cathode material for rechargeable sodium batteries. *Journal of Materials Chemistry A* **3**, 18059-18063, doi:10.1039/c5ta03173g (2015).

25 Sakurai, H., Osada, M. & Takayama-Muromachi, E. Hydration of Sodium Cobalt Oxide. *Chemistry of Materials* **19**, 6073-6076, doi:10.1021/cm0714786 (2007).

26 Rai, A. K., Anh, L. T., Gim, J., Mathew, V. & Kim, J. Electrochemical properties of Na_xCoO_2 (x~0.71) cathode for rechargeable sodium-ion batteries. *Ceramics International* **40**, 2411-2417, doi:https://doi.org/10.1016/j.ceramint.2013.08.013 (2014).

27 D'Arienzo, M. *et al.* Layered $Na_{0.71}CoO_2$: a powerful candidate for viable and high performance Na-batteries. *Physical Chemistry Chemical Physics* **14**, 5945-5952, doi:10.1039/c2cp40699c (2012).

28 Wen, J. in *Physical Properties of Polymers Handbook* (ed James E. Mark) 145-154 (Springer New York, 2007).

29 Abello, L., Chhor, K., Barj, M., Pommier, C. & Delmas, C. Heat capacity and Na^+ ion disorder in Nasicon-type solid electrolytes $Na_3M_2P_3O_{12}$ (M_2= Fe_2, Cr_2, ZrMg) in the temperature range 10 to 300 K. *Journal of Materials Science* **24**, 3380-3386, doi:10.1007/bf01139069 (1989).

30 Cui, Y., Rohde, M., Mahmoud, M. M., Ziebert, C. & Seifert, H. J. Phosphate Based Ceramics As Solid Electrolyte for High Temperature Lithium Ion Batteries. *Meeting Abstracts* **MA2016-01**, 120 (2016).

5. Summary and Outlook

5.1. Summary

During our research on improving thermoelectric power factors and quantitatively understanding mechanisms behind the enhanced thermoelectric power factors, we fabricated PEDOT:PSS / undoped Si and PEDOT:PSS / undoped Ge heterostructures. Modulation doping as a power factor enhancement mechanism for Si / PEDOT:PSS heterojunction was proven by comparing experiment and two different simulations *with and without band alignment* between PEDOT:PSS and Si. For Ge / PEDOT:PSS heterostructures, valence band offset was spectroscopically measured by Kraut's method, and revealed hole migration from PEDOT:PSS to undoped Ge. Thickness dependence of electrical conductivity, Seebeck coefficient, and power factor was observed for both types of heterostructures. For the Si / PEDOT:PSS heterostructure, thinner thicknesses of both PEDOT:PSS and Si resulted in the highest power factor. For the Ge / PEDOT:PSS heterostructure, power factor showed maximum at the smallest PEDOT:PSS thickness. Because modulation doping can only dope interfaces of Si and Ge, farther away from the interface, hole concentrations in non-interfacial Si and Ge remain unchanged. Therefore, volumes of Si and Ge far from interface could not contribute to improve electrical conductivity and power factor. The maximum power factor for Si / PEDOT:PSS and Ge / PEDOT:PSS were 26.2 $\mu W/m \cdot K^2$ and 154 $\mu W/m \cdot K^2$, respectively. These power factors were 17.5 and 47 fold larger compared to that of bulk PEDOT:PSS. The methodology to explore thermoelectric properties of PEDOT:PSS-based heterostructures can be extended to predict electronic properties of other thin film heterostructures, such as transistors and photovoltaics.

During our research on the flow battery-based autonomous electrochemical heat harvester, we explored aqueous redox couples with intersecting half-cell potentials, so that heat harvesting cycle without need for recharging by external electrical energy can be designed. After searching for multiple aqueous redox couples, it was revealed that only $Co(bpy)_3^{2+/3+}$ anolyte (+1.2 mV/K) and $Fe(CN)_6^{3-/4-}$ catholyte (-1.7 mV/K) could fulfill the requirement. They were separated by Nafion membrane to prevent short-circuit. The cells underwent thermodynamic cycles, which consisted of (i) galvanostatic discharging to 0 mV at 20 ^oC, (ii) thermal recharging under open-circuit condition at 60 ^oC, (iii) galvanostatic discharging to 0 mV at 60 ^oC, (iv) thermal recharging

under open-circuit condition at 20 ^{o}C. The average volumetric energy, power, and charge capacities during a thermodynamic cycle were 132.1 mJ/mL, 13.95 μW/mL, and 2.84 C/mL, respectively. The heat to electricity conversion efficiency of the autonomous electrochemical heat harvester was 0.10 % at 20 ^{o}C – 60 ^{o}C operating temperature range. This low efficiency was mainly caused by high heat capacity of water. Another major issue of this autonomous electrochemical heat harvester was substantial growth of overpotential over time because $Co(bpy)_3^{2+/3+}$ species were absorbed into Nafion. Within 4 hours after the cell fabrication, overpotential became larger than thermally recharged voltage, making the autonomous electrochemical heat harvester completely unusable. In order to address this issue, we coated Nafion surface by layer-by-layer (LbL) deposited polyelectrolytes, so that large $Co(bpy)_3^{2+/3+}$ species could be selectively filtered before it contacted to Nafion. Two different polyelectrolyte films composed of $(PAH^+/PSS^-)_n$ and $(PDADMAC^+/PSS^-)_n$ were examined for this purpose. 3.5 repetitions of LbL deposition for $(PAH^+/PSS^-)_n$ turned out optimal (n = 3.5). Also, it was revealed that the performance of $(PAH^+/PSS^-)_n$ depended on pH of LbL deposition solution. Because the weak electrolyte, PAH^+ can be dissociated to have positive charge only in acidic environments[1,2], $(PAH^+/PSS^-)_n$ could be meaningfully LbL deposited only under acidic condition. Upon changing supporting salt concentration during LbL process, selective filtering capability of $Co(bpy)_3^{2+/3+}$ was greatly affected. As polyelectrolytes are composed of hydrophobic carbon backbones and dissociable functional groups, there are two different driving forces exerted in the polyelectrolytes. Attraction between the carbon backbones causes coiling, whereas Coulombic repulsion between dissociated functional groups with same charges results in disentanglement. The salt plays a key role in shielding electrostatic repulsion among the functional groups. Therefore, the higher the supporting salt concentration, the thicker the LbL deposited film. At solubility limit of the supporting NaCl in water (5.0 M), $(PAH^+/PSS^-)_n$–coated Nafion membrane showed complete impermeability not only to $Co(bpy)_3^{2+/3+}$, but also to K^+. Except for this extreme case, $(PAH^+/PSS^-)_{3.5}$ showed best Nafion protection capability at high NaCl concentration (1.0 M). In comparison, $(PDADMAC^+/PSS^-)_n$ could not inhibit $Co(bpy)_3^{2+/3+}$ absorption into Nafion for a long time, at all LbL deposition conditions, such as repetition and supporting NaCl concentration. pH-dependency test was excluded, as both $PDADMAC^+$ and PSS^- are strong polyelectrolytes, of which dissociation is independent from H^+ or OH^- concentrations. Why only $(PAH^+/PSS^-)_n$ had $Co(bpy)_3^{2+/3+}$ blocking

capability was attributed to size-based exclusion. Polyelectrolyte films have nanoscale pores which can filter out certain molecules or ions of which sizes are larger than the nanopores. The sizes of nanopores are determined by charge density of polyelectrolytes, as the charge density governs how tight oppositely charged polyelectrolytes can bind together. The definition of charge density of polyelectrolytes is valence of functional group at the polylelectrolyte per number of carbons in the constituent monomer. Charge densities of monomers of PAH^+, PSS^-, $PDADMAC^+$ were +e per 3 carbons, -e per 10 carbons, and +e per 8 carbons, respectively. As PAH^+ had the highest charge density among them, $(PAH^+/PSS^-)_n$ could possess nanopores as small as 0.67 nm, while nanopores of $(PDADMAC^+/PSS^-)_n$ were as large as 0.82 nm[3,4]. Given that hydrated ionic radii of K^+ and $Co(bpy)_3^{2+/3+}$ are 0.28 nm[5] and 0.68 nm[6] respectively, $Co(bpy)_3^{2+/3+}$ should be filtered by $(PAH^+/PSS^-)_n$ films by size. $(PDADMAC^+/PSS^-)_n$ could not exclude $Co(bpy)_3^{2+/3+}$ by size, causing much shorter lifetime of Nafion. If polyelectrolytes with even higher charge densities, due to less carbons in their monomers, are available, even smaller size of nanopores are expected. These findings can be extended to where molecular or ionic filtration by size is needed.

Lastly, solid-state electrode-based autonomous electrochemical heat harvester was explored in order to avoid issues from the previous version of flow-battery type autonomous electrochemical heat harvester. This newer type of electrochemical heat harvester did not need expensive Nafion, hence overpotential growth over time may be dodged. Their electrochemical potential could be tuned continuously. Furthermore, higher conversion efficiency could be achieved by removing water which costs high heat capacity. P2-Na_xCoO_2 was chosen for solid-state electrode-based autonomous electrochemical heat harvester, because its high ionic and electronic conductivity was expected to reduce the overpotential. Because plateau potential was the necessary condition to keep the electrochemical potential steady upon inevitable self-discharge, the widest plateau potential of P2-Na_xCoO_2 at 2.3 V vs. Na/Na^+ was chosen as the operating condition. Tuning the structural disorder of P2-Na_xCoO_2 by ball-milling process led to huge enhancement of electrochemical thermopower from -0.65 mV/K to +9.50 mV/K at 2.3 V vs. Na/Na^+. Stacking those 2 cells with P2-Na_xCoO_2 and BM-Na_xCoO_2 toward the opposite directions was expected to produce total thermopower 10.15 mV/K at 0 V of the combined dual cell stack voltage. Thus, a thermodynamic heat harvesting cycle without the need for charging by external energy could be designed. The estimated efficiency of this autonomous electrochemical heat

harvester reached up to 6.3 %, operating between 20 ºC - 40 ºC. This prototypical design of the autonomous electrochemical heat harvester can further progress toward flexible and more efficient electrochemical heat harvesters, provided highly conductive, less heat capacitive solid-state electrolyte and printing technology are combined in optimized architectures.

5.2. Outlook

5.2.1. PEDOT:PSS-based Heterostructured Thermoelectric Systems

We found that modulation doping can improve power factors in Si / PEDOT:PSS and Ge / PEDOT:PSS systems. This operating principle can be more broadly applied for nanoscale composites of thermoelectric systems. In order to maximize the effect of modulation doping on thermoelectric performance enhancement, it is necessary to increase portion of interfaces in the composite system, while maintaining electrical conduction pathway. Higher static dielectric constant of modulation-doped material is also favorable, because it can enlarge Debye length, facilitating diffusion of the charge carriers deeper into the modulation-doped material.

Another critical requirement is band alignment, which should be directed to foster charge transfer at the interface. Assuming Mott-Schottky rule is followed at a heterojunction, valence band edge of the modulation dopant material should be located farther from the vacuum level for p-type modulation doping, whereas conduction band of modulation dopant material should be closer to the vacuum level for n-type modulation doping. However, Mott-Schottky rule is often violated; this rule of thumb may not be useful for practical heterojunctions to predict if modulation doping can happen for a given heterojunction. As demonstrated in this thesis, spectroscopic band offset measurements[7,8] can function as the simplest indicator to modulation doping in generic heterojunctions. Lastly, if other conductive polymers with high carrier concentration and different electronic band structures are discovered, it may open unexplored possibilities to conductive polymer / inorganic nanoscale composites with improved thermoelectric characteristics, along with longstanding impacts on organic electronics in general.

5.2.2. Autonomous Electrochemical Heat Harvesters

In the earlier part of autonomous electrochemical heat harvester research, although LbL deposition could protect Nafion from $Co(bpy)_3^{2+/3+}$ absorption, LbL processing time was usually long, which may restrict its widespread usage[9]. In order to bypass LbL process, other aqueous redox species with intersecting half-cell potentials and the same sign of the charges can be explored. For instance, if both catholyte and anolyte are only composed of negatively charged redox species, then negatively charged Nafion will not absorb any of redox active species, and possibly

overpotential growth issue can be avoided. Or both catholyte and anolyte can have positively charged redox species only, and anion permeation membrane can be selected in place of the Nafion to bypass the absorption issue.

Recent research revealed that thermopowers of solution-based redox couples can be further enhanced up to -9.9 mV/K by relying not only on redox entropy, but also on phase transformation entropy[10]. This design principle of entropy incorporation from different physical origins can be further developed in order to push thermopowers toward even higher degree.

Engineering difficulty in building autonomous electrochemical heat harvesters using solid-state electrode materials situated on self-discharge, which complicated keeping the set voltages steady over long time. The effect of self-discharge on potential can be minimized by utilizing electrode materials with very flat plateau profile, such as $Li_{4+x}Ti_5O_{12}$ and Li_xFePO_4[11,12]. If electronically insulating nature of those materials can be relieved by high carbon content in the composite electrodes, they may become competitive candidates to engineer autonomous electrochemical heat harvesters in the future.

Correlation between electrochemical mode of energy storage (e.g. secondary batteries / supercapacitors) and electrochemical thermopowers is clear in **Figure 5.1**, which gathered electrochemical thermopowers in the previous studies[13-27] and this study. For Na_xCoO_2, the effect of transition from the battery electrode material to the EDLC electrode material was also proven drastic on redox activity and thermopower. The relationship between modes of electrochemical energy storage and thermopowers may be generalized through more systematic investigations in the future.

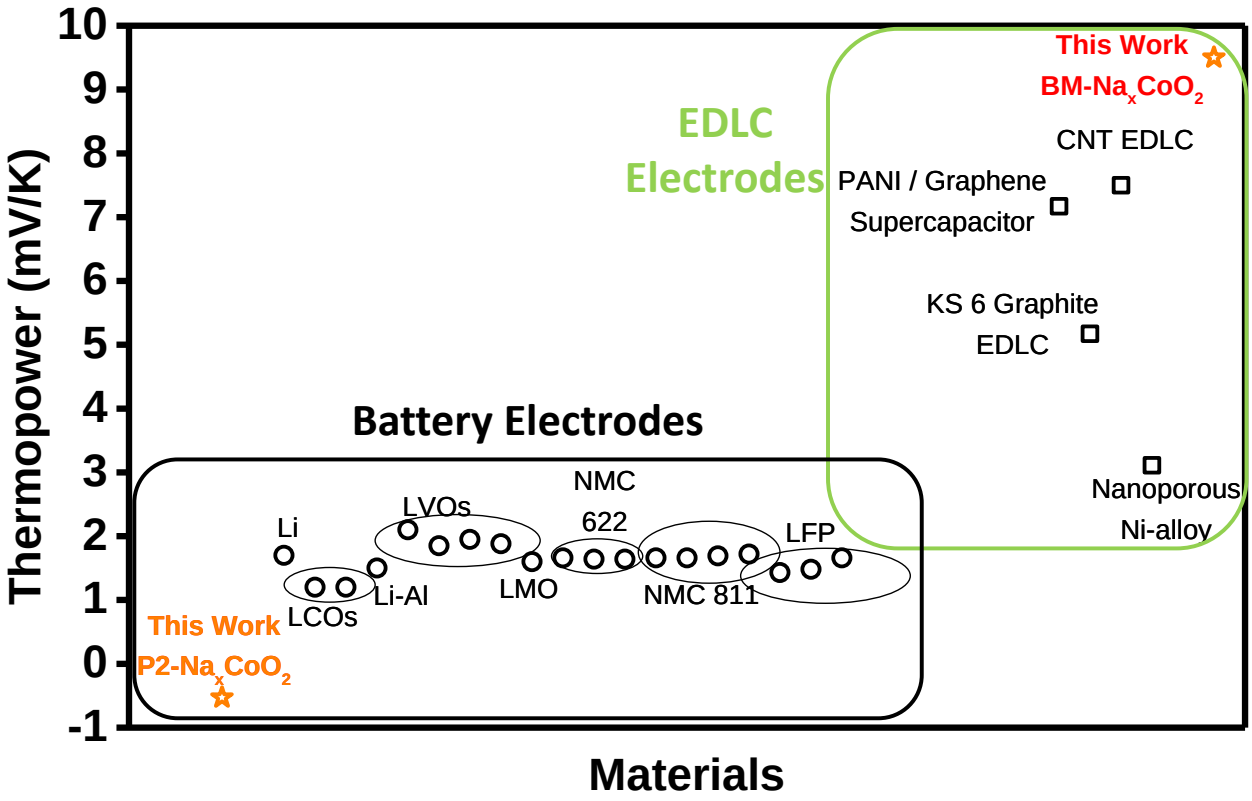

Figure 5.1. A map of electrochemical thermopowers of various materials from previous reports[96-99,106,125-134]. The general trend here proposes that electrochemical thermopowers of EDLC electrodes are higher than rechargeable battery electrodes, such as Li-ion battery and Na-ion battery electrodes in general. From the left hand side, identities of the listed materials are as follows. Li[23], LCO: Li_xCoO_2[15,18,21,22], Li-Al: Lithium-Aluminum alloy[28], LVO: $Li_xV_2O_5$[13,22,26], LMO: $Li_xMn_2O_4$[20,24,25], NMC 622: $Li_xNi_{0.6}Mn_{0.2}Co_{0.2}O_2$[22], NMC 811: $Li_xNi_{0.8}Mn_{0.1}Co_{0.1}O_2$[22], LFP: Li_xFePO_4[22] in 'Battery Electrodes' category. PANI / Graphene Supercapacitor: polyaniline / graphene electrode in supercapacitor[29], CNT EDLC: carbon nanotube electrode in EDLC[30], Ni-coated MWCNT: Nickel-coated multi-walled carbon nanotube in EDLC[31], Nanoporous Ni-alloy: nanoporous Nickel-Copper alloy electrode in EDLC[32] in 'EDLC Electrodes' category, respectively.

References

1 Cho, C. & Zacharia, N. S. Film Stability during Postassembly Morphological Changes in Polyelectrolyte Multilayers Due to Acid and Base Exposure. *Langmuir : the ACS journal of surfaces and colloids* **28**, 841-848, doi:10.1021/la203522z (2012).

2 Ferreira, Q. *et al.* Determination of Degree of Ionization of Poly(allylamine hydrochloride) (PAH) and Poly[1-[4-(3-carboxy-4 hydroxyphenylazo)benzene sulfonamido]-1,2-ethanediyl, sodium salt] (PAZO) in Layer-by-Layer Films using Vacuum Photoabsorption Spectroscopy. *Langmuir : the ACS journal of surfaces and colloids* **29**, 448-455, doi:10.1021/la304036h (2013).

3 Jin, W., Toutianoush, A. & Tieke, B. Size- and charge-selective transport of aromatic compounds across polyelectrolyte multilayer membranes. *Applied Surface Science* **246**, 444-450, doi:https://doi.org/10.1016/j.apsusc.2004.11.067 (2005).

4 Tieke, B., Toutianoush, A. & Jin, W. Selective transport of ions and molecules across layer-by-layer assembled membranes of polyelectrolytes, p-sulfonato-calix[n]arenes and Prussian Blue-type complex salts. *Advances in Colloid and Interface Science* **116**, 121-131, doi:https://doi.org/10.1016/j.cis.2005.05.003 (2005).

5 Marcus, Y. Ionic radii in aqueous solutions. *Chemical reviews* **88**, 1475-1498, doi:10.1021/cr00090a003 (1988).

6 Hupp, J. T. & Weaver, M. J. Solvent, ligand, and ionic charge effects on reaction entropies for simple transition-metal redox couples. *Inorganic Chemistry* **23**, 3639-3644, doi:10.1021/ic00190a042 (1984).

7 Kraut, E. A., Grant, R. W., Waldrop, J. R. & Kowalczyk, S. P. Semiconductor core-level to valence-band maximum binding-energy differences: Precise determination by x-ray photoelectron spectroscopy. *Physical Review B* **28**, 1965-1977 (1983).

8 Kraut, E. A., Grant, R. W., Waldrop, J. R. & Kowalczyk, S. P. Precise Determination of the Valence-Band Edge in X-Ray Photoemission Spectra: Application to Measurement of Semiconductor Interface Potentials. *Physical review letters* **44**, 1620-1623 (1980).

9 Peng, C. *Electrostatic layer-by-layer assembly of hybrid thin films using polyelectrolytes and inorganic nanoparticles* 3533236 thesis, Georgia Institute of Technology, (2011).

10 Zhou, H. & Liu, P. High Seebeck Coefficient Electrochemical Thermocells for Efficient Waste Heat Recovery. *ACS Applied Energy Materials* **1**, 1424-1428, doi:10.1021/acsaem.8b00247 (2018).

11 Park, J.-K. *Principles and applications of lithium secondary batteries*. (Weinheim, Germany : Wiley-VCH ; [Chichester, England : Distributor, John Wiley], c2012., 2012).

12 Sasaki, T., Ukyo, Y. & Novák, P. Memory effect in a lithium-ion battery. *Nature materials* **12**, 569, doi:10.1038/nmat3623 (2013).

13 Toroshchina, E., Ravdel, B. & Tikhonov, K. Thermodynamic Properties of the Electrochemical-Cell Li / $LiCiO_4$ (Propylene Carbonate) / $Li_xV_2O_5$. *Sov Electrochem* **23**, 1435-1438 (1987).

14 Dahn, J. R. & Haering, R. R. Entropy measurements on Li_xTiS_2. *Canadian Journal of Physics* **61**, 1093-1098, doi:10.1139/p83-140 (1983).

15 Viswanathan, V. V. *et al.* Effect of entropy change of lithium intercalation in cathodes and anodes on Li-ion battery thermal management. *Journal of Power Sources* **195**, 3720-3729, doi:https://doi.org/10.1016/j.jpowsour.2009.11.103 (2010).

16 Fultz, B. Vibrational thermodynamics of materials. *Progress in Materials Science* **55**, 247-352, doi:https://doi.org/10.1016/j.pmatsci.2009.05.002 (2010).

17 Reynier, Y. F., Yazami, R. & Fultz, B. Thermodynamics of Lithium Intercalation into Graphites and Disordered Carbons. *Journal of The Electrochemical Society* **151**, A422-A426, doi:10.1149/1.1646152 (2004).

18 Reynier, Y. *et al.* Entropy of Li intercalation in Li_xCoO_2. *Physical Review B* **70**, doi:10.1103/PhysRevB.70.174304 (2004).

19 Reynier, Y., Yazami, R. & Fultz, B. The entropy and enthalpy of lithium intercalation into graphite. *Journal of Power Sources* **119-121**, 850-855, doi:https://doi.org/10.1016/S0378-7753(03)00285-4 (2003).

20 Ravdel, B., Pozin, M. Y., Tikhonov, K. & Rotinyan, A. Thermodynamic Properties of the Electrochemical Cell: Li / $LiClO_4$ (Propylene Carbonate) / Li_xMnO_2. *Sov Electrochem* **23**, 1459-1464 (1987).

21 Honders, A., der Kinderen, J. M., van Heeren, A. H., de Wit, J. H. W. & Broers, G. H. J. The thermodynamic and thermoelectric properties of Li_xTiS_2 and Li_xCoO_2. *Solid State Ionics* **14**, 205-216 (1984).

22 Linford, P. A., Lithium ion power generator : a novel system for direct thermal to electric energy conversion. *Thesis from Department of Mechanical Engineering at Massachusetts Institute of Technology* (2017).

23 Schmid, M. J., Xu, J., Lindner, J., Novák, P. & Schuster, R. Concentration Effects on the Entropy of Electrochemical Lithium Deposition: Implications for Li+ Solvation. *The Journal of Physical Chemistry B* **119**, 13385-13390, doi:10.1021/acs.jpcb.5b07670 (2015).

24 Takano, K. *et al.* Entropy change in lithium ion cells on charge and discharge. *Journal of Applied Electrochemistry* **32**, 251-258, doi:10.1023/a:1015547504167 (2002).

25 Lu, W., Belharouak, I., Liu, J. & Amine, K. Thermal properties of $Li_{4/3}Ti_{5/3}O4$ / $LiMn_2O_4$ cell. *Journal of Power Sources* **174**, 673-677, doi:https://doi.org/10.1016/j.jpowsour.2007.06.199 (2007).

26 Pereira-Ramos, J. P., Messina, R., Piolet, C. & Devynck, J. A thermodynamic study of electrochemical lithium insertion into vanadium pentoxide. *Electrochimica Acta* **33**, 1003-1008, doi:https://doi.org/10.1016/0013-4686(88)80102-6 (1988).

27 Hudak, N. S. & Amatucci, G. G. Energy Harvesting and Storage with Lithium-Ion Thermogalvanic Cells. *Journal of The Electrochemical Society* **158**, A572, doi:10.1149/1.3568820 (2011).

28 Yao, N. P., Herédy, L. A. & Saunders, R. C. Emf Measurements of Electrochemically Prepared Lithium-Aluminum Alloy. *Journal of The Electrochemical Society* **118**, 1039-1042, doi:10.1149/1.2408242 (1971).

29 Kim, S. L., Lin, H. T. & Yu, C. Thermally Chargeable Solid-State Supercapacitor. *Advanced Energy Materials* **6**, 1600546-n/a, doi:10.1002/aenm.201600546 (2016).

30 Wang, J. *et al.* "Thermal Charging" Phenomenon in Electrical Double Layer Capacitors. *Nano letters* **15**, 5784-5790, doi:10.1021/acs.nanolett.5b01761 (2015).

31 Lim, H., Shi, Y. & Qiao, Y. Thermally chargeable supercapacitor working in a homogeneous, changing temperature field. *Applied Physics A* **122**, 443, doi:10.1007/s00339-016-9981-2 (2016).

32 Qiao, Y., Punyamurtula, V. K. & Han, A. Thermally induced capacitive effect of a nanoporous monel. *Applied Physics Letters* **91**, 153102, doi:10.1063/1.2798245 (2007).